100 Gbps Optical Coherent Modem for Low Earth Orbit Optical Inter-Satellite Links

by

Raichelle Joy Aniceto

B.S., Massachusetts Institute of Technology (2016)
S.M., Massachusetts Institute of Technology (2017)

Submitted to the Department of Aeronautics and Astronautics
in partial fulfillment of the requirement for the Degree of

Doctor of Philosophy in Aeronautics and Astronautics
at the
MASSACHUSETTS INSTITUTE OF TECHNOLOGY
~~December 2019~~ February 2020

Author ..... Signature redacted
Department of Aeronautics and Astronautics
December 20, 2019

Certified by ..... Signature redacted .....
Prof. Kerri Cahoy
Associate Professor, Aeronautics and Astronautics
Thesis Supervisor

Certified by ..... Signature redacted .....
Prof. Vincent Chan
Professor, Electrical Engineering and Computer Science

Certified by ..... Signature redacted
Dr. Hamid Hemmati
Director of Engineering, Facebook

Certified by ..... Signature redacted
Dr. Randall Milanowski
President, Milanowski and Associates, Inc.

Certified by ..... Signature redacted
Dr. Slaven Moro
Communication Systems Engineering Lead, Facebook

Accepted by ..... Signature redacted .....
Sertac Karaman
Associate Professor, Aeronautics and Astronautics
Chair, Graduate Program Committee

100 Gbps Optical Coherent Modem for Low Earth Orbit Optical Inter-Satellite Links

by

Raichelle Joy Aniceto

Submitted to the Department of Aeronautics and Astronautics
on December 20, 2019 in Partial Fulfillment of the
Requirements for the Degree of Doctor of Philosophy in
Aeronautics and Astronautics

ABSTRACT

Free space optical communication (FSOC) provides a viable and cost-effective solution for future satellite systems with advantages in bandwidth, unregulated frequencies, and reduced system mass, volume, and power consumption in comparison with radio frequency systems. Several FSOC systems successfully demonstrated links between spacecraft and Earth ground stations as well as inter-satellite links. Commercial industry, including companies such as SpaceX and Telesat, have taken an interest in utilizing the benefits of FSOC for proposed LEO constellations and using optical inter-satellite links (OISLs) to reduce the need for expensive worldwide ground tracking networks. State-of-the-art FSOC space terminal data rate performance is 5.625 Gbps using coherent BPSK detection, achieved by the Tesat and DLR laser communication terminal (LCT) in 2008. The Tesat and DLR LCT demonstrated LEO to LEO OISLs over a link distance of 5100 km.

Within the past decade, the terrestrial communications industry advances in optical coherent DSP ASICs and integrated fiber optic component packages have enabled high capacity optical coherent communications systems with data rates of 100 Gbps and greater. It is desirable to leverage the data rate performance and cost point of these technologies to develop a state-of-the-art optical coherent modem system for FSOC space applications.

The goal of this work is to develop an optical coherent communications modem for LEO-to-LEO inter-satellite links with improvement in data rate of 10 times the current state of the art of 5.6 Gbps using commercial off the shelf components, such as optical coherent DSP ASICs, coherent transmitters, coherent receivers, and lasers, with minimal modifications as needed for space use. This work focuses on developing an optical coherent communications modem for data rates up to 100 Gbps using commercial telecommunications industry components compatible with 100G wavelength division multiplexed (WDM) coherent systems.

We develop a process for selecting commercial optical coherent technologies that can meet performance requirements in a LEO space environment. We develop optical coherent modem hardware and assess the selected commercial optical coherent technologies for uses in the space environment. We identify and develop cost-effective modifications based on radiation characterization, ensuring that we can achieve successful space operation and meet performance requirements.

Thesis Supervisor: Kerri Cahoy
Title: Associate Professor of Aeronautics and Astronautics

Contents

List of Figures

List of Tables

Acknowledgements

This work was sponsored by fellowships from the National Science Foundation Graduate Research Fellowship Program (GRFP) and Facebook Connectivity Lab.

I would like to acknowledge and thank my graduate advisor, Dr. Kerri Cahoy, for her support and her guidance throughout my time in the MIT Department of Aeronautics and Astronautics. I would not be where I am today without Kerri's continued support and mentorship since the freshman year of my MIT undergraduate education. I would like to thank Dr. Vincent Chan for his support as a committee member and for providing his expertise in terrestrial fiber optic communications technology.

Dr. Slaven Moro has served as my technical mentor for optical coherent communications technology throughout my entire graduate education. I would like to thank him for his support and for the opportunities he has provided for me to learn and grow technically.

Completion of this work would not have been possible without the support of Blue Marble Communications, Inc. I would like to thank Neal Nicholson, Daniel Greene, Ken Iles, Dan Heckel, Nathan Woodcock, Kelli Montigel, Seth Block, Ethan Block, and Bernard Parmac for their support with development of the optical coherent modem hardware.

Dr. Randall Milanowski has served as my technical radiation effects mentor throughout my entire graduate education. I would like to thank Dr. Randall Milanowski, Steve McClure, and Greg Allen for their support and guidance with radiation effects modeling and radiation testing. I would like to thank Mike Sivertz and Adam Rusek for their support with heavy ion radiation testing at the NASA Space Radiation Laboratory in Brookhaven National Laboratory. Camille Belanger-Champagne, Mike Trinczek, and Ewart Blackmore provided support with proton radiation testing at TRIUMF National Laboratory.

I would like to thank the Facebook team for technical support of this work. Dr. Chien-Chung Chen and Dr. Yassir Azziz are the technical reviewers of this work, and I would like to thank them for their technical guidance and mentorship. Stephen Efthyvoulos provided technical guidance and support with development of optical coherent modem hardware and radiation testing. Matt Hunwardsen, Eric D. Miller, and Alexa Aguilar provided on-site support with radiation testing. I would like to thank Dominic Jandrain for support with processing of radiation testing data files.

I am grateful to my colleagues and friends for their support. I would like to thank my personal mentor, Dr. Whitney Lohmeyer, who is the source of my inspiration to pursue graduate school. I would like to thank Michael Lin, Choah Kim, and my parents, Romeo and Ruth Aniceto, for their encouragement throughout my Doctorate program. I would like to thank Íñigo del Portillo, who has been my graduate school "older brother," providing me with guidance with my graduate school work and research. I would like to thank my Doctorate Qualifying Exam support group Eric Hinterman, Matthew Moraguez, and Alejandro Trujillo.

Chapter 1

Background

1.1 Introduction

Global Internet Protocol (IP) traffic is estimated to reach 2.3 zettabytes (ZB) (10^{21}) per year by 2020 [Cisco, 2016]. Satellite communications systems have the potential to play a key role in meeting worldwide demand by providing capacity that can augment or compete with terrestrial broadband. Satellite systems are well-suited for providing connectivity to large areas with low population densities. Subscribers can connect to broadband and Internet backbone networks rapidly with low overhead required for the ground terminal, only a modem and an antenna. The cost to field satellite terminals for providing connectivity is approaching costs of point-by-point roll out of terrestrial fiber networks [ITU and UNESCO, 2015].

The development and launch of satellites as well as the construction of satellite broadband infrastructure is still a significant investment. Second to satellite launch costs, which can reach tens of millions of dollars, capital and operating expenditures for radio frequency (RF) gateways dominate the cost of connectivity via broadband systems. Due to limited bandwidth, increasing capacity requires additional spatially diverse ground gateway sites.

Free space optical communications (FSOC) are a viable and cost-effective solution for future satellite systems. The higher carrier frequency and narrow transmit beamwidth of optical communications have advantages over RF [Hemmati, 2008]. Higher frequency enables greater bandwidth, reduces system mass, volume, and power consumption for transmit and receive apertures, and avoids the frequency regulation and spectrum restrictions of RF communications systems [Toyoshima, 2005; Cornwell, 2016].

The National Telecommunications and Information Administration (NTIA) of the United States Department of Commerce does not currently require authorization for the use of frequencies above 3000 GHz [NTIA, 2015]. FSOC systems typically use frequencies of 277.6 THz to 291.1 THz (1080 nm – 1030 nm) or 181.7 THz to 197.2 THz (1650 nm – 1520 nm). The Laser Clearing House (LCH) is tasked with ensuring orbital assets are not negatively impacted by lasers and requires US Department of Defense (DoD) laser projects to coordinate with the LCH. Many non-DoD laser projects choose to coordinate with the LCH to ensure no damage to satellites [Cornwell, 2017].

However, the higher frequency of optical communications is vulnerable to weather outages, such as cloud coverage, if crosslinks and multiple optical ground stations are not incorporated in the overall system design. A geographically diverse set of ground stations is required to mitigate the effects of clouds and achieve higher real-time system reliability. Optimization tools and models have been used to determine optical ground station locations and cloud detection systems have been developed to mitigate cloud impacts on FSOC downlink systems [Aliss and Felton, 2012 and Barrios Del Portillo, 2016].

A narrow beamwidth enables greater power efficiency and increased security, but at the cost of requiring precision pointing control [Yoon, 2017]. FSOC systems are currently not as prevalent as RF communications systems on satellites due to challenges with fine beam pointing and cloud coverage [Hemmati, 2008]. As fine beam pointing technology advances, mitigation strategies for cloud coverage are adopted, and development of optical communications systems advances, space-based, FSOC systems will become more prevalent in the near future.

1.2 Free Space Optical Communication Demonstrations

1.2.1 Demonstrated Space-Based FSOC Systems

Within the past two decades, several FSOC systems have been successfully demonstrated with optical links between Earth-orbiting spacecraft and Earth ground stations as well as optical inter-satellite links (OISLs). Demonstrated space-based FSOC systems in near-Earth or Earth-orbiting applications are summarized in Table 1. Table 1 is representative and does not include all FSOC demonstrations. Limited literature is available for some previous demonstrations including the US DoD GEOLite (2001) downlink from a geostationary earth orbit (GEO) satellite to an Earth ground station, China National Space Administration (CNSA) Laser Communication Experiment (LCE) (2011) from a low earth orbit (LEO) satellite to an Earth ground station, and Russian company "Precision Systems and Instruments" laser space communication technology demonstration from the International Space Station (ISS) to an Earth ground station (2014) [Cornwell, 2016; Zhang and Wang, 2017; Grigoryev et al., 2014].

Table 1. Demonstrated FSOC systems and key parameters

FSOC System	Transmit Parameters						Maximum Link Distance	Receiver Parameters		
	Terminal Source	Aperture ($1/e^2$)	λ	Transmit Power	Terminal Mass	Power Consumption		Terminal Source	Data Rate	Detection
LCE (NICT 1994)	Elliptical Orbit (ETS-VI)	-	830 nm	13.8 mW	22.4 kg	-	38700 km	Ground Terminal (NICT, JPL)	1.024 Mbps	Direct
SILEX (ESA 2001)	LEO (SPOT4)	250 mm	847 nm	70 mW	150 kg	150 W	38000 km	GEO (ARTEMIS)	50 Mbps	Direct OOK – NRZ
SILEX (ESA 2004)	GEO (ARTEMIS)	125 mm	819 nm	10 mW (avg.)	157 kg	200 W	38000 km	Ground Terminal (OGS)	2.0 Mbps	Direct 2-PPM
SILEX (ESA 2004)	Ground Terminal (OGS)	40-300 mm	847 nm	300 mW (max)	-	-	38000 km	GEO (ARTEMIS)	49.37 Mbps	Direct NRZ
LUCE (JAXA 2005)	LEO (OICETS)	260 mm	847 nm	100 mW	170 kg	150 W	38000 km	GEO (ARTEMIS)	50 Mbps	Direct OOK-NRZ
SILEX (ESA 2005)	GEO (ARTEMIS)	125 mm	819 nm	37 mW	157 kg	200 W	38000 km	LEO (OICETS)	2.048 Mbps	Direct
LCT (Tesat / DLR 2008)	LEO (NFIRE)	125 mm	1064 nm	700 mW	35 kg	120 W	5100 km	LEO (TerraSAR-X)	5.625 Gbps	Coherent (BPSK)
LCT (Tesat / DLR 2008)	LEO (NFIRE)	125 mm	1064 nm	700 mW	35 kg	120 W	1000 km	Ground Terminal (ESA)	5.625 Gbps	Coherent (BPSK)
LLCD (NASA / MIT LL 2013)	Lunar Orbit (LADEE)	108 mm	1550 nm	500 mW	30 kg	90 W	400000 km	Ground Terminal	622 Mbps	Direct
OPALS (JPL 2014)	ISS	-	1550 nm	> 800 mW	50 kg	-	700 km	Ground Terminal (JPL)	50 Mbps	Direct
EDRS (ESA 2014) Tesat LCT Gen 2	LEO (Sentinel 1A)	135 mm	1064 nm	2.2 W	45 kg	160 W	45000 km	GEO (Alphasat)	1.8 Gbps	Coherent BPSK

EDRS (ESA 2016) Tesat LCT Gen 2	LEO (Sentinel 2A/1B/2B)	135 mm	1064 nm	2.2 W	45 kg	160 W	45000 km	GEO (EDRS A/C)	1.8 Gbps	Coherent BPSK
OSIRIS v2 (DLR 2016)	LEO (BiROS)	-	1550 nm	-	1.65 kg	37 W	500 km	Ground Terminal	1.0 Gbps	Direct OOK
OSIRIS v1 (DLR 2017)	LEO (Flying Laptop)	-	1550 nm	1 W	1.3 kg	26 W	600 km	Ground Terminal	1000 Mbps	Direct OOK
OCSD (Aerospace Corporation 2018)	LEO (AeroCube 7B)	-	1064 nm	3 W	2.3 kg	10 - 20 W	450 km, 51.6 deg	Ground Terminal (Aerospace Corporation)	200 Mbps	Direct OOK

The National Institute of Information and Communications Technology (NICT) performed the first bi-directional optical communications demonstration in 1994 between the Laser Communication Experiment (LCE) onboard the Engineering Test Satellite (ETS-VI) and both a NICT optical ground station in Tokyo, Japan and a Jet Propulsion Laboratory (JPL) optical ground station in Table Mountain, California. During the demonstration, ETS-VI was in a highly elliptical orbit with a 38,700 km apogee, 8560 km perigee, and 13-degree inclination. LCE weighed 22.4 kg and transmitted data with Manchester coded pulse modulation at ~1 Mbps. An average optical output power of 13.8 mW was transmitted over a 37,800 km link distance. A laser diode with center wavelength of 830 nm was used as the downlink transmitter source and an argon ion laser with center wavelength of 514.5 nm was used as the uplink source [Araki et al., 1997].

In 2001, the European Space Agency (ESA) demonstrated Semiconductor Inter-satellite Link Experiment (SILEX), the first OISL from a LEO French spacecraft, Satellite Pour l'Observation de la Terre 4 (SPOT4), to a GEO spacecraft, Advanced Relay and TEchnology MIssion Satellite (ARTEMIS). The optical link was at a distance of ~40,000 km with data rate of 50 Mbps using On-Off Keying (OOK) modulation with Non-Return to Zero (NRZ) coding. The SPOT-4 terminal used a GaAlAs diode at 847 nm for the transmitter optical source with a 60 mW optical output power level through a transmit telescope aperture of 250 mm. The SILEX LCT on ARTEMIS used a GaAlAs laser diode at 819 nm for the transmitter optical source with 37 mW optical output power through an aperture ($1/e^2$) of 125 mm [Tolker-Nielsen and Oppenhauser, 2002]. The receiver was a silicon avalanche photodiode with telescope diameter of 250 mm [Alonso et al., 2004]. The SILEX terminals were ~100 kg [Fletcher et al., 1991].

The Japanese Aerospace Exploration Agency (JAXA) designed an optical communications terminal, Laser Utilizing Communications Equipment (LUCE), onboard the JAXA spacecraft Optical Inter-orbit Communications Engineering Test Satellite (OICETS). The LUCE system weighed 140 kg and transmitted an average optical power of 100 mW. In 2005, LUCE and SILEX, onboard ARTEMIS, demonstrated the first bi-directional optical inter-orbit communications experiment between LEO and GEO. The optical link was nearly 40,000 km with the LEO to GEO uplink transmitting at data rate of 50 Mbps and the GEO to LEO downlink transmitting at data rate of 2 Mbps using 2-PPM [Fujiwara et al., 2007; Toyoshima et al., 2004].

In 2004, successful bi-directional optical links were completed between SILEX LCT on ARTEMIS spacecraft in GEO and ESA optical ground station (OGS) at the Observatorio del Teide operated by the Instituto de Astrofisica de Canarias (IAC). The link distance was ~38,000 km. Optical downlink from ARTEMIS to OGS achieved a data rate of 2.048 Mbps using 2-PPM, and optical uplink from OGS to ARTEMIS achieved a data rate of 49.3724 Mbps using NRZ [Alonso et al., 2004].

MIT Lincoln Laboratory designed the Lunar Laser Communications Demonstration (LLCD) FSOC system, Lunar Laser Space Terminal (LLST) with a mass of 30 kg, onboard the NASA mission, Lunar Atmosphere and Dust Environment Explorer (LADEE). In 2013, the LLST transmitted an optical downlink with center wavelength of 1550 nm from lunar orbit to the Lunar Laser Ground Terminals (LLGT) in White Sands, New Mexico with data rate of 622

Mbps and 0.5 W optical output power over a 400,000 km maximum link distance [Robinson et al., 2011; Boroson et al., 2014].

In 2014, NASA JPL demonstrated the Optical Payload for Laser Communications Science (OPALS) system with an optical downlink from the International Space Station (ISS) to a ground station at Table Mountain, California. The OPALS system transmitted with a data rate of 50 Megabits per second (Mbps) using OOK modulation and Reed Solomon forward error correction (FEC). The system weighed 50 kg and transmitted an average optical output power greater than 0.83 W with 1550 nm laser center wavelength [Oaida et al., 2014].

The German Aerospace Center (DLR) demonstrated two optical communications missions as part of the Optical Space Infrared Downlink System (OSIRIS) program. In 2016, the BiROS satellite, a LEO Earth observation satellite, was launched with the OSIRIS v2 terminal. The OSIRIS terminal achieved optical downlink data rates up to 1 Gbps with 1550 nm laser source. The terminal had a 37 W power consumption and mass of 1.65 kg. In 2017, OSIRIS v1 was launched on the Flying Laptop satellite developed by the University of Stuttgart. OSIRIS v1 achieved optical downlink data rate of 200 Mbps with a 1550 nm laser source and 1 W optical output power. OSIRIS v1 had a power consumption of 26 W and a mass of 1.3 kg. Both OSIRIS v1 and OSIRIS v2 were technology demonstration missions for the concept of applying commercial off the shelf (COTS) components in the satellite design [Fuchs and Schmidt, 2018].

Under the NASA Optical Communications and Sensors Demonstration (OCSD) program, the Aerospace Corporation demonstrated optical downlink using a laser transmitter on a LEO 1.5 U, 2.3 kg CubeSat at 900 km altitude to an Aerospace Corporation optical ground station in El Segundo, California in 2018. Data rates achieved include 50 Mbps, 100 Mbps and 200 Mbps using OOK modulation. A distributed feedback (DFB) laser output 10 mW of optical power at 1064 nm and the optical signal was encoded by modulating the current of the DFB (master oscillator configuration). The modulated optical signal passed through a filter and isolator into an ytterbium (Yb) fiber amplifier, consisting of single mode polarization maintained (PM) Yb-doped fiber pumped with a 10 W pump diode at 915 nm, to output a maximum optical power level of 3 W. The amplified optical signal exited the transmitter through an output collimator lens. The transmitter components are all COTS components and the transmitter is designed to operate over a temperature range of 10°C to 50°C [Janson and Welle, 2016; Rose et al., 2018].

The demonstrated systems were reviewed to provide a background on current state-of-the-art for space-based FSOC systems. Demonstrated space-based FSOC systems and systems currently in development (described in next sub-section) are evaluated for the key parameters and techniques correlated with achieving the highest data rates.

1.2.2 Space-Based FSOC Systems in Development

Currently, there are several efforts by industry, government entities, and academic institutions to develop FSOC systems for satellites. This subsection covers a representative subset, but others exist.

Mynaric (formerly Vialight) is a spin-off company from the DLR and offers a LEO OISL terminal, MLT-80 for high volume production available in 2019. The terminal is 10 Gigabit

Ethernet IEEE 802.3 compatible and is designed for a five to seven year lifetime in LEO polar orbit [Mynaric, 2018]. Laser Light Communications intends to deploy a global optical network, HALO, consisting of up to 12 optical satellites in medium Earth orbit (MEO) with data rates up to 200 Gigabits per seconds (Gbps) for OISLs and up to 100 Gbps for uplinks and downlinks between MEO and ground stations [Laser Light Communications, 2014].

Sinclair Interplanetary is working on optical communications for small spacecraft. Datasheets have been released for a laser crosslink system with data rates up to 100 Mbps at 250 km range and up to 6.25 Mbps at 1000 km range. The transmitter is designed with 1 W optical output power and the system weighs ~0.4 kg. A downlink laser transmitter system has been designed with data rates up to 1 Gbps for distances up to 1000 km and data rates up to 250 Mbps for distances up to 2000 km. The downlink transmitter system is designed with 1 W output power and has a mass of ~0.34 kg [Sinclair Interplanetary, 2017; Sinclair and Riesing, 2017].

Massachusetts Institute of Technology (MIT) is developing two FSOC demonstrations on CubeSats as part of the CubeSat Lasercom Infrared CrosslinK (CLICK) program. Both FSOC systems are designed with COTS components. CLICK A, previously Nanosatellite Optical Downlink Experiment (NODE) is designed for an optical downlink with 0.2 W transmit power and data rates up to 70 Mbps. CLICK B/C are designed to demonstrate optical crosslinks between two LEO CubeSats with data rates greater than 10 Mbps. The CLICK B/C laser terminals are designed to operate full duplex at 1537 nm and 1563 nm. A chip-scale atomic clock (CSAC) is used for precision ranging between the two CubeSats [Clements et al., 2016; Serra et al., 2019; Cahoy et al., 2019].

NASA is developing the Laser Communications Relay Demonstration (LCRD) mission, which will demonstrate optical communications relay services between GEO and Earth or LEO users. LCRD will be implemented on an Orbital ATK GEO satellite and will consist of two independent LCTs connected through an electronic switch to provide high-speed frame switching and routing between the LCTs. NASA is developing the Integrated LCRD LEO User Modem and Amplifier Terminal (ILLUMA-T) for integration on the Japanese Experiment Module Exposed Facility (JEM-EF) of the ISS. ILLUMA-T will serve as the LEO terminal for bi-directional OISL with LCRD in GEO as well as a bi-directional link to ground station on Earth. ILLUMA-T is designed to achieve 1.244 Gbps downlink to ground from ISS and 51 Mbps uplink from ground to ISS [Seas et al., 2018].

Another ongoing development by NASA is the Orion EM-2 Optical Communications Terminal (O2O), whose mission is to provide bi-directional optical communications capability between the Orion Multi-Purpose Crew Vehicle spacecraft and Earth. EM-2 is a seven to fourteen-day mission to transport a human crew to lunar vicinity. O2O is designed to demonstrate transmission of optical downlink to Earth with data rate of 80-250 Mbps and to receive an optical uplink from Earth with data rate of 20 Mbps [Seas et al., 2018].

As a continuation of the OSIRIS program, a collaboration between the DLR and Tesat is developing OSIRIS 4 CubeSat and OSIRIS v3. OSIRIS 4 CubeSat is a miniaturized version of OSIRIS v1 and OSIRIS v2, in the form factor of a 1 U CubeSat. The terminal is designed for 8 W power consumption, mass of 300 grams, 100 mW transmitted optical power, and downlink data rate of 100 Mbps from LEO to Earth ground station. The first demonstration mission will be in 2020. OSIRIS v3 is designed for application to the ISS Bartolomeo platform

to demonstrate optical downlink from LEO to Earth ground station with data rate of 10 Gbps. The terminal design requirements include a mass of 5 kg and a power consumption of 50 W [Fuchs and Schmidt, 2018].

As an expansion of the European Data Relay System (EDRS), a GEO node for the optical communications network will be added through a Tesat LCT on the EDRS-D GEO satellite. EDRS-D will enable GEO-GEO OISL via bi-directional links of 80,000 km to EDRS-A and EDRS-C GEO satellites with LCTs. EDRS-D LCT will be an upgraded design from Tesat GEO LCTs (second generation) with dual wavelength capability to also include 1550 nm operation. Development of the EDRS-D LCT will include cooperation among Airbus, Tesat, and NEC [Hauschildt et al., 2018].

Tesat is now working to develop the "SMART" LCT supported by the DLR for a proposed "Galileo" MEO constellation of satellites with OISLs. The first flight model of the SMART LCT is scheduled for 2020. The Galileo constellation is proposed as a 27/3/1 Walker constellation at 23,222 km. The SMART LCT for Galileo application is designed for data transmission capability of 120 kbps over a link distance up to 45,000 km and provide 5 cm ranging accuracy. Key parameters for the SMART LCT include operating wavelength of 1064 nm, transmit optical power of 5W, 70 mm aperture, 45 kg mass, and 135 W power consumption [Zech et al., 2019].

The NASA TeraByte InfraRed Delivery (TBIRD) program is developing a 200 Gbps optical downlink capability from a 6U CubeSat in LEO using two 100G commercial integrated optical transceiver modules and a 1 W commercial EDFA. The transmit telescope is a 1.2 cm collimator and each transceiver will operate at 1550 nm center wavelength [Robinson et al., 2018].

1.3 Motivation

This work is motivated by three factors: (1) State-of-the-art FSOC space demonstrations, (2) optical coherent communication COTS components from the terrestrial communications industry, and (3) recent interest in OISLs for LEO constellations.

1.3.1 State-of-the-Art Free Space Optical Communication with Coherent Detection

State-of-the-art for FSOC space terminal data rate performance is 5.625 Gbps using coherent detection, achieved by the Tesat and DLR laser communication terminal (LCT) in 2008. The Tesat and DLR LCT demonstrated LEO to LEO OISLs over a link distance of 5100 km and LEO to ground optical downlink over a link distance of 1000 km.

Under contract from the DLR and ESA, Tesat developed LCTs based on coherent homodyne binary phase shift keying (BPSK) at 1064 nm. The first generation version of the Tesat LCTs (v1) have a mass of 35 kg, a peak transmit power of 0.7 W, 125 mm Tx aperture ($1/e^2$), and 120 W power consumption [Fields et al., 2009; Sodnik et al., 2010]. One LCT (v1) was flown on the US satellite, Near Field Infrared Experiment (NFIRE) and a second LCT (v1) was flown on German satellite, Synthetic Aperture Radar for Earth Observation (TerraSAR-X). In 2008, the two LCTs demonstrated a LEO to LEO OISL over a 5000 km distance at 5.625 Gbps with coherent BPSK detection [Gregory et al., 2011]. The LCT on TerraSAR-X also

demonstrated an optical link at 5.625 Gbps for a maximum link distance of 1000 km from LEO to ESA Optical Ground Station (OGS) in Tenerife, Spain [Ciminelli et al., 2016].

The LCT uses a common transmit and receive path separated by polarization and laser frequency. In the LCT transmitter design, a seed laser provides the optical signal input to a modulator and the modulated optical signal is amplified with a fiber amplifier. Data electronics interface to the modulator driver required for biasing the modulator. In the LCT receiver design, a continuous wave single frequency LO source is co-aligned to the received optical signal input. The LO frequency offset from the received optical signal is chosen to be in the range of an electronically matched filter, which rejects background light interference and electronic noise. Tesat built the LCT receiver, which is a double quad cell optimized for pulsed coherent single photon detection. The coherent receiver system includes Doppler frequency compensation, adjusting the LO frequency based on the expected Doppler shift of the incoming optical signal [Heine, 2014]. No commercial technologies have been implemented in the development of the demonstrated LCTs. Note that the LCTs are designed to be mounted externally to the spacecraft bus with exposure to space without the additional structural shielding that can provide radiation and thermal management support.

The Tesat LCTs serve as the basis for the ESA EDRS, which is the first operational laser-based data relay service utilizing LCTs on high altitude long endurance (HALE) platforms, LEO spacecraft, and GEO spacecraft [Heine, 2014]. Tesat has designed second generation LCTs (v2) derived from the first generation LCT design, which was designed for LEO constellation applications. The second generation LCTs have been designed for LEO to GEO OISL applications and have been space qualified for a 15-year GEO mission. The second generation LCT has a mass of 45 kg, a 135 mm Tx aperture ($1/e^2$), transmit power of 2.2 W, and a power consumption of 160 W. The LCTs are designed to operate at 1064 nm center wavelength. In 2014, a LCT on LEO spacecraft Sentinel 1A demonstrated an optical link to a LCT on GEO spacecraft Alphasat over a maximum link distance of 45,000 km at data rate of 1.8 Gbps using coherent homodyne BPSK detection [Zech et al., 2015; Zech et al., 2017]. Second generation Tesat LCTs on LEO spacecraft Sentinel-2A/-1B/-2B and GEO spacecraft EDRS-A/-C have demonstrated LEO to GEO OISLs since the end of 2016, serving as the operational EDRS [Zech et al., 2019].

1.3.1.1 Coherent Detection

A majority of the space-based FSOC demonstrations have used a direct detection system. However, the highest data rates achieved by current space-based FSOC demonstrations have used a coherent detection system [Ip et al., 2008]. In a direct detection system, the received optical signal is focused directly onto a photodetector (PD), which generates a signal current proportional to the number of photons received. In a coherent system receiver, the received optical signal is superimposed with a light wave generated by a local oscillator (LO) laser and both optical signals are focused onto a PD. Figure 1 shows a basic functional block diagram of a (a) direct detection system and (b) coherent detection system.

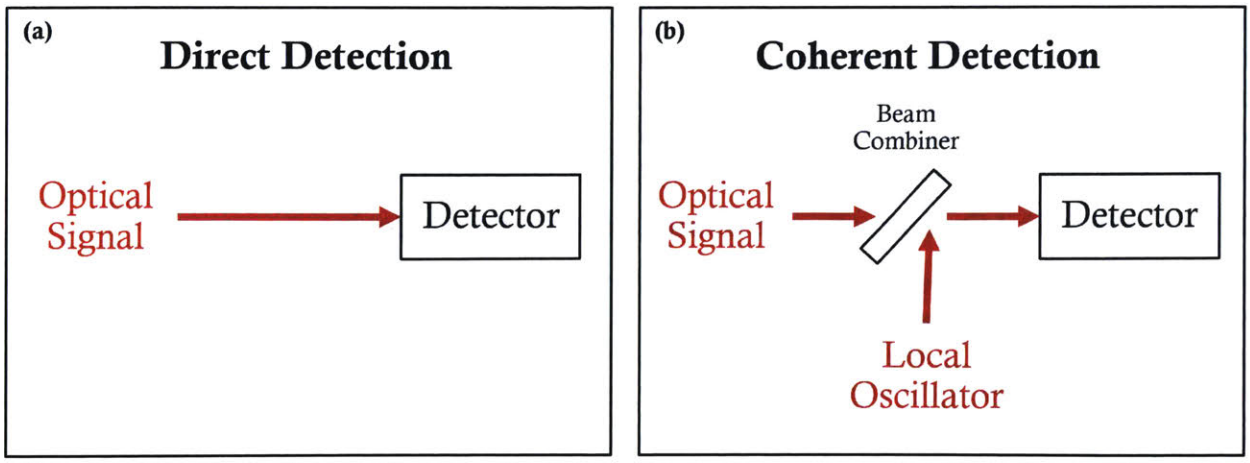

Figure 1. Basic functional diagram of (a) direct detection system and (b) coherent detection system.

The signal current from the PD in a coherent detection system is non-linear and is dependent on the amplitude, phase, and polarization of the received optical signal and LO optical signal [Pribil and Hemmati, 2008]. A coherent receiver with photodetectors computes decision variables based on the recovery of the full electric field, with information encoded in both the amplitude and phase or in the in-phase and quadrature components of a carrier [Ip et al., 2008].

Coherent detection has two key advantages over direct detection. Coherent detection is limited primarily by shot noise. The LO power is much higher than the signal power and the corresponding LO shot noise power spectral density exceeds other noise contributions. The limitation of shot noise alone allows for higher signal to noise ratio (SNR). Electronics noise, beat noise, and shot noise contribute to direct detection systems [Leeb and Winzer, 2009].

Coherent detection encodes information in the optical phase (i.e. Phase Shift Keying (PSK)) and converts phase variations into amplitude [Agrawal, 2012]. Higher order modulation formats, such as quadrature phase shift keying (QPSK) and quadrature amplitude modulation (QAM), of coherent detection allow this type of system to meet high bandwidth and data capacity demands [Xiang et al., 2014]. Coherent systems have potential to achieve highest receiver sensitivity, high spectral efficiency, tolerance against dispersion effects, and superior performance over long transmission distances [Pfau et al., 2008]. The performance of optical coherent detection systems could enable future systems with transmission at 200 Gbps, 400 Gbps, and up to 1000 Gbps per wavelength [Roberts et al., 2009].

In comparison to direct detection, coherent systems have greater design complexity associated with required digital signal processing (DSP) and dependence on key coherent components based on CMOS and photonic integrated circuit (PIC) technology. Since polarization is used to modulate and demodulate data in a coherent system (i.e. X and Y orthogonal polarizations for 100G QPSK), non-polarizing optics must be used the system. For a coherent system, there are requirements for key electro-optical components, such as a narrow (few hundred kHz) laser linewidth. A lower optical signal to noise ratio (OSNR) threshold of a coherent DSP ASIC is ideal to provide more link margin. The details and key specifications of optical coherent components is further described in Section 2.2.

For the same modulation format, spectral efficiency of a direct detection transmission system is at most 1 bps per Hertz less than the spectral efficiency of coherent detection transmission system [Mecozzi, 2018]. In order to achieve greater data rate performance than state-of-the-art coherent FSOC system by Tesat and DLR (2008), development of an optical modem for future laser communication terminal should utilize coherent detection.

1.3.2 Commercial Optical coherent Communication Technologies

Optical coherent communications were studied in the 1980s, however, interest shifted toward wavelength-division multiplexed (WDM) direct detection using erbium-doped fiber amplifiers (EDFAs). In the past few years, there has been revived interest in coherent systems since recent technological advancements in optical coherent receivers and high-speed digital circuits now allow for realization of optical coherent communications [Kikuchi, 2010]. Optical coherent receivers require high-speed analog-to-digital converters (ADCs) with sampling rates which can reach the symbol rate of high data rate signals. Fast circuit ADCs have been developed with sampling rates greater than 10 Giga-samples per second to meet the needs of high data rate optical coherent communications systems [Pfau et al., 2008]. Advances to Complementary Metal Oxide Semiconductor (CMOS) application specific integrated circuits (ASICs) and PICs are the technology building blocks of optical coherent communication systems.

We are currently in a technological era of optical coherent wavelength division multiplexed (WDM) communications, which began with coherent system implementations of 40 Gbps (40G) in 2008 and transformed toward 100 Gbps (100G) with the dual polarization (DP) QPSK modulation format in 2010 [Agrell, 2016]. There was growth toward commercialization of pluggable 100G coherent transceivers, such as the C-Form Factor Pluggable (CFP2) modules, driven through the "100G Ultra Long Haul DWDM Framework Document" and related electro-optical component documents by the Optical Internetworking Forum (OIF). These standards influenced inter-operability and cost reduction of components required for coherent systems and pluggable modules [Venghaus and Norbert, 2017]. The 100G Ultra Long Haul DWDM Framework Document defined DP-QPSK as a standard modulation method and outlined functional architectures for integrated photonic components, specifically transmitter modulators and receivers [OIF, 2009].

Currently the telecommunications industry is moving toward optical coherent communication systems of 400 Gbps (400G) and beyond. The OIF recently released the "Flex Coherent DWDM Transmission Framework Document" for a 400G implementation technology option for optical communication systems [OIF, 2017]. Telecommunications industry vendors, who have successfully developed competitive 100G optical modules and components, are developing lower cost 100G solutions while introducing products for 200G, 400G, and beyond [Stanley, 2017]. The key electronic components for commercial optical coherent transceiver modules are the optical coherent DSP ASIC with DACs and ADCs and the four driver amplifiers (based on DP-QPSK modulation).

The key optical components include a transmit laser, coherent transmitter (modulator and modulator driver), local oscillator receive laser, and coherent receiver. Pluggable coherent transceiver modules, known as C-Form Pluggable (CFP) modules, have been commercially offered, containing the key optical components as well as commercial microelectronics and

power components required to operate the key components and the module system functionality. Figure 2 displays a block diagram of the key components and the functional relationship for an optical coherent modem system. For the transmit path, an optical signal from a laser is input to a coherent transmitter. A modulator driver is required to bias the modulator and encode the data provided through the coherent DSP ASIC. In the case for a 100G coherent system with DP-QPSK modulation, a total of 8 RF signals (differential pairs for in-phase and quadrature of X and Y polarizations: XI, XQ, YI, YQ) are output from the coherent DSP ASIC and input into the modulator. The modulated optical signal is output from the modem into a fiber amplifier. On the receive side, the optical signal is input to the coherent receiver, typically coming from a low noise fiber amplifier. The coherent receiver takes a second input optical signal from a laser serving as the local oscillator source. The coherent receiver outputs 8 RF signals (differential pairs as in the case of the signals input to the modulator), which is input to the coherent DSP ASIC.

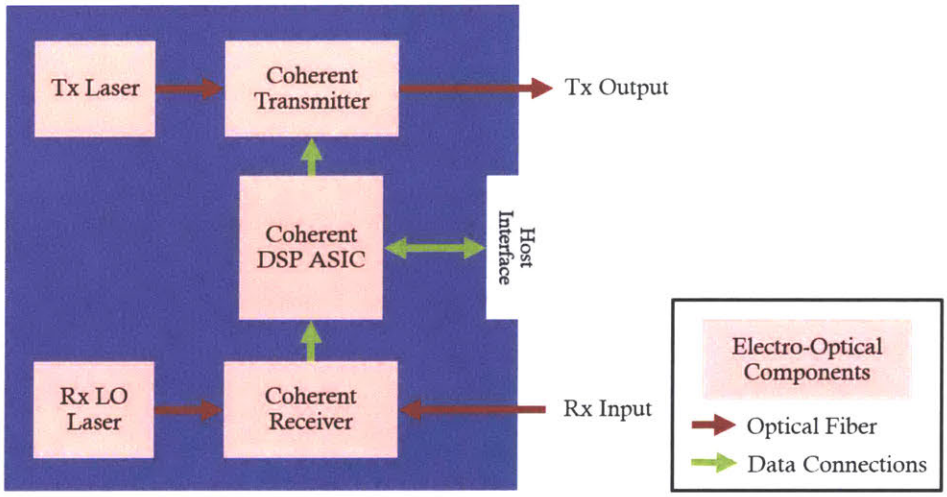

Figure 2. Block diagram of key electro-optical components for optical coherent modem.

The first CFP Multi-Source Agreement (MSA) defined the CFP module to support 40 Gbps and 100 Gbps with a package width of 82 mm and a power consumption of less than 24 W [Lipscomb, 2015; CFP, 2010]. The first commercial CFP modules were "CFP – Digital Coherent Optics (DCO)" including the coherent DSP ASIC in the module with the three key optical components (laser, coherent transmitter, coherent receiver). A CFP2 form factor was released in 2013 with MSA, which defined data rate capability of 40 Gbps and 100 Gbps, a module width of 41.5 mm, and power consumption of 12 W. Based on the lower power consumption in comparison to the CFP module, the CFP2 modules only included the three key optical components (no coherent DSP ASIC) and were referred to as CFP2 – Analog Coherent Optics (ACO) modules [Lipscomb, 2015]. The most recent CFP MSA has been released for the CFP8 module, which is defined to support data rates of 400 Gbps [CFP, 2017].

Developments of key optical coherent components and coherent DSP ASICs, such as reduced package volume and power consumption, have been driven by the commercial desire to be compatible for integration in CFP modules for fiber optic communication. These key optical coherent components have been standardized through OIF IAs and are compliant to Telcordia generic reliability (GR) standards, which assure optical devices function

satisfactorily for long periods of time under adverse environmental conditions in terrestrial applications. The standards include qualification testing, lot-to-lot controls, defined operational shock and vibration conditions, temperature limits, and fiber integrity stress tests [Telcordia GR-468, 2004; Telcordia GR-1221, 2010]. Table 2 displays thermal, shock, and vibration qualification test conditions from Telcordia GR-468. In comparing Telcordia qualification standards to NASA space qualification standards for thermal and vibration testing, there is a high probability that commercial optical devices can withstand space flight thermal and vibration environments [Ott et al., 2002].

Table 2. Thermal, shock, and vibration qualification test parameters from Telcordia GR-468

Test		Conditions	Other Notes
Thermal	Temperature Cycling	-40°C to +85°C ≥ 500 cycles	Unpowered
	High-Temperature Storage	85°C 2000 Hours	Unpowered
	Low-Temperature Storage	-40°C 72 Hours	Unpowered
	High Temperature Operation	85°C ≥ 2000 Hours	Powered
Shock		500 g, 1.0 ms 5 × / direction	Optoelectronic diodes and modules
		300 g, 1.0 ms 5 × / direction	Optoelectronic integrated modules ≤ 0.225 kg
Vibration		20 g 20 to 2000 to 20 Hz 4 min/cycle 4 cycles/axis	Non-powered
		5 g 10 to 100 to 10 Hz 1 min/cycle 10 cycles/axis	Powered

Commercial optical coherent components can be used in the design of a low-cost, high performance optical coherent modem with data rate capabilities of 100 Gbps or greater. The internal structure and material composition of technologies used to fabricate these technologies are evaluated in Chapter 3, Chapter 4, Chapter 5, and Chapter 6. Understanding the material composition of these components is critical to this work since the radiation sensitivity of the devices will be evaluated for applications within the LEO radiation environment.

1.3.2.1 Optical Coherent DSP ASICs

DSP through application specific integrated circuits (ASICs) is the key technological advancement to the realization of optical coherent communications systems. Prior to the development of optical coherent DSP ASICs in 2007, coherent systems would store transmitted data in a computer and analyze bit errors offline. The combination of coherent detection and DSP through an ASIC provides for real-time operation of digital coherent receivers [Savory, 2008; Kikuchi, 2010]. CMOS ASIC technology provides for the ADCs and DSP required to access and manipulate optical electric field signals for optical coherent systems [Roberts et al., 2009].

Optical coherent DSP ASICs have streamlined complex optical and analog functions to simplify transceiver implementation. DSP ASICs have integrated capabilities of high-speed analog-to-digital conversion (ADCs) and high bandwidth signal processing for soft-decision (SD) forward error correction (FEC), fixed equalizer (FEQ) for chromatic dispersion compensation (CDC), and adaptive equalizer (AEQ) for polarization de-multiplexing and phase and frequency recovery [Ishida, 2016]. DSP ASICs optimize optical coherent system performance by providing robustness to additive noise and tolerance to linear transmission impairments, such as chromatic dispersion (CD) and polarization mode dispersion (PMD) [Rasmussen et al., 2013].

Optical coherent DSP ASICs are used in commercial optical transceiver packages. Acacia Communications, Inc. (Acacia) developed the first industry product line of 100 Gbps optical coherent transceivers with DSP ASICs for analog-to-digital conversion and soft-decision (SD) FEC. With long-haul system experiments over 1000 km, Acacia demonstrated the robustness of their 120 Gbps coherent, polarization-multiplexed (PM) QPSK optical transceiver package [Nelson, 2012].

Over the last decade, there has been continued technological advancement in these specialized ASICs through three generations of coherent DSP implemented in 40, 20, and 16-nm CMOS technologies. Developments in optical coherent DSP ASICs with thinner oxide layers have resulted in reduced power consumption and increased performance, such as reduced optical signal to noise ratio (OSNR) threshold. Reduced OSNR threshold for the optical coherent receiver provides greater link margin for the FSOC system. State-of-the-art optical coherent DSP ASICs with 16-nm fin-FET CMOS technology can achieve sub-10-watt per 100 Gbps in 100 Gbps DP-QPSK and 200 Gbps DP-16QAM transport mode [Ishida, 2016].

Optical coherent DSP ASICs can reduce the size, cost, and power consumption of optical communications systems. Optical coherent ASICs with advanced DSP techniques can improve transmission capacity and performance for a given set of optoelectronic components, and DSP can be used to compensate for high dispersion, error, or noise [Xiang et al. 2014].

1.3.2.2 Commercial Optical Coherent Components

The telecommunications industry has focused research and development on PICs and analog electronic integrated circuits (ICs) for application toward the development of optical coherent components in integrated packages [Neophotonics, 2018]. The second generation of coherent transmitters and receivers has required photonic and electronic integration to achieve smaller size and lower power consumption. These components include micro- or nano- tunable lasers, modulators, and receivers.

The OIF has released implementation agreements (IAs) for 100G optical coherent components, such as the micro-intradyne coherent receiver (μICR) [OIF-DPC-MRX-01.0, 2015], micro-integrable tunable laser assembly (μITLA) [OIF-Micro-ITLA-01.1, 2015], and the high bandwidth coherent driver modulator (HB-CDM) [OIF-HB-CDM-01.0, 2018]. The IAs define required functionality and performance, electrical interfaces, mechanical requirements, environmental requirements, and opto-electronic interfaces. The intent of the IAs is to allow interoperability between coherent pluggable modules, which utilize these key optical coherent components. Standardization of the components has created a competitive

market for telecommunications industry vendors to provide these optical components as short lead time and low-cost solutions for 100G coherent systems with high performance. The key optical components and the detailed functionality are further discussed in Chapter 3, Chapter 4, Chapter 5, and Chapter 6.

1.3.2.3 Space Qualification of Commercial Optical Coherent Communication Technologies

Implementation of a DSP ASIC with integrated low-cost optoelectronic components can yield an overall lower-cost optical communications system. However, customized optical coherent DSP ASICs can have high development costs in the range of tens of millions of dollars with CMOS technologies [Rasmussen et al., 2013]. Significant investments of time and money would be required to fabricate space-qualified versions of commercial ASICs.

ASICs created with state-of-the-art commercial processes have been at least two generations ahead of space-qualified ASICs created with radiation-hardened (rad-hard) processes. Alternatives to creating space-grade ASICs with cost and time intensive rad-hard processes include (1) applying CMOS hardness-by-design approaches (e.g. guard banding around MOS transistors or using redundant latches) to custom ASICs created in commercial foundries and (2) testing or qualifying commercially-made ASICs against space mission radiation requirements. The latter option of using commercial ASICs has been recently approached based on increasing demand for higher system performance with the continuously evolving commercial processes [Lacoe, 2000]. With the small satellite revolution, and even for larger satellites, there has been a shift over the past decade toward evaluating, qualifying, and using commercial components for space applications [Sinclair and Dyer, 2013].

For a commercial ASIC to be used for a space mission, space systems engineers typically require the device to undergo extensive qualification tests for survivability and reliability in the space environment, including exposure to ionizing radiation. Spacecraft mission parameters, such as orbit and duration, as well as spacecraft materials and geometry play a role in the radiation environment and total ionizing dose (TID) that spacecraft components will encounter. Non-rad-hard, commercial components must be tested for survival at the TID requirements of the mission as well as tested for exposure to high energy protons and heavy ion particles. Radiation damage from high-energy protons and energetic proton events in the space environment can have detrimental effects on microelectronics, such as increased noise in photonics and single event effects (SEEs) [Petersen, 2011; Hiemstra & Blackmore, 2003]. The purpose of this work is not focused on describing in detail the effects of radiation on materials and devices in spacecraft applications. There is literature that can provide further detail on this topic [Hastings and Garrett, 2004; Petersen, 2011; Stark, 2011]. This work has a focus on characterizing radiation effects on commercial optical coherent DSP ASICs.

The lowest lead time and cost option for applying current commercial optical coherent DSP ASICs and other electro-optical components to a space-based system would be to test them to specific space-mission radiation requirements. There have not yet been published studies on space radiation testing and qualification of commercial electro-optical components, optical coherent DSP ASICs, or optical coherent transceivers with integrated DSP ASICs beyond previous work of the author. Radiation testing and performance characterization of active PIC building blocks, such as lasers and SOAs, for InP PICs has not been performed [Alt, 2016].

Radiation assessments on commercial optical coherent DSP ASICs, Inphi CL20010A1 and Acacia DSP ASIC within the AC100M optical coherent transceiver, have been completed in previous studies by the author [Aniceto, 2017; Aniceto, 2018]. The radiation assessments exposed the commercial optical coherent DSP ASICs to gamma radiation and proton radiation to test for TID effects and single event effects (SEEs) on the performance of the ASICs. The details and results of the two radiation assessments are further discussed in Chapter 3. No destructive proton SEEs on the commercial optical coherent ASICs were observed from the radiation assessments. Both studies reveal the potential of using commercial optical coherent DSP ASICs for space applications. The studies concluded that further testing is required with (1) a greater number of proton energy levels to better characterize proton SEE rates of the ASICs and (2) heavy ion radiation to evaluate for any destructive heavy ion SEEs and characterize heavy ion SEE rates of coherent DSP ASICs. Further radiation testing of a commercial optical coherent DSP ASIC will be completed as a contribution for this proposed work, described in Section 3.3.

1.3.3 Optical Inter-Satellite Links

High capacity inter-satellite crosslinks enabled through FSOC can permit more efficient and more reliable operations of future satellite systems and eliminate the need for expensive worldwide ground tracking networks and ground stations [Chan, 1989]. Commercial industry has taken an interest in utilizing the benefits of FSOC for proposed LEO constellations. Satellite constellation Federal Communications Commission (FCC) filings for OISLs have been made by SpaceX, Telesat, and LEOSat in 2016. Table 3 includes a summary of the proposed satellite constellations with OISLs.

Table 3. Satellite constellation FCC filings for optical inter-satellite links

Operator	Number of Satellites	Orbit Parameters
SpaceX SAT-LOA-20161115-00118	4,425	1110 – 1325 km, 53 - 81°
Telesat SAT-PDR-20161115-00108	117	Polar: 1000 km, 99.5° Inclined: 1248 km, 37.4°
LEOSat SAT-PDR-20161115-00112	78	1400 km, polar

Development of an inter-satellite FSOC system can be less complex in comparison to downlink or uplink systems from the perspective that inter-satellite link systems are not subject to attenuation losses from the Earth's atmosphere. Note there is potential for a LEO to LEO inter-satellite link path to cross the upper atmosphere, but the mission can limit OISL operations for paths that will not encounter Earth's atmosphere. Atmospheric attenuation losses yield loss of optical beam irradiance and random degradation of the optical beam quality [Piazzolla and Hemmati, 2009]. Specific sources of atmospheric attenuation include absorption, scattering, cloud blockage, turbulence, background noise and sky radiance, and atmospheric seeing [Kaushal, 2016]. Gas molecules and aerosols in the atmospheric channel as well as weather effects, such as fog, rain, and snow, cause absorption and scattering of the optical signal. Details of the optical signal losses due to absorption and scattering from the various contributions listed above are included in work by Piazzolla and Hemmati [2009] and Kaushal [2016]. Atmospheric attenuation is a primary limitation for link distance in FSOC uplink and downlink systems.

Geographic location is a key design consideration for uplink and downlink FSOC systems due to the significant impact of weather and clouds. Ideal locations for optical ground stations should be chosen based on requirements summarized by Del Portillo Barrios [2016]: low probability of link outage due to cloud covered, high altitude location to reduce air mass that the optical signal must traverse, non-isolated from common-purpose infrastructure and within reasonable distance from wide area network (WAN) point of access, and lack of natural features and man-made structures that could interfere with line of sight. Ground stations for GEO relay satellites should be close to the equator to reduce slant range and allow for operation in angles close to the zenith angle [Del Portillo Barrios, 2016]. Work by Del Portillo Barrios [2016] can be referenced for more details about optimal locations for optical ground stations, and Section 1.2.1 discusses ground stations from previous downlink FSOC demonstrations.

Although FSOC inter-satellite links are not limited by Earth's atmosphere or weather conditions like uplink or downlink systems, these systems have key design considerations and potential increased complexity associated with greater Doppler shift and a more complex acquisition and tracking scenario of two simultaneously moving satellites with different relative velocities. If optical amplifiers in the system have fixed gain, the optical signal can be too strong when satellites are in shorter range or can be too weak when satellites are at maximum range. Inter-satellite links may have longer distances than uplinks or downlinks, and thus may require power efficient FSOC systems with receiver sensitivities of phase-coherent techniques with high capacity [Kaushal, 2016].

1.4 Project Definition

A performance and cost-competitive, space-based coherent FSOC system could be a solution for meeting growing worldwide data capacity demand or providing connectivity to large areas with low population densities compared with terrestrial fiber networks and RF systems on satellites. A space-based, coherent FSOC system could be applied to the proposed LEO satellite constellations with OISLs by commercial companies.

The design of a space-based coherent FSOC system for a LEO OISL constellation application would be based on commercial optical coherent components from the terrestrial communications industry. The standardization of these components through the OIF implementation agreements have resulted in creating a market for low cost and low lead time components with guarantee performance and compatibility for 100G coherent systems. Using the standardized commercial electro-optical components allows for vendor flexibility so that the optical modem design is not dependent on a single vendor. The number of satellites required to provide coverage for the LEO constellation requires development of a cost-sensitive solution, which can be met through the price point of commercial components. Satellites in the constellation may require frequent replacement, and the strong demand of terrestrial communications industry can provide a robust supply of commercial components. Finally, there are currently no publicly and commercially available space-grade optical coherent components developed that can achieve the data rate performance of existing commercial coherent components from the terrestrial communications industry. It would require significant financial and time investment to develop custom, space-grade coherent DSP ASICs and PIC-based electro-optical components.

Compared to terrestrial optical coherent modem, a space-based optical coherent modem with commercial components would have additional requirements based on the following design considerations: Doppler shift, dynamic range of optical links, discrimination between transmit and receive paths, atmospheric effects, and space environment radiation effects. Although these design considerations yield additional challenges for development a space-based system, these do not impede the potential of developing an optical coherent modem for LEO to LEO in plane and cross plane OISL applications.

For a terrestrial optical coherent modem, there are natural clock uncertainties between transmit and receive reference clocks with different crystal oscillator sources. The transmit and receive reference clock variations influence Doppler requirements for coherent DSP ASICs. The Doppler specifications for commercial coherent DSP ASICs must encompass the expected Doppler shift and Doppler shift rates of a LEO OISL application. Link configurations with different ranges in a terrestrial optical network can have power variations. The dynamic range of cross-plane LEO OISLs will also have optical power variations, impacting the requirements for a fiber amplifier to provide the required optical power gain to close the communication link. Using a commercial optical coherent DSP ASIC requires transmit and receive path differentiation based on wavelength. Polarization discrimination cannot be used in a coherent system, which utilizes two orthogonal polarizations for QPSK detection scheme, and polarizing optics must be avoided in the design to minimize degradation to system performance. In a space-based FSOC system, optical links passing through the atmosphere will have time varying fade effects. For the application of this work (LEO OISLs), the scope will be limited to focus on OISLs operating when the path does not intersect Earth's upper atmosphere.

Previous work on radiation assessments of commercial optical coherent DSP ASICs have shown the potential of using this technology for a space-based optical coherent communication system [Aniceto, 2017; Aniceto, 2018]. We have observed that commercial optical coherent DSP ASICs are susceptible to proton-induced single event effects (SEEs), which can lead to system outages. To use commercial optical coherent DSP ASICs, we must characterize SEE-induced ASIC behavior and calculate the SEE rate for the space mission. The key optical components are sensitive to displacement damage radiation effects, which can lead to gradual performance degradation of the system.

The key innovation of this work is to design a LEO OISL optical coherent modem, based on discrete optical coherent commercial off the shelf components, as a reliable and fault tolerant system to space radiation effects. The novelty of this work is the design of a radiation mitigation approach with hardware, software, and firmware techniques for minimal system impact and recovery time. To our knowledge there is no published literature on radiation assessments of state-of-the-art commercial coherent DSP ASICs beyond the work of the author or on radiation assessments of state-of-the-art electro-optical components with InP based PICs [Aniceto et al., 2017; Aniceto et al., 2018]. We will characterize radiation effects on the selected commercial components. From the radiation assessments we can determine if periodic resets will help mitigate against SEEs, how often resets would be needed, and what the impact would be on the system level performance.

1.4.1 Technical Problem Statement and Research Statement

Within the past decade, the terrestrial communications industry has made technological advancements, optical coherent DSP ASICs and integrated fiber optic component packages, which have enabled high capacity optical coherent communications systems. Can we leverage the data rate performance and cost points of these technologies to develop a state-of-the-art optical coherent modem system for free space optical communications applications in Earth orbit?

The goal of this work is to develop an optical coherent communications modem for LEO-to-LEO in-plane and cross-plane inter-satellite links with improvement in data rate performance by 10 times from state of the art [DLR, 2008] using COTS components. A commercial optical coherent DSP ASIC, a coherent transmitter, a coherent receiver, and lasers with novel modifications for space use will be used for the design. The optical coherent communications modem will be designed for data rate of 100 Gbps using commercial telecommunications industry components compatible with 100G coherent WDM systems.

1.4.1.1 Scope of Work

The optical communications payload sub-system of a spacecraft has several assemblies, including an optical pointing assembly, a fiber amplifier, and an optical modem assembly (OMA). The spacecraft power, thermal, and command and data handling (C&DH) sub-systems interact with the optical communications payload and maintain operation of the payload during the mission. Figure 3 displays a high-level functional diagram of the optical communications payload sub-system of a spacecraft.

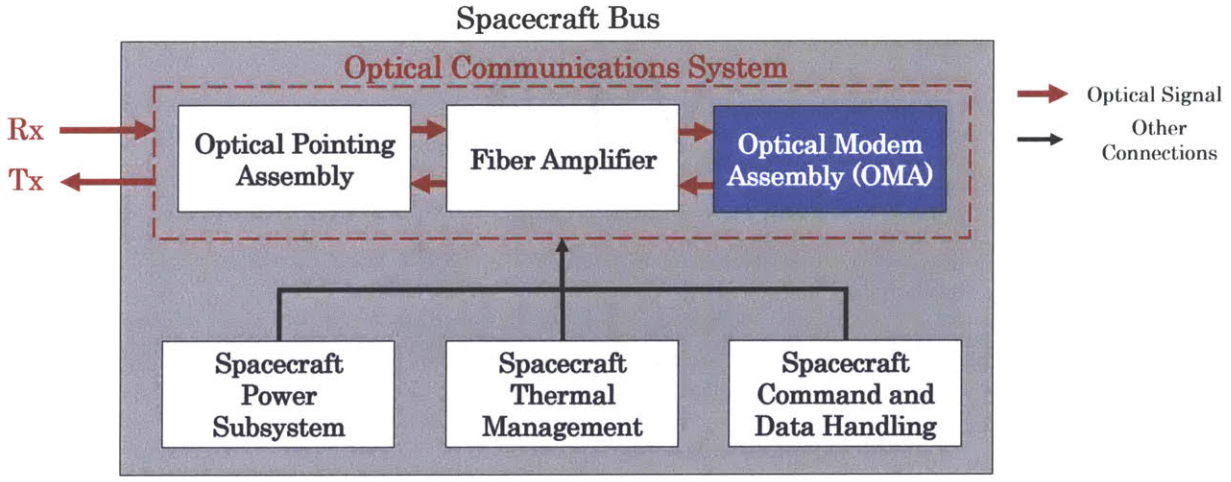

Figure 3. Functional block diagram of optical communications payload sub-system in spacecraft bus, highlighting focus of work on the optical modem assembly

The optical pointing assembly functionality includes beam steering and stabilization for the transmitted and received optical signals using coarse and fine pointing mechanisms as well as free space optics. The optical pointing assembly would need to consider the pointing, acquisition, and tracking (PAT) required to find the other satellite in an OISL application. The fiber amplifier serves to amplify the transmitted optical signal to the required optical output power level needed to close the optical link as well as to amplify the received optical

signal with a low noise figure to achieve an OSNR above the OSNR threshold required by the coherent DSP ASIC. The OMA serves as the optical transmitter and receiver. Figure 2 outlined a high-level functional diagram of an optical coherent modem with the key optical components.

The scope of this work is focused on the optical modem assembly (OMA) within the optical communications system payload of a spacecraft, specifically on the electro-optical component design of the optical modem assembly including the optical coherent DSP ASIC, coherent transmitter, coherent receiver, and lasers.

1.4.2 Contributions

This work makes the following contributions toward the development of a state-of-the-art optical coherent communications modem for LEO-to-LEO inter-satellite links using COTS components with novel modifications for space use.

1. Development of a process for selecting commercial optical coherent technologies, which can meet performance requirements in a LEO space environment.
2. Assessment of selected commercial optical coherent technologies for the LEO space environment.
3. Identification and development of cost-effective modifications, which ensure the system meets performance requirements and operates successfully in space.

1.4.2.1 Contribution 1

The first contribution is to develop a process for selecting commercial optical coherent technologies, which can meet performance requirements in a LEO space environment. LEO OISL requirements and key design parameters will be defined from simulation and modeling analyses of a selected OISL case study. LEO OISL radiation requirements will be defined from LEO OISL space environment radiation modeling. LEO OISL orbit modeling will determine maximum OISL distances and Doppler shift. An OISL link budget will be analyzed to evaluate the required OSNR for the commercial optical coherent DSP ASIC.

1.4.2.2 Contribution 2

The second contribution is to assess selected commercial optical coherent technologies for the LEO space environment. Performance testing of commercial optical coherent components is presented in detail, including benchtop laboratory characterization. Survivability testing, including radiation assessments, of the selected commercial optical coherent technologies is discussed.

1.4.2.3 Contribution 3

The third contribution is to identify and develop cost-effective modifications, which ensures the system meets performance requirements and successfully operates in space. Necessary modifications for operating the commercial optical coherent components in an OISL space application will be identified. Results from the radiation assessments of commercial optical coherent technologies will be used to determine radiation risk mitigation strategies, such as software techniques for periodic device resets.

1.4.3 Overview

Chapter 2 details requirements for a LEO OISL application, including space radiation environment modeling, Doppler shift analyses, and an optical link budget. The sample LEO OISL application chosen for this work is the proposed Telesat constellation. Chapters 3 through 6 focus on individual key commercial, electro-optical components for design of a 100G optical coherent modem for LEO OISL application.

Chapter 3 focuses on commercial optical coherent DSP ASICs. The chapter includes a background on commercial optical coherent DSP ASICs, a radiation susceptibility evaluation of commercial optical coherent DSP ASICs, and radiation assessments of previous generation commercial optical coherent DSP ASICs with 28 nm bulk CMOS technology. A third generation coherent DSP ASIC with 16 nm FinFET plus CMOS technology is proposed for the design of the OISL optical coherent modem. Two heavy ion radiation assessments of the commercial optical coherent DSP ASIC with 16 nm FinFET plus CMOS technology are completed. The heavy ion radiation test results inform necessary modifications for designing an optical modem with the commercial coherent DSP ASIC. A proton radiation assessment of the commercial optical coherent DSP ASIC with 16 nm FinFET plus CMOS technology is completed. The results of the proton radiation assessment are used to calculate the proton SEE rate for periodic software resets of the coherent DSP ASIC for the Telesat OISL mission. Future development of optical modems with commercial optical coherent DSP ASICs for OISL applications is discussed.

Chapter 4 focuses on commercial coherent receivers, and Chapter 5 focuses on commercial coherent transmitters. Both chapters include a background on the commercial component, a radiation susceptibility evaluation of the component, and proposed modifications for designing an optical modem with the component. Proton radiation assessments were completed for commercial coherent receivers and commercial coherent transmitters. The proton SEE rates were calculated for both types of components for the Telesat OISL mission.

Chapter 6 proposes a commercial laser for the design of the optical coherent modem. Laboratory benchtop testing of the selected commercial laser is completed to characterize performance related to the optical coherent modem requirements. Necessary modifications are proposed for using the commercial lasers in an OISL application. The chapter concludes with suggested commercial lasers for consideration in future optical coherent modem designs.

Chapter 7 summarizes the contributions of this work, the optical coherent modem system proton SEE rates and availability for the Telesat OISL constellation, and future work.

Chapter 2

Low Earth Orbit Optical Inter-Satellite Link Requirements

To design an optical modem for an OISL application, the Telesat OISL constellation was selected as a base case for determining system requirements, specifically radiation requirements, Doppler shift requirements, and link budget requirements. The proposed Telesat OISL constellation consists of two orbits: (1) polar orbit with Walker Star configuration 99.5°:91/7/1[1], and (2) inclined orbit with Walker Delta configuration 37.4°:200/20/1[2] [FCC, 2016 (SAT-PDR-20161115-00108)]. Table 4 summarizes the details of the two Telesat orbits for the OISL constellation. Figure 4(a) shows a three-dimensional model of the Telesat polar orbit constellation and Figure 4(b) shows a two-dimensional model of the Telesat polar orbit constellation. Figure 5(a) shows a three-dimensional model of the Telesat inclined orbit constellation and Figure 5(b) shows a two-dimensional model of the Telesat inclined orbit constellation.

Table 4. Telesat OISL Constellation – polar and inclined orbital parameters.

Parameter	Telesat Polar	Telesat Inclined
Inclination	99.5°	37.4°
Altitude	1000 km	1248 km
Constellation Configuration	Walker Star 99.5°: 91/7/1	Walker Delta 37.4°:200/20/1

[1] Walker constellation notation. The proposed Telesat polar constellation consists of 91 total satellites in 7 planes inclined at 99.5°, distributed over a span of 180 degrees (Walker Star configuration).

[2] Walker constellation notation. The proposed Telesat inclined constellation consists of 200 total satellites in 20 planes inclined at 37.4°, distributed evenly over a span of 360 degrees in right ascension.

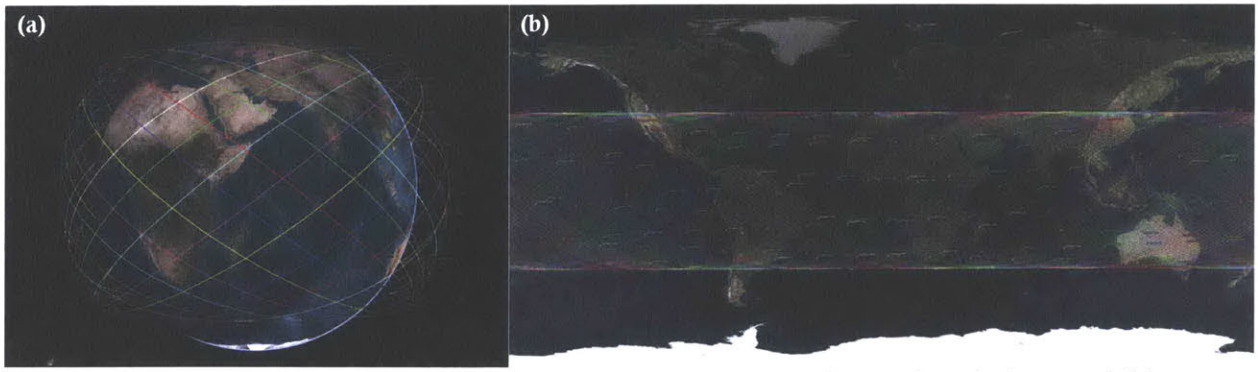

Figure 4. Telesat OISL constellation polar orbit: (a) three-dimensional view and (b) two-dimensional view.

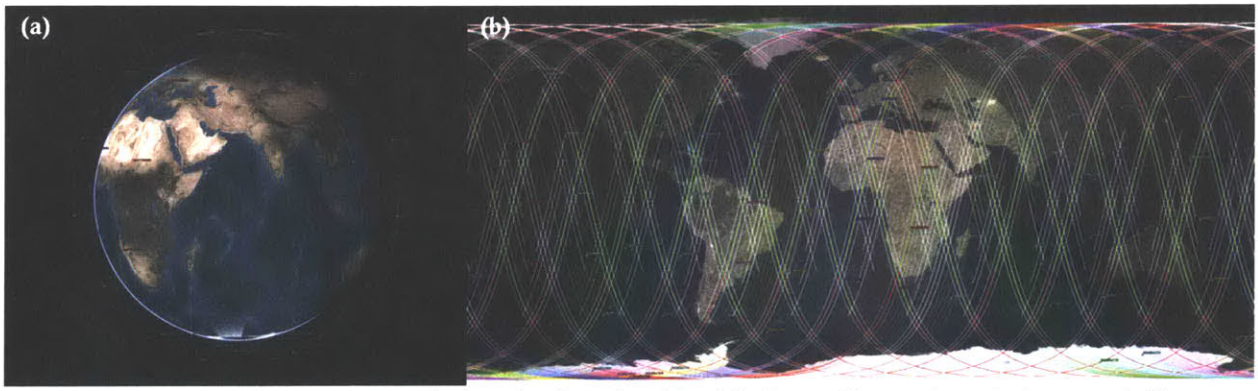

Figure 5. Telesat OISL constellation inclined orbit: (a) three-dimensional view and (b) two-dimensional view.

2.1 Radiation Requirements

2.1.1 Low Earth Orbit Radiation Environment and Effects

LEO spacecraft are affected by (1) trapped protons and trapped electrons in the inner belt, (2) protons and ions from solar energetic particles (SEPs), and (3) protons and ions from galactic cosmic rays (GCRs) [Badhwar, 1997]. The South Atlantic Anomaly (SAA) is a region with increased energetic particle fluxes [Stark, 2011]. Highly energetic protons in the SAA can affect spacecraft at orbital altitudes of up to ~1000 km and orbital inclinations of 35-60 degrees [Lohmeyer, 2015]. The SAA is caused by an offset between the Earth's magnetic field axis and Earth's rotational axis by angle of ~ 11 degrees and by an additional Northward offset of ~ 500 km [Varotsou, 2017; ESA, 2008; Stark, 2011]. The SAA is generally located in the region to the southeast of Brazil, but the geomagnetic field is dynamic and influences the geographic location of the SAA [Heynderickx, 2002]. Table 5 summarizes the types of particles from each LEO radiation environment source, the particle energy levels in LEO, and the relevant areas in LEO that are affected by each type of particle.

Table 5. Summary of LEO radiation sources, particles from radiation sources, particle energy level in LEO, and affects areas in LEO

Radiation Source	Particle Type	Particle Energy Level in LEO	Affected Areas in LEO

Inner Belt	Protons	10 keV – 300 MeV	SAA and high inclinations (> 60°)
	Electrons	10 keV – 5 MeV	SAA and high inclinations (> 60°)
GCR	Protons	< ~ 1 GeV	High inclinations (> 60°)
	Ions	< ~ 300 MeV/n	High inclinations (> 60°)
SEP	Protons	keV – 500 MeV	High altitudes and low inclinations
	Ions	1 – 100 MeV/n	High altitude and low inclinations

Particles from the space radiation environment generate total ionizing dose (TID) effects, total non-ionizing dose (TNID) or displacement damage dose (DDD) effects, and single event effects (SEEs). Figure 6 outlines the main LEO radiation environment sources, the types of particles from each source, and the radiation effects caused by the particles. An in-depth background of the LEO radiation environment sources and the radiation effects caused by the particles of each LEO radiation source are further described in Suparta [2014] and Aniceto [2017].

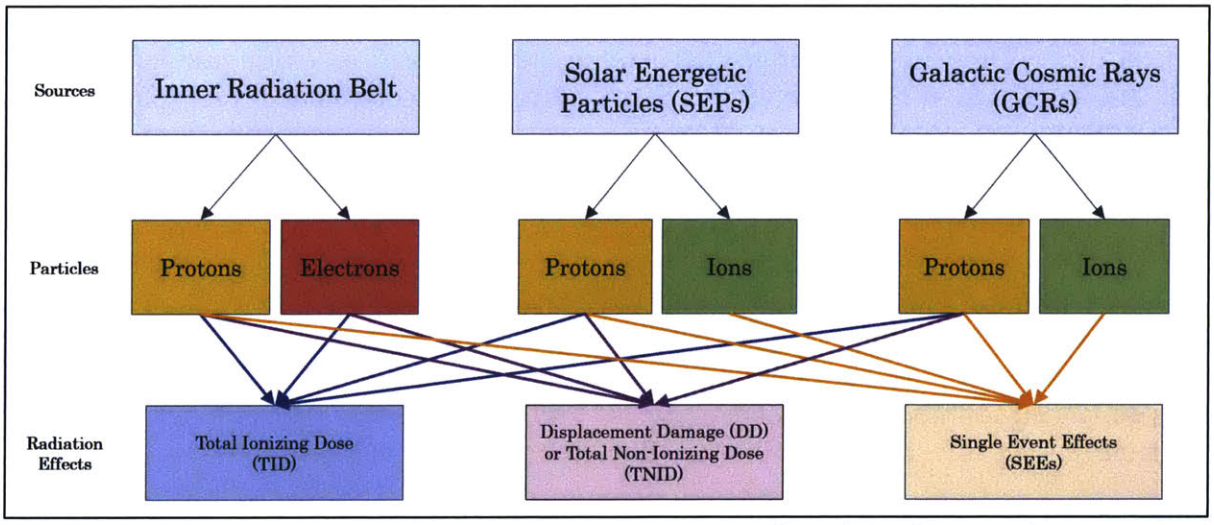

Figure 6. LEO radiation environment sources, types of particles from each source, and radiation effects caused by each type of particle

The mission orbit determines the types of radiation effects that the spacecraft and components could encounter, while the mission duration and timeline determine the potential amount of cumulative dose or probability of single event occurrences. Each type of radiation effect is characterized to generate mission radiation requirements. Table 6 summarizes the types of radiation effects in a LEO environment based on the types of particles inducing each effect, examples of susceptible devices and technologies, and characterization of each type of radiation effect. Further background details about characterizations and calculations for each radiation effect can be found in Aniceto [2017].

Table 6. Summary of radiation effects, types of particles inducing each effect, susceptible devices and technologies to radiation effects, and characterization of radiation effects

Radiation Effect	Types of Particles Inducing Effect	Susceptible Devices and Technologies	Characterization

TID	Protons Electrons	CCDs, optical devices, MEMs, memory devices, MOS transistors, FETs, linear ICs, BJTs, microelectronics	Fluence, LET
TNID or DDD	Protons Electrons	Opto-electronic devices, bipolar ICs, MOS transistors, FETs	Fluence, NIEL
SEE	Protons Ions	Memories, microelectronics, ASICs, FPGAs, programmable ICs, CMOS devices, MOSFET devices	SEE Cross Section, LET, Transported Energy

2.1.1.1 Total Ionizing Dose Effects

Trapped protons and electrons from the radiation belts, protons from SPEs, and protons from GCRs are sources of TID effects on spacecraft electronics [Varotsou, 2017]. TID effects occur when charged particles deposit ionizing energy into target material and the ionization alters the material by generating electron-hole pairs and inelastic Coulombic scattering [Alig and Bloom, 1975; Miroshnichenko, 2003]. TID is a cumulative radiation effect and is characterized based on the total mission duration.

TID effects in electronic devices result from charge trapping in insulators, such as gate oxides, and semiconductor/insulator interfaces. TID effects are observed as electrical device parameters drift [Tuite, 2013]. Trapped particles in the inner belt can cause interference with sensors and degradation of spacecraft electronic parts from accumulated TID [Stark, 2011; Suparta, 2014].

Technologies sensitive to TID effects include MOS (Metal Oxide Semiconductor) transistors, field effect transistors (FETs), linear integrated circuits (ICs), and bipolar junction transistors (BJTs). TID effects can cause a shift in the threshold voltage of NMOS devices and a decrease in the drive current of PMOS devices. For CMOS devices, TID effects can result in decreased switching speed and increased leakage current. The effects of ionizing radiation on CMOS devices are further detailed in Section 3.2. In junction gate FETs or JFETs, TID effects include enhanced source-drain leakage currents. TID effects on BJTs include degradation to the gain current for low current conditions [Poizat, 2009].

Common spacecraft electronic devices with MOS, FET, IC, and BJT technologies include charged-coupled devices (CCDs), optical components, micro-electro-mechanical systems (MEMS), memory chips, bipolar electronic devices, and general microelectronics. The most sensitive devices to TID failures are bipolar electronic devices. CCDs and optical components can experience increased dark current. Charge build-up in the dielectric layers of MEMS from TID can lead to a shift in response. Memory devices, such as static random access memory (SRAM) chips are also sensitive to TID failures due to CMOS, BJT, and FET technologies within the chips [Sukhaseum, 2017]. Potential TID damage on digital microelectronics includes enhanced transistor leakage and logic failures due to reduced gain in BJTs or shifted threshold voltages and reduced switching speeds in CMOS. TID effects can cause gain degradation and change the offset voltage, offset current, and bias-current of analog microelectronics [Poizat, 2009].

TID sensitivity of an electronic device is dependent on the technology passivation, device structure, and when and where the device was manufactured. Different foundries manufacture electrical devices with different doping levels that produce cause dose sensitivity

levels. Although manufacturing quality of semi-conductor regions is controlled based on doping levels, there are differences in the manufacturing quality of the oxide layer among different foundries or even among different manufacturing lots of the same foundry [Dodd et al., 2010].

2.1.1.2 Total Non-Ionizing Dose or Displacement Damage Effects

Trapped protons and electrons from the radiation belts, protons from SPEs, and protons from GCRs cause DDD or TNID effects on spacecraft electronics [Varotsou, 2017]. TNID effects are caused by incident particles entering the target material and interacting with nuclei. When an incident particle hits a nucleus, the nucleus can become displaced in the crystal lattice, causing elastic scattering and nuclear reactions. Displacement damage results from the cumulative physical degradation of the lattice material [Miroshnichenko, 2003].

TNID effects cause stable defects, which behave as recombination centers, trap centers, and diffusion centers. Recombination centers impact the carrier lifetime, trap centers impact resistivity of electronic circuits, and diffusion centers impact mobility of electrons and holes. The following types of devices are sensitive to displacement damage effects and are listed in order of most sensitive: opto-electronics, bipolar ICs, MOS transistors, power MOSFETs, and CMOS. The most sensitive devices are minority carrier devices[3] [Sukhaseum, 2017].

2.1.1.3 Single Event Effects

Protons and heavy ions from both GCRs and solar flares as well as trapped protons in the inner radiation belt cause SEEs in electronic devices on LEO spacecraft [Varotsou, 2017]. The greatest potential hazard from GCRs for LEO spacecraft are SEEs, caused primarily by abundant deposition of iron nuclei [Suparta, 2014]. Energetic heavy ions from GCRs can deposit significant amounts of energy in spacecraft electronics, and large amount of kinetic energy from GCRs can have permanent, damaging effects on materials through which the particles may pass [ESA, 2008; Stark, 2011]. Heavy ions from GCRs and energetic protons can trigger latch up by producing charge in the well-substrate junction of electronic devices. In some LEO environments, trapped protons can have greater energy levels (such as in the SAA) than GCR heavy ions and may induce more SEEs [Petersen, 1996].

SEEs occur when a charged particle is deposited or passed through active components with electrical circuits, such as memory, power, and logic devices. Specifically, SEE radiation damage is caused when a charged, high-energy particle, commonly a proton, impacts the energy structure and lattice structure of a semiconductor material in an electronic device. The charged particle transmits energy to the semiconductor material and can cause a displacement of a lattice atom in the material. Local ionization occurs within the material from the generated charge along the ion path and an impulsive release of charge from the ionization process causes a SEE [Stark, 2011]. Within microelectronic devices, SEEs result from energetic protons interacting with silicon nuclei and producing ionizing nuclear recoils [Hiemstra, 2003]. SEEs cause a disruption in electronic device operation and can have either destructive or non-destructive consequences to devices.

[3] A minority carrier device is a device in which the current conduction is controlled by the diffusion of minority carriers, such as electrons in the p region and holes in the n region in a p-n junction diode [Li, 2006].

SEEs are particular to certain electronics and components, based on the structure or technology, and can be destructive or non-destructive. Table 7 lists the types of SEEs as well as devices and technologies that are susceptible to each type of SEE. The types of SEEs relevant to CMOS-based optical coherent DSP ASICs are indicated in Table 7 with a "*" including single event upsets (SEUs), single event functional interrupts (SEFIs), multiple bit upsets (MBUs), multiple cell upsets (MCUs), single event latch-ups (SELs), and single event hard errors (SEHEs) [Mutuel, 2016].

Table 7. Types of SEEs and susceptible devices and technologies.

Single Event Effect	Susceptible Devices and Technologies	Destructive?
Single Event Upset (SEU)*	Digital devices, analog devices, CMOS devices, microprocessors, FPGAs, ASICs, memories, buffers, latches, converters, and optical components	Non-Destructive
Single Event Functional Interrupt (SEFI)*	Memories, microprocessors, state controllers, FPGAs, ASICs, ADCs, DACs	Non-Destructive
Single Event Transient (SET)	Memories, Analog devices, linear devices, power devices, converters	Non-Destructive
Multiple Bit Upset (MBU)*	Memories, microprocessors, FPGAs, latches, ASICs	Non-Destructive
Multiple Cell Upset (MCU)*	Memories, microprocessors, FPGAs, latches, ASICs	Non-Destructive
Single Event Latch-Up (SEL)*	CMOS devices	Destructive
Single Event Hard Error (SEHE)*	Memories, latches, microprocessors, FPGAs, ASICs, buffer devices	Destructive
Single Event Gate Rupture (SEGR)	Power MOSFETs, converters	Destructive
Single Event Burn-out (SEB)	N-channel power MOSFETs, converters, analog devices	Destructive
Single Event Dielectric Rupture (SEDR)	FPGAs, programmable ICs, linear devices, Power MOSFETs	Destructive

SEUs are one of the most common SEEs for spacecraft electronics. SEUs occur in digital, analog, and optical components, and device areas sensitive to SEUs include memories, buffers, and latches. SEUs change the logic state of a circuit in an electronic device and induce soft errors [Baker, 2002]. Within MOS devices, Off NMOS and PMOS drain transistors are sensitive to SEUs [McMorrow, 2004]. A reset or rewrite of the device logic after an SEU occurrence can typically restore normal operation of the device.

An SEU can trigger a single event transient (SET), which is an electrical pulse of signal or voltage generated in the device and propagated from the device to the system [Normand, 2004]. SETs occur in analog and linear devices, such as voltage references, operational amplifiers, voltage regulators, and comparators [Samaras, 2014]. Peaks in voltage amplitude or extended durations of high voltage above typical device voltage specification characterize a SET. Although a SET can be non-destructive to a device, the effects of a SET can be

destructive to a system if there are connected components which take voltage input from the SET-affected device.

Both MBUs and MCUs occur when a single particle triggers several bit flips, typically within memory devices. An MBU induces the corruption of several bits in the same memory word or address [Normand, 2004]. An MCU triggers several upsets or transients as it penetrates through a device or system.

SEFIs are characterized by a loss of normal device operation and are identified by device functional "hangs" in which the device falls into an unknown or unmanaged state. SEFIs can also result in permanent damage to a device. To counteract a SEFI, devices must be reset or power cycled to recover normal operation. SEFIs occur in complex devices with built-in state or control sections such as field programmable gate arrays (FPGAs), ASICs, dynamic random-access memory (DRAM), ADCs, and digital-to-analog converters (DACs) [Normand, 2004; Samaras, 2014].

SELs have an induced high current state, which can result in the loss of device functionality or potentially permanent damage. SELs are short-circuits between the ground and supply voltage and occur in CMOS and BiCMOS technologies. A power reset can be used to return to normal operation after occurrence of an SEL, but this type of SEE can also be destructive [Samaras, 2014].

SEHEs result from a SEU causing permanent change to the state of a memory element or buffer. Single event stuck bits (SESBs) result in the change to device functionality or operation from a stuck bit in a memory device. SESBs are a type of SEHE with only semi-permanent damage since annealing can recover functionality of the memory device [Samaras, 2014].

A single event gate rupture (SEGR) results from an ion-induced formation of a conducting path in the gate oxide of N-channel or P-channel power MOSFETs. A SEGR is observed through the dielectric breakdown of a power MOSFET gate [Samaras, 2014]. A single event burn-out (SEB) occurs in power transistors, specifically N-channel power MOSFETs. This type of SEE results in a high current state and is caused by the activation of parasitic NPN bipolar transistor in a vertical power MOSFET [Normand, 2004, Miroshnichenko, 2003]. A single event dielectric rupture (SEDR) is the result of the breakdown of thin oxide layer in programmable IC, linear devices, such as FPGAs.

SEE device sensitivity is characterized by the probability of a SEE occurrence or the device cross section. The device cross section is determined based on specific conditions, such as the type of device, particle, and SEE. For a device and spacecraft mission, the SEE rate is calculated to gain an understanding of the device sensitivity to SEEs and to determine how often the device should be power cycled or reset in order to restore nominal operation from SEE occurrences. Heavy ion and proton radiation assessments are used to collect SEE cross section data and determine SEE rates for a mission.

2.1.2 Telesat Radiation Environment Modeling

The radiation environments for the Telesat LEO constellation polar and inclined orbits were modeled to generate mission radiation requirements. Ten-year mission durations were used for the models with start date of January 1, 2022. Radiation requirements will determine levels

required for radiation testing of commercial technologies. OMERE version 5.2 radiation modeling software was used to simulate the radiation environment based on models for trapped proton and electron fluxes, solar particle fluxes, and GCRs.

Trapped proton fluxes were modeled using the European standard trapped proton model AP8-MIN and trapped electron model AE8-MAX, which were both created by NASA [Xapsos et al., 2012]. The AP8-MIN model includes proton energy levels from 0.1 MeV to 400 MeV and represents the worst cases trapped proton fluxes, which occur during solar minimum. The AE8-MAX model includes electron energy levels from 0.04 MeV to 7 MeV and represents the worst case trapped electron fluxes, which occur during solar maximum. OMERE uses the data from both AP8-MIN and AE8-MAX models to calculate the mean flux for trapped particles by calculating the flux spectrum at each orbit point and taking the average of the flux spectrum [Varotsou, 2017].

The fluxes and fluences from solar ions and protons are calculated with OMERE solar particle modules: Average Statistical Models and Solar Flare Models [Xapsos et al., 2012]. Cumulative solar particle effects are calculated with Average Statistical Models. The mean solar proton fluxes and fluences for each mission are calculated with the ESP model for a 90% confidence level. The ESP model is an ECSS 10-04 standard for solar proton fluences and covers energy levels ranging from 1 MeV to 300 MeV. The mean solar ion fluxes and fluences for each mission are calculated with the PSYCHIC solar ion model for a 90% confidence level. Peak ion and proton fluxes during solar flares for single event rates are calculated using Solar Flare Models. Proton solar events for each mission are modeled using the ONERA model for the worst case 1-week proton fluxes at each energy level. Heavy ion solar events for each mission are modeled using the CRÈME 96 model for elements He to U. CRÈME 96 is the ECSS 10-04 standard for heavy ion solar event fluxes [Varotsou, 2017].

GCRs are modeled with the OMERE Cosmic Ray module. The GCR ISO 15390 model is used to calculate the proton and heavy ion fluxes from cosmic rays for each mission. The GCR ISO 15390 is the standard model for cosmic rays. The 1996.4 Solar Minimum temporal configuration is used with the model, since this represents a worst case scenario for GCRs.

TID is quantified using dose model SHIELDOSE-2, with shielding configuration set as center of aluminum spheres and target material set as silicon. For a given orbit, SHIELDOSE-2 determines the absorbed dose behind a range of aluminum shielding thicknesses on different detector materials from user-input electron and proton fluences [Seltzer, 1980; Seltzer, 1994]. SHIELDOSE-2 quantifies total ionizing dose based on calculations of electrons, bremsstrahlung photons, and protons in the radiation environment of a given orbit. On-orbit dose rates generated by SHIELDOSE-2 are generally consistent with dose rates less than or equal to 10 mrad per second, specified in the Enhanced Low Dose Rate Sensitivity (ELDRS) radiation test procedure in MIL-STD-883H [Bogorad et al., 2010; Lohmeyer, 2015]. Figure 7 displays the dose depth curves for various aluminum shielding thicknesses estimated with the SHIELDOSE-2 model for the polar and inclined orbits with mission durations of ten years. The TID values at 100 mils, 200 mils, and 300 mils aluminum shielding thickness are marked on the TID curves in the figures. For a space mission, the dose depth curve is used to define the top-level dose requirement assuming a conservative shielding thickness, typically 100 mils (2.54 mm) of aluminum shielding [Poivey and Day, 2002]. Table 8 lists the TID levels for Telesat LEO constellation polar and inclined orbits for 100 mils, 200 mils, and 300 mils

aluminum shielding thicknesses. The Telesat inclined orbit has higher TID levels due to the higher altitude.

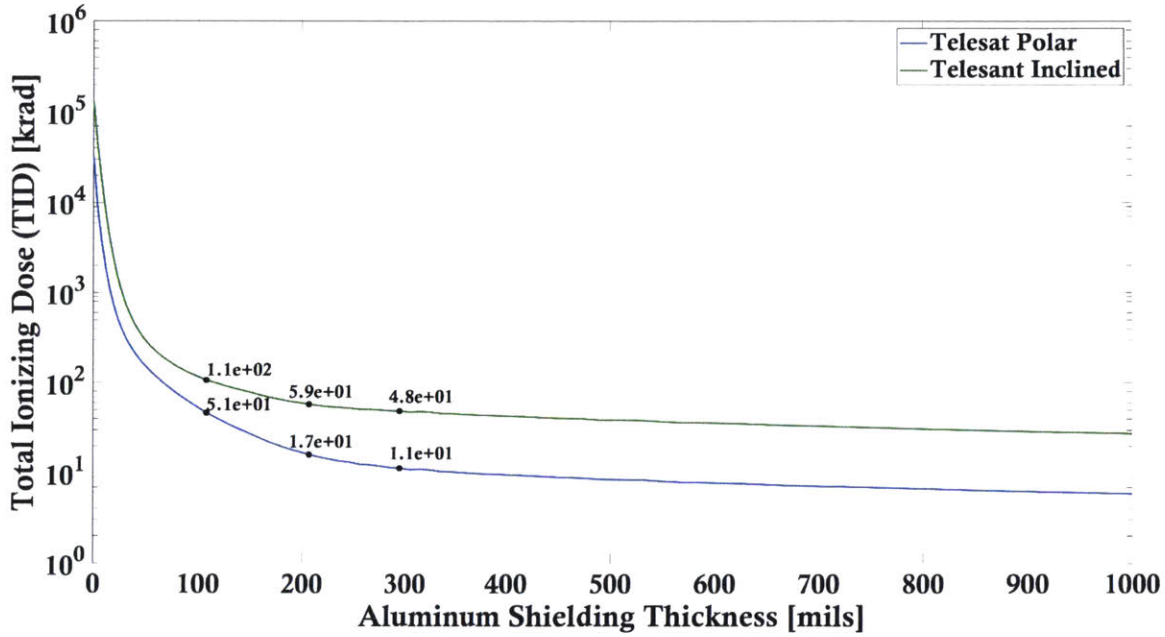

Figure 7. Dose depth curves for the Telesat LEO constellation polar and inclined orbits for a 10-year mission duration.

Table 8. Total ionizing dose levels for the Telesat LEO constellation polar and inclined orbits for 100 mils, 200 mils, and 300 mils aluminum shielding thicknesses.

Aluminum Shielding [mils]	Telesat Polar Orbit [krad(Si)]	Telesat Inclined Orbit [krad(Si)]
100	51	110
200	17	59
300	11	48

The displacement damage dose levels for the 10 MeV proton energy level were calculated based on aluminum shielding thicknesses. The non-ionizing energy loss (NIEL) data was based on protons through silicon material. Figure 8 shows the displacement damage dose curves for Telesat LEO constellation polar and inclined orbits. Table 9 identifies the displacement damage dose levels based on 10 MeV protons for 100 mils, 200 mils, and 300 mils aluminum shielding thicknesses.

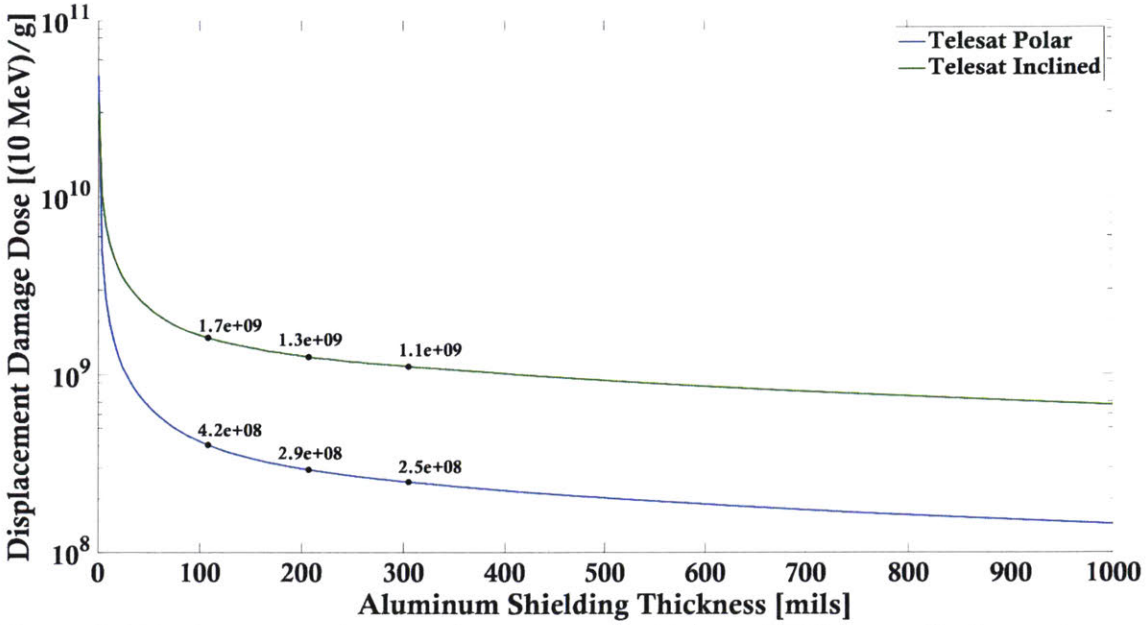

Figure 8. Displacement damage dose curves for Telesat LEO constellation polar and inclined orbits.

Table 9. Displacement damage dose levels based on 10 MeV protons for 100 mils, 200 mils, and 300 mils aluminum shielding thicknesses.

Aluminum Shielding [mils]	Polar Displacement Damage Dose [10 MeV/g]	Inclined Displacement Damage Dose [10 MeV/g]
100	4.2×10^{8}	1.7×10^{9}
200	2.9×10^{8}	1.3×10^{8}
300	2.5×10^{8}	1.1×10^{8}

The integral flux spectra for the LEO Telesat constellation polar and inclined orbits were generated over different LET levels based on trapped protons, solar mean protons, and galactic cosmic ray ions as source contributions. The integral flux spectrum sets were based on 100 mils, 200 mils, and 300 mils aluminum shielding thicknesses. The integral flux spectrum is used to identify the minimum onset LET at integral flux level of 1×10^{-7} [1/cm^{2}s]. Figure 9 shows the integral flux spectrum based on LET levels, and Table 10 identifies the minimum onset LET at integral flux of 1×10^{-7} [1/cm^{2}s] for 100 mils, 200 mils, and 300 mils aluminum shielding. The minimum onset LET levels will be used to determine LET levels for heavy ion radiation testing. Heavy ion radiation testing is performed to screen for destructive heavy ion single event effects up to the minimum onset LET value for the mission.

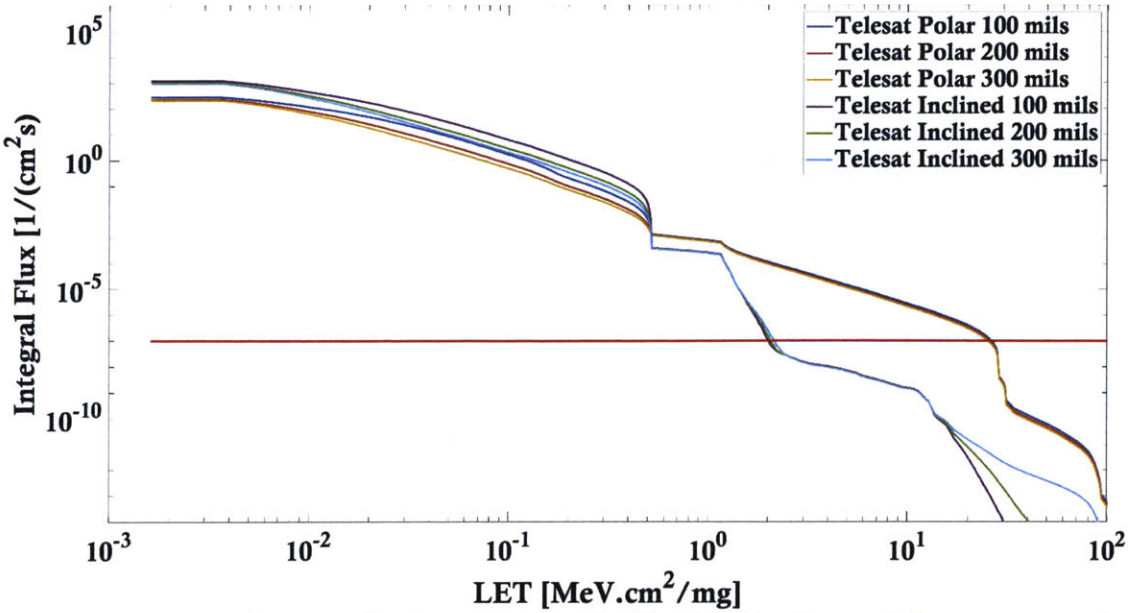

Figure 9. Telesat LEO constellation polar and inclined orbits integral flux spectrum based on LET.

Table 10. Minimum onset LET at integral flux of 1×10^{-7} [1/cm^{2}s] for 100 mils, 200 mils, and 300 mils aluminum shielding.

Shielding [mils (Al)]	Telesat Polar Minimum Onset LET [MeV cm^2/mg]	Telesat Inclined Minimum Onset LET [MeV cm^2/mg]
100	26.20	2.02
200	25.73	2.05
300	25.22	2.14

2.2 Telesat OISL Orbit Modeling

The Telesat OISL constellation was modeled using STK 11 software, based on orbit parameters from FCC filing, Telesat SAT-PDR-20161115-00108 (Table 4). Doppler shift, Doppler shift rate, range and range rates for 1550 nm optical communication links between satellites were determined using STK 11 software and used to set system requirements for the design of the optical modem. Link distance requirements based on the expected minimum and maximum range values will serve as a key input to an optical link budget used to determine the required OSNR threshold value for the optical coherent DSP ASIC in the modem design. Separate analyses were completed for the inclined orbit constellation and the polar orbit constellation.

2.2.1 Telesat Inclined Orbit Doppler Shift and Link Range Analyses

For analyses, the full Telesat OISL constellation of satellites in the inclined orbit was reduced to evaluate six orbital planes: two intersecting sets of three adjacent planes. Figure 10(a) shows the full Telesat OISL inclined orbit constellation. Figure 10(b) shows six orbital planes, which were used for analyses, from the full constellation.

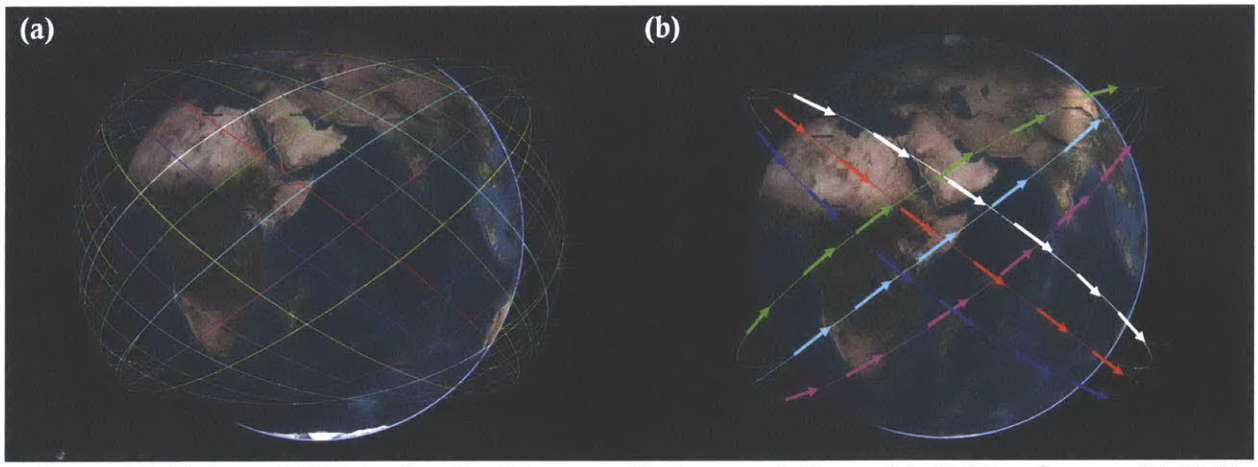

Figure 10. Telesat OISL inclined orbit constellation modeling with STK software. (a) Full Telesat OISL constellation inclined orbit compared against (b) six selected orbital planes used for analyses.

Using STK v.11, transmitters and receivers for a 1550 nm (193.3 THz) optical communications application were added to the satellites in the reduced inclined orbit constellation model. The "Access" calculation tool in STK v.11 outputs when there is visibility between two satellites in different orbital planes for a communication link between transmitter and receiver. A limitation was enabled in the calculation tool to exclude links which would intersect through Earth's atmosphere. Figure 11 shows the communication links analyzed in the reduced Telesat OISL inclined orbit constellation. Figure 11(a) and Figure 11(b) show the links modeled between satellites in adjacent planes. Figure 11(c), Figure 11(d), Figure 11(e), and Figure 11(f) show the links modeled between satellites in cross planes.

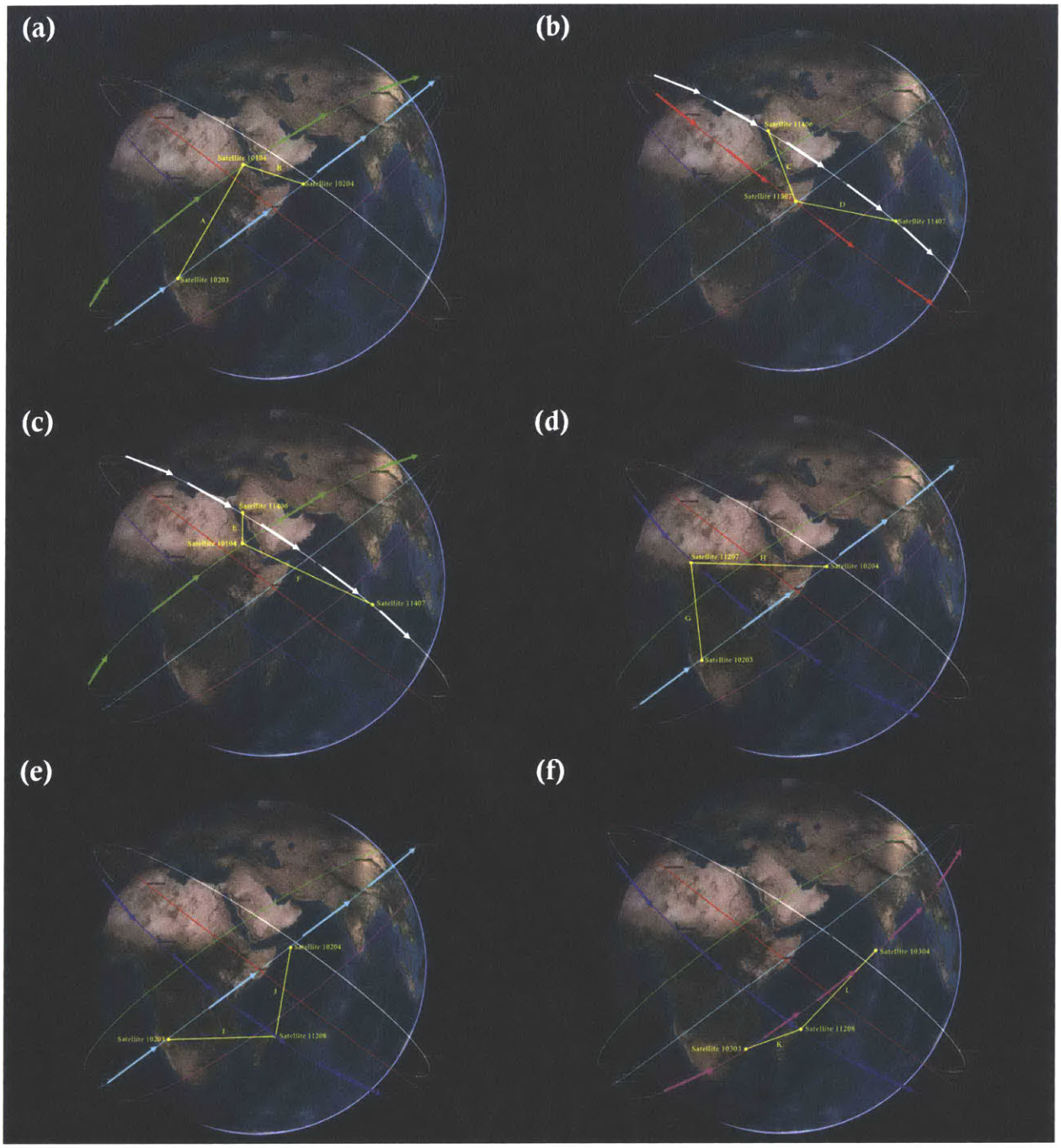

Figure 11. STK v.11 model of communication links analyzed in the reduced Telesat OISL inclined orbit constellation. (a) and (b) show the links modeled between satellites in adjacent planes. (c), (d), (e), and (f) show the links modeled between satellites in cross planes.

For each "Access" between satellites, STK v.11 was used to calculate the Doppler shift, Doppler shift rate, and range for links between satellites throughout the orbits. Equation 1 is used to calculate the expected Doppler shift or change in frequency of a signal transmitted from an optical communications terminal on a moving satellite and received on an optical communications terminal on another moving satellite [Everett, 2011]. The relative velocity of the two spacecraft is the key parameter influencing the Doppler shift of the signal. Table

11 summarizes the Doppler shift values and Doppler shift rates, and Table 12 summarizes the ranges and range rates for each of the communication links analyzed in the STK model of the reduced Telesat OISL inclined orbit constellation. For the reduced Telesat OISL inclined orbit constellation analysis, the minimum Doppler shift is -5.444 GHz and the maximum Doppler shift is 5.444 GHz, based on optical communication link G and link J between satellites in cross planes. The greatest range values occur in optical communication link H between satellites in cross planes. For link H, the minimum link distance is ~4093 km and the maximum link distance is ~8363 km.

$$\Delta f = \frac{\Delta v}{c} \cdot f_0$$

Equation 1. Doppler shift calculation for signal transmitted and received between two moving spacecraft [Everett, 2011]. Δv represents the relative velocity of the two spacecraft, c is the speed of light, and f_0 is the frequency of the transmitted signal.

Table 11. Optical communication link Doppler shift and Doppler shift rates analyzed in the STK model of the reduced Telesat OISL inclined orbit constellation.

Link Type	Link Label	Satellite Tx Identifier	Satellite Rx Identifier	Minimum Doppler Shift [GHz]	Maximum Doppler Shift [GHz]	Mean Doppler Shift [GHz]	Minimum Doppler Shift Rate [GHz/sec]	Maximum Doppler Shift Rate [GHz/sec]	Mean Doppler Shift Rate [GHz/sec]
Adjacent	A	10203	10104	-0.197	0.197	0.001	-0.00039	0.000358	0
Adjacent	B	10104	10204	-0.494	0.494	0.002	-0.001281	0.00074	-0.000003
Cross	C	11406	11307	-0.272	0.272	0.001	-0.000577	0.000467	0.000002
Cross	D	11307	11407	-0.19	0.19	0.001	-0.000381	0.000344	0
Cross	E	11406	10104	-5.118	5.118	0.015	-2.644492	0.004856	0.002972
Cross	F	10104	11407	-3.252	3.252	-0.032	-0.01033	-0.003523	-0.001695
Cross	**G**	11207	10203	**-5.444**	**5.444**	-0.071	-0.135675	0.004845	-0.001753
Cross	H	11207	10204	-3.689	3.689	-0.042	-0.01217	0.003152	-0.002921
Cross	I	10203	11208	-3.957	3.957	-0.103	-0.014682	0.003745	-0.002462
Cross	**J**	11208	10204	**-5.444**	**5.444**	-0.048	-0.135669	0.004845	-0.001753
Cross	K	11208	10303	-4.865	4.865	-0.052	-0.03066	0.00465	-0.001707
Cross	L	11208	10304	-4.347	4.347	-0.065	-0.021233	0.004411	-0.001843

Table 12. Optical communication link ranges and range rates analyzed in the STK model of the reduced Telesat OISL inclined orbit constellation.

Link Type	Link Label	Satellite Tx Identifier	Satellite Rx Identifier	Minimum Range [km]	Maximum Range [km]	Mean Range [km]	Minimum Range Rate [km/sec]	Maximum Range Rate [km/sec]	Mean Range Rate [km/sec]
Adjacent	A	10203	10104	3625.548	3948.206	3788.5	-1.443319	0.305207	-0.002324
Adjacent	B	10104	10204	1103.337	1911.507	1533.35	-0.786267	0.766858	-0.003539
Cross	C	11406	11307	1888.392	2333.864	2117.79	-1.00272	0.422257	-0.001888
Cross	D	11307	11407	2860.936	3172.943	3019.09	-1.211754	0.295522	-0.002093
Cross	E	11406	10104	15.417	8361.23	5274.46	-7.946832	7.947332	-0.022987
Cross	F	10104	11407	3952.057	8361.545	6011.24	-5.048788	5.048903	0.050109
Cross	G	11207	10203	367.109	8361.18	4843.01	-8.452304	8.452577	0.110026
Cross	**H**	11207	10204	**4092.56**	**8362.406**	6003.22	-5.728161	5.728263	0.065721
Cross	I	10203	11208	3392.333	8362.25	5755.29	-6.144088	6.144232	0.15932
Cross	J	11208	10204	367.125	8361.179	4861.61	-8.452289	8.452563	0.074766
Cross	K	11208	10303	1565.971	8362.016	5113.2	-7.273931	7.274124	0.080362
Cross	L	11208	10304	2261.048	8361.206	5348.9	-6.749705	6.749853	0.101652

2.2.2 Telesat Polar Orbit Doppler Shift Link Range Analyses

Six communication links over three adjacent orbital planes were analyzed in the Telesat OISL polar orbit constellation (Figure 12). Optical communication link A, link B, and link C are links between satellites in adjacent planes moving in the same direction. Optical communication link D, link E, and link F are links between satellites in adjacent planes at the seam of the Walker Star constellation with the satellites moving in opposite directions. A majority of the communication links will occur between satellites in adjacent planes moving in the same direction with only two seams in the Walker Star constellation.

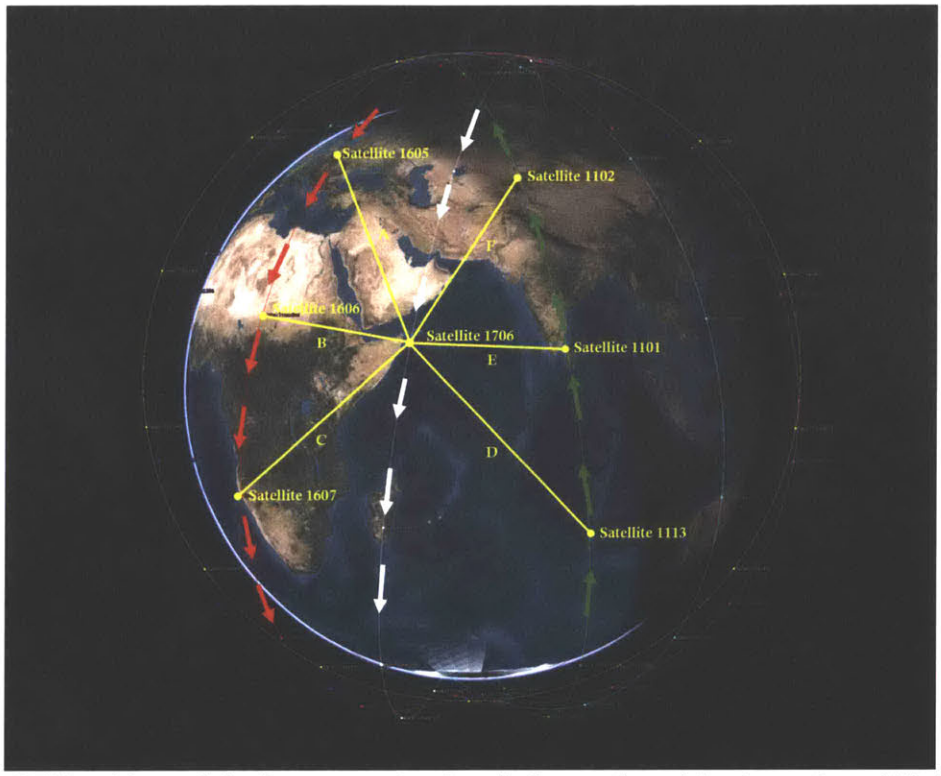

Figure 12. STK v.11 model of communication links analyzed in the reduced Telesat OISL inclined orbit constellation.

Table 13 summarizes the Doppler shift values and Doppler shift rates, and Table 14 summarizes the ranges and range rates for each of the communication links analyzed in the STK model of the reduced Telesat OISL polar orbit constellation. For the Telesat OISL polar orbit constellation analysis, the minimum Doppler shift is -7.863 GHz and the maximum Doppler shift is 7.864 GHz, based on optical communication link F between satellites in adjacent planes in the seam of the Walker Star constellation. For satellites in adjacent planes in the non-seam regions of the Walker Star constellation, the minimum Doppler shift is -2.053 GHz and the maximum Doppler shift is 2.053 GHz for optical communication link B. For the optical communication links in the non-seam adjacent plane scenarios, the greatest range values occur in optical communication link C with the minimum link distance as ~3489 km and the maximum link distance is ~4761 km. For the optical communication links in the seam adjacent plane scenarios, the greatest maximum range of ~7429 km occurs in optical communication link F.

Table 13. Optical communication link Doppler shift and Doppler shift rates analyzed in the STK model of the reduced Telesat OISL polar orbit constellation.

Link Type	Link Label	Satellite Tx Identifier	Satellite Rx Identifier	Minimum Doppler Shift [GHz]	Maximum Doppler Shift [GHz]	Mean Doppler Shift [GHz]	Minimum Doppler Shift Rate [GHz/sec]	Maximum Doppler Shift Rate [GHz/sec]	Mean Doppler Shift Rate [GHz/sec]
Adjacent	A	1706	1605	-0.832	0.832	0.001	-0.001974	0.00143	0.000017
Adjacent	**B**	1706	1606	**-2.053**	**2.053**	0.008	0.002073	0.000007	0.000007
Adjacent	C	1706	1607	-0.817	0.817	0.008	-0.001925	0.001411	0.00001
Seam	D	1706	1113	-7.155	7.155	-0.378	-0.037084	0.000706	-0.0132
Seam	E	1706	1101	-7.456	7.456	-0.16	-0.044811	0.002032	-0.13591
Seam	**F**	1706	1102	**-7.863**	**7.864**	-0.276	-0.061091	0.003326	-0.012925

Table 14. Optical communication link ranges and range rates analyzed in the STK model of the reduced Telesat OISL polar orbit constellation.

Link Type	Link Label	Satellite Tx Identifier	Satellite Rx Identifier	Minimum Range [km]	Maximum Range [km]	Mean Range [km]	Minimum Range Rate [km/sec]	Maximum Range Rate [km/sec]	Mean Range Rate [km/sec]
Adjacent	A	1706	1605	3401.459	4696.585	4082.098	-1.29	1.29	-0.000147
Adjacent	B	1706	1606	45.0655	3238.862	2075.617	-3.182	3.182	-0.012464
Adjacent	**C**	1706	1607	**3489.129**	**4760.506**	4152.974	-2.192	1.267	-0.012776
Seam	D	1706	1113	3476.022	7418.41	5287.378	-11.090091	11.090515	0.585624
Seam	E	1706	1101	2876.629	7419.696	4905.109	-11.556775	11.557239	0.248271
Seam	**F**	1706	1102	2110.058	**7428.694**	4620.307	-12.188275	12.188811	0.428119

2.3 LEO OISL Link Budget Calculations

A LEO OISL link budget calculation was completed to evaluate requirements for an optical coherent modem design. Designing an optical coherent modem for a 100G system with a third generation commercial optical coherent DSP ASIC, the OSNR threshold was fixed to 11.0 dB [Ishida, 2016]. A transmit wavelength of 1550 nm was assumed for the application, which is a typical frequency used for free space optical communications applications. The optical communications system is assumed to use an optical fiber amplifier with transmit optical output power ranging from 33.0 dB (2.0 W) to 37.0 dB (5.0 W), and an optical low noise amplifier (LNA) with 40 dB gain and 4.0 dB noise figure on the optical receive path [Gonthier et al., 2018]. The LLCD FSOC system was designed with a 10.8 cm diameter aperture and demonstrated a pointing accuracy of 2.5 μrad [Robinson et al., 2011; Boroson et al., 2014]. LCT was designed with a 13.5 cm diameter aperture and demonstrated a pointing accuracy of 100 μrad [Zech et al., 2015; Zech et al., 2017]. A pointing accuracy of 5.0 μrad is assumed for the LEO OISL link budget. The assumed aperture size and pointing accuracy are used to calculate the pointing error in the OISL link budget. The optical pointing assembly of the OISL system is responsible for the pointing, acquisition, and tracking (PAT) required to find the other satellite in an OISL application; determining the pointing accuracy and related PAT parameters for the OISL system is not within the scope of this work, which is focused on the optical coherent modem.

The link margin is calculated based on evaluating the optical signal to noise ratio (OSNR), which is the ratio of total signal power measured in both polarizations and the total noise power for both polarizations measured in a reference bandwidth of 0.1 nm centered at the signal carrier frequency. OSNR is a function of the ideal receiver sensitivity at 0.1 nm bandwidth (58 dBm), input optical power to the LNA, and the noise figure of the LNA (Equation 2) [O'Sullivan and Cartledge, 2018]. We calculate link margin based on solving for the margin between optical link OSNR and the required OSNR (ROSNR) or OSNR threshold of the coherent DSP ASIC (Equation 3). We assume a ROSNR of 11.0 dB for commercial optical coherent DSP ASIC with 16 nm FinFET plus CMOS technology [Ishida, 2016].

$$OSNR\ [dBm] = 58.0\ [dBm] + Pin_{LNA}[dBm] - NF_{LNA}[dB]$$

Equation 2. OSNR threshold equation based on ideal receiver sensitivity, noise figure of low noise amplifier, and optical power input to low noise amplifier [O'Sullivan and Cartledge, 2018].

$$Link\ Margin\ [dB] = OSNR\ [dBm] - ROSNR_{ASIC}[dBm]$$

Equation 3. Optical coherent link margin calculation.

For a link margin of 10 dB or greater, the OISL link budget was used to determine the achievable link ranges based on free space path loss (FSPL) and the required combination of transmit power, which would be provided through an optical amplifier, and aperture size. The purpose of the link budget is to evaluate if the achievable link ranges and the required transmit power for the 100G optical coherent modem are feasible for an OISL application. Table 15 summarizes three sample OISL link budget calculations for 10 dB link margin: **Case A** scenario of OISL system with 33.0 dBm (2.0 W) optical transmit power and 7.0 cm aperture

for a 2000 km range, **Case B** scenario of OISL system with 34.0 dBm (2.5 W) optical transmit power and 11.5 cm aperture for a 4800 km range, and **Case C** scenario of OISL system with 37.0 dBm (5.0 W) optical transmit power and 13.0 cm aperture for a 8550 km range. Case A models an OISL system designed for minimized size, weight, and power (SWaP) through minimum values for optical transmit power and aperture size. Case B models an OISL system for an intermediate SWaP between case A and case C. The 4800 km link range in Case B encompasses the maximum link range for all Telesat polar orbit adjacent links and for some of the Telesat inclined adjacent and cross plane links. Case C models an OISL system for maximum SWaP feasible for a LEO small satellite, with higher optical transmit power and aperture size. The 8500 km link range in Case C encompasses all maximum link ranges for Telesat polar and Telesat inclined orbit link ranges.

Table 15. Sample OISL link budget calculations for 10 dB link margin.

Parameter	**Case A – Minimum Tx Power / Minimum Aperture**		**Case B – Mid-Range Tx Power / Mid-Range Aperture**		**Case C – Maximum Tx Power / Maximum Aperture**	
	Value	**dB**	**Value**	**dB**	**Value**	**dB**
Transmit wavelength	1.550E-06 m	-	1.550E-06 m	-	1.550E-06 m	-
Transmit Power	**2.0 W**	**33.0 dBm**	**2.5 W**	**34.0 dBm**	**5.0 W**	**37.0 dBm**
Transmit Aperture	**8.0 cm**	**104.2 dB**	**11.5 cm**	**107.4 dB**	**13.5 cm**	**108.7 dB**
Transmit Throughput	70 %	-1.5 dB	70 %	-1.5 dB	70 %	-1.5 dB
Transmit Wavefront Error	0.10 waves RMS	-1.7 dB	0.10 waves RMS	-1.7 dB	0.10 waves RMS	-1.7 dB
Transmit Pointing Error	5.0 µrad	-0.6 dB	5.0 µrad	-1.1 dB	5.0 µrad	-1.6 dB
Range (km)	**2400 km**	**-265.8 dB**	**4800 km**	**-271.8 dB**	**8500 km**	**-276.8 dB**
Atmospheric Losses	-	0.0 dB	-	0.0 dB	-	0.0 dB
Receive Aperture	**8.0 cm**	**104.2 dB**	**11.5 cm**	**107.4 dB**	**13.5 cm**	**108.7 dB**
Receive Throughput	70 %	-1.5 dB	70 %	-1.5 dB	70 %	-1.5 dB
Receive Wavefront Error	0.10 waves RMS	-1.7 dB	0.10 waves RMS	-1.7 dB	0.10 waves RMS	-1.7 dB
Receive Pointing Error	5.0 µrad	-0.6 dB	5.0 µrad	-1.1 dB	5.0 µrad	-1.6 dB
Receive Fiber Coupling Efficiency	80 %	-1.0 dB	80 %	-1.0 dB	80 %	-1.0 dB
Input Power to LNA		-33.0 dBm		-33.0 dBm		-33.0 dBm
LNA Noise Figure		-4.0 dB		-4.0 dB		-4.0 dB
Required OSNR	**(0.1 nm BW)**	**11.0 dB**	**(0.1 nm BW)**	**11.0 dB**	**(0.1 nm BW)**	**11.0 dB**
Ideal Receiver Sensitivity	(0.1 nm BW)	-58.0 dB	(0.1 nm BW)	-58.0 dB	(0.1 nm BW)	-58.0 dB
LINK MARGIN		**10.0 dB**		**10.0 dB**		**10.0 dB**

A MATLAB script (Appendix section A1. LEO OISL Link Budget Calculations for 100 Gbps Optical Coherent Modem) was created to evaluate the combinations of optical transmit power, aperture size, and OISL range, which close the OISL budget with 10 dB link margin or greater. The script input optical transmit power levels between 30.0 dBm (1.0 W) and 37.0 dBm (5.0 W), transmit and receive aperture sizes between 7.0 cm and 13.5 cm, and OISL ranges between 1000 km and 8500 km. Figure 13 shows a three-dimensional graph from the MATLAB link budget analyses for the combinations of optical transmit power, aperture size, and OISL range, which close the OISL budget with 10 dB link margin or greater. These combinations show the open trade space for the OISL system design with the 100G optical coherent modem with 11.0 dB ROSNR.

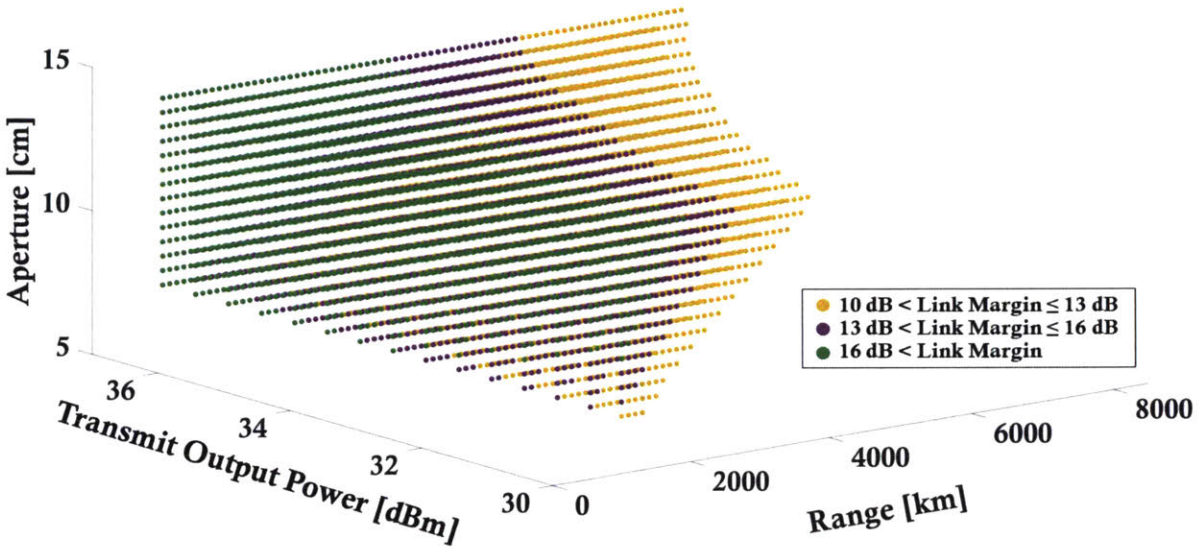

Figure 13. MATLAB OISL link budget analyses for combinations of optical transmit power, aperture size, and OISL range, which close the OISL budget with 10 dB link margin or greater.

Several optical fiber amplifiers with output powers in the required range of the sample link budget exist commercially or are currently in development for space applications. As summarized in Chapter 1.2, FSOC demonstrations by Aerospace Corporation OCSD utilized a 3 W fiber amplifier on a CubeSat and Tesat LCTs utilized fiber amplifiers for a 2.2 W optical output [Hauschildt et al., 2018; Rose et al., 2018]. For 1550 nm optical communications links, Fibertek has developed a 0.5 W amplifier for CubeSat applications and a 6 W amplifier for deep space applications. The 6 W amplifier can provide optical output power of up to 12 W with mass of 4 kg and 34 W of average electrical power consumption. Fibertek has completed thermal vacuum and vibration testing of the 6 W amplifier [Engin et al., 2019]. LGS Innovations LLC has developed a laser transmitter assembly with integrated fiber amplifier for average optical output power of greater than 4 W. The fiber amplifier is designed using COTS erbium (Er) doped fiber and proprietary erbium ytterbium (Er/Yb) co-doped fibers. The transmitter is less than 6 kg and has an electrical power consumption of less than 40 W [Engin et al., 2019]. MPB Communications, Inc. is developing a 1550 nm combined transmission booster amplifier and receiver preamplifier for OISL applications. The transmit

booster amplifier can provide 1 W optical output power and the receiver preamplifier can provide up to 40 dB of gain for input signals in the range of -35 dBm to -45 dBm. The prototype unit has a volume of 160 mm by 120 mm by 50 mm, a mass of less than 1 kg, and a power consumption of less than 12 W [Gonthier et al., 2018].

2.4 Summary of 100 Gbps Optical Coherent Modem Requirements

The Telesat OISL constellation radiation environment, orbit, and link budget analyses inform requirements for development of the optical coherent modem. We define radiation requirements based on 200 mils of aluminum shielding thickness, which is a reasonable assumption to account for the optical coherent modem chassis (typically 100 mils thickness) and additional shielding from a spacecraft. Greater aluminum shielding thicknesses will have diminishing return for TID and DDD. We define 100 krad(Si) as the TID level for which the optical coherent modem will survive and experience no parametric performance degradation. The TID level of 100 krad(Si) is greater than 2× margin for the Telesat polar orbit and is ~1.7× margin for the Telesat inclined orbit.

Excluding OISLs between in-seam planes of the Telesat polar constellation (Doppler shift range of +/- 7.86 GHz), the limiting Doppler shift range is – 5.44 GHz to + 5.44 GHz. OISLs between in-seam planes only occur between two sets of planes and do not represent the majority of OISLs for the constellation. The optical coherent modem will need to compensate for the expected Doppler shift on a system level but can utilize features of the key electro-optical components, specifically the coherent DSP ASIC, to help contribute to meeting overall system level requirements for Doppler shift compensation. On a system level, the optical coherent modem shall tolerate Doppler shift of range – 8.0 GHz to + 8.0 GHz without OISL outage. The +/- 8.0 GHz Doppler shift range requirement for the system incorporates additional margin beyond the expected +/- 5.44 GHz range for Telesat inclined constellation and encompasses the limiting case of expected +/- 7.86 GHz range for the in-seam planes of the Telesat polar constellation. With slight penalty to the ROSNR, coherent DSP ASICs can compensate for carrier frequency offset (CFO) between the coherent receiver input optical signal and the input LO due to Doppler shift [Bennett et al., 2014]. The optical coherent DSP ASIC shall compensate for carrier frequency offset (CFO) of $\leq$ - 5.5 GHz and $\geq$ + 5.5 GHz with less than 1.0 dB impact to OSNR. Beyond the coherent DSP ASIC CFO compensation, additional techniques (Chapter 6) can be used to compensate for the expected Doppler shift.

We analyze the open trade space for the coherent OISL system based on a coherent DSP ASIC ROSNR of 11.0 dB. A lower optical signal to noise ratio (OSNR) threshold or ROSNR of a coherent DSP ASIC is ideal to provide more link margin. For a general coherent system, transmit and receive lasers require a narrow (few hundred kHz) laser linewidth. For an OISL application, transmit and receive lasers shall have optical output signals with center wavelengths within the C-band (1530 nm – 1565 nm). For the transmit laser, the required optical output power is based on the insertion loss of the optical signal input to the coherent transmitter. For the receive laser, the required optical output power is based on the coherent receiver input optical signal versus LO power mask. For compatibility with a 100 Gbps DP-

QPSK optical coherent ASIC, the coherent transmitter and the coherent receiver shall have symbol rates of 32 GBaud and capabilities to modulate/de-modulate DP-QPSK signals.

Table 16 summarizes key requirements for the 100 Gbps optical coherent modem. Note that Table 16 is not a comprehensive set of requirements and only defines key high-level functional, environment, and performance requirements for the optical coherent system and components, which are used for optical coherent modem component selection in the following chapters.

Table 16. Requirements for 100 Gbps optical coherent modem for Telesat OISL constellation

Requirement	Parent	Type	Description	Verification	Rationale
L0 – Optical Coherent Modem System Requirements					
L0 – 01	–	Functional	The optical coherent modem shall support a transmit data rate of ≥ 100 Gbps.	Test	Optical coherent technology compatibility
L0 – 02	–	Functional	The optical coherent modem shall support a receive data rate of ≥ 100 Gbps.	Test	Optical coherent technology compatibility
L0 – 03	–	Functional	The optical coherent modem shall transmit and receive data simultaneously.	Test	
L0 – 04	–	Functional	The optical coherent modem shall operate with independent transmit and receive center wavelengths (center frequency) between 1530 nm (195.9 THz) and 1565 nm (191.6 THz).	Test	Optical coherent technology compatibility; FSOC C-Band
L0 – 05	–	Performance	The optical coherent modem shall encode a 100 Gbps DP-QPSK signal over 32 GHz optical bandwidth	Test	Optical coherent technology compatibility
L0 – 06	–	Performance	The optical coherent modem shall decode a 100 Gbps DP-QPSK signal over 32 GHz optical bandwidth with required optical signal to noise ratio (ROSNR) of ≤ 11.0 dB.	Test	Telesat OISL Link Budget Analyses
L0 – 07	–	Performance	The optical coherent modem shall have an availability of ≥ 99.999% (five nines) in the nominal radiation environment for the mission.	Analysis	Telecom Industry Requirement
L0 – 08	–	Performance	The optical coherent modem shall tolerate Doppler shift between -8.0 and +8.0 GHz.	Test	Telesat OISL Doppler Shift Analyses
L0 – 09	–	Environment	The optical coherent modem shall survive and operate up to total ionizing dose (TID) level of ≥ 100 krad(Si) without performance degradation.	Test	Telesat OISL Radiation Environment Modeling
L0 – 10	–	Environment	The optical coherent modem shall survive and operate up to displacement damage dose level of ≥ 5.8×10^8 (10 MeV)/g(Si).	Test	Telesat OISL Radiation Environment Modeling
L0 – 11	–	Environment	The optical coherent modem shall have minimum onset linear energy transfer (LET) value of 26 MeV·cm^2/mg for destructive single event effects.	Test	Telesat OISL Radiation Environment Modeling
L1 – Optical Coherent DSP ASIC					
L1 – 01	L0 – 05	Performance	The optical coherent DSP ASIC shall provide 100 Gbps DP-QPSK voltage signals as input to a coherent transmitter.	Test	Coherent DSP ASIC Design Standard
L1 – 02	L0 – 06	Performance	The optical coherent DSP ASIC shall take input of 100 Gbps DP-QPSK voltage signals output from a coherent receiver.	Test	Coherent DSP ASIC Design Standard
L1 – 03	L0 – 06	Performance	The optical coherent DSP ASIC shall have a ROSNR of ≤ 11.0 dB.	Test	Telesat OISL Link Budget Analyses

L1 – 04	L0 – 08	Performance	The optical coherent DSP ASIC shall compensate for carrier frequency offset (CFO) of ≤ - 5.5 GHz and ≥ + 5.5 GHz with less than 1.0 dB impact to OSNR.	Test	Based on Telesat Inclined Orbit Doppler shift analyses
L1 – Coherent Transmitter					
L1 – 05	L0 – 05	Functional	The coherent transmitter shall support 100 Gbps DP-QPSK with 32 Gbaud symbol rate.	Test	Coherent Receiver Design Standard
L1 – Coherent Receiver					
L1 – 06	L0 – 06	Functional	The coherent receiver shall support 100 Gbps DP-QPSK with 32 Gbaud symbol rate.	Test	Coherent Transmitter Design Standard
L1 – Lasers					
L1 – 07	L0 – 04	Functional	The transmit laser and the receive LO laser shall operate with center wavelengths (center frequency) between 1530 nm (195.9 THz) and 1565 nm (191.6 THz).	Test	Optical Coherent System Compatibility
L1 – 08	L0 – 08	Performance	The transmit laser and the receive LO laser shall have capability to phase continuously tune the center frequency of the output optical signal +/- 8.0 GHz from the center frequency.	Test	Telesat OISL Doppler Shift Analyses
L1 – 09	–	Performance	The transmit laser and the receive LO laser shall output an optical signal with ≥ 10 dBm optical output power.	Test	Expected Insertion Loss Through Coherent Transmitter
L1 – 10	–	Performance	The transmit laser and the receive LO laser shall have a linewidth of ≤ 100 kHz.	Test	Optical Coherent System Requirement
L1 – 11	–	Functional	The transmit laser shall output a polarization maintained (PM) optical signal and interface with the coherent transmitter via PM optical fiber.	Test	Optical Coherent System Requirement
L1 – 12	–	Functional	The receive LO laser shall output a polarization maintained (PM) optical signal and interface with the coherent receiver via PM optical fiber.	Test	Optical Coherent System Requirement

Chapter 3

Commercial 100G/200G Optical Coherent DSP ASIC

3.1 Background

Digital coherent DSP technology, enabled through developments in CMOS ASICs, has been the cornerstone to coherent fiber optic communication implementation over the last decade. The optical coherent DSP ASIC is the key electro-optical component, which interfaces to the coherent transmitter and coherent receiver in an optical coherent modem, as shown in Figure 14.

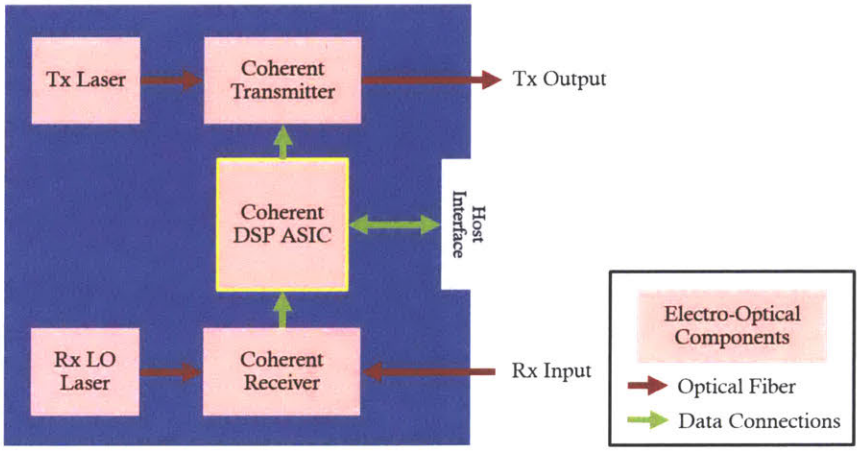

Figure 14. Optical coherent modem electro-optical component functional block diagram with coherent DSP ASIC highlighted.

There have been three generations of coherent DSP ASICs, which have developed to improve power efficiency in each generation through multi-function integration, function adaptation to turn off un-used circuits, CMOS process advancement, and implementation optimization [Ishida, 2016]. Table 17 below summarizes the key features of each DSP generation including the CMOS process, power consumption for 100G Gbps and OSNR tolerance [Ishida, 2016]. The differences among the three generations of coherent DSP ASICs has been further detailed

by Ishida (2016). Ciena Corp., Cisco Systems Inc., Infinera Corp., Nokia Corp, Acacia Communications Inc., Inphi Corp., NTT Electronics Corp., Broadcom, ViaSat, and Macom are major vendors of coherent DSP technology [Melle, 2018]. Key parameters for coherent DSP ASICs, such as OSNR threshold and power consumption, are proprietary and confidential information to vendors.

Table 17. Summary of three generations of coherent DSP ASICs and key parameters [Ishida, 2016].

Generation	**1**	**2**	**3**
CMOS Process	40 nm Bulk	20-28 nm Bulk	16 nm FinFET
Sample Release	2011	2014	2016
Power Consumption for 100G	40 W (Core DSP) 60 W (+ external chips)	18 W	9 W
OSNR Tolerance for 100G DP QPSK	12 dB	12 dB	10 – 11 dB

The third generation DSP uses a FinFET CMOS process and has capability for 200G DP 16-QAM [Ishida, 2016]. The FinFET structure consists of a thin (~10 nm or less), vertical fin of silicon body on a substrate, allowing the gate capacitance to be physically closer to the whole channel and the gate to control the leakage path. The channel for FinFET CMOS technology is vertical and the height of the fin determines the device width. In comparison, the channel in bulk CMOS technology is horizontal. FinFET technology provides advantages, such as higher drive current for given transistor footprint, higher speed, lower leakage, lower power consumption, no random dopant fluctuation, and better mobility and scaling of the transistor beyond 28 nm, in comparison to bulk CMOS technology [Vora and Lad, 2017]. Figure 15 shows diagrams comparing (a) bulk CMOS technology and (b-c) FinFET CMOS technology structures [Vora and Lad, 2017].

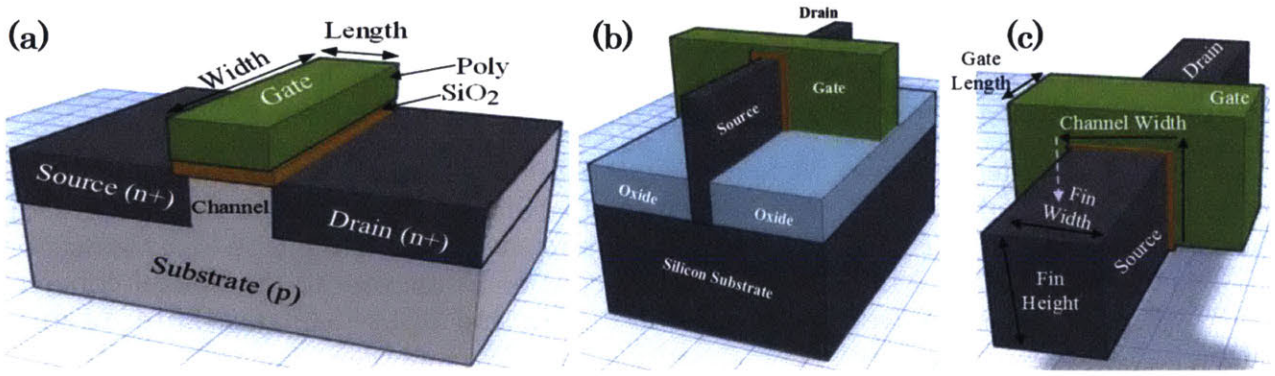

Figure 15. Bulk CMOS vs. FinFET CMOS technology. (a) Structure of bulk CMOS technology. (b) and (c) Structure of FinFET CMOS technology. [Vora and Lad, 2017]

In an optical transceiver, the coherent DSP ASIC interfaces between a host side and optical components (line side). The transmit path is the host side to line side and consists of inputting data from the host to the ASIC for DSP, framing, and FEC processing. The processed data from the ASIC is then output to line side optical components, such as an optical modulator. The receive path is the line side to the host side, in which received data from optical coherent

receiver is input to the ASIC. The received processed data from the ASIC is then sent to the host system.

An example detailed data path through a 100G coherent DSP ASIC is modeled in Figure 16, adapted from Kisaka et al. [2016]. For the transmit path, 100G data enters from the host side into a framer and then into the DSP portion of the ASIC, which includes FEC encoding, constellation signal mapping, spectral shaping, pre-compensation, and other features. The data exits the ASIC after conversion with a 4-channel DAC and is output as 4 signals for 100G DP-QPSK (XI, XQ, YI, YQ) into the coherent modulator. For the receive path, analog 100G DP-QPSK signals are converted with a 4-channel ADC at the receive side input of the ASIC. The data undergoes DSP, which includes spectral shaping, dispersion compensation, AEQ, signal mapping, and FEC decoding. The data goes through a de-framer prior to output to the host-side [Kisaka et al., 2016].

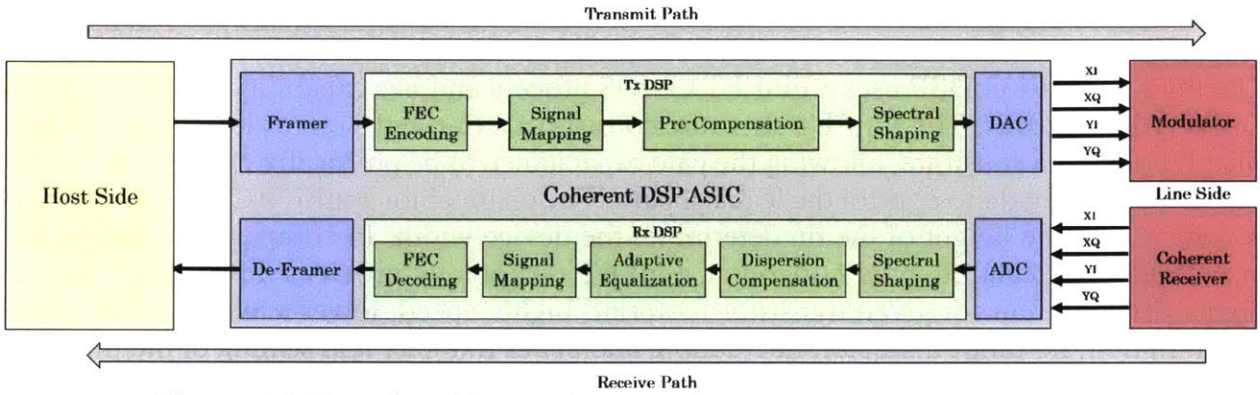

Figure 16. Functional block diagram of general coherent DSP ASIC.

3.2 Radiation Susceptibility

The space radiation environment has the potential to damage or degrade optical transceiver systems. Proton-induced SEEs in optoelectronic receivers can contribute to link bit error rate (BER), and displacement damage can occur in optoelectronics [LaBel, 1998]. TID effects and SEEs can also damage supporting microelectronics.

As CMOS based technologies, coherent DSP ASICs with internal microprocessors are susceptible to TID effects and SEEs. Non-destructive SEEs relevant to optical coherent DSP ASICs include SEUs, SEFIs, MBUs, and MCUs (reference to background on SEEs in Section 2.1.1.3) [Samaras, 2014; Mutuel, 2016]. Destructive SEEs relevant to the optical coherent DSP ASICs with CMOS technology include SEHEs and SELs [Samaras, 2014; Mutuel, 2016].

As coherent DSP ASICs move toward FinFET plus CMOS technologies with thinner active regions, we expect both reduced TID effects and probability of SEE striking the active region. Bulk FinFET technologies are more robust to TID that planar CMOS technologies and have been found to have TID tolerance for hundreds of krad(Si) [Roche et al., 2013]. If a heavy ion or proton directly strikes the thin active region, we expect the SEE impact to be more significant than for thicker active regions due to proximity of several circuit nodes and strong charge sharing between several circuit nodes [Lilja et al., 2013]. Karp et al. (2018) observed increased SEL sensitivity in a 16-nm FinFET CMOS prototype in comparison to 20-nm

planar technology Xilinx products for 64 MeV proton radiation and neutron radiation. The three times shallower trench isolation of FinFET technology reduces the base width of the lateral bipolar parasitic transistor by a factor of two. This significantly increases the gain product of parasitic CMOS silicon controlled rectifier (SCR) [Karp et al., 2018].

3.3 Previous Radiation Assessments of Commercial Optical Coherent DSP ASICs with 28 nm Bulk CMOS Technology

Radiation assessments of commercial optical coherent DSP ASICs have been completed and show potential for applying this technology for a space-based optical communications system. Radiation assessments on commercial 100G optical coherent DSP ASICs with 28 nm bulk CMOS technology, Inphi CL20010A1 and Acacia DSP ASIC within the AC100M, have been completed in previous studies [Aniceto, 2017; Aniceto, 2018]. The details of these radiation assessments can be found in the referenced literature. The previous studies conclude that further proton and heavy ion radiation testing of commercial coherent DSP ASICs is required.

No destructive SEEs were observed from 64 MeV and 480 MeV proton radiation test campaigns of the Inphi CL20010A1 [Aniceto, 2017]. The CL20010A1 ASIC survived and experienced no performance degradation from a proton total fluence of 1.27×10^{12} p/cm^2 with an equivalent TID exposure up to 170 krad(Si) while tested in the noise-loaded optical loopback configuration with 64 MeV protons. The results of these proton radiation assessments reveal the potential to use a commercial optical coherent DSP ASIC in a space application. Figure 17 shows the test setup from the Inphi CL20010A1 proton radiation assessment.

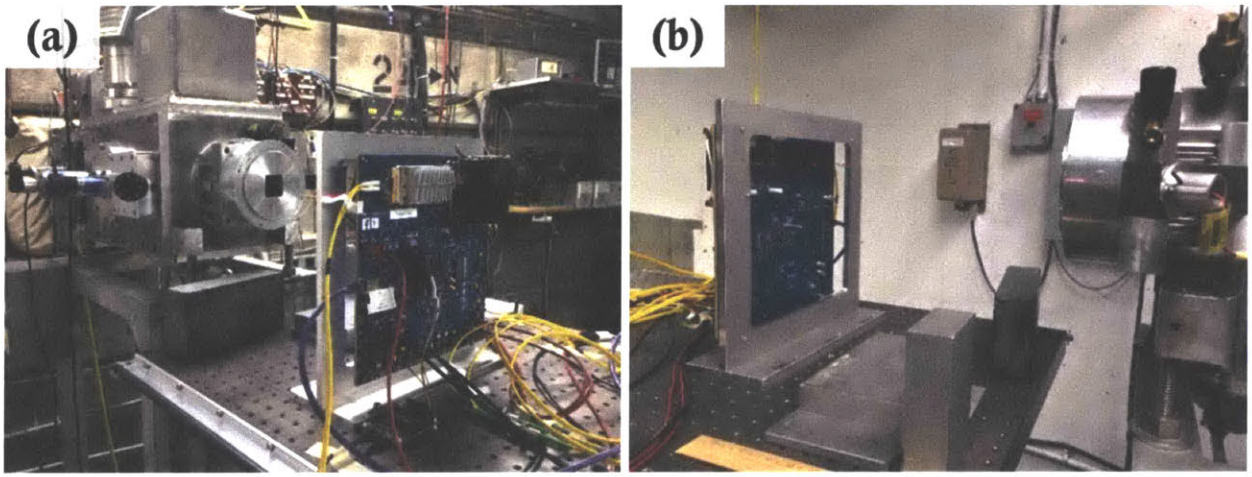

Figure 17. Inphi CL20010A1 proton radiation assessment test setup.

A gamma radiation assessment and 65 MeV proton radiation assessment of the Acacia coherent DSP ASIC integrated in the AC100M optical transceiver were completed. Figure 18(a) and Figure 18(b) show the test setup of the gamma radiation assessment of the Acacia coherent DSP ASIC. Figure 18(c) and Figure 18(d) show the test setup of the proton radiation assessment of the Acacia coherent DSP ASIC. Failure of a power component in the AC100M from gamma radiation exposure at a TID level of 13.7 krad(Si) indicates that replacement of auxiliary components around the optical coherent DSP ASIC is necessary to reduce risk for space missions in orbits with high altitudes and high inclinations beyond ISS orbit. This

motivates designing the OMA using a discrete commercial optical coherent DSP ASIC and selecting auxiliary components that may be more radiation-tolerant, rather than just using a commercial optical coherent pluggable module with integrated components.

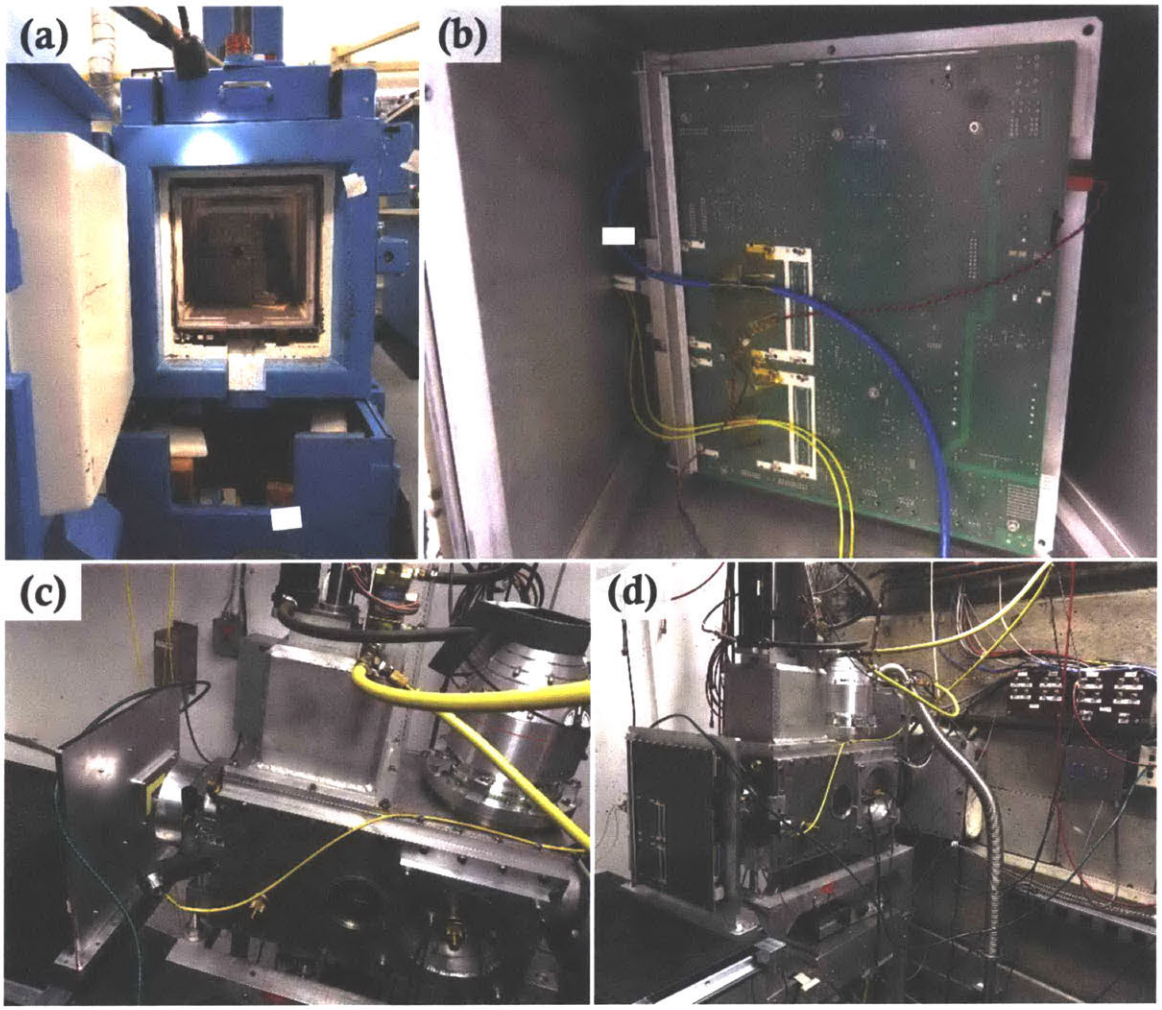

Figure 18. Acacia coherent DSP ASIC radiation assessment test setups. (a, b) Evaluation board for Acacia AC100M inside gamma radiation chamber. (c, d) Evaluation board for Acacia AC100M mounted on proton radiation beam.

This work focuses on use a state-of-the-art commercial 100G/200G optical coherent DSP ASIC (third generation of optical coherent DSP ASICs) with 16 nm FinFET CMOS technology for the OMA design. The third generation (2016) optical coherent DSP ASICs have lower power consumption (sub-10 Watt per 100 Gbps) and enhanced performance features and capabilities in comparison to the previous generation 28 nm bulk CMOS ASICs [Ishida, 2016]. Since there have been observations of increased single event latchup (SEL) sensitivity in FinFET in comparison to planar CMOS technologies, it is critical to complete a heavy ion radiation assessment for a commercial optical coherent DSP ASIC with FinFET CMOS technology [Karp, 2018].

3.4 Heavy Ion Radiation Assessments of Commercial Optical Coherent DSP ASICs with 16 nm FinFET plus CMOS Technology

Two heavy ion test campaigns were completed on a 100G/200G commercial optical coherent DSP ASICs manufactured in a 16 nm Fin Field Effect Transistor (FinFET) CMOS technology. There have been observations of increased single event latchup (SEL) sensitivity in FinFET CMOS technologies in comparison to planar CMOS technologies [Karp et al., 2018]. We assess the viability of state-of-the-art commercial optical coherent DSP for space applications through heavy ion testing at NASA Space Radiation Laboratory (NSRL). The first heavy ion radiation test campaign screened for destructive SELs and observed behavior of the ASIC to non-destructive heavy ion SEEs. The second heavy ion radiation test campaign gathered additional data to calculate heavy ion SEE cross section values and determine the ASIC heavy ion SEE rate for sample LEO OISL missions.

3.4.1 Heavy Ion Test Hardware, Test Configuration, and Test Setup

We developed a 100G/200G optical coherent modem assembly (OMA) to perform heavy ion radiation testing of the commercial optical coherent DSP ASIC as the device under test (DUT). The optical modem was designed with a commercial CFP2-ACO module as the line-side interface to the ASIC and a 4×28 Gbps QSFP loopback module for the host-side interface. For 200G mode, a 4×28 Gbps CAUI-4 loopback cable served as the second host-side interface. The host side was operating in optical transport network (OTN) mode with CAUI-4 electrical specification. The heavy ion test campaign was performed with the optical modem in 100G mode. The CFP2 module slot was designed with a heat sink and fan. A control loop was implemented, using the fan speed and temperature sensors in the DUT for thermal stabilization of the DUT at the maximum rated junction temperature. ASIC performance data was collected during tests, including the line-side and host-side post-FEC uncorrected errors and pre-FEC BER, as well as ASIC telemetry, including all voltage rails, current rails, and temperature sensors. Figure 19 shows the 100G/200G OMA developed for radiation testing of the commercial coherent DSP ASIC.

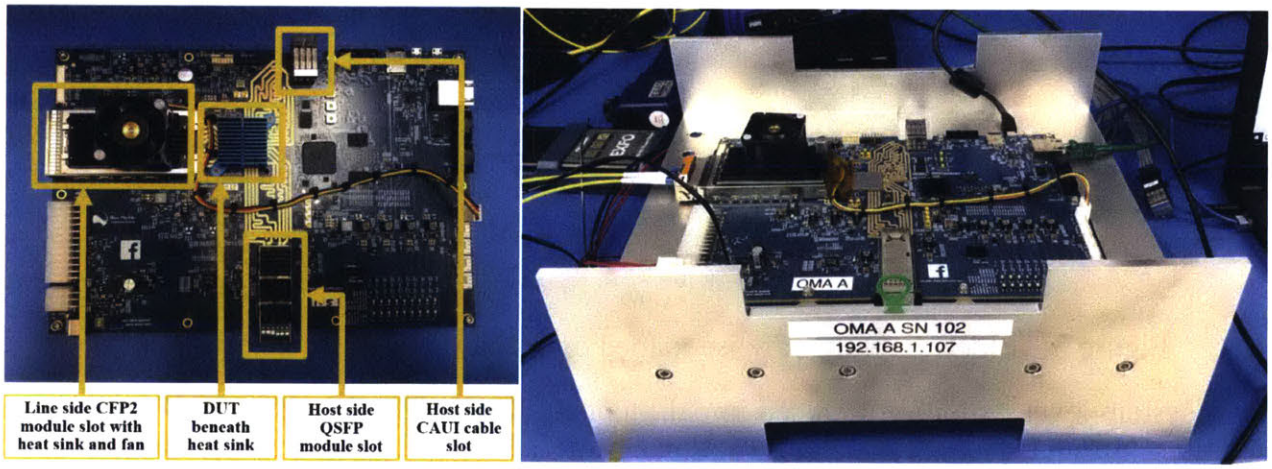

Figure 19. 100G/200G Optical Modem Assembly (OMA) developed for radiation test campaigns of commercial coherent DSP ASIC.

Laboratory benchtop testing and heavy ion radiation testing were performed in a noise-loaded optical loopback test configuration between two identical OMAs, one system serving as the test OMA and the other serving as the "ground" OMA (GOMA). Figure 20 shows the laboratory benchtop test setup with GOMA and OMA in noise-loaded optical loopback test configuration.

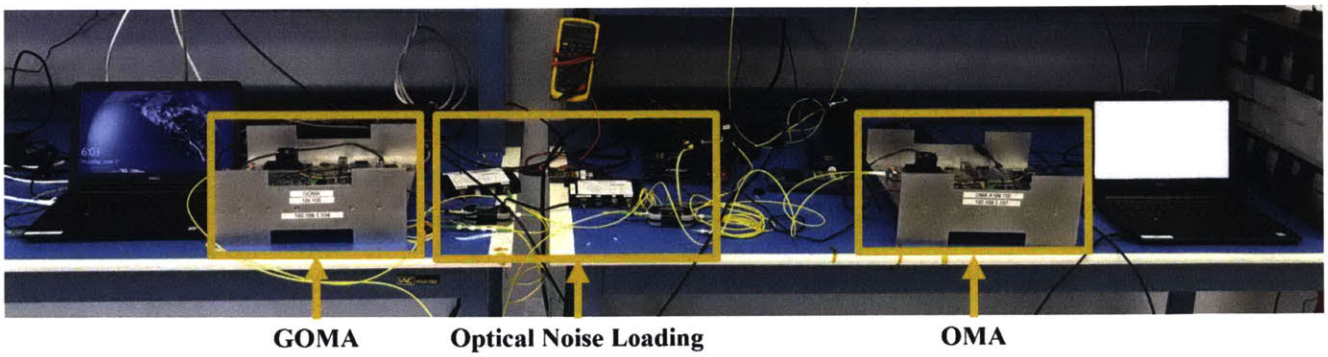

Figure 20. Laboratory benchtop test setup with GOMA and OMA in noise-loaded optical loopback test configuration.

The transmit path was noise-loaded to set the optical signal-to-noise ratio (OSNR) level near the ASIC receiver FEC correction threshold. This configuration represents the most stress for the OMA system because the optical communication link is signal-starved and the receiver is operating near the FEC threshold. The noise loading was accomplished by connecting the CFP2-ACO module transmit output to a variable optical attenuator (VOA), which introduced noise in the system. The VOA attenuation was set 2 dB from the ASIC OSNR threshold. The output of the VOA was input to an erbium doped fiber amplifier (EDFA), which amplified the signal with the introduced noise. The amplifier output was filtered with a 100 GHz optical band-pass filter. Figure 21 shows a block diagram of the noise-loaded optical loopback test configuration. In addition to the environmental stress induced by optical noise-loading, the ASIC was operated at the maximum rated junction temperature to simulate the worst-case thermal state during testing.

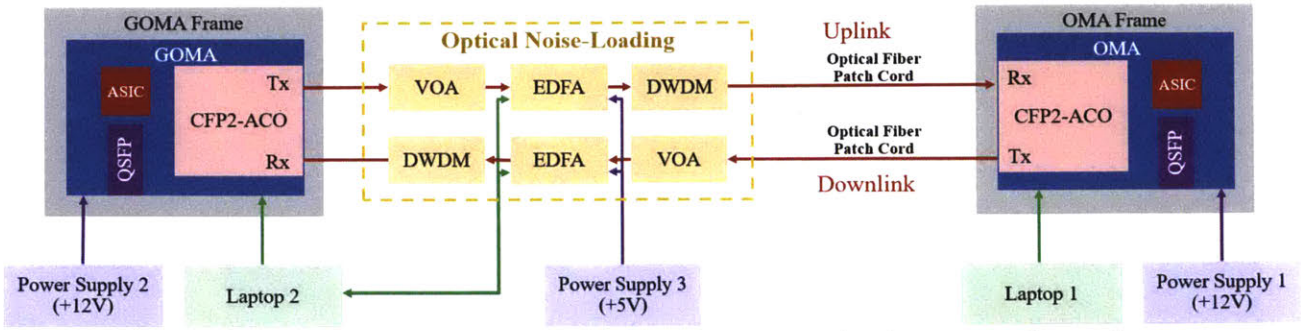

Figure 21. Block diagram of noise-loaded optical loopback test configuration.

On a system level, radiation induced impairments to the receive-side of the DUT would be identified through performance degradation on the OMA (DUT telemetry), and radiation impairments to the transmitter-side of the DUT would be identified through performance degradation on the GOMA ASIC.

Heavy ion radiation testing was conducted at NASA Space Radiation Laboratory (NSRL) at Brookhaven National Laboratory (BNL) in Long Island, NY. The OMA was fixed to a test stand in-line of heavy ion beam penetration, and a laser was used to align the DUT to the center of the heavy ion beam. Lead blocks were placed in front of the OMA with a small square hole above the DUT area to block the peripheral OMA components from heavy ion radiation and to ensure heavy ion radiation was isolated to the DUT. The test setup equipment for optical noise-loading, GOMA, laptops, and power supplies were set-up on a cart next to the OMA and out of the direct path of the heavy ion beam. Figure 22 shows the heavy ion radiation test setup at NSRL. Figure 22(b) shows the OMA with laser alignment of DUT in the center of the heavy ion beam path and Figure 22(c) shows the lead blocks used to shield the rest of the OMA from heavy ion radiation.

Figure 22. Heavy ion radiation test setup at NSRL. (a) The OMA fixed to a test stand in line of heavy ion beam and (b) the DUT aligned to center of the heavy ion beam path using lasers. (c). Lead blocks used to shield the rest of the OMA from heavy ion radiation.

The NSRL cyclotron delivers heavy ions in "spills," as a non-uniform flux over time. Each ion spill has a duration of 500 milliseconds over a period of 3.6 seconds. For each radiation test round, the start time of the first ion spill, the radiation end time, and the total irradiation time duration were recorded. The time stamp of observed SEEs and error messages from the DUT GUI console were recorded during each radiation test round. Two types of resets, a soft reset and a hard reset, were used between radiation sets if anomalous behavior persisted or GUI error messages continuously appeared after the end of irradiation. A soft reset included re-running the GUI software to initialize and power sequence the DUT as well as starting a new data file for recorded telemetry. A hard reset included power cycling the OMA then re-running the GUI software.

ASIC performance telemetry monitored for radiation assessments include line and host post-FEC uncorrected error count and pre-FEC bit error rate (BER). Since the host-side of the OMA was not noise-loaded or attenuated, the host pre-FEC BER was low (less than 10^{-10}) and recorded as a value of 0. The current was recorded for five voltage rails. Voltage rails V1 and V2 are the digital core voltage power supply. Voltage rails V3 and V4 are the analog

power supplies. Voltage rail V5 is the CMOS high speed I/O power supply. Table 18 summarizes the coherent DSP ASIC voltage rails and nominal current ranges for the coherent DSP ASIC operating in 100G SDFEC mode. Temperature data from temperature sensors in the ASIC was recorded. Figure 23 is the pre-radiation telemetry recorded from the first heavy ion radiation test campaign of the noise-loaded optical loopback test configuration.

Table 18. Coherent DSP ASIC voltage rails

Voltage Rail	Description	Voltage	Nominal Current Range
V1	Digital core voltage power supply	0.7 V	12.788 – 13.069 A
V2	Digital core voltage power supply	0.8 V	0.521 – 0.528 A
V3	Analog power supply	0.9 V	1.318 – 1.328 A
V4	Analog power supply	1.8 V	1.947 – 1.953 A
V5	CMOS high speed I/O power supply	1.8 V	0.033 – 0.035 A

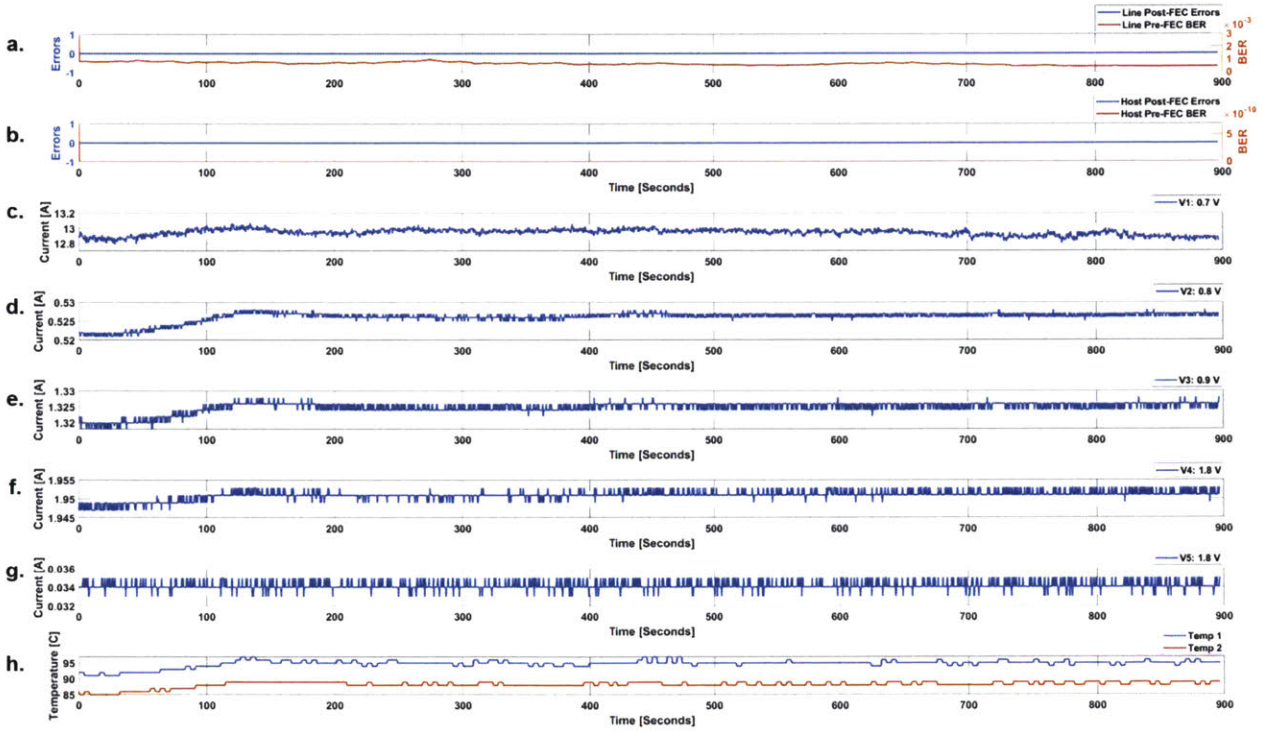

Figure 23. Commercial coherent DSP ASIC data set from pre-radiation testing. (a) Line post FEC uncorrected errors (left y-axis) and line pre-FEC BER (right y-axis) over time. (b) Host post FEC uncorrected errors (left y-axis) and host pre-FEC BER (right y-axis) over time. (c) Current for voltage rail V1 at 0.7 V. (d) Current for voltage rail V2 at 0.8 V. (e) Current for voltage rail V3 at 0.9 V. (f) Current for voltage rail V4 at 1.8 V. (g) Current for voltage rail V5 at 1.8 V. (h) Temperature sensors of DUT.

3.4.2 Heavy Ion Radiation Test Campaign 1

The test campaign consisted of ten total irradiation rounds with one radiation round of 3.6 GeV Carbon ions and nine radiation rounds of 46.2 GeV Xenon ions. Each radiation test round generated a different heavy ion linear energy transfer (LET) level. As a heavy ion penetrates an electronic device, energy is transferred from the particle to the device material

and the particle slows down. Electrons within the device material act as a viscous medium to slow down particles and cause ionizing energy loss. Ions with greater energy levels lose energy at a slower rate through material than ions with lower energy levels. LET is a function of the ionizing energy loss by path length of a particle and normalized by the target density (Equation 4) [McMorrow, 2004]. LET is expressed in units of MeV·cm^2/mg. Layers of polyethylene material ranging from 15 mm to 22 mm in 1 mm increments were used to degrade the Xenon ions energy levels to generate higher LET levels of ions penetrating the active region of the DUT.

$$LET = \left(\frac{1}{\rho}\right) \cdot \left(\frac{dE}{dx}\right)_{Ionizing} \left[\frac{MeV \cdot cm^2}{mg}\right]$$

Equation 4. Linear Energy Transfer calculation [McMorrow, 2004].

Table 19 summarizes the test parameters for each heavy ion radiation test round. For the first radiation set, the DUT was irradiated with 3.6 GeV Carbon ions to a total fluence level of 9.7×10^6 ions/cm^2 over seven rounds with a total irradiation time of ~ 75 minutes. The first Carbon radiation round had an average spill fluence of 200 ions per spill, and the spill fluence was increased for each radiation set up to 20,000 ions per spill. After the Carbon ions test round, we conducted a soft reset of the OMA and GOMA. No SEEs were observed.

For the second radiation test set, the DUT was irradiated with 46.2 GeV Xenon ions to a total fluence of 1.97×10^5 ions/cm^2 over nine rounds with a total irradiation time of ~ 86.5 minutes. A spill fluence of 300 ions per spill was used for the first seven radiation sets. After observing a persistent SEE with continuous GUI error messages in the seventh irradiation set, the spill fluence was decreased to 30 ions per spill for the eighth radiation set. The spill fluence was increased to 100 ions per spill for the last Xenon radiation set.

Due to time constraints at the radiation test facility, we completed each of the eight radiation test rounds with 46.2 GeV Xenon ions and polyethylene degrader in two to five minute time durations. Each radiation round with Xenon ions and polyethylene degrader had a spill fluence of 200 ions per spill and a total fluence ranging from 4602 to 16391 ions/cm^2. A hard reset was performed after each radiation round, with exception of round #3 with 15 mm polyethylene degrader, to establish separation between data sets of each radiation round. Radiation round #6 with 18 mm polyethylene degrader and radiation round #9 with 21 mm degrader did not require a hard reset since no GUI error message continuously appeared or no anomalous behavior persisted after the end of the radiation round.

Table 19. Summary of heavy ion radiation test rounds including spill fluence, irradiation time, total fluence, number of SEEs observed, and indication of reset after radiation round.

Round	Ion	Polyethylene Degrader	Spill Fluence [ions/spill]	Time [sec]	Fluence [ions/cm^2]	Total SEEs Observed	Reset Post Radiation?
1	3.6 GeV Carbon	-	19-1062	2534	9.7×10^6	0	Soft
2.1	46.2 GeV Xenon	-	406-497	169	15712	4	-
2.2			243-515	216	20003	10	-
2.3			51-521	540	49998	23	-
2.4			409-517	274	22584	9	Soft
2.5			431-518	61	5667	3	Soft
2.6			399-569	328	27250	11	Soft

2.7			422-560	190	16500	9	Soft 2×, Hard
2.8			2-55	1185	8948	2	-
2.9			67-159	1145	30009	20	Hard
3		15 mm	115-285	118	4602	7	-
4		16 mm	15-309	118	6635	8	Hard
5		17 mm	243-295	151	8657	9	Soft, Hard
6		18 mm	239-301	119	6841	4	Hard
7.1		19 mm	241-287	119	6684	4	Hard
7.2		19 mm	151-280	79	4297	5	Hard
8		20 mm	234-287	126	6834	7	Hard
9.1		21 mm	178-287	118	6472	2	Hard
9.2		21 mm	222-290	298	16067	9	Hard
10		22 mm	233-300	299	16391	1	-

We observed a total of 145 non-destructive heavy ion SEEs over ten sets of radiation rounds. No destructive SEEs were observed. After analyzing the collected data, we categorized the observed SEEs into two main categories: single event upsets (SEUs) and single event functional interrupts (SEFIs). We further categorized similar SEUs and SEFIs into three sub-categories of three types of SEUs and three types of SEFIs. Out of the 145 SEEs observed, 137 were SEUs and 8 were SEFIs. There was a total of 91 SEEs on the DUT receiver side, and a total of 54 SEEs on the DUT transmitter side.

3.4.2.1 Observed Heavy Ion Single Event Upsets

We define a heavy ion induced SEU as an anomalous event that did not require a soft or hard reset of the OMA to re-establish nominal functionality. After a period of less than 12 seconds, the anomalous behavior for heavy ion induced SEUs disappeared. There were three types of SEUs observed during radiation testing. Figure 24 is a data set from radiation round 2.4 with Xenon ions, showing a total of four SEUs during radiation, labeled according to SEU type.

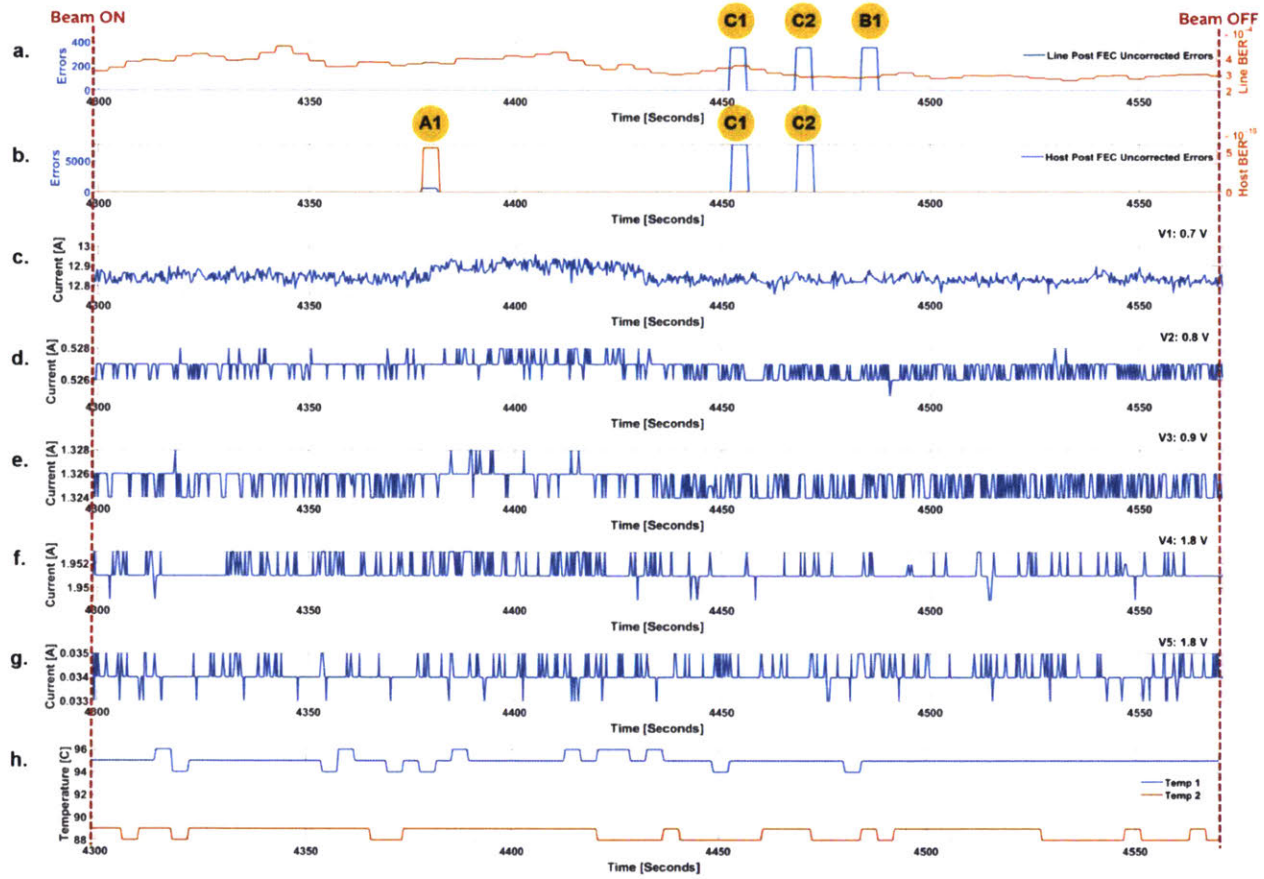

Figure 24. Data set from radiation round 2.4 with Xenon ions, showing a total of four SEUs during radiation with labels of each SEU type.

SEU type A occurred when the host post-FEC uncorrected error count was greater than zero. After a time-period of less than 8 seconds, the ASIC host FEC was able to correct all host-side errors and establish a host post-FEC uncorrected error count of zero. We observed a total of 43 occurrences of SEU type A. We observed a host post-FEC uncorrected error count ranging from 7 to 1.98×10^4, and the host post-FEC uncorrected error count remained constant during each SEU. The typical duration of this SEU was 3.6 seconds (exactly 15 timestamps from recorded data file) for 39 of the 42 total occurrences. There were 3 occurrences with a time duration of ~7.5 seconds (exactly 30 timestamps from recorded data file). We generally observed that the host post-FEC uncorrected error count during the SEU would increase with increasing LET level. Figure 24 shows one SEU type A with 3.6 second duration observed during radiation round 2.4 with Xenon ions, labeled A1. There were some occurrences with "stepped increase" of voltage rails V3 and V4 in the range of tens of milliamps, but this current increase is not out of nominal range for the voltage rails.

SEU type B occurred when the line post-FEC uncorrected error count was greater than zero. We observed a line post-FEC uncorrected error count ranging from 16 to 1.49×10^3, and the line post-FEC uncorrected error count remained constant during each SEU. After a time-period of ~3.6 seconds (exactly 15 timestamps from recorded data file), the ASIC line FEC was able to correct all line-side errors and establish line post-FEC uncorrected error count of zero. We observed a total of 26 occurrences of SEU type B. We only observed type B SEUs

for radiation round 2 with Xenon ions. Figure 24(a) shows one SEU type B with 3.6 second duration observed during radiation round 2.4 with Xenon ions, labeled B1.

SEU type C occurred when the line post-FEC uncorrected error count was greater than zero, and in the following time stamp the host post-FEC uncorrected error count was greater than zero. After a time-period of ~3.6 seconds, the line post-FEC uncorrected error returned to zero, and in the following time stamp the host post-FEC uncorrected error count returned to zero. Table 20 shows the data log from radiation round 2.4 with Xenon ions as an example of SEU type C. The line post-FEC uncorrected error count ranged from 350 to 552 and the host post-FEC uncorrected error count ranged from 80 to 2.95×10^4. Figure 24 show two SEU type Cs with 3.6 second duration observed during radiation round 2.4 with Xenon ions, labeled C1 and C2. We observed a total of 13 occurrences of SEU type C. There were two variations we observed of SEU type C. There was one occurrence in which the host post-FEC uncorrected error count did not return to zero in the following time stamp from the line post-FEC uncorrected error count. In this occurrence, the host post-FEC uncorrected error count did not return to zero until ~ 3.6 seconds later (15 timestamps). There were two occurrences in which the host post-FEC uncorrected error count was greater than zero for a ~3.6 second time period (similar to SEU type A), followed by the line post-FEC uncorrected error count changing to a value greater than zero. In the following timestamp, the host post-FEC uncorrected error count was greater than zero. Both the line and host post-FEC uncorrected error counts returned to zero after ~3.6 seconds and in subsequent time stamps.

Table 20. Data log from radiation round 2.4 with Xenon ions, showing SEU type C.

Time Stamp	Line Post-FEC Errors	Line Pre-FEC BER	Host Post-FEC Errors	Host Pre-FEC BER	Temp [C]	Current [Amps]				
						V1 0.7V	V2 0.8V	V3 0.9V	V4 0.7V	V5 1.8V
4451.580	0.00E+00	3.40E-04	0.00E+00	0.00E+00	95	12.806	0.526	1.326	1.951	0.034
4451.986	**3.60E+02**	2.98E-04	0.00E+00	0.00E+00	95	12.869	0.526	1.324	1.951	0.034
4452.361	3.60E+02	2.98E-04	**7.70E+03**	0.00E+00	95	12.869	0.527	1.324	1.951	0.034
4452.768	3.60E+02	2.85E-04	7.70E+03	0.00E+00	95	12.831	0.526	1.326	1.951	0.034
4452.955	3.60E+02	2.85E-04	7.70E+03	0.00E+00	95	12.825	0.527	1.324	1.951	0.034
4453.127	3.60E+02	2.85E-04	7.70E+03	0.00E+00	95	12.85	0.526	1.326	1.953	0.034
4453.299	3.60E+02	2.85E-04	7.70E+03	0.00E+00	95	12.85	0.526	1.326	1.951	0.034
4453.471	3.60E+02	2.85E-04	7.70E+03	0.00E+00	95	12.85	0.527	1.326	1.951	0.034
4453.658	3.60E+02	2.85E-04	7.70E+03	0.00E+00	95	12.837	0.527	1.326	1.951	0.034
4453.83	3.60E+02	2.85E-04	7.70E+03	0.00E+00	95	12.844	0.527	1.326	1.951	0.034
4454.002	3.60E+02	2.85E-04	7.70E+03	0.00E+00	95	12.825	0.526	1.326	1.951	0.034
4454.19	3.60E+02	2.85E-04	7.70E+03	0.00E+00	95	12.825	0.527	1.326	1.953	0.034
4454.361	3.60E+02	2.85E-04	7.70E+03	0.00E+00	95	12.819	0.527	1.324	1.951	0.034
4454.768	3.60E+02	2.85E-04	7.70E+03	0.00E+00	95	12.825	0.527	1.324	1.951	0.034
4455.143	3.60E+02	2.85E-04	7.70E+03	0.00E+00	95	12.863	0.526	1.324	1.951	0.034
4455.533	**3.60E+02**	2.85E-04	7.70E+03	0.00E+00	95	12.812	0.527	1.324	1.951	0.035
4455.924	0.00E+00	2.85E-04	**7.70E+03**	0.00E+00	95	12.837	0.526	1.324	1.951	0.035
4456.315	0.00E+00	2.85E-04	0.00E+00	0.00E+00	95	12.831	0.526	1.326	1.951	0.034

A total of 83 SEUs occurred on the DUT receiver side and a total of 54 SEUs occurred on the DUT transmitter side. For the DUT receiver side, the highest number of SEUs were Type A (host post-FEC uncorrected errors) and for the DUT transmitter side, the highest number of SEUs were Type B (line post-FEC uncorrected errors). Table 21 summarizes the SEUs

observed on the DUT receiver and transmitter sides for each radiation round and categorizes the observed SEUs.

Table 21. Heavy ion radiation test campaign 1 single event upset count

Round	Ion	Polyethylene Degrader	Rx SEUs				Tx SEUs				Total SEUs
			A	B	C	Total	A	B	C	Total	
1	3.6 GeV Carbon	-	-	-	-	0	-	-	-	0	0
2.1	46.2 GeV Xenon	-	-	2	-	2	1	1	-	2	4
2.2			2	4	1	7	1	2	-	3	10
2.3			8	7	1	16	-	7	-	7	23
2.4			1	1	2	4	-	2	3	5	9
2.5			-	-	-	0	-	1	1	2	2
2.6			-	4	2	6	-	3	1	4	10
2.7			2	3	1	6	-	2	-	2	8
2.8			1	-	-	1	-	-	-	0	1
2.9			4	5	2	11	1	7	1	9	20
3		15 mm	4	-	1	5	1	1	-	2	7
4		16 mm	3	-	1	5	-	1	1	2	7
5		17 mm	6	-	-	6	2	-	-	2	8
6		18 mm	4	-	-	4	-	-	-	0	4
7.1		19 mm	-	-	-	0	2	-	-	2	2
7.2		19 mm	-	-	1	1	2	-	-	2	3
8		20 mm	4	-	1	5	1	-	1	2	7
9.1		21 mm	-	-	-	0	1	1	-	2	2
9.2		21 mm	4	-	-	4	4	1	-	5	9
10		22 mm	-	-	-	0	-	1	-	1	1
Radiation Rounds Total			43	26	13	83	16	30	8	54	137

SEUs observed during radiation testing typically occurred over a ~3.6 second period. The coherent DSP ASIC line side and host side performance were impacted during SEUs, but the line side and host side functionality were restored to nominal after SEU occurrences. SEUs of the coherent DSP ASIC will impact optical coherent modem system availability, and downtime due to SEUs of the ASIC will be accounted in system SEE rate and system availability.

3.4.2.2 Observed Heavy Ion Single Event Functional Interrupts

We define a single event functional interrupt (SEFI) as an anomalous event that required a soft reset or hard reset of the OMA to re-establish nominal functionality. The anomalous behavior and GUI error messages did not disappear or self-correct after a period of more than 12 seconds.

SEFI type A occurred when both the line and host pre-FEC BER changed to values of "-1," indicating an erroneous state of the DUT. GUI error messages of the ASIC line side indicated continuous loss of lock during the SEFI, even after the radiation round was completed and the DUT was no longer exposed to heavy ions. Two occurrences of SEFI type A were observed, once in radiation round 2.5 and once in radiation round 2.6 with Xenon ions. In radiation round 2.5, the line side and host side post-FEC uncorrected error counts were zero prior to the SEFI occurring, and the line-side pre-FEC BER was 2.67×10^{-4}. The line and host

pre-FEC BER changed to "-1" at the same timestamp. We completed a soft reset prior to radiation round 2.6, restoring nominal line and host side pre-FEC BERs and the error message no longer appeared. Figure 25 shows the data graph from radiation round 2.5 with the SEFI indicated with label "A". Near the end of radiation round 2.6, we observed the second occurrence of SEFI type A. The line side pre-FEC BER was 2.38×10^{-4} prior to the SEFI, and a SEU type C had resolved one time stamp before the SEFI occurrence. The line side pre-FEC BER changed to the "-1" error state four seconds prior to the host side pre-FEC BER changed to "-1" error state. The error message and BER state of "-1" continued even after the heavy ion beam was off. We observed the SEFI for two minutes after the beam was off, then performed a soft reset. The soft reset restored nominal functionality.

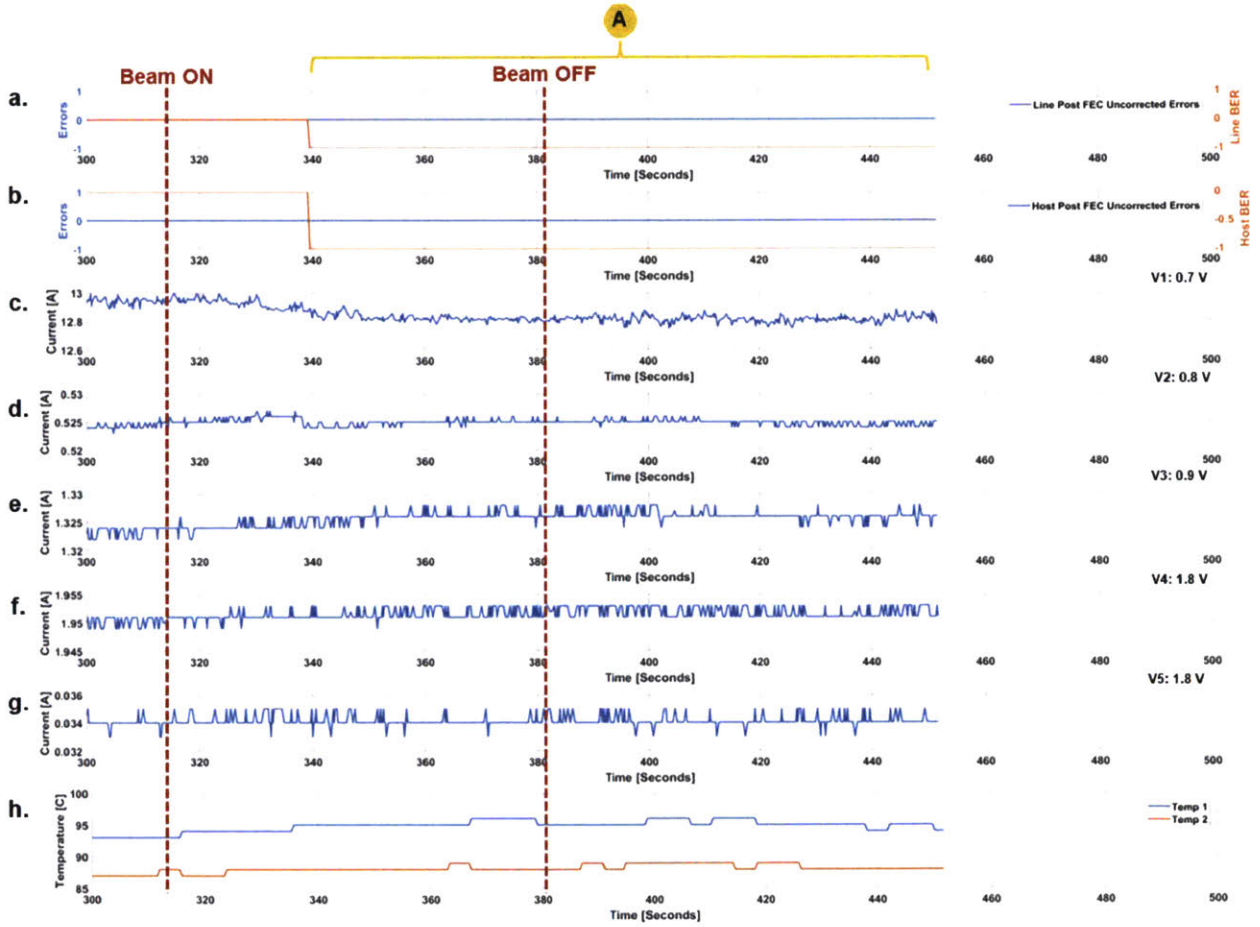

Figure 25. Data graphs from radiation round 2.5 with Xenon ions. SEFI type A with line side and host side pre-FEC BER in error state of "-1" and error state continued even after heavy ion beam was off.

SEFI type B occurred when the host side post-FEC error count was greater than zero for a time period of over 12 seconds and an error message for the host post FEC errors appeared continuously on the GUI. The host side post-FEC non-zero error count and error message continued even after the heavy ion beam was off and hard reset was required to establish nominal functionality. We observed three occurrences of SEFI type B. We observed a SEFI type B in radiation round 2.7 with xenon ions. The host side post-FEC error count was 4.09×10^{7} when the SEFI began. Prior to the SEFI (3.4 seconds), we observed a stepped

decrease in current of the analog voltage rails V3 (~ 20 mA) and V4 (~110 mA), but the change in current is not significant. Voltage rail V3 decreased by 20 mA and V4 decreased by ~100 mA. We performed two soft resets of the OMA, both of which were not successful in restoring nominal functionality, and the host side post-FEC error message continued to appear on the GUI after each soft reset. A hard reset successfully re-established nominal functionality.

The second observation of SEFI type B occurred during radiation round 5 with Xenon ions and 17 mm of polyethylene degrader. The third SEFI type B occurred during radiation round 7.2 with Xenon ions and 19 mm of polyethylene degrader. The host side post-FEC error count was 9280 during the SEFI, and we observed a slight stepped current increase in the analog power supply voltage rails. Voltage rail V3 increased by 12 mA and V4 increased by 50 mA. The increased current levels are within nominal range of the voltage rails. Figure 26 shows the data graphs from radiation round 7.2 with Xenon ions and 19 mm of polyethylene degrader. SEFI type B and the stepped current increase in voltage rails V3 and V4 are labeled.

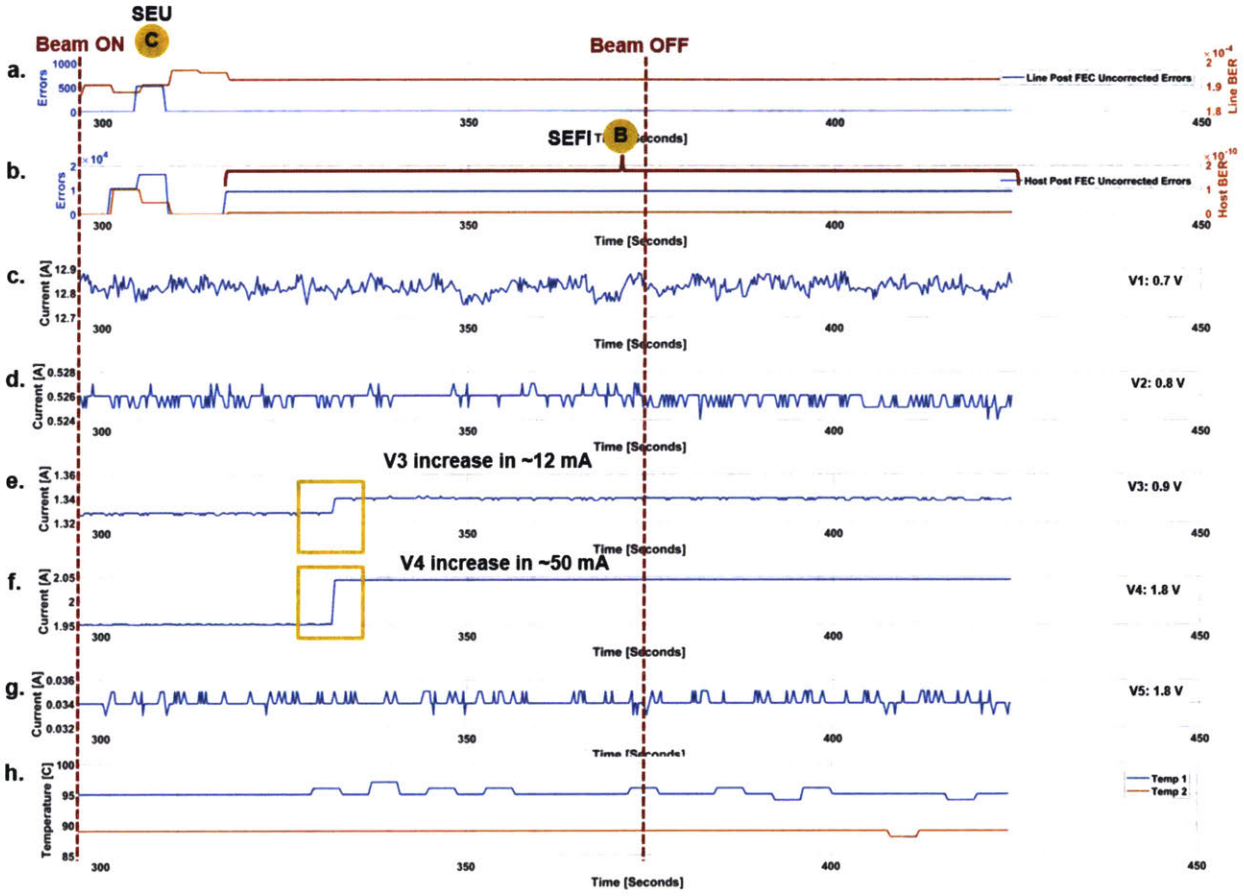

Figure 26. Data graphs from radiation round 7.2 with Xenon ions and 19 mm of polyethylene degrader. SEFI type B, SEU type C, and the stepped current increase in voltage rails V3 and V4 are labeled.

SEFI type C occurred when a GUI error message associated with the SPI data polling appeared and data recording was stopped. We observed the error message would repeat on the GUI and no data was logged in the telemetry file. After a 70 second period, there was nominal functionality and data was logged. The error behavior repeated later during the

radiation round, even when the heavy ion beam was off. A hard reset was required to establish nominal functionality and prevent the error from re-appearing in a subsequent radiation round. The first occurrence of SEFI type C was in radiation rounds 2.8 and 2.9 with Xenon ions. The first set of error messages appeared after the beam was off in radiation round 2.8. We did not perform any reset after radiation round 2.8 since the error message disappeared and nominal functionality was established after ~70.3 seconds. During radiation round 2.9, the type C anomalous behavior (missing data logging over ~70.3 second periods) repeated three times during irradiation and two times after the beam was off. We performed a hard reset after radiation round 2.9 and did not observe SEFI type C in radiation round 3.

The second occurrence of SEFI type C was in radiation round 4 with Xenon ions and 16 mm of polyethylene degrader. The first error messages and missing data logging over ~26.3 second period occurred ~4.8 seconds after the beginning of the radiation round. There were three instances after the beam was off with similar anomalous behavior with missing data logging over ~26.3, ~30.7, and ~25.6 second periods. A hard reset was performed after radiation round 4. Figure 27 shows the data graphs from radiation round 4 with Xenon ions and indicates the missing recorded data. The third occurrence of SEFI type C was in radiation round 7.1 with Xenon ions and 19 mm of polyethylene degrader. Immediately when the beam was turned on, we observed the SPI data polling error repeat on the GUI and no data was recorded in the telemetry file. A hard reset was performed, and we did not observe the SEFI type C behavior in radiation round 7.2.

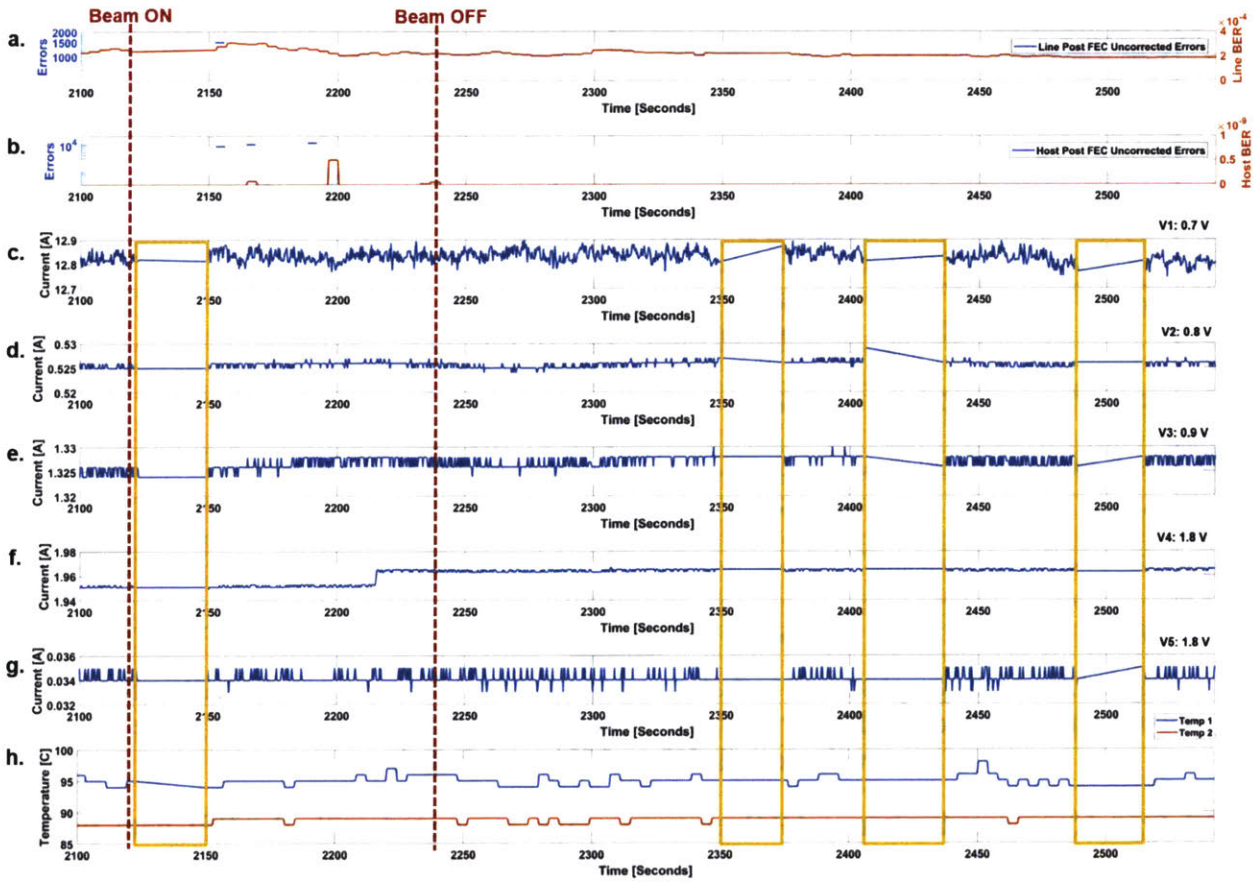

Figure 27. Data graphs from radiation round 4 with Xenon ions and 16 mm polyethylene degrader to show SEFI type C behavior with missing data logging.

A total of 8 SEFIs occurred. All SEFIs occurred on the DUT receiver side and were observed through DUT performance telemetry on the OMA. Table 22 summarizes the SEFIs observed on the DUT receiver side for each radiation round and categorizes the observed SEFIs. There were three types of SEFIs observed during radiation testing. The coherent DSP ASIC SEFIs, which impact the line side and host side performance and require reset or power cycle to restore nominal functionality, will cause downtime and reduced availability of the optical coherent modem. The coherent DSP ASIC SEFI rates and downtime until reset or power cycle need to be incorporated in the optical coherent modem system SEE rate and availability.

Table 22. Heavy ion radiation test campaign 1 single event functional interrupts on DUT receiver side

Round	Ion	Polyethylene Degrader	OMA – Rx SEFIs			
			A	B	C	Total
1	3.6 GeV Carbon	-	-	-	-	0
2.1	46.2 GeV Xenon	-	-	-	-	0
2.2			-	-	-	0
2.3			-	-	-	0
2.4			-	-	-	0
2.5			1	-	-	1
2.6			1	-	-	1
2.7			-	1	-	1
2.8			-	-	1	1
2.9			-	-	-	0
3		15 mm	-	-	-	0
4		16 mm	-	-	1	1
5		17 mm	-	1	-	1
6		18 mm	-	-	-	0
7.1		19 mm	-	-	1	1
7.2		19 mm	-	1	-	1
8		20 mm	-	-	-	0
9.1		21 mm	-	-	-	0
9.2		21 mm	-	-	-	0
10		22 mm	-	-	-	0
Radiation Rounds Total			2	3	3	8

3.4.2.3 Heavy Ion Radiation Test Campaign 1 Summary

In the first heavy ion radiation test campaign of the commercial optical coherent DSP ASIC with 16 nm FinFET plus CMOS technology, we observed a total of 145 non-destructive heavy ion SEEs over ten sets of radiation rounds. The SEEs were categorized into three types of heavy ion SEUs and three types of heavy ion SEFIs.

No destructive heavy-ion SEEs were observed up to an LET of ~65 MeV·cm^2/mg. The maximum achieved LET value from the first heavy ion radiation assessment was calculated from an approximated attenuation model of heavy ions penetrating through the back-side of the OMA prototype PCB and into the ASIC. The DUT was irradiated through the back-side of the PCB for the first heavy ion test campaign. In the original test setup plan an aluminum heat sink was mounted on top of the ASIC and we planned to irradiate from the back-side of the PCB, which would be the path of least attenuation for the heavy ions in comparison to the front side path through the heat sink. In the final test setup, the aluminum heat sink was

removed to stabilize the ASIC temperature at the maximum rated junction temperature, but the OMA had been mounted and aligned with the proton beam for back-side irradiation.

There are multiple paths of attenuation for heavy ions traveling through the back-side of the OMA into the active region of the ASIC. The PCB has 32 layers of alternating dielectric material, signal layers, and internal planes of copper. The signal layers and internal planes are not uniform and contain copper vias distributed throughout the layer. X-ray images of copper coupons of various thicknesses were compared to an X-ray image section of the ASIC on the OMA prototype board to develop an approximated attenuation model of the path into the ASIC active region. Stopping Range in Matter (SRIM) radiation simulation program was used to model the different attenuation paths and determine the range of achieved LET values into the ASIC active region (Figure 28). Table 23 summarizes the minimum and maximum LET values achieved for each radiation round. The details of the approximated attenuation model and the analysis for the achieved LET ranges are in Appendix A1.

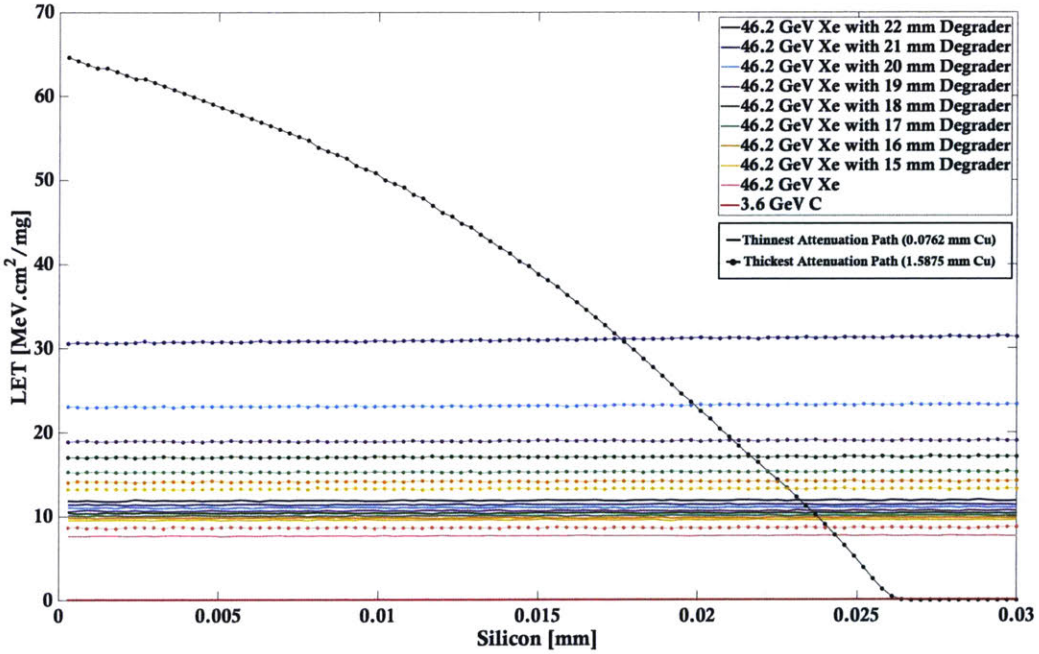

Figure 28. SRIM simulations of ions entering the silicon ASIC active region for all radiation rounds. Only the thinnest and thickest attenuation paths for ions are modeled to evaluate the minimum and maximum achieved LET values into the ASIC active region.

Table 23. Summary of minimum and maximum achieved LET in silicon ASIC active region for each radiation round. The asterisk "*" indicates the overall maximum LET of heavy ions achieved from radiation testing.

Radiation Round	Ion	Initial Energy [GeV]	Polyethylene Degrader Thickness [mm]	Minimum LET in Si (0.0762 mm Cu) [MeV·cm²/mg]	Maximum LET in Si (1.5875 mm Cu) [MeV·cm²/mg]
1	C	3.6	-	0.1	0.1
2	Xe	46.2	-	7.7	30.6
3	Xe	46.2	15.0	9.6	13.3
4	Xe	46.2	16.0	9.9	14.1

5	Xe	46.2	17.0	10.1	15.3
6	Xe	46.2	18.0	10.5	17.1
7	Xe	46.2	19.0	10.6	18.9
8	Xe	46.2	20.0	11.1	23.1
9	Xe	46.2	21.0	11.4	30.6
10	Xe	46.2	22.0	11.9	64.6*

3.4.3 Heavy Ion Radiation Test Campaign 2

A second heavy ion radiation test campaign at NSRL was conducted to gather more SEE data at higher fluence levels for SEE cross section calculations and to determine heavy ion SEE rates of the commercial optical coherent DSP ASIC for various orbits. In the first test campaign, the radiation test rounds using Krypton ions with various thicknesses of polyethylene degrader were tested to fluence levels only up to 10^3 and 10^4 ions/cm^2. At these low fluence levels, it is not statistically significant to calculate the SEE cross sections. In the second test campaign, the first three sets of radiation rounds collected SEE data for fluence levels up to 10^6 ions/cm^2 for statistical significance of fluence for calculating SEE cross sections [Buchner et al., 2002]. Due to time limitations at the facility, data for radiation round 4 with Gold ions could only be collected up to a fluence level of 10^5 ions/cm^2.

In the second test campaign, we performed testing on the same DUT. The same GOMA and noise-loading equipment from the first test campaign were used. In this test campaign, the DUT was irradiated from the front side of the board allowing ions to penetrate through the top of the ASIC packaging. The second heavy ion test campaign consisted of four sets of radiation rounds with (1) 32.172 GeV Krypton ions, (2) 32.172 GeV Krypton ions with 37 mm polyethylene degrader, (3) 32.172 GeV Krypton ions with 43.6 mm polyethylene degrader, and (4) 32.505 GeV Gold ions. Table 24 provides details of the key test parameters for each of set of radiation rounds.

Table 24. Heavy Ion Test Campaign 2 Radiation Round Parameters

Round	Ion	Polyethylene Degrader	Spill Fluence [ions/spill]	Time [sec]	Fluence [ions/cm^2]	Total SEEs	Rx SEUs	Rx SEFIs	Rx (OMA) Reset	Tx SEUs	Tx SEFIs	Tx (GOMA) Reset
1.1	32.172 GeV Krypton	-	408-1312	609	156736	0	0	0	-	0	0	-
1.2			1513-3571	312	248485	0	0	0	-	0	0	-
1.3			3093-14971	78	179498	1	0	1	Soft	0	0	-
1.4			3585-9581	92	167225	1	0	1	Hard	0	0	-
1.5			1630-5356	181	197931	6	1	1	Soft	3	1	Soft
1.6			1779-4319	174	165744	1	0	1	Soft	0	0	-
1.7			764-2188	371	165449	3	1	1	Soft	0	1	Soft
1.8			942-10377	78	140717	1	0	1	Soft	0	0	-
1.9			6514-10485	23	71349	1	0	1	Hard	0	0	-
1.10			847-3364	565	340857	3	2	1	Soft	0	0	-
Total				-	1.83×10^6	17	4	8	-	3	2	-
2.1	32.172 GeV Krypton	37 mm	1109-3152	472	306445	9	6	2	Soft, Hard	1	0	-
2.2			2034-2838	34	25643	2	0	1	Soft	1	0	-
2.3			1276-3201	456	310046	8	0	1	Soft	7	0	-
2.4			1149-2957	258	168954	4	2	1	Soft, Hard	1	0	-
2.5			1036-4010	595	379032	10	7	1	Soft	2	0	-
Total				-	1.19×10^6	33	15	6	-	12	0	-
3.1	32.172 GeV Krypton	43.6 mm	898-2533	269	129766	28	18	1	Soft	9	0	-
3.2			987-2681	404	202963	36	16	1	Hard	19	0	-
3.3			1967-2638	41	30120	4	0	1	Soft	3	0	-
3.4			1124-2630	146	80348	17	8	1	Soft	8	0	-
3.5			827-2319	262	132408	26	15	1	Soft	10	0	-
3.6			1131-2247	64	34964	8	2	5	Soft	5	0	-
3.7			914-2321	167	83074	14	7	2	Soft, Hard	5	0	-
3.8			380-2748	343	178658	30	16	1	Soft	12	1	Soft
3.9			508-2656	391	206739	22	0	2	Soft, Hard	20	0	-
Total				-	1.08×10^6	185	82	15	-	87	1	-
4.1	32.505 GeV Gold	-		85	32840	9	0	3	Soft, Hard	5	1	Soft
4.2				133	10630	12	5	1	Soft, Hard	6	0	-
4.3				251	19666	25	16	1	Soft	8	0	-
4.4				574	44518	58	36	2	Soft, Hard	20	0	-
4.5				377	28854	32	19	1	Soft, Hard	11	1	
Total			-	-	1.37×10^5	136	76	8	-	50	2	-

A total of 371 SEEs (333 SEUs and 39 SEFIs) were observed over the four sets of radiation rounds. Table 25 summarizes the heavy ion radiation test campaign SEE results.

Table 25. Heavy Ion Test Campaign 2 Radiation Round Summary

Round	Ion	Polyethylene Degrader	Total Fluence [ions/cm^2]	Total SEEs	SEU	SEFI – Reset	SEFI – Power Cycle
1	32.172 GeV Krypton	-	1.83×10^6	17	7	8	2
2	32.172 GeV Krypton	37 mm	1.19×10^6	33	27	4	2
3	32.172 GeV Krypton	43.6 mm	1.08×10^6	185	173	10	2
4	32.505 GeV Gold	-	1.37×10^5	137	126	7	4

3.4.3.1 Observed Heavy Ion Single Event Upsets

The same three types of SEUs from the first heavy ion test campaign were observed in the second test campaign. Similar to the first test campaign, the highest number of SEUs on the DUT receiver side were Type A (host side post-FEC uncorrected errors), and the highest number of SEUs on the DUT transmitter side were Type B (line side post-FEC uncorrected errors). Table 26 categorizes the observed SEUs for each radiation round by type of SEU. Note that SEUs were observed on both the transmit (egress) side and receive (ingress) side of the ASIC DUT on the OMA. The SEUs impacting the transmit (egress) side of the ASIC DUT on the OMA were observed by the receive (ingress) side of the GOMA ASIC.

Table 26. Heavy Ion Test Campaign 2 Single Event Upsets by Category

Round	Ion	Polyethylene Degrader	Rx SEUs (Observed via OMA ASIC DUT)				Tx SEUs (Observed via GOMA ASIC)				Total SEUs
			A	B	C	Total	A	B	C	Total	
1.1	32.172 GeV Krypton	-	-	-	-	0	-	-	-	0	0
1.2			-	-	-	0	-	-	-	0	0
1.3			-	-	-	0	-	-	-	0	0
1.4			-	-	-	0	-	-	-	0	0
1.5			1	-	-	1	2	-	1	3	4
1.6			-	-	-	0	-	-	-	0	0
1.7			1	-	-	1	-	-	-	0	1
1.8			-	-	-	0	-	-	-	0	0
1.9			-	-	-	0	-	-	-	0	0
1.10			2	-	-	2	-	-	-	0	2
Total			4	0	0	4	2	0	1	3	**7**
2.1	32.172 GeV Krypton	37 mm	5	1	-	6	-	1	-	1	7
2.2			-	-	-	0	-	1	-	1	1
2.3			-	-	-	0	-	7	-	7	7
2.4			1	1	-	2	-	1	-	1	3
2.5			3	4	-	7	-	2	-	2	9
Total			9	6	0	15	0	12	0	12	**27**
3.1	32.172 GeV Krypton	43.6 mm	7	11	-	18	-	9	-	9	27
3.2			4	1	11	16	-	18	1	19	35
3.3			-	-	-	0	-	3	-	3	3
3.4			1	6	1	8	1	6	1	8	16
3.5			3	12	-	15	1	9	-	10	25
3.6			-	1	1	2	-	5	-	5	7

3.7			2	5	-	7	-	5	-	5	12
3.8			1	14	1	16	-	12	-	12	28
3.9			-	-	-	0	-	20	-	20	20
Total			18	50	14	82	2	87	2	91	**173**
4.1	32.505 GeV Gold	-	-	-	-	0	5	-	-	5	5
4.2			2	3	-	5	4	2	-	6	11
4.3			15	-	1	16	7	1	-	8	24
4.4			31	4	1	36	14	4	2	20	56
4.5			18	1	-	19	9	2	-	11	30
Total			66	8	2	76	39	9	2	50	**126**
Radiation Rounds Total			97	64	16	177	43	108	5	156	**333**

3.4.3.1 Observed Heavy Ion Single Event Functional Interrupts

Four new types of SEFIs were observed in addition to the three types of SEFIs observed in the first test campaign. The four new SEFIs are categorized as SEFI Type D, Type E, Type F, and Type G. SEFIs were observed in both the DUT receiver-side through the OMA performance data and the DUT transmitter-side through the GOMA performance data. Table 27 summarizes the seven types of SEFIs observed from both radiation test campaigns.

Table 27. Types of Heavy Ion Single Event Functional Interrupts on the DUT and Type of Reset Required to Restore Nominal Functionality

SEFI Type	Description	Reset
A	Line and host pre-FEC BER change to values of "-1,"	Soft
B	Host side post-FEC error count greater than zero for time period of over 12 seconds	Hard
C	SPI data polling GUI error message and loss in telemetry recording	Soft
D	GUI communication lost	Hard
E	Line side post-FEC error count greater than zero for time period of over 12 seconds	Soft
F	Line post-FEC uncorrected error count greater than zero, and in the following time stamp the host post-FEC uncorrected error count was greater than zero. Both error counts greater than zero for time-period of over 12 seconds	Soft
G	Anomalous temperature telemetry values	-
	1. Drop in temperature telemetry values to 0°C	Soft
	2. Shift in temperature telemetry values to 65517 °C	Hard
	3. Oscillating temperature telemetry values	Soft

In the second heavy ion test campaign, there were three occurrences of SEFI type A: one occurrence in radiation round 2.3 with Krypton ions and 37 mm polyethylene degrader, one occurrence in radiation round 3.9 with Krypton ions and 43.6 mm polyethylene degrader, and one occurrence in radiation round 4.4 with Gold ions. All SEFI type A occurrences were on the ASIC receiver-side, observed on the OMA DUT telemetry. When a SEFI type A occurred in the first test campaign, both the line and host pre-FEC BER changed to values of "-1" at the same time stamp or the host pre-FEC BER changed ~ 4 seconds after the line pre-FEC BER. Soft resets of the OMA were successful in establishing nominal functionality. In radiation round 2.3, both the line and host pre-FEC BER shifted to "-1" at the same time stamp. There were no line or host post-FEC uncorrected errors prior to the pre-FEC BER shift to "-1".

The type A SEFIs observed in radiation rounds 3.9 and 4.4 slightly deviated from the criteria in the first heavy ion test campaign. In radiation round 3.9, only the host pre-FEC BER shifted to value of "-1." There were no host post-FEC uncorrected errors prior to the BER shift to "-1". About seven seconds prior to the Host pre-FEC BER shift to "-1", we observed changes in current rails. There was a ~6.5 A drop in V1/VDD (0.7 V digital voltage power supply rail). Less significant changes in the rails included a ~36 mA increase in V2/VDDA (0.8 V digital voltage power supply), a ~14 mA increase in V3/VDDA (0.9 V analog power supply), and a ~ 100 mA drop in V4/VDDA18 (1.8 V analog voltage power supply rail). A soft reset was successful in establishing nominal host pre-FEC BER and current values. Figure 29 displays the telemetry from radiation round 3.9 and indicates the host pre-FEC BER shift to "-1" and the current changes in the voltage rails.

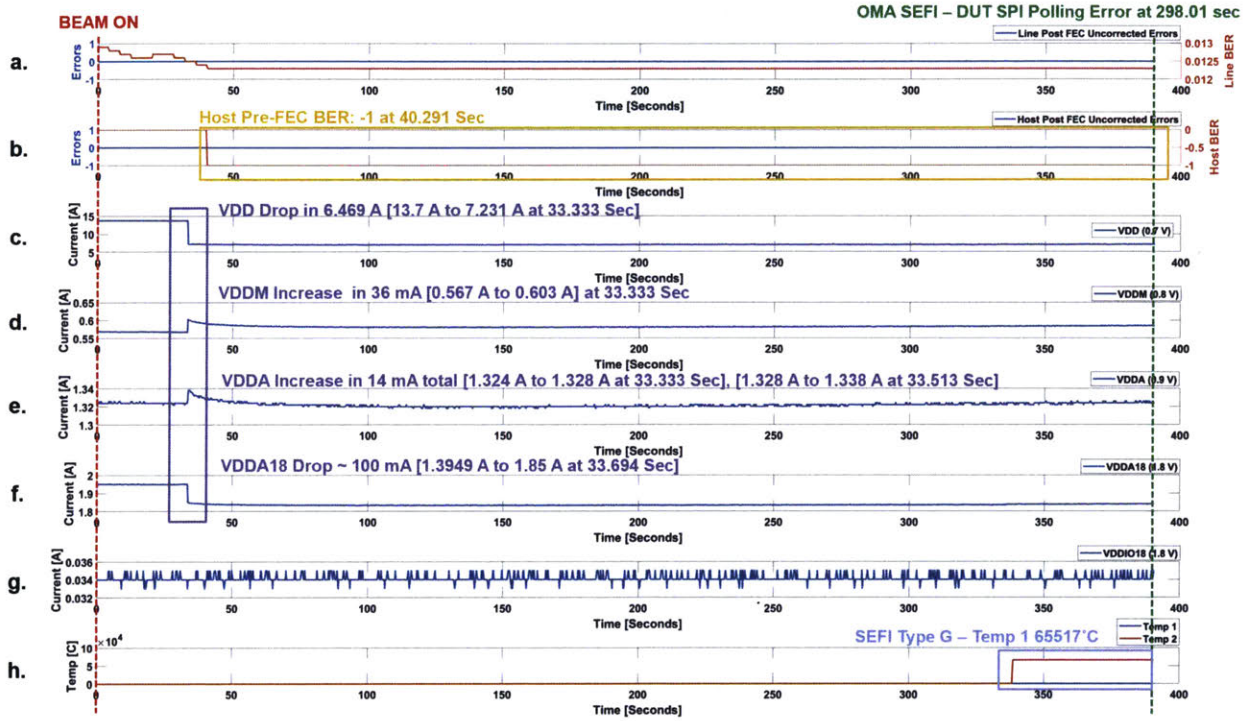

Figure 29. Heavy ion radiation test 2 SEFI type A example from radiation round 3.9 with Krypton Ions and 43.6 mm polyethylene degrader. Host pre-FEC BER shift to value of "-1" and current changes in voltage rails indicated.

In radiation round 4.4, we observed continuous oscillation of line and host Pre-FEC BER shifting from values of "0" to "-1", indicating error states. This version of SEFI type A started with the line pre-FEC BER shifting from a nominal pre-FEC BER of 1.25×10^{-2} to "-1" with 3.65×10^{5} line post-FEC uncorrected errors. After 15 timestamps (duration of ~3.6 seconds) the line post-FEC uncorrected errors changed to 0 and the line pre-FEC BER changed to "0". The host post-FEC uncorrected error count changed from 0 to 3.65×10^{5} and the host pre-FEC BER shifted from "0" to "-1". The line side and host side continued to repeat this behavior continuously, even after the heavy ion beam was off. There was a pattern in which the host side experienced the same post-FEC uncorrected error count as the line side post-FEC uncorrected error count after 15 timestamps. Note that the time duration of the pre-FEC BER state as "-1" was 15 timestamps (~ 3.6 seconds), the same time period as SEUs. There were 13 cycles of both the line pre-FEC BER and host pre-FEC BER shifting to error states of "-1)

for a time period of ~ 3.6 seconds. Table 28 shows a portion of the DUT telemetry when the SEFI type A started in radiation round 4.4. Figure 30 shows the plotted telemetry from radiation round 4.4 and indicates the SEFI type A behavior on the line and host side of the DUT.

Table 28. Heavy ion radiation test 2 SEFI type A example from radiation round 4.4 with Gold ions. Telemetry section with areas highlighted to show SEFI type A behavior on line and host post-FEC uncorrected errors and pre-FEC BER.

Line		Host		VDD Current [A]	VDDM Current [A]	VDDA Current [A]	VDDA18 Current [A]	VDDIO18 Current [A]	Temp 1 [°C]	Temp 2 [°C]	Timestamp
Post-FEC Uncorrected Errors	Pre-FEC BER	Post-FEC Uncorrected Errors	Pre-FEC BER								
3.65E+05	1.25E-02	0.00E+00	0.00E+00	14.087	0.594	1.422	2.746	0.034	0	0	500.554
3.65E+05	-1.00E+00	0.00E+00	0.00E+00	14.119	0.595	1.422	2.746	0.034	52	4	**500.946**
3.65E+05	-1.00E+00	0.00E+00	0.00E+00	14.044	0.594	1.42	2.746	0.034	52	4	501.131
3.65E+05	-1.00E+00	0.00E+00	0.00E+00	14.05	0.594	1.422	2.746	0.034	52	4	501.314
3.65E+05	-1.00E+00	0.00E+00	0.00E+00	14.038	0.595	1.422	2.746	0.034	52	4	501.496
3.65E+05	-1.00E+00	0.00E+00	0.00E+00	14.038	0.594	1.422	2.746	0.034	52	4	501.679
3.65E+05	-1.00E+00	0.00E+00	0.00E+00	13.988	0.593	1.422	2.746	0.034	52	4	501.86
3.65E+05	-1.00E+00	0.00E+00	0.00E+00	14.038	0.594	1.422	2.746	0.034	52	4	502.039
3.65E+05	-1.00E+00	0.00E+00	0.00E+00	14.069	0.594	1.422	2.746	0.034	52	4	502.222
3.65E+05	-1.00E+00	0.00E+00	0.00E+00	14.062	0.595	1.422	2.746	0.035	52	4	502.402
3.65E+05	-1.00E+00	0.00E+00	0.00E+00	14.056	0.594	1.422	2.746	0.033	52	4	502.584
3.65E+05	-1.00E+00	0.00E+00	0.00E+00	14.075	0.594	1.42	2.746	0.034	52	4	502.98
3.65E+05	-1.00E+00	0.00E+00	0.00E+00	14.019	0.594	1.422	2.746	0.034	52	4	503.379
3.65E+05	-1.00E+00	0.00E+00	0.00E+00	14.05	0.594	1.422	2.746	0.034	52	4	503.771
0.00E+00	-1.00E+00	0.00E+00	0.00E+00	14.081	0.595	1.424	2.746	0.034	52	4	504.172
0.00E+00	-1.00E+00	3.65E+05	0.00E+00	14.075	0.595	1.424	2.75	0.034	52	4	504.567
0.00E+00	0.00E+00	3.65E+05	-1.00E+00	14.081	0.59	1.424	2.746	0.034	0	0	504.97
0.00E+00	0.00E+00	3.65E+05	-1.00E+00	14.038	0.595	1.422	2.746	0.034	0	0	505.153
0.00E+00	0.00E+00	3.65E+05	-1.00E+00	14.075	0.594	1.422	2.746	0.034	0	0	505.337
0.00E+00	0.00E+00	3.65E+05	-1.00E+00	14.081	0.594	1.422	2.746	0.034	0	0	505.519
0.00E+00	0.00E+00	3.65E+05	-1.00E+00	14.087	0.595	1.422	2.746	0.034	0	0	505.702
0.00E+00	0.00E+00	3.65E+05	-1.00E+00	14.106	0.595	1.422	2.746	0.034	0	0	505.883
0.00E+00	0.00E+00	3.65E+05	-1.00E+00	14.15	0.594	1.424	2.746	0.034	0	0	506.067
0.00E+00	0.00E+00	3.65E+05	-1.00E+00	14.081	0.594	1.424	2.746	0.034	0	0	506.246
0.00E+00	0.00E+00	3.65E+05	-1.00E+00	14.025	0.594	1.424	2.746	0.034	0	0	506.427
0.00E+00	0.00E+00	3.65E+05	-1.00E+00	14.031	0.592	1.422	2.746	0.035	0	0	506.61

0.00E+00	0.00E+00	3.65E+05	-1.00E+00	14.025	0.592	1.422	2.746	0.034	0	0	506.999
0.00E+00	0.00E+00	3.65E+05	-1.00E+00	14.019	0.592	1.424	2.746	0.034	0	0	507.396
0.00E+00	0.00E+00	3.65E+05	-1.00E+00	14.056	0.592	1.422	2.746	0.034	0	0	507.787
3.65E+05	0.00E+00	3.65E+05	-1.00E+00	14.031	0.593	1.424	2.746	0.034	0	0	508.185
3.65E+05	0.00E+00	0.00E+00	-1.00E+00	14.05	0.592	1.422	2.746	0.034	0	0	508.576

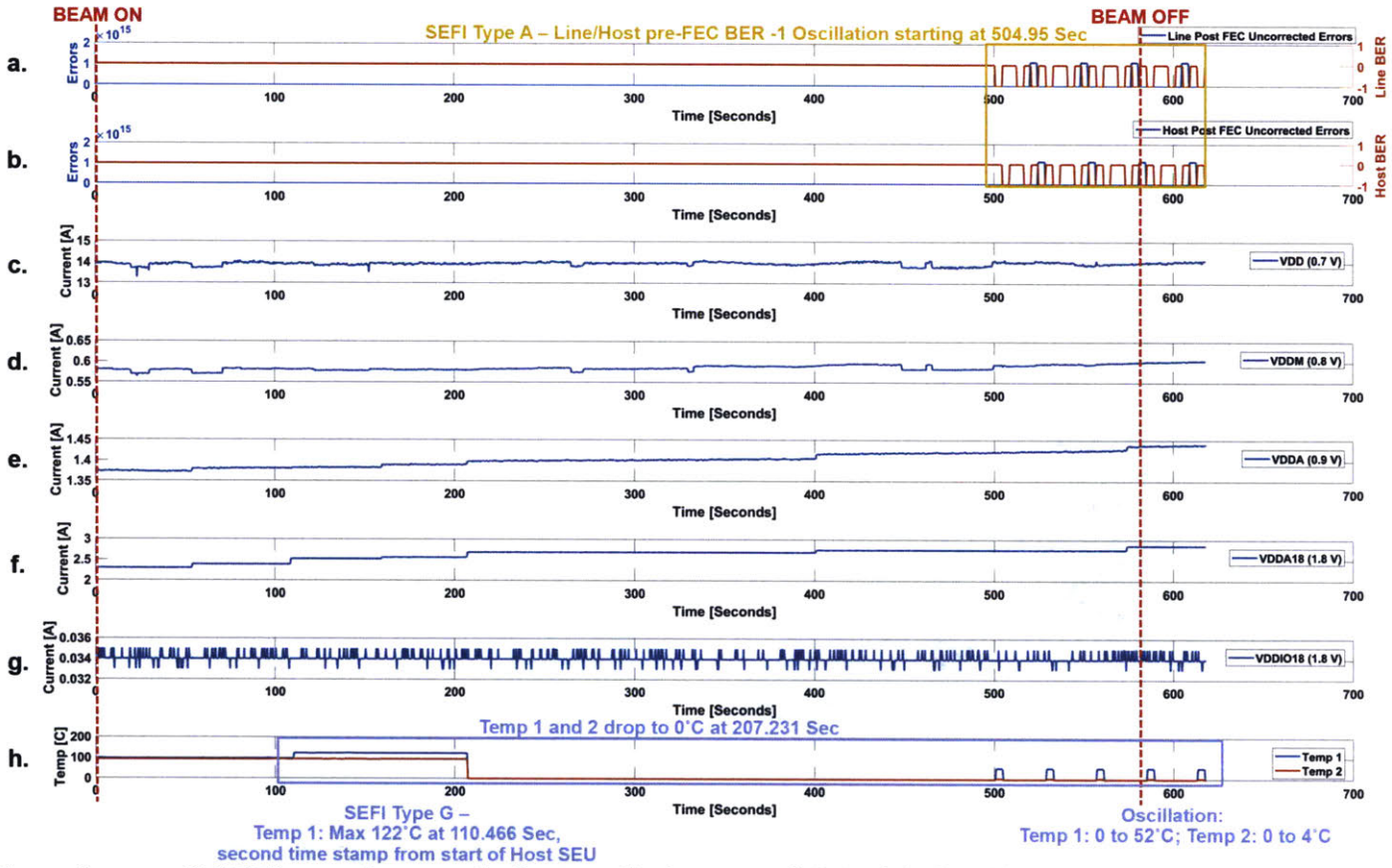

Figure 30. Heavy ion test 2 SEFI type A example from radiation round 4.4 with Gold ions. Plotted telemetry from OMA ASIC (DUT). Oscillating line and host post-FEC uncorrected errors and pre-FEC BER highlighted.

There were four occurrences of SEFI type B, all of which occurred on the DUT receiver side. Two occurrences were in the first set of radiation rounds with Krypton ions and two occurrences were in the third set of radiation rounds with Krypton ions and 43.6 mm polyethylene degrader. Similar to the first heavy ion test campaign, we observed that soft resets were not successful in establish nominal post-FEC uncorrected error count of 0. Hard resets are required for type B SEFIs.

In the first heavy ion test campaign, there were SEFI type C occurrences in which a DUT SPI polling error message appeared on GUI and telemetry/data polling timed out for a time period of few tens of seconds. A hard reset was used to establish nominal functionality after SEFI type C occurred. There were only two SEFI type C occurrences in the first test campaign, which was a small sample size to observe the behavior and try different reset techniques. In the second heavy ion test campaign, there were 16 occurrences of SEFI type C, all of which occurred on the DUT receiver side. SEFI type C had the highest number of occurrences out of any SEFI observed in the second heavy ion test campaign. Performing a soft reset of the OMA was successful in establishing nominal functionality after DUT SPI polling error for every SEFI type C occurrence in the second test campaign.

SEFI type D occurred when the connection to the DUT GUI program was lost. An ethernet connection is used for connecting the OMA to the test computer with GUI program. When SEFI type D occurred, there was a loss in communication to the ASIC and the GUI displayed a "loss in connection" error message. SEFI type D did not affect the GOMA. SEFI type D required a hard reset of the OMA. There were three occurrences of SEFI type D, all of which occurred on the DUT receiver side. Two type D SEFIs occurred in the first set of radiation rounds with Krypton ions and one type D SEFI occurred in the third set of radiation rounds with Krypton ions and 43.6 mm polyethylene degrader.

SEFI type E occurred when the line side post-FEC error count was greater than zero for a time period of over 12 seconds. The behavior persisted even after the heavy ion beam was off. A soft reset established nominal line side post-FEC error count of zero. There were three occurrences of SEFI type E, all of which occurred on the DUT transmitter side. Two type E SEFIs occurred in the first set of radiation rounds with Krypton ions (radiation rounds 1.5 and 1.7), shown respectively in Figure 31 and Figure 32. The third type E SEFI occurred in the radiation round 4.1 with Gold ions. For all three occurrences, the DUT experienced a type C SEFI (SPI bus polling error timeout) prior to the type E behavior appearing through the GOMA telemetry. We do not believe type C SEFIs on the DUT induce the type E SEFI since there are 13 occurrences of type C SEFIs without type E SEFI behavior observed on the GOMA ASIC telemetry.

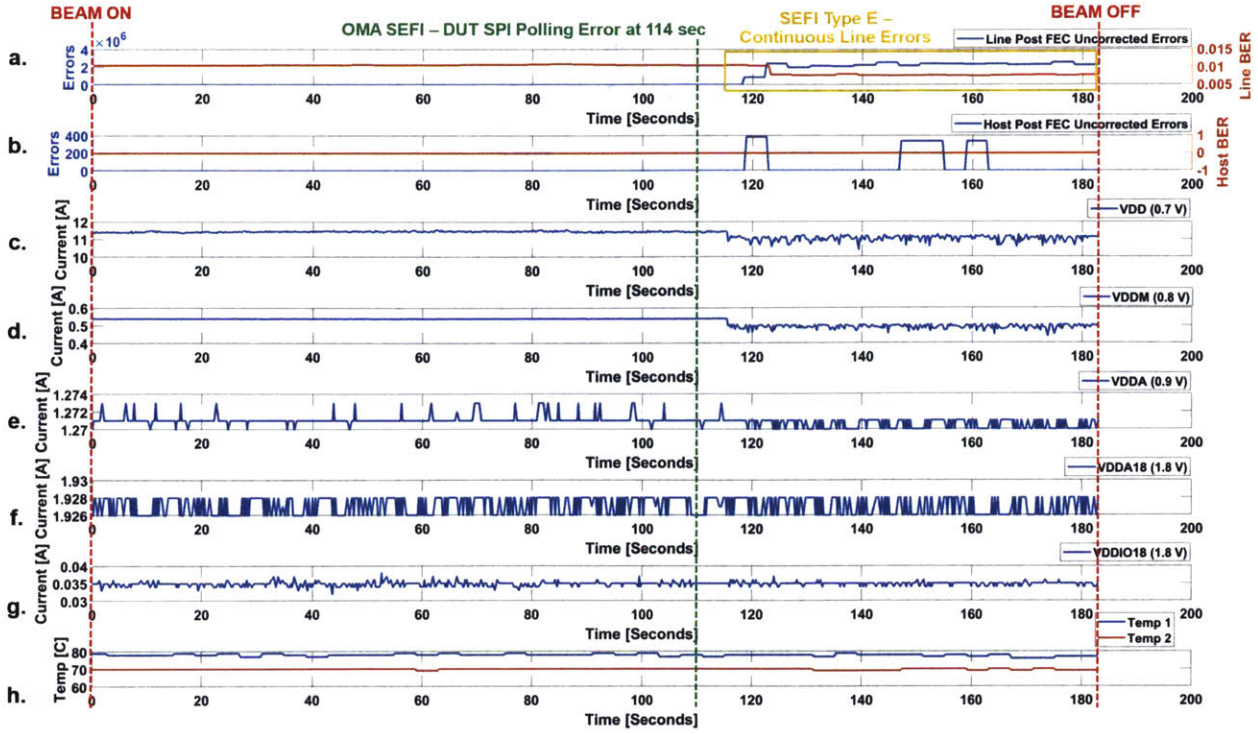

Figure 31. Heavy ion test 2 SEFI type E example from radiation round 1.5 with Krypton ions. Graphed telemetry from GOMA ASIC. SEFI Type E behavior of continuous line post-FEC errors highlighted.

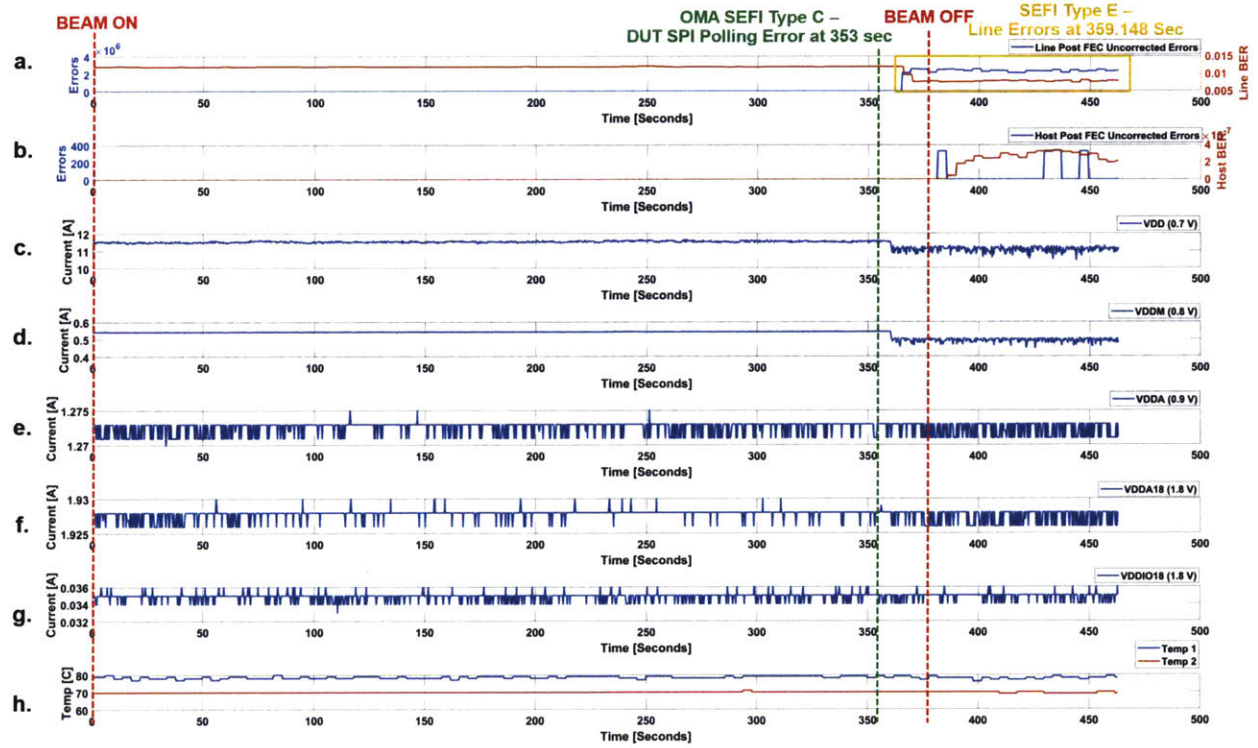

Figure 32. Heavy ion test 2 SEFI type E example from radiation round 1.7 with Krypton ions. Graphed telemetry from GOMA ASIC. SEFI Type E behavior of continuous line post-FEC errors highlighted.

Similar to SEU type C, SEFI type F occurred when the line post-FEC uncorrected error count shifted to a value greater than zero, and in the following time stamp the host post-FEC uncorrected error count shifted to a value greater than zero. Both line and host post-FEC error counts were greater than zero for time-period of over 12 seconds, while SEU type C behavior self-corrected after a period of ~3.6 seconds. The errors persisted even after the heavy ion beam was off. A soft reset was successful in establishing zero post-FEC errors on both the line and host side. There was a total of four Type F SEFI occurrences on both the DUT receiver and transmitter sides. Type F SEFIs occurred on the DUT receiver side in radiation round 3.7 with Krypton ions and 43.6 mm polyethylene degrader and in radiation round 4.5 with Gold ions. Type F SEFIs occurred on the transmitter side in radiation round 3.8 with Krypton ions and 43.6 mm polyethylene degrader and in radiation round 4.5 with Gold ions.

The first occurrence of SEFI type F behavior was in radiation round 3.7 on the DUT transmitter side. Even after the beam was off, continuous line and host post-FEC errors persisted, and the total time duration of the SEFI was 96.734 seconds until a soft reset was performed. The maximum number of host post-FEC errors was 1.17×10^{19} and the maximum number of line post-FEC errors was 1.12×10^{19}. Figure 33 shows the plotted telemetry from the DUT in radiation round 3.7 and highlights the SEFI type F behavior.

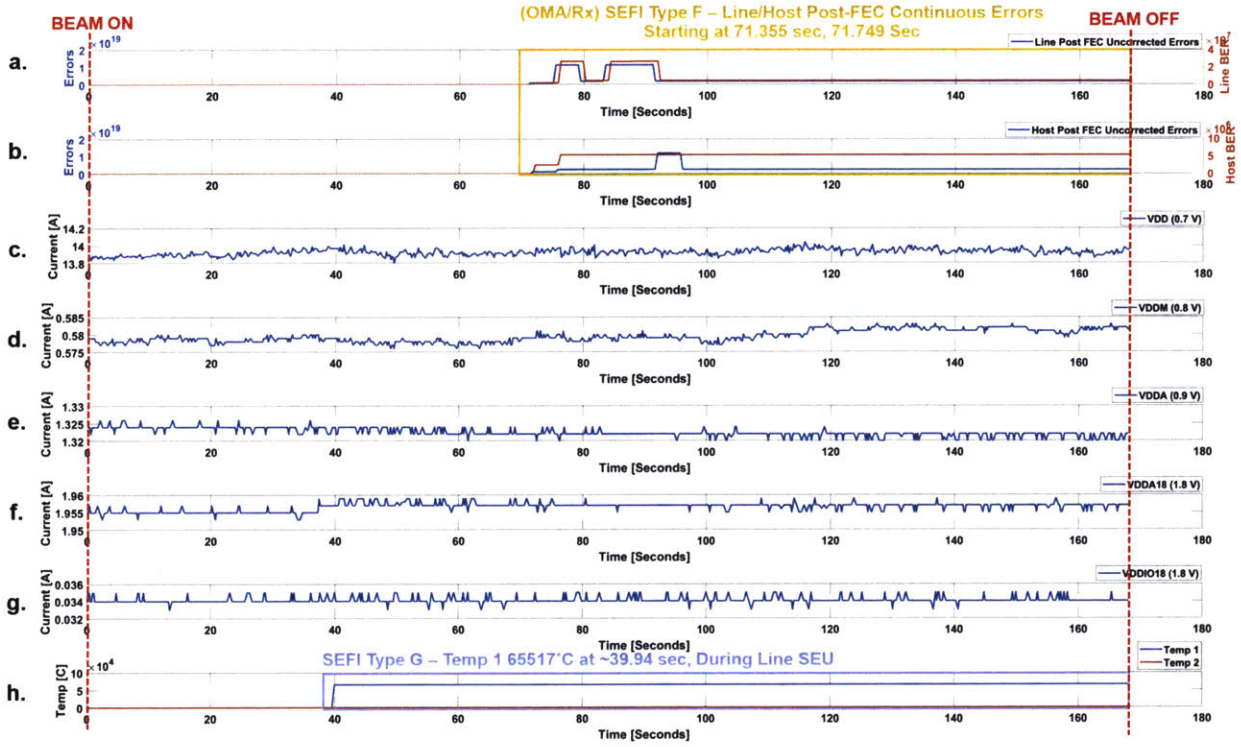

Figure 33. Heavy ion test 2 radiation round 3.7 with Krypton ions and 43.6 polyethylene degrader. Plotted telemetry from DUT / OMA ASIC. SEFI Type F behavior of continuous line and host post-FEC errors highlighted, and SEFI Type G behavior with anomalous temperature 1 value of 65517°C labeled.

SEFI type F behavior in radiation round 3.8 occurred on the DUT receiver side. The SEFI started ~ 3 seconds prior to the end of the heavy ion radiation round when the beam was powered off. Even after the beam was off, continuous line and host post-FEC errors persisted for a total duration of 33.6 seconds until a soft reset was performed. The maximum number of host post-FEC errors was 3.89×10^{7} and the maximum number of line post-FEC errors was 2.41×10^{4}. Four seconds prior to the SEFI occurring, there was ~ 1 A drop in voltage rail VDD and ~ 110 mA drop in voltage rail VDDM.

In radiation round 4.5, type F SEFIs occurred on both the DUT receiver and transmitter side. The behavior on the DUT receiver side deviated from the typical criteria of type F SEFIs from radiation round 3.7, radiation round 3.8, and radiation round 4.5 transmitter side. On the DUT receiver side (OMA telemetry), the line and host post-FEC error values had an oscillating pattern with variation in the order of magnitude from minimum value of 1.23×10^{13} errors to maximum value of 4.80×10^{18} errors. Figure 34 shows the plotted telemetry from the OMA, with the continuous oscillating pattern of line and host post-FEC errors. On the DUT transmitter side (GOMA telemetry), the line post-FEC error values ranged from 2.82×10^{5} to 2.31×10^{6} and the host post-FEC error values ranged from 6.80×10^{5} to 1.64×10^{6} during the type F SEFI. While the GOMA was running, we performed a soft reset on the OMA which was successful in restoring the GOMA telemetry line and host-post FEC errors to zero. The soft reset on the OMA was successful in restoring the OMA telemetry line post-FEC errors to zero, but continuous host post-FEC errors persisted. A hard reset of the OMA was required to restore the OMA host post-FEC errors to zero. Figure 35 shows the graphed telemetry from the GOMA, with continuous line and host post-FEC errors.

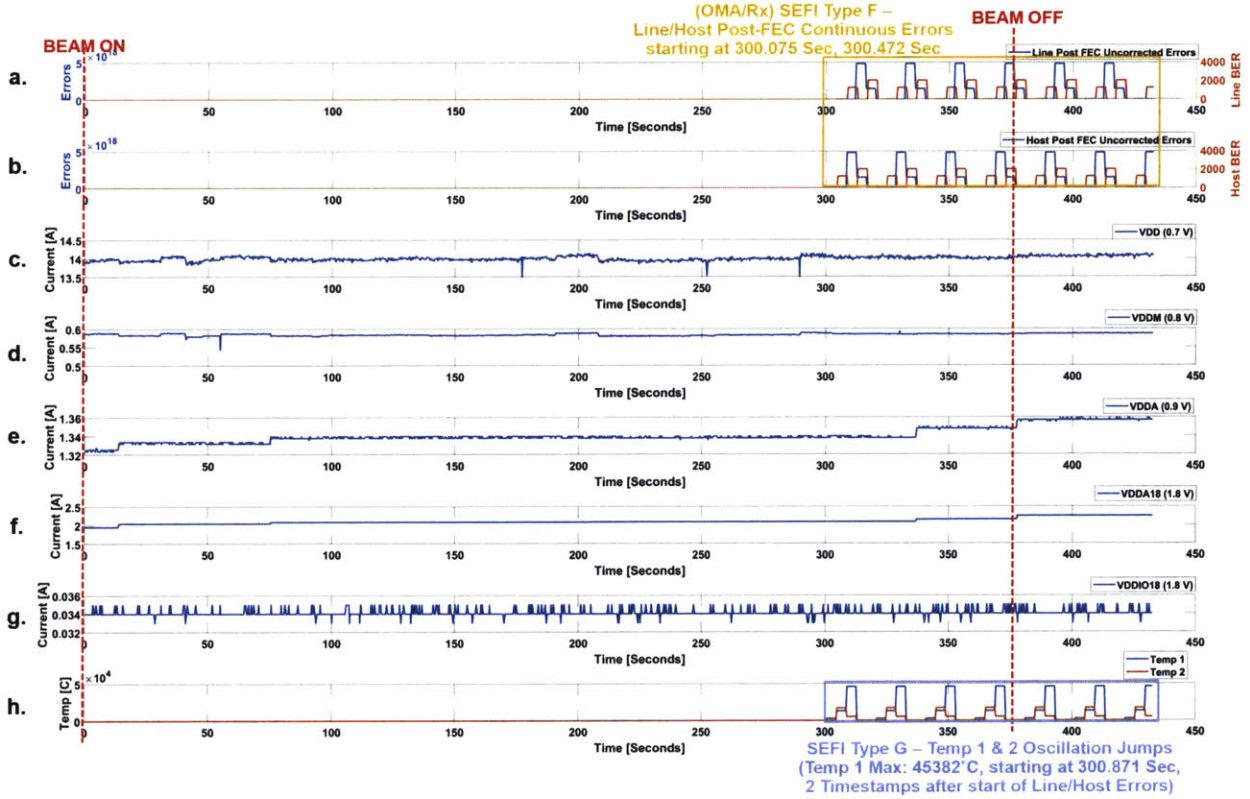

Figure 34. Heavy ion test 2 SEFI type F example from radiation round 4.5 with Gold ions. Plotted telemetry from DUT / OMA ASIC. SEFI Type F behavior of continuous line and host post-FEC errors highlighted and SEFI Type G behavior of anomalous temperature values.

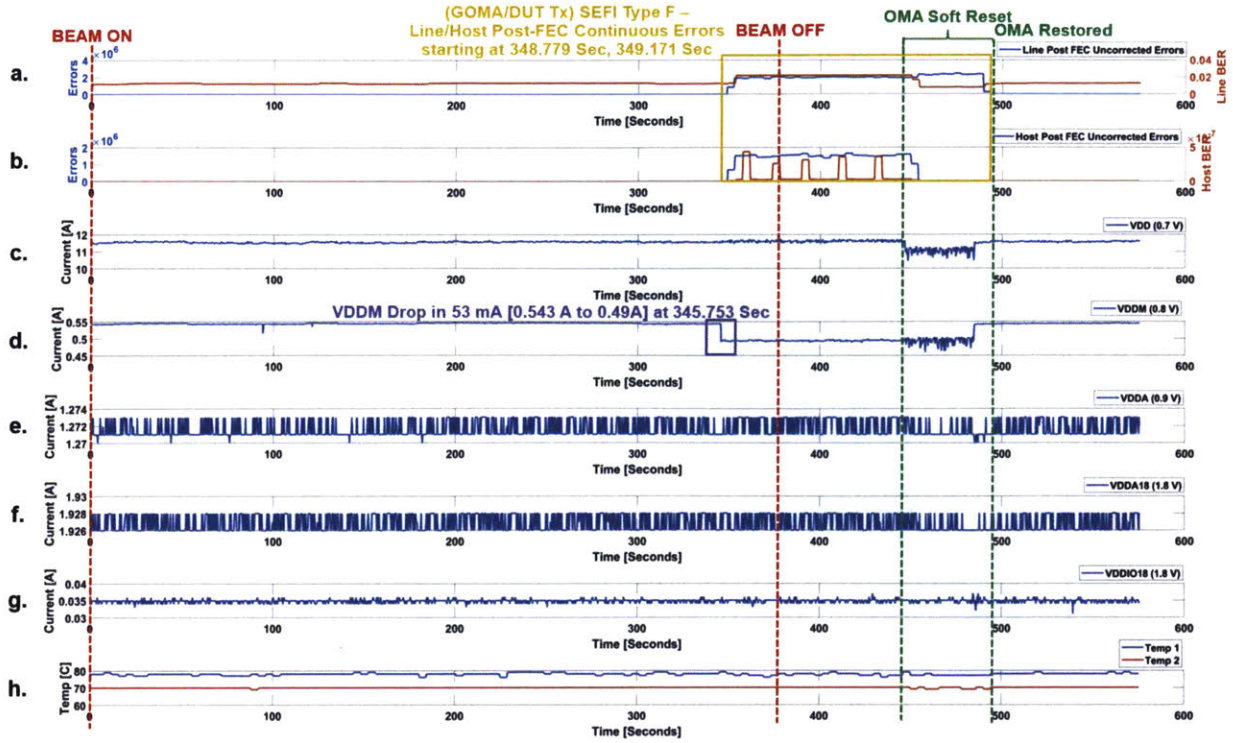

Figure 35. Heavy ion test 2 SEFI type F example from radiation round 4.5 with Gold ions. Plotted telemetry from GOMA ASIC. SEFI Type F behavior of continuous line and host post-FEC errors highlighted.

Type G SEFIs were characterized by anomalous temperature values of the DUT. We observed type G SEFIs in six radiation rounds: 2.1, 3.7, 3.9, 4.1, 4.4, and 4.5. There were three variations in the SEFI type G behavior: (1) temperature values would drop from a nominal value to anomalous value of 0°C, (2) temperature values would shift from a nominal value to anomalous value of 65517°C, and (3) temperature values would continuously shift to anomalous values in a repeated pattern. SEFI type G variation 1 and variation 3 were resolved by performing a soft reset of the OMA, while variation 2 required a hard reset to restore nominal temperature values and behavior.

In radiation round 2.1, temperature 1 dropped from 95°C to 0°C and temperature 2 dropped from 90°C to 0°C at 175.049 seconds. No SEUs, SEFIs, or significant current changes coincided with the anomalous change in temperature data. A soft reset of the OMA restored temperature 1 and temperature 2 to nominal non-zero values. Figure 36 shows the plotted OMA telemetry from radiation round 2.1, including the drop in temperature values to 0°C.

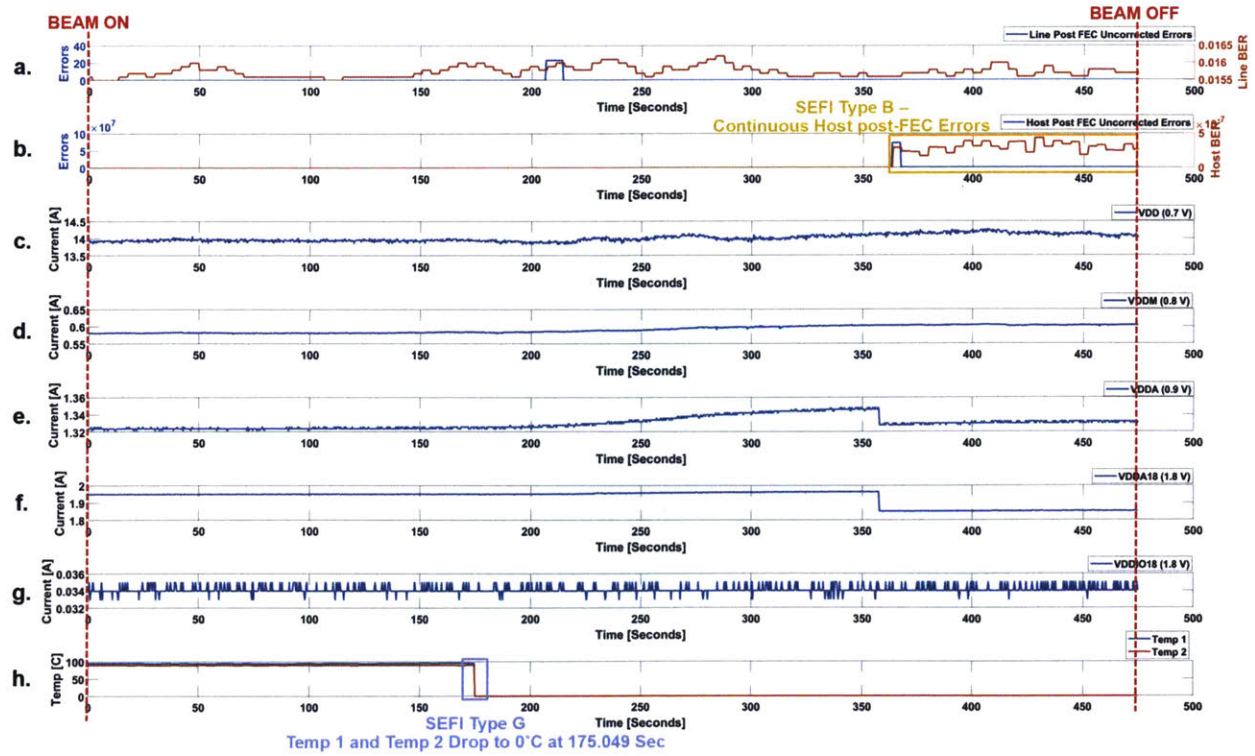

Figure 36. Heavy ion test 2 SEFI type G example from radiation round 2.1 with Krypton ions and 37 mm polyethylene degrader. Plotted telemetry from OMA ASIC. SEFI Type G behavior of drop in temperature 1 and temperature 2 to 0°C.

In radiation round 3.7, temperature 1 changed from nominal value of 94°C to anomalous value of 65517°C. This SEFI type G coincided with a type B SEU (line post-FEC errors), which started 4.83 seconds prior to the SEFI. Temperature 1 remained at 65517°C for 157.176 seconds (even after the heavy ion beam was off) until a soft reset was performed. The soft reset was not successful in restoring the nominal temperature 1 values, and temperature 1 value remained as 65517°C. A hard reset was successful in restoring nominal temperature 1 values. Temperature 2 remained at nominal values ~ 89°C.

In radiation round 3.9, there was a 6.469 A drop on voltage rail 1 (VDD, digital core voltage power supply) at 33.513 seconds, which did not coincide with any SEUs or SEFIs. After ~2.749 seconds from the drop in current, temperature 1 decreased from nominal value of 95°C to 90°C and temperature 2 decreased from nominal value of 89°C to 85°C. At 338.745 seconds, SEFI type G occurred in which temperature 2 changed from 78°C to 65517°C, while temperature 1 remained at 81 °C. Temperature 2 remained at the anomalous value of 65517°C for 96.822 seconds until a soft reset was performed on the OMA. The soft reset was not successful and temperature 2 remained at the anomalous value of 65517°C. A hard reset of the OMA was successful in establishing nominal temperature 2 values.

In radiation round 4.1 temperature 2 increased from 90°C to 65517°C at 1.59 seconds after the beam was turned on. Temperature 1 remained at nominal values of ~95°C. After a soft reset of the OMA, temperature 2 remained at an anomalous value of 65517°C. A hard reset of the OMA was successful in establishing nominal temperature 2 values. Figure 37 shows

the plotted OMA telemetry from radiation round 4.1 and labels the SEFI type G with anomalous temperature 2 data.

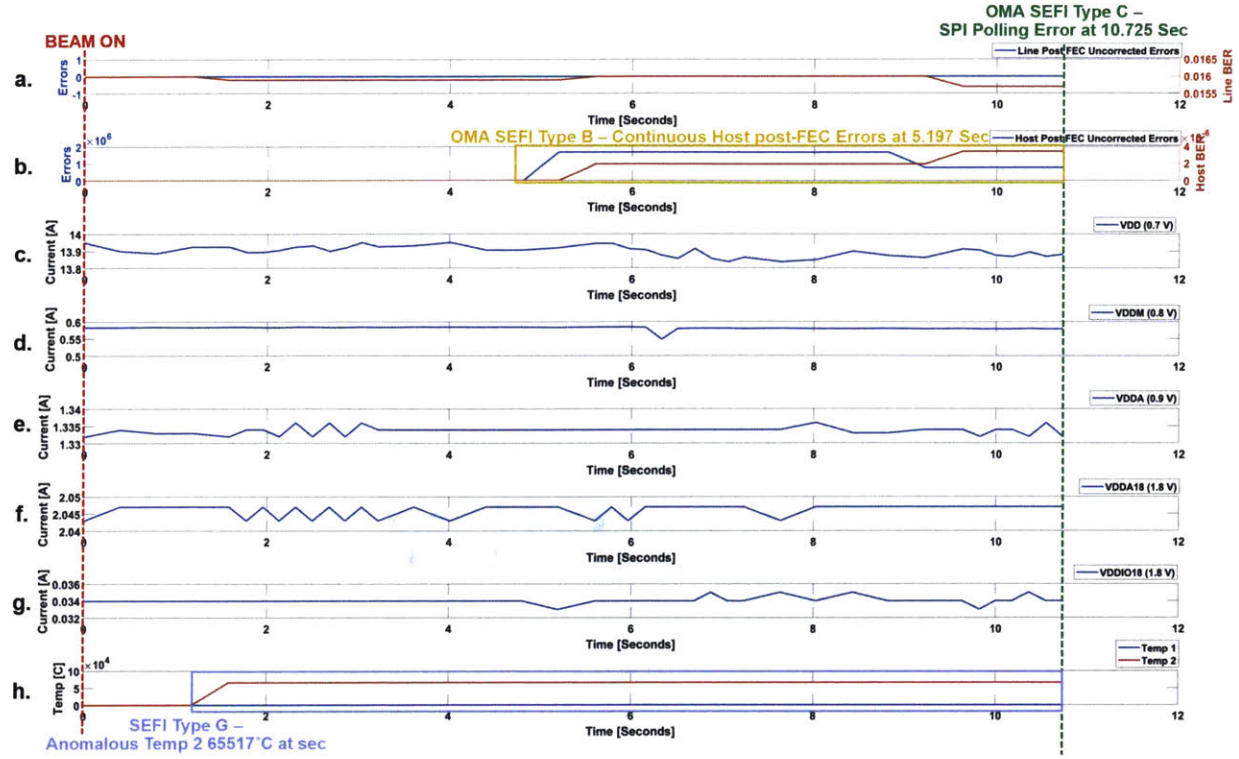

Figure 37. Heavy ion test 2 SEFI type G example from radiation round 4.1 with Gold ions. Plotted telemetry from OMA ASIC. SEFI Type G behavior of anomalous temperature 2 value of 65517°C.

In radiation round 4.4, we observed three anomalous shifts to DUT temperature values. Temperature 1 shifted from nominal value of 96°C to 122°C at 110.466 seconds, which was two time stamps after the start of a type A SEU (host post-FEC errors) at 110.055 seconds. Temperature 2 had nominal values of 92°C to 93°C. At 207.231 seconds into the radiation round, the temperature 1 value dropped from 122°C to 0°C and the temperature 2 value dropped from 93°C to 0°C. The drop to 0°C in both temperatures occurred two time stamps after the start of a type A SEU (host post-FEC errors) at 206.824 seconds. No noticeable changes to the current rails coincided with the drop to anomalous temperature values of 0°C.

Later in radiation round 4.4, a SEFI type A occurred in which both the line and host pre-FEC BER values had oscillating patterns to anomalous "-1" values. We observed a total of 5 occurrences of oscillating temperature values, which coincided with the line pre-FEC BER anomalous state of "-1" for a period of 15 time stamps (~3.6 seconds). In all occurrences, temperature 1 changed from 0°C to 52°C and temperature 2 changed from 0°C to 4°C. After a period of 15 time stamps, the temperature values would both return to 0°C. After 91 timestamps (~24 seconds) from both temperature values returning to 0°C, temperature 1 and temperature 2 values would shift back to 52 °C and 4 °C, respectively, and back to 0 °C after 15 time stamps. Note there were a total of 13 occurrences of the line pre-FEC BER oscillation to "-1" value and not all occurrences coincided with the shift in temperature values. Two of the five temperature oscillation occurrences were observed after the heavy ion beam was off.

The first observation of the temperature oscillation was at 500.946 seconds into the radiation run. Figure 30 displays the plotted telemetry from the OMA in radiation round 4.4 and highlights both the SEFI type G and SEFI type A with oscillating line pre-FEC BER, host pre-FEC BER, and temperature. A soft reset of the OMA was not successful in restoring nominal temperature values and temperature 1 remained fixed at 121°C. A hard reset was successful in restoring nominal temperature values.

Similar to radiation round 4.4, we observed continuous temperature value oscillations in radiation round 4.5. For each cycle, temperature 1 values oscillated from 95°C to 2862°C to 13111°C to 45834°C to 36°C and temperature 2 values oscillated from 90°C to 0°C to 17040°C to 5147°C to 4°C. Each shift to a different temperature value encompassed 15 timestamps or ~3.6 seconds, and the entire cycle was a total of 60 timestamps or ~16 seconds. The cycles repeated a total of three times. The anomalous temperature behavior started at 300.871 seconds into the radiation round and two time stamps after the start of the SEFI type F continuous line and host post-FEC errors. A soft reset was successful in restoring nominal temperature values and behavior.

Table 29 summarizes the SEFI count for the second heavy ion radiation test campaign and details the count for each type of SEFI and whether the SEFI occurred on the DUT receiver or transmitter side.

Table 29. Heavy Ion Test Campaign 2 Single Event Functional Interrupts by Category

Round	Ion	Polyethylene Degrader	Rx SEFIs (OMA DUT)									Tx SEFIs (GOMA ASIC)									Total SEFIs
			A	B	C	D	E	F	G	Total	Reset	A	B	C	D	E	F	G	Total	Reset	
1.1	32.172 GeV Krypton	-	-	-	-	-	-	-	-	0	-	-	-	-	-	-	-	-	0	-	0
1.2			-	-	-	-	-	-	-	0	-	-	-	-	-	-	-	-	0	-	0
1.3			-	-	1	-	-	-	-	1	Soft	-	-	-	-	-	-	-	0	-	1
1.4			-	-	-	1	-	-	-	1	Hard	-	-	-	-	-	-	-	0	-	1
1.5			-	-	1	-	-	-	-	1	Soft	-	-	-	-	1	-	-	1	Soft	2
1.6			-	-	1	-	-	-	-	1	Soft	-	-	-	-	-	-	-	0	-	1
1.7			-	-	1	-	-	-	-	1	Soft	-	-	-	-	1	-	-	1	Soft	2
1.8			-	-	1	-	-	-	-	1	Soft	-	-	-	-	-	-	-	0	-	1
1.9			-	-	-	1	-	-	-	1	Hard	-	-	-	-	-	-	-	0	-	1
1.10			-	-	1	-	-	-	-	1	Soft	-	-	-	-	-	-	-	0	-	1
Total			-	-	6	2	-	-	-	8	-	-	-	-	-	2	-	-	2	-	10
2.1	32.172 GeV Krypton	37 mm	-	1	-	-	-	-	1	2	Soft, Hard	-	-	-	-	-	-	-	0	-	2
2.2			-	-	1	-	-	-	-	1	Soft	-	-	-	-	-	-	-	0	-	1
2.3			1	-	-	-	-	-	-	1	Soft	-	-	-	-	-	-	-	0	-	1
2.4			-	1	-	-	-	-	-	1	Soft, Hard	-	-	-	-	-	-	-	0	-	1
2.5			-	-	1	-	-	-	-	1	Soft	-	-	-	-	-	-	-	0	-	1
Total			1	2	2	-	-	-	1	6	-	-	-	-	-	-	-	-	0	-	6
3.1	32.172 GeV Krypton	43.6 mm	-	-	1	-	-	-	-	1	Soft	-	-	-	-	-	-	-	0	-	1
3.2			-	-	-	1	-	-	-	1	Hard	-	-	-	-	-	-	-	0	-	1
3.3			-	-	1	-	-	-	-	1	Soft	-	-	-	-	-	-	-	0	-	1
3.4			-	-	1	-	-	-	-	1	Soft	-	-	-	-	-	-	-	0	-	1
3.5			-	-	1	-	-	-	-	1	Soft	-	-	-	-	-	-	-	0	-	1
3.6			-	-	1	-	-	-	-	1	Soft	-	-	-	-	-	-	-	0	-	1
3.7			-	-	-	-	-	1	1	2	Soft, Hard	-	-	-	-	-	-	-	0	-	2
3.8			-	-	1	-	-	-	-	1	Soft	-	-	-	-	-	1	-	1	Soft	2
3.9			1	-	-	-	-	-	1	2	Soft, Hard	-	-	-	-	-	-	-	0	-	2
Total			1	-	6	1	-	1	2	11	-	-	-	-	-	-	1	-	1	-	12

4.1	32.505 GeV Gold	-	-	1	1	-	-	-	1	3	Soft, Hard	-	-	-	-	1	-	-	1	Soft	4
4.2			-	1	-	-	-	-	-	1	Soft, Hard	-	-	-	-	-	-	-	0	-	1
4.3			-	-	1	-	-	-	-	1	Soft	-	-	-	-	-	-	-	0	-	1
4.4			1	-	-	-	-	-	1	2	Soft, Hard	-	-	-	-	-	-	-	0	-	2
4.5			-	-	-	-	-	1	1	2	Soft, Hard	-	-	-	-	-	1	-	1	Soft	3
Total			1	2	2	-	-	1	3	9	-	-	-	-	-	1	1	-	2	-	11
Radiation Rounds Total			3	4	16	3	-	2	6	34	-	-	-	-	-	3	2	-	5	-	39

3.4.2.3 Heavy Ion Radiation Test Campaign 2 Single Event Effect Rates

In the second heavy ion radiation test campaign, the maximum achieved LET of heavy ions into the ASIC active region was 36.58 MeV·cm^2/mg. Between the Telesat polar orbit and Telesat inclined orbit (OMERE radiation environment modeling of the Telesat OISL mission in Chapter 2.1), the greater minimum onset LET value is 26.20 MeV·cm^2/mg for the Telesat polar orbit with 100 mils aluminum shielding. The second heavy ion test serves as another destructive SEE screening assessment by testing to an LET greater than 26.20 MeV·cm^2/mg and observing no destructive SEEs.

SRIM was used to model the front-side irradiation of the commercial optical coherent DSP ASIC and determine the achieved LET values from each radiation round. The details of the SRIM modeling to determine the heavy ion radiation test 2 LET values can be found in Appendix A3. Table 30 summarizes the LET levels from each radiation round of the second heavy ion radiation test campaign. Table 30 includes the SEE cross section values, based on the data collected in each radiation round.

Table 30. Heavy ion radiation test campaign 2 LET values and SEE cross section values

Round	Ion, Degrader	LET MeV·cm^2/mg	SEU Cross Section	SEFI – Soft Reset Cross Section	SEFI – Hard Reset Cross Section
1	32.172 GeV Kr, 0 mm	3.36	3.83×10^{-6} ($-1.53,+7.87 \times 10^{-6}$)	4.37×10^{-6} ($-1.86,+8.63 \times 10^{-6}$)	1.09×10^{-6} ($-0.11,+3.93 \times 10^{-6}$)
2	32.172 GeV Kr, 37 mm	5.99	2.27×10^{-5} ($-1.50,+3.29 \times 10^{-5}$)	3.36×10^{-6} ($-0.84,+8.57 \times 10^{-6}$)	1.68×10^{-6} ($-0.17,+6.05 \times 10^{-6}$)
3	32.172 GeV Kr, 43.6 mm	10.08	1.60×10^{-4} ($-/+0.12 \times 10^{-4}$)	9.26×10^{-6} ($-4.35,+17.0 \times 10^{-6}$)	1.85×10^{-6} ($-0.19,+6.67 \times 10^{-6}$)
4	32.505 GeV Au, 0 mm	36.58	9.20×10^{-4} ($-/+0.82 \times 10^{-4}$)	5.11×10^{-5} ($-2.04,+10.5 \times 10^{-5}$)	2.92×10^{-5} ($-0.73,+7.45 \times 10^{-6}$)

The LET values and SEE cross section values from the second heavy ion radiation test were used to calculate the heavy ion SEE rates for the Telesat OISL missions. The "SEE Rate Estimate" tool from OMERE radiation environment modeling software was used to calculate the SEE rates for the modeled Telesat polar and inclined orbit missions. Figure 38 shows the LET versus cross section curves with Weibull distribution fit. The details of the SEE rate calculations are in Appendix A4.

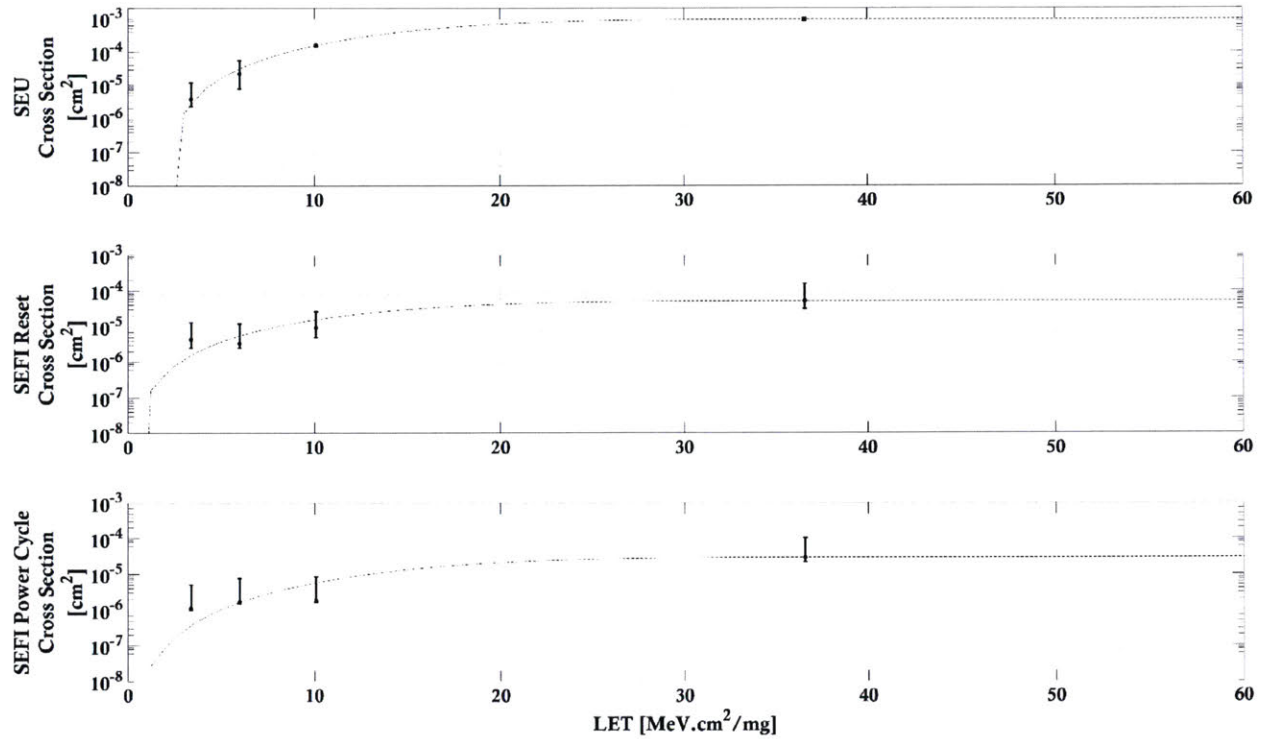

Figure 38. LET versus SEU, SEFI reset, and SEFI power cycle cross section curves with Weibull distribution fit.

The heavy ion nominal case is based on cosmic ray ions from the GCR-ISO model of the Telesat polar and Telesat inclined orbits. The heavy ion solar flare cases are based on CREME96 worst case models for 1 week, 1 day, and peak 5 minute with respect to the Telesat polar and Telesat inclined orbits. Table 31 and
Table 32 summarize the heavy ion best estimate and worst case SEE rates for the Telesat polar and Telesat inclined orbits, based on assuming 200 mils of aluminum shielding. For both Telesat polar and Telesat inclined nominal heavy ion environment cases, there are less than 1 expected SEEs per ASIC per year. For the Telesat polar orbit solar flare cases, the heavy ion SEU rates range from ~6 SEUs per ASIC per year (SEU best estimate for solar flare worst case 1 week model) to ~982 SEUs per ASIC per year (SEU worst case estimate for solar flare worst case peak 5 minute model). The heavy ion SEFIs rates range from less than 1 SEFI per ASIC per year to ~323 SEFIs per ASIC per year (soft reset SEFI worst case for solar flare worst case peak 5 minute model). For all Telesat inclined orbit solar flare cases, the heavy ion SEU and SEFI rates are all less than 1 SEE per ASIC per year.

Table 31. Heavy ion SEE rate calculations for Telesat polar orbit

SEE Rate Assumption	SEE Units	Nominal – Cosmic Rays GCR ISO	Solar Flare – CREME96 Worst Case Models		
			1 Week	1 Day	Peak 5 Minutes
SEU Best Estimate	/Device/Day	4.29×10^{-4}	0.02	0.04	0.15
	/Device/Year	0.16	5.73	15.55	56.21
	/Device/Day	8.55×10^{-4}	0.16	0.73	2.69

SEU Worst Case	/Device/Year	0.31	58.77	265.72	981.85
SEFI – Soft Reset	/Device/Day	7.32×10^{-5}	0.02	0.07	0.26
Best Estimate	/Device/Year	0.03	5.58	25.3	93.8
SEFI – Soft Reset	/Device/Day	1.06×10^{-4}	0.05	0.24	0.88
Worst Case	/Device/Year	0.04	18.91	87.2	322.30
SEFI – Hard Reset	/Device/Day	2.18×10^{-5}	2.25×10^{-3}	9.44×10^{-3}	0.03
Best Estimate	/Device/Year	7.96×10^{-3}	0.82	3.45	12.70
SEFI – Hard Reset	/Device/Day	3.64×10^{-5}	0.01	0.05	0.20
Worst Case	/Device/Year	0.01	4.20	19.2	71.18

Table 32. Heavy ion SEE rate calculations for Telesat inclined orbit

SEE Rate Assumption	**SEE Units**	**Nominal – Cosmic Rays GCR ISO**	**Solar Flare – CREME96 Worst Case Models**		
			1 Week	**1 Day**	**Peak 5 Minutes**
SEU	/Device/Day	2.77×10^{-5}	5.78×10^{-6}	1.04×10^{-6}	4.21×10^{-6}
Best Estimate	/Device/Year	0.01	2.11×10^{-3}	3.80×10^{-4}	1.54×10^{-3}
SEU	/Device/Day	1.53×10^{-4}	1.89×10^{-5}	3.22×10^{-6}	1.30×10^{-5}
Worst Case	/Device/Year	0.06	6.90×10^{-3}	1.18×10^{-3}	4.57×10^{-3}
SEFI – Soft Reset	/Device/Day	1.31×10^{-5}	1.71×10^{-6}	2.88×10^{-7}	1.17×10^{-6}
Best Estimate	/Device/Year	4.78×10^{-3}	6.24×10^{-4}	1.05×10^{-4}	4.27×10^{-4}
SEFI – Soft Reset	/Device/Day	2.34×10^{-5}	2.53×10^{-6}	4.40×10^{-7}	1.79×10^{-6}
Worst Case	/Device/Year	8.54×10^{-3}	9.23×10^{-4}	1.61×10^{-4}	6.53×10^{-4}
SEFI – Hard Reset	/Device/Day	2.91×10^{-6}	4.36×10^{-7}	7.36×10^{-8}	2.98×10^{-7}
Best Estimate	/Device/Year	1.06×10^{-3}	1.59×10^{-4}	2.69×10^{-5}	1.09×10^{-4}
SEFI – Hard Reset	/Device/Day	7.29×10^{-6}	8.50×10^{-7}	1.45×10^{-7}	5.89×10^{-7}
Worst Case	/Device/Year	2.66×10^{-3}	3.10×10^{-4}	5.29×10^{-5}	2.15×10^{-4}

The level of system availability is a key factor for satellite operator service level agreements. The calculated SEE rates are used to evaluate the OISL system availability, based on expected "outage" time from occurrence of an SEU or a SEFI. From the two heavy ion radiation assessments, we observed that heavy ion SEUs had a self-recovery time of ~ 3.7 seconds, but for a conservative calculation we assume a SEU outage time of 8 seconds. For heavy ion SEFIs, outage time would primarily be based on soft or hard resets of the optical modem system. For estimated OISL system availability, we assume a conservative reset period or power cycle period of 90 seconds for system outage time. With the designed OMA prototype, performing an ASIC reset or ASIC power cycle takes ~60 seconds for the ASIC line-side to establish lock and nominal functionality. Note that these availability calculations are based only on SEUs and SEFIs occurring in the commercial optical coherent DSP ASIC or only an outage to the optical modem assembly of the OISL system. Table 33 and Table 34 shows the estimated OISL system availability based only on SEUs and SEFIs for the Telesat polar and Telesat inclined orbit missions over a 1 year period.

Table 33. Telesat polar orbit OISL system availability based only SEUs and SEFIs occurring in commercial optical coherent DSP ASIC.

SEE Type	**Outage [seconds]**	**Nominal – Cosmic Rays GCR ISO**	**Solar Flare – CREME96 Worst Case Models**		
			1 Week	**1 Day**	**Peak 5 Min**
SEU	8	99.99999%	99.99986%	99.99961%	99.99857%

Best Estimate					
SEU Worst Case	8	99.99999%	99.99851%	99.99326%	99.97509%
SEFI – Soft Reset Best Estimate	90	99.99999%	99.99841%	99.99278%	99.97323%
SEFI – Soft Reset Worst Case	90	99.99999%	99.99460%	99.97510%	99.90802%
SEFI – Hard Reset Best Estimate	90	≥ 99.99999%	99.99977%	99.99902%	99.99638%
SEFI – Hard Reset Worst Case	90	≥ 99.99999%	99.99880%	99.99452%	99.97969%

Table 34. Telesat inclined orbit OISL system availability based only SEUs and SEFIs occurring in commercial optical coherent DSP ASIC.

SEE Type	Outage [seconds]	Nominal – Cosmic Rays GCR ISO	Solar Flare – CREME96 Worst Case Models		
			1 Week	1 Day	Peak 5 Min
SEU Best Estimate	8	≥ 99.99999%	≥ 99.99999%	≥ 99.99999%	≥ 99.99999%
SEU Worst Case	8	≥ 99.99999%	≥ 99.99999%	≥ 99.99999%	≥ 99.99999%
SEFI – Soft Reset Best Estimate	90	≥ 99.99999%	≥ 99.99999%	≥ 99.99999%	≥ 99.99999%
SEFI – Soft Reset Worst Case	90	≥ 99.99999%	≥ 99.99999%	≥ 99.99999%	≥ 99.99999%
SEFI – Hard Reset Best Estimate	90	≥ 99.99999%	≥ 99.99999%	≥ 99.99999%	≥ 99.99999%
SEFI – Hard Reset Worst Case	90	≥ 99.99999%	≥ 99.99999%	≥ 99.99999%	≥ 99.99999%

Satellite operators and commercial industry aim to achieve an availability of 99.999% ("five nines). In some cases, millions of dollars per minute are lost in the event of a system outage from satellite failure [Young, 2010]. For the nominal heavy ion environment cases, the Telesat polar orbit and inclined orbit OISL system availability for SEUs and SEFIs is greater than 99.99999% ("seven nines"). For all Telesat inclined orbit solar flare environments, the OISL system availability for SEUs and SEFIs is greater than 99.99999% ("seven nines"). For the Telesat polar orbit solar flare environments, the lowest availability is 99.90802% with "three nines" for SEFI soft reset worst case scenario in a solar flare peak 5 minute environment.

3.5 Proposed Modifications for Commercial Optical Coherent DSP ASIC

The type of reset used to restore nominal functionality of the coherent DSP ASIC provided insight to which part of the ASIC was impaired by heavy ion radiation. The optical coherent modem for an OISL application would need modifications for performing specific resets and power cycles of the coherent DSP ASIC and software for monitoring ASIC performance, anomalous temperature telemetry, and increased current on the voltage rails.

SEFIs affecting transceiver performance, such as SEFI type A, SEFI type E, and SEFI type F, are linked to radiation effects on the embedded microprocessor within the ASIC since a soft reset of the ASIC restored nominal functionality. Based on discussions with the ASIC

vendor, there is currently no ability to reset the microprocessor independently of disrupting other functions and independently from performing a soft reset of the ASIC. Working with the vendor to enable an independent reset of the ASIC embedded microprocessor could provide for enhanced SEE mitigation.

Instead of performing a hard reset of the ASIC, a reset of the host side interface of the coherent DSP ASIC, such as the QSFP module in the optical coherent modem prototype, could be used to resolve SEFI type B. Further investigation will need to be completed to evaluate which aspect of the host interface was impacted by radiation or if this type of SEFI could have been caused by scatter radiation events to the host QSFP module.

Based on SEFI type C observations, the ASIC SPI bus was impacted by heavy ion radiation. The external microcontroller on the optical modem controlled and configured the ASIC using the host SPI interface. To resolve SEFI type C, a soft reset of the ASIC was performed and this included a reset to the SPI bus. A modification to mitigate against SEEs on the SPI bus could include separate functionality of resetting the SPI bus without resetting the entire ASIC and disrupting the transceiver data path functionality. Based on discussion with the ASIC vendor, SPI functionality can be recovered through a SPI reset by writing to a register address associated with the SPI interface, clearing the SPI error, and flushing the SPI interface FIFOs. We did not observe data outages to the GOMA when a SEFI type C occurred on the OMA DUT. The ability to reset only the SPI bus to restore OMA telemetry after SEFI type C occurrence could result in minimal impact to overall system performance (i.e. no link outages during reset of ASIC).

Lost communication with the GUI (SEFI type D) could be related to a SEE to the area of the ASIC that interfaces with the GUI or could be related to radiation scatter events to the commercial FPGA (external to the ASIC) on the optical modem. On the optical coherent modem prototype, the commercial FGPA initializes and sequences the power supply for bring-up of the coherent DSP ASIC. The commercial FPGA as well as the software and firmware for bring-up of the coherent DSP ASIC was incorporated from the ASIC vendor evaluation board reference design. For an OISL application, the commercial FPGA would need to be replaced with a device which can meet the space radiation environment requirements. The Xilinx Zynq Ultrascale+ System on Chip (SoC) with 16 nm FinFET technology could be a viable solution for a radiation tolerant commercial device for bring-up of the coherent DSP ASIC [Xilinx, 2018]. Hiemstra et al. [2017] performed SEU characterization of the Zynq Ultrascale+ MPSoC with 105 MeV protons and suggest the device's SEE and TID performance are acceptable for many LEO short duration missions. Multiple radiation assessments of the Xilinx Zynq Ultrascale+ SoC have been completed and can be referenced for details [Hiemstra et al., 2017; Maillard and Barton, 2017; Glorieux et al., 2018]. Software and firmware for coherent DSP ASIC bring-up would need to be developed on the Zynq SoC. Software and firmware development for the SoC are not within the scope of this work.

Type G SEFIs with anomalous temperature data could be induced by heavy ion SEEs on the embedded microprocessor of the ASIC or on temperature sensing circuits with integrated ADCs in the ASIC. SEFI G.1 and SEFI G.3 could be due to heavy ion SEEs on the embedded processor, which processes temperature data from the temperature sensing circuit, since soft

resets of the ASIC resolve the anomalous behavior. SEFI G.2 could be due to heavy ion SEEs on the temperature sensing circuits. An external chip on the optical modem supplies power to the temperature sensing circuit. Performing a hard reset of the optical modem restored nominal behavior from SEFI G.2 since it would reset the external chip, which powered the temperature circuitry. A proposed modification could include designing the optical modem with the ability to perform an independent reset of the external chip that powers the temperature sensing circuitry without performing a hard reset of the entire optical modem.

Table 35 summarizes the types of SEFIs observed from heavy ion radiation testing of the coherent DSP ASIC, the required reset to establish nominal functionality, and the proposed modification to mitigate against the SEFI.

Table 35. Types of Heavy Ion Single Event Functional Interrupts on the DUT, Reset Required to Restore Nominal Functionality, and Proposed Modification to Mitigate against Radiation Effects

SEFI Type	Description	Reset	Proposed Modification / Mitigation
A	Line and host pre-FEC BER change to values of "-1,"	Soft	Soft Reset for Embedded Microprocessor Reset
B	Host side post-FEC error count greater than zero for time period of over 12 seconds	Hard	Reset of circuitry associated with host interface
C	SPI data polling GUI error message and loss in telemetry recording	Soft	Independent Soft Reset of SPI Interface
D	GUI communication lost	Hard	N/A – Could be radiation scatter event. Replacement of commercial FPGA
E	Line side post-FEC error count greater than zero for time period of over 12 seconds	Soft	Soft Reset for Embedded Microprocessor Reset
F	Line post-FEC uncorrected error count greater than zero, and in the following time stamp the host post-FEC uncorrected error count was greater than zero. Both error counts greater than zero for time-period of over 12 seconds	Soft	Soft Reset for Embedded Microprocessor Reset
G	Anomalous temperature telemetry values	-	-
	1. Drop in temperature telemetry values to 0°C	Soft	Soft Reset for Embedded Microprocessor Reset
	2. Shift in temperature telemetry values to 65517 °C	Hard	Independent Hard Reset of External Chip, which powers ASIC temperature sensing circuitry
	3. Oscillating temperature telemetry values	Soft	Soft Reset for Embedded Microprocessor Reset

3.6 Proton Radiation Assessment of Commercial Optical Coherent DSP ASIC

A proton radiation test campaign of a commercial 100G/200G optical coherent DSP ASIC with 16 nm CMOS plus FinFET technology was completed to evaluate the radiation sensitivity of the ASIC to proton SEEs and equivalent TID and to calculate the proton SEE rate for the device. Proton radiation testing was completed at TRIUMF particle accelerator center in Vancouver, Canada.

3.6.1 Proton Radiation Test Hardware, Test Configuration, and Test Setup

Radiation Engineering Development Units (R-EDUs) were developed for radiation testing of the commercial optical coherent DSP ASICs as well as the coherent driver modulators (CDMs) and micro-intradyne coherent receivers (μICRs). Figure 39 shows a functional block diagram of the OMA R-EDU. External tunable lasers (Optilab TWL-C) were used as the LO inputs to the μICRs and CDMs. A Xilinx Zynq Ultrascale+ is the SoC for the OMA EDU. The SoC initializes and sequences the power supply to bring up the coherent DSP ASIC. The SoC controls bring-up of the μICR and implements a control loop for operating the μICR internal transimpedance amplifiers (TIAs) in manual gain control (MGC) mode. The μICR modifications with the SoC are further described in Chapter 4.3. For the CDM, the SoC executes automatic bias control (ABC), TEC control, and bring-up of the CDM. The CDM modifications with the SoC are further described in Chapter 5.3.

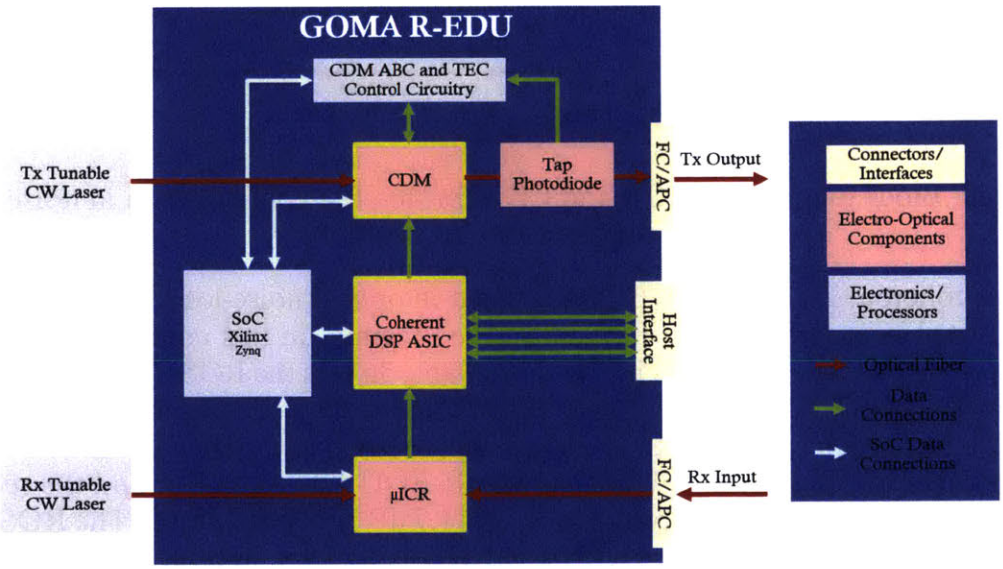

Figure 39. Functional block diagram of optical coherent modem Radiation Engineering Development Unit (R-EDU)

For testing different components, the OMA R-EDU was replaced for each proton test. The same R-EDU (R-EDU GOMA) was designated as the GOMA for all proton tests. R-EDU #1 and R-EDU #2 were the OMAs used for testing μICRs and CDMs.

Proton radiation testing was completed in a noise-loaded optical loopback configuration, like heavy ion radiation testing of commercial optical coherent DSP ASIC. In a noise-loaded optical loopback configuration, the transmit path optical output of a R-EDU (CDM and tap photodiode optical output) is noise-loaded prior to input of the receive path of the other R-EDU (μICR optical signal input). The optical noise-loading consists of a VOA, which attenuates the optical output from the transmit path, an EDFA which amplifies the optical signal with the noise introduced from the VOA, and a 100 GHz DWDM, which filters the optical signal. Figure 41 shows a block diagram of the proton test configuration in noise-loaded optical loopback configuration.

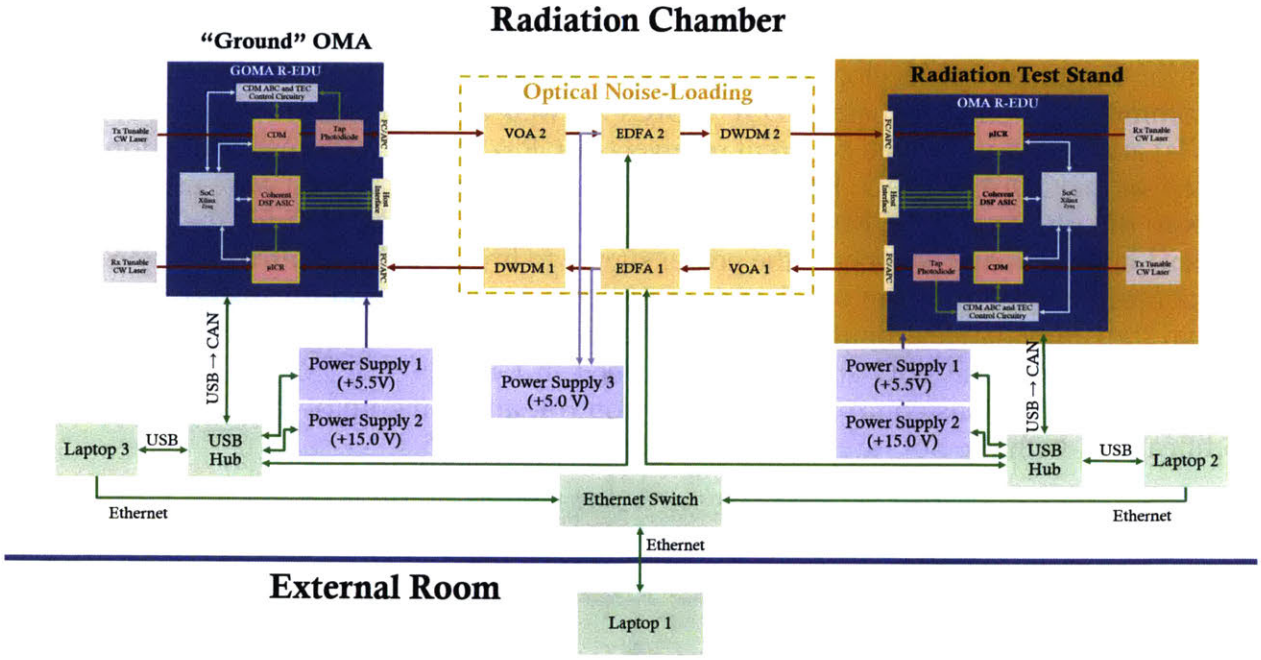

Figure 40. Block diagram of μICR and CDM proton test configuration in noise-loaded optical loopback configuration.

The optical coherent DSP ASIC DUT was tested in optical noise-loaded configuration with OSNR adjusted near operation in a signal-starved regime. In this configuration, the power consumption of the OMA R-EDUs is ~37.5 W. Table 36 lists the ROSNR for the commercial optical coherent DSP ASICs in the R-EDUs, calculated based on the EDFA noise figure values and optical input power to the EDFAs adjusted with a tunable VOA. The ROSNR of the optical coherent DSP ASIC DUT on OMA R-EDU #3 is 12.9 dB, and the receive path into the ASIC DUT was set at OSNR of 14.6 dB (1.7 dB above ROSNR). The ROSNR of the optical coherent DSP ASIC on the GOMA R-EDU is 12.4 dB, and the receive path into the GOMA ASIC (transmit path out of OMA R-EDU) was set at OSNR of 13.7 dB (1.4 dB above the ROSNR). Note for the R-EDUs, the ROSNR was not optimized to the lowest achievable ROSNR specified by the vendor. Adjustments to ASIC optical skew as well as CDM dither amplitude, RF amplitude, RF channel tuning, gain, and peaking would be used to improve the OSNR performance of the commercial optical coherent DSP ASIC. Optimizing the OSNR performance of the coherent DSP ASIC is not within the scope of this work. The BER shown in Table 36 is the pre-FEC BER threshold of the ASIC required to correct all errors with FEC. For the commercial coherent DSP ASIC used in this work, the pre-FEC BER of the optical communication link must be $< 2.0 \times 10^{-2}$ in order for the ASIC FEC to correct all errors on the link.

Table 36. OMA Radiation Engineering Development Unit optical coherent DSP ASIC ROSNR from laboratory benchtop testing. ROSNR was not optimized for R-EDUs.

OMA R-EDU	EDFA NF	VOA Output	ROSNR	BER
R-EDU GOMA	3.8 dB	- 41.8 dBm	12.4dB	2.0×10^{-2}
R-EDU #1	3.6 dB	- 41.5 dBm	12.9 dB	2.0×10^{-2}
R-EDU #2	3.6 dB	- 41.5 dBm	12.9 dB	2.0×10^{-2}
R-EDU #3	3.6 dB	- 41.5 dBm	12.9 dB	2.0×10^{-2}

The EDFAs were operated in fixed optical output power mode of 0 dBm. EDFA #1 along the receive path into the GOMA had a noise figure of 3.8 dB, and EDFA #2 along the receive path into the OMA had a noise figure of 3.6 dB. The external tunable laser input to the CDM provided an optical power of ~9 dBm. The optical input power to the CDM was limited due to saturation of the external tap photodiode, which interfaces with the CDM output. Both external tunable lasers provided optical signal centered at 1563.863 nm. The DWDMs were 100 GHz filters centered at 1563.863 nm. The external tunable laser provided 12 dBm optical power to the μICR LO input, which required the μICR optical signal input to be less than or equal to -10 dBm.

Since a heat sink was mounted to the top of the optical coherent DSP ASIC, the DUT was irradiated from backside of the component and through the OMA R-EDU PCB. The OMA was mounted to the radiation test stand with the ASIC DUT centered with the proton beam collimator using laser alignment. The dimensions of the ASIC footprint are 23 mm by 23 mm, and the proton beam collimator dimensions are 30 mm by 30 mm. The EDUs were designed with a "keep-out area" dimension of 20 mm by 20 mm from the outer edge of the ASIC. The keep out area contains no peripheral, supporting electronic components and provides clearance for peripheral components on the EDU away from direct proton beam irradiation during testing. Figure 41 shows the test setup for proton radiation testing of the optical coherent DSP ASIC. Figure 41(a) and Figure 41(b) show OMA R-EDU #3 mounted on the radiation test stand for back-side irradiation of the optical coherent DSP ASIC through the PCB. The ASIC DUT was aligned to the center of the proton beam collimator using laser alignment as seen with the faint laser cross section in Figure 41(a). On the radiation test stand, Figure 41(a) shows a benchtop fan, which provided convective cooling over the fins of the blue heat sink on the top of the ASIC. Note for a space application, another thermal solution would be designed to replace the fan and heat sink used for laboratory benchtop testing. The yellow arrow in Figure 41(b) indicates the proton beam path to the back-side ASIC DUT area on the PCB. All supporting equipment, such as the GOMA, test computers, power supplies, and optical-noise loading equipment, were placed on a cart near the OMA R-EDU on the radiation test stand (Figure 41(c). The cart was positioned at an angle away from the direct proton beam path, and polyethylene degrader and cement blocks were used to shield the equipment from radiation scatter. Figure 41(d) shows the full test radiation test setup in the radiation chamber room.

Figure 41. Optical coherent DSP ASIC proton radiation test setup. (a) OMA R-EDU mounted on radiation test stand with ASIC DUT aligned to center of proton beam collimator using laser alignment. (b) OMA R-EDU mounted for back-side proton radiation of ASIC through PCB. (c) Supporting test equipment, such as the GOMA R-EDU, test computers, power supplies, and optical-noise loading equipment, on a cart near the radiation test stand. (d) Full proton radiation test setup in the radiation chamber room.

The commercial optical coherent DSP ASIC was operated in 100G mode for proton radiation testing. A host-side interface board with QSFP module slots was developed to allow operation in OTN mode with OTU-4 electrical specification, as in the heavy ion radiation assessments. The host-side interface board would provide host-side performance telemetry during the radiation test. This interface board was not fully functional in time for the proton radiation assessment, thus host-side performance statistics were not collected for the ASIC proton radiation test. The host-side of the ASIC was operated with Ethernet mode and CAUI-4 electrical specification. Based on ASIC vendor specifications, this mode has fewer features and uses less power than the OTN mode with OTU-4.4 electrical specification, which was used for the heavy ion radiation assessments.

3.6.3 Proton Radiation Test Results

One commercial optical coherent DSP ASIC with 16 nm CMOS plus FinFET technology, which was integrated in OMA R-EDU #3, was tested with a 105 MeV proton beam. The ASIC was irradiated for 3 hours, 18 minutes, and 59 seconds to a total fluence of 1.01×10^{12} p/cm^2 or equivalent TID of 91.6 krad(Si) at the TRIUMF particle accelerator. At the beginning of the radiation test, the proton flux was set to of 1.01 (+/-0.02)$\times10^8$ p/cm^2/sec (proton equivalent TID rate of 9.14 rad(Si)/sec). Immediately when the proton beam was turned on, the OMA ASIC and GOMA ASICs both lost lock, there were line post-FEC uncorrected error bursts, and there was an increase in the pre-FEC BER over the 2.0×10^{-2} threshold. The proton beam was powered off and both the OMA and GOMA ASICs were reset. The proton flux was reduced to 5.00(+/-0.02)$\times10^7$ p/cm^2/sec (proton equivalent TID rate of 4.53 rad(Si)/sec). Throughout the radiation test, the flux was slowly increased in intervals up to 1.20 (+/-0.02)$\times10^8$ p/cm^2/sec (proton equivalent TID rate of 10.86 rad(Si)/sec).

At the end of the radiation test, a radiation scatter event impacted the OMA computer hard drive. The OMA computer could not be restarted, and the coherent DSP ASIC radiation test was stopped at total fluence level of 1.01×10^{12} p/cm^2 or equivalent TID of 91.6 krad(Si). The original test plan was to irradiate the ASIC up to total fluence level of 1.22×10^{12} p/cm^2 or equivalent TID of 110 krad(Si). Although communication was lost with the OMA computer, the coherent DSP ASIC on the GOMA was still locked without post-FEC uncorrected error bursts. This showed that the radiation scatter event did not impact the coherent DSP ASIC on the OMA R-EDU. The OMA computer showed an error "hard drive not installed" and could no longer be used to continue radiation testing. As seen in Figure 41, the supporting test equipment, including the OMA computer, was placed on a cart, which was angled away from direct proton beam radiation. Cement blocks were used to shield scatter radiation. In future test campaigns, additional shielding should be used to better protect supporting test equipment.

The ASIC survived radiation testing without permanent degradation to component performance. No proton SEUs were observed. No destructive proton SELs were observed on the ASIC current rails. A total of 54 SEFIs were observed, categorized into six main types of SEFIs. Table 37 summarizes the proton SEE data for the optical coherent DSP ASIC proton radiation assessment.

Table 37. Proton SEE data from optical coherent DSP ASIC 105 MeV proton test campaign

SEFI Type	Description	Required Action	Count
A	ASIC DUT line-side Pre-FEC BER drop to "0"	ASIC Reset	10
B	Repeated error messages, no impact to ASIC DUT line-side performance	ASIC Reset	21
C	Repeated error messages, loss in OMA ASIC DUT data	ASIC Reset	17
D	ASIC DUT LOL and post-FEC uncorrected errors	ASIC Reset	1
E	GOMA ASIC LOL and post-FEC uncorrected errors	ASIC Reset	2
F	ASIC DUT and GOMA ASIC: LOL and post-FEC uncorrected errors	ASIC Reset	1
G	ASIC DUT Temperature Digital Sensor 1 Anomalous Values	ASIC Power Cycle	2
Total SEFIs			54

For proton SEFI type A, the ASIC DUT line-side pre-FEC BER dropped from ~1.0×10^{-2} to anomalous value of "0". The ASIC DUT telemetry showed no impact to the ASIC DUT line-side performance or to the GOMA R-EDU ASIC line-side performance (no loss of lock or post-FEC uncorrected error bursts). Proton SEFI type A could have been caused a proton SEE impact to the section of the ASIC internal microprocessor, which processes pre-FEC BER data. Performing a reset of the ASIC DUT was successful in establishing the nominal line-side pre-FEC BER. Proton SEFI type A is similar to heavy ion SEFI type A, which was observed when the ASIC DUT line-side and host-side pre-FEC BER changed to an anomalous value of "-1" and was resolved by ASIC reset.

Repeated error messages appeared on the console window when type B proton SEFIs were observed. The errors returned by the ASIC APIs include "command not allowed in this mode" messages, "command failed" messages, issues with the ASIC unable to complete all monitor cycle APIs in one second, and host-side related connection issues. There was no impact to the ASIC DUT line-side performance or to the GOMA R-EDU ASIC line-side performance (no loss of lock, no post-FEC uncorrected error bursts, nominal pre-FEC BER). A reset of the ASIC DUT was successful in clearing the error messages.

Type C proton SEFIs were characterized with a loss in ASIC DUT telemetry displayed on the Grafana program and repeated data error messages on the console window. An ASIC reset was successful in restoring the ASIC DUT telemetry. Proton SEFI type C is similar to heavy ion SEFI type C, which was characterized by a SPI data polling GUI error message and a loss in the ASIC DUT telemetry and restored with an ASIC reset.

The ASIC DUT had a loss of lock and continuous post-FEC uncorrected errors during proton SEFI type D. For this SEFI, a proton SEE could have impacted the section of ASIC DUT internal microprocessor which processes the receive (ingress) data path of the ASIC. A reset of the ASIC was successful in restoring the DUT ASIC line-side performance to lock, zero post-FEC uncorrected errors, and nominal pre-FEC BER. Proton SEFI type D is similar to heavy ion SEFI type E, which was characterized by ASIC DUT continuous line-side post-FEC uncorrected errors and restored with an ASIC reset.

The GOMA R-EDU ASIC had a loss of lock and continuous post-FEC uncorrected errors during proton SEFI type E. For this SEFI, a proton SEE could have impacted the section of OMA R-EDU ASIC DUT internal microprocessor which processes the transmit (egress) data path of the ASIC. A reset of the ASIC DUT was successful in restoring nominal GOMA R-EDU ASIC line-side performance.

Proton SEFI type F was characterized by both ASIC DUT and GOMA R-EDU ASIC line-side performance impairments. Both ASICs had loss of lock, continuous post-FEC uncorrected errors, and jumps in pre-FEC BER above the 2.0×10^{-2} threshold. Based on these observations, it appears that the sections of the ASIC DUT internal microprocessor, which process both the receive (ingress) and transmit (egress) data paths, were impacted by a proton SEE. There was only one occurrence of the proton SEFI type F, which occurred immediately when the proton beam was first turned on. A reset of the ASIC DUT was successful establishing nominal ASIC DUT and GOMA R-EDU ASIC line-side performance.

Proton SEFI type G was characterized by anomalous telemetry values from the ASIC DUT temperature digital sensor 1. There were two occurrences of proton SEFI type G. The ASIC

DUT temperature digital sensor 1 dropped to anomalous value of -23°C during the first occurrence and shifted to anomalous values ranging from 110°C to 116°C during the second occurrence. Performing a reset of the temperature digital sensor by setting the temperature monitor to a low power mode and performing a reset of the ASIC DUT were not successful in restoring nominal temperature values between 82°C and 88°C. A power cycle of the ASIC DUT was successful for restoring nominal telemetry readings for temperature digital sensor 1. Proton SEFI type G is similar to heavy ion SEFI type G-2, which was characterized by a shift in temperature telemetry to an anomalous value and required a power cycle of the ASIC DUT to restore the temperature telemetry to a nominal value.

Table 38 summarizes the 105 MeV proton cross section data from ASIC testing at TRIUMF, based on the required type of action (ASIC reset or ASIC power cycle) to restore nominal functionality in the ASIC.

Table 38. 105 MeV proton SEE cross section data from optical coherent DSP ASIC proton test campaign

	SEFI Count	Fluence	SEFI Cross Section
SEFI – ASIC Reset	52	1.01×10^{12} p/cm^2	5.15×10^{-11}
SEFI – ASIC Power Cycle	2	1.01×10^{12} p/cm^2	1.98×10^{-12}

3.6.3 Proton Single Event Effect Rate Calculations

CREME96 software was used to calculate the commercial optical coherent DSP ASIC proton SEFI reset rate and SEFI power cycle rate for the Telesat polar orbit (Table 39) and the Telesat inclined orbit (Table 40), based on the cross section data from the 105 MeV proton radiation test. Appendix A4 describes the method and model details used for calculating the SEE rates with CREME96. The nominal proton environment case includes trapped protons, which are modeled using AP8-MIN environmental model. The solar flare proton environment cases are based on solar flare proton contributions, which are modeled from the October 1989 solar flare data for worst week, worst day, and peak 5 minutes.

Table 39. Coherent DSP ASIC Proton SEE Rates for Telesat Polar Orbit

ASIC SEFI Rate	SEFI Rate Units	Nominal Trapped Protons AP8-MIN	Solar Flare – Worst Case October 1989 Model		
			Worst Week	Worst Day	Peak 5 Minutes
ASIC Reset	**[/Device/Second]**	1.39×10^{-8}	5.42×10^{-8}	2.10×10^{-7}	7.65×10^{-7}
	[/Device/Day]	1.21×10^{-3}	4.69×10^{-3}	1.82×10^{-2}	6.61×10^{-2}
	[/Device/Year]	0.44	1.71	6.63	24.14
ASIC Power Cycle	**[/Device/Second]**	5.38×10^{-10}	2.09×10^{-9}	8.10×10^{-9}	2.95×10^{-8}
	[/Device/Day]	4.65×10^{-5}	1.81×10^{-4}	7.00×10^{-4}	2.55×10^{-3}
	[/Device/Year]	0.02	0.07	0.26	0.93

For the Telesat polar nominal proton environment, there is less than one ASIC reset SEFI and ASIC power cycle SEFI expected per device per year. The expected ASIC reset SEFI rates range from ~2 SEFIs per ASIC per year for solar flare worst week model to ~25 SEFIs

per ASIC per range for solar flare peak 5 minute model. The expected ASIC power cycle SEFI rates are less than one SEFI per ASIC per year for all solar flare models.

Table 40. Coherent DSP ASIC Proton SEE Rates for Telesat Inclined Orbit

ASIC SEFI Rate	SEFI Rate Units	Nominal Trapped Protons AP8-MIN	Solar Flare – Worst Case October 1989 Model		
			Worst Week	Worst Week	Worst Week
ASIC Reset	[/Device/Second]	6.47×10^{-8}	2.72×10^{-12}	3.10×10^{-12}	1.38×10^{-11}
	[/Device/Day]	5.59×10^{-3}	2.35×10^{-7}	2.68×10^{-7}	1.19×10^{-6}
	[/Device/Year]	2.04	8.58×10^{-5}	9.79×10^{-5}	4.35×10^{-4}
ASIC Power Cycle	[/Device/Second]	2.49×10^{-9}	1.05×10^{-13}	1.19×10^{-13}	5.31×10^{-13}
	[/Device/Day]	2.15×10^{-4}	9.04×10^{-9}	1.03×10^{-8}	4.59×10^{-8}
	[/Device/Year]	0.08	3.30×10^{-6}	3.76×10^{-6}	1.67×10^{-5}

For the Telesat inclined nominal proton environment, there are ~2 ASIC reset SEFIs expected per device per year and less than one ASIC power cycle SEFIs expected per device per year. and ASIC power cycle SEFI expected per device per year. The expected ASIC reset and ASIC power cycle SEFI rates are less than one SEFI per ASIC per year for all solar flare models.

3.7 Future Development

In this work, we selected a commercial third generation coherent DSP ASIC with 16 nm FinFET plus CMOS technology for the 100G/200G optical coherent modem for OISL application. In comparison to previous generation coherent DSP ASICs, the third generation coherent DSP ASIC has lower power consumption, which is attractive for reduced SWaP, and lower ROSNR, which is attractive for the optical link budget. We assessed the ASIC with heavy ion and proton radiation assessments. There were no destructive heavy ion or proton SELs observed in the assessments, reducing the risk of increased SEL sensitivity in FinFET in comparison to planar CMOS technologies for this commercial component [Karp, 2018]. The calculated SEE rates for the nominal heavy ion and proton environments show the feasibility of using the commercial coherent DSP ASIC with 16 nm FinFET plus CMOS technology for the Telesat OISL constellation or similar LEO orbits. Future work with the selected coherent DSP ASIC could include additional heavy ion radiation test campaigns to test more devices and to test devices at angles as well as additional proton radiation test campaigns to test more devices and to test devices at different proton energy levels.

Coherent DSP ASIC vendors in the terrestrial fiber-optic communications industry are focused on developing the next generation of coherent DSP ASICs with 7 nm silicon node technology to achieve reduced power consumption and cost per bit [Melle, 2018; Stiller, 2018]. The coherent DSP ASICs with 7 nm FinFET technology are developed for 16-QAM 400 Gbps applications and samples of these ASICs will be released in early 2020 [OFC, 2019]. An optical coherent modem with the new coherent DSP ASICs could be used for optical communication links with data rates up to 400 Gbps (16-QAM, 64 GBaud), but have modes for 100 Gbps (QPSK, 32 GBaud) or 200 Gbps (QPSK, 64 GBaud). Reduced technology nodes of future commercial coherent DSP ASICs can provide higher reductions in SWaP and cost

for space OISL applications. In comparison to a coherent DSP ASIC with 28 nm node technology (second generation ASIC), a DSP ASIC with 7 nm technology can provide 78% to 95% in power consumption savings from ADCs, chromatic dispersion compensation, polarization demultiplexing and carrier recovery [Morsy-Osman et al., 2018]. As coherent DSP ASICs move toward FinFET plus CMOS technologies with thinner active regions, we expect increased TID tolerance and reduced probability of a heavy ion or proton SEE strike to the active region. We expect coherent DSP ASICs with 7 nm FinFET technology to have TID tolerance up to hundreds of krad(Si). Heavy ion and proton radiation assessments of commercial coherent DSP ASICs with 7 nm FinFET plus CMOS technology would need to be completed to screen for destructive SELs and to collect SEE cross section data for SEE rate calculations.

Chapter 4

Commercial Optical Coherent Receiver

The coherent receiver is a key electro-optical component, which interfaces with the optical coherent DSP ASIC in an optical coherent modem as shown in Figure 42. A coherent receiver has two inputs, the received optical signal and a local oscillator (LO) optical signal. The coherent receiver is intradyne, which defines the frequency difference between the received optical signal and the LO optical signal as within the bandwidth of the detectors although the lasers are not phase-locked. In an optical modem, the output of the intradyne coherent receiver (ICR) are four analog signal inputs (XI, XQ, YI, and YQ signal voltages) to the high speed, four channel ADC of the coherent DSP ASIC.

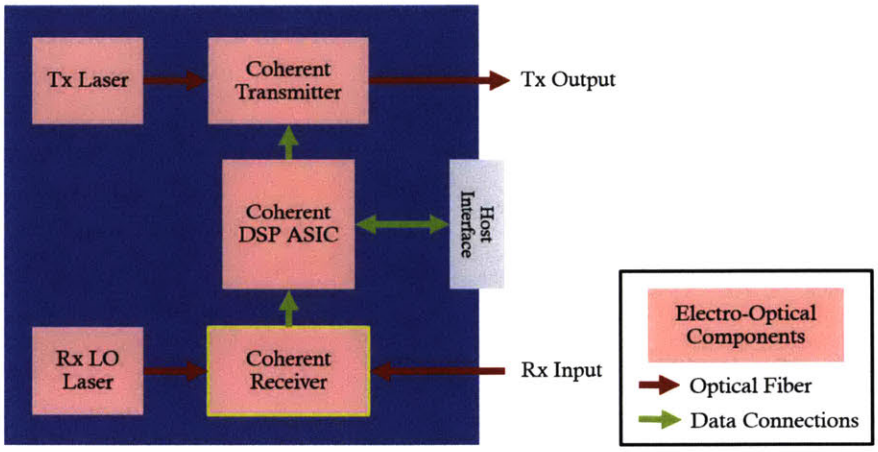

Figure 42. Optical coherent modem electro-optical component functional block diagram with coherent receiver highlighted.

4.1 Commercial Intradyne Coherent Receiver Background

OIF has released IAs to define performance, mechanical, and electrical standards for commercial ICRs with symbol rate capabilities for optical coherent systems for 100G applications. A symbol rate of 32 Gbaud is utilized for 100G applications and 64 Gbaud for 200G applications. The first two OIF IAs for ICRs were released in September 2011 and November 2013 and focused on "Integrated Dual Polarization ICRs." The following two IAs

were released in March 2015 and June 2017 for "Integrated Dual Polarization Micro-ICRs (μICRs)."

The "Implementation Agreement for Integrated Dual Polarization ICRs" defined 100G ICRs for DP-QPSK demodulation and 32 GBaud sample rate with the following components: a phase demodulator, photodiodes, trans-impedance amplifiers (TIAs) and polarization splitters and rotators within a 50 mm x 27 mm gold box [OIF (OIF-DPC-RX-01.1), 2011]. In 2013, OIF defined a Type 2 ICR which encompassed half the area of the Type 1 ICR. The most recent standard is the μICRs, which has a maximum dimension of 27 mm x 12 mm and less than 25% of the Type 1 ICR footprint area. Micro-ICRs (μICRs) include an integrated polarization splitter, variable optical attenuators (VOAs) to adjust the signal level, and monitor photodiodes (MPDs) [OIF (IA # OIF-DPC-MRX-02.0), 2017].

Indium Phosphide (InP) PICs have been the key enabling technology, which have allowed miniaturization, cost reduction, and high volume manufacturability of ICRs. [Takechi et al., 2013]. InP based μICRs have high symbol rate capabilities for systems with 100 Gbps and up to 600 Gbps, such as the recent release of Neophotonics 64 Gbaud μICRs in 2017. Neophotonics, Lumentum (previously Oclaro), and Fujitsu are commercial vendors of μICRs, with capabilities up to 64 GBaud symbol rates [Neophotonics, 2019; Lumentum, 2019; Fujitsu, 2019]. Figure 43 shows μICRs from (a) Neophotonics, Lumentum (b), and Fujitsu (c), which are all mechanically compliant (maximum dimensions of 27 mm × 12 mm × 6 mm) to the OIF IAs for μICRs.

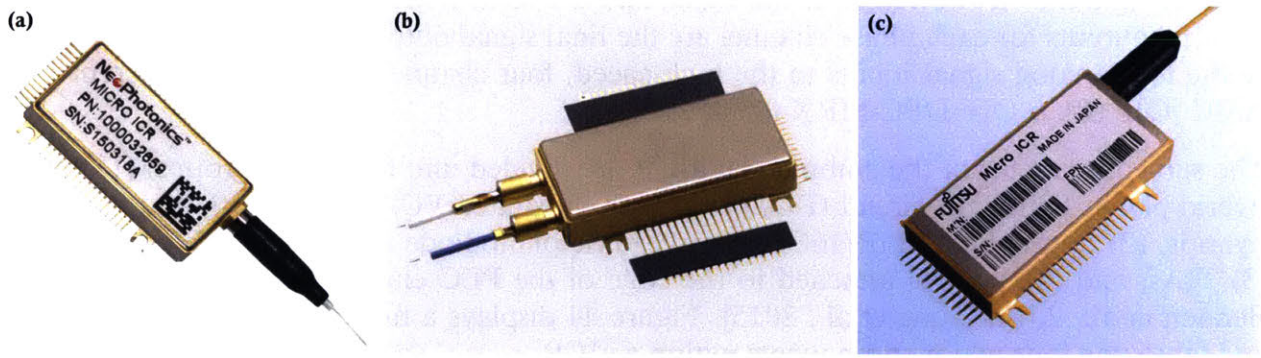

Figure 43. Type 1 Micro Intradyne Coherent Receivers from commercial vendors (a) Neophotonics, (b) Lumentum, and (c) Fujitsu [Neophotonics, 2019; Lumentum, 2019; Fujitsu, 2019]. All mechanically compliant to IA # OIF-DPC-MRX-02.0) [2017] (maximum dimensions of 27 mm × 12 mm × 6 mm) and have capabilities for 600 Gbps applications with 64 GBaud symbol rate.

Key parameters of the Neophotonics and Lumentum (previously Oclaro) μICRs are proprietary. Information, such as datasheets, are not openly public on the vendor websites. Fujitsu provides information for two μICRs: 100G DP-QPSK and 200G DP-16QAM and 200G DP-QPSK and 400G DP-xQAM optical communication system applications, listed in Table 41 [Fujitsu, 2019].

Table 41. Fujitsu Micro-Intradyne Coherent Receiver Specifications [Fujitsu, 2019]

Part	Application	Baud Rate [GBaud]	Wavelength [nm]	Output Voltage Swing	Typ. Power Consumption [W]	Temperature [°C]

				[mVp-p]		
FIM24901	400G DP-xQAM 200G DP-QPSK	64	1528 – 1567	300 – 700	1.4	-5 to +85
FIM24725	200G DP-xQAM 100G DP-QPSK	32	1528 – 1567	300 – 900	1.7	-5 to +85

4.1.1 Functionality and Sub-Components of Micro-Intradyne Coherent Receivers

The input optical signal to the μICR enters an optical tap which splits a portion of the input optical signal to an MPD and the remaining optical signal is passed to a VOA, which serves to limit the amount of optical signal into the μICR. From the VOA, the optical signal enters polarization beam splitter (PBS), which splits the input optical signal into two orthogonal polarizations, X-polarization and Y-polarization. Each polarization enters a separate 90-degree hybrid mixer, defining a X-polarization mixer and a Y-polarization mixer.

The local oscillator signal into the μICR enters a polarization maintaining power splitter or beam splitter (BS), which divides the local oscillator signal power equally to two paths. The split local oscillator signals enter into the X-polarization and Y-polarization hybrid mixers. The two 90-degree hybrid mixers yield differential output phase channels: XI, XQ, YI, YQ. I and Q are mutually orthogonal phase channels in each X and Y polarization. Each phase channel is detected by a balanced PD, which outputs a current level, and the current is converted to voltage and amplified by a TIA with differential alternating current (AC) coupled outputs "p" and "n," complementary for each phase channel. The output voltage "p" increases and the "n" decreases as the signal and LO form constructive interference. The "p" and "n" outputs for each phase channel are the final signal outputs from the μICR and serve as the four analog signal inputs to the high speed, four channel ADC of the coherent DSP ASIC [OIF (IA # OIF-DPC-MRX-02.0), 2017].

The sub-components of the commercial μICR are divided into four main groups: (1) optical hybrid planar lightwave circuit (PLC) chip with integrated VOA, a PBS, BS, and 90-degree hybrids, (2) four-channel InP/InGaAs waveguide photodiode arrays for each polarization, (3) TIAs, and (4) a MPD attached to the edge of the PLC chip [Tsunashima et al., 2012; Bennett et al., 2014; Dong et al., 2015]. Figure 44 displays a functional diagram of a μICR and labels the four major components within a μICR.

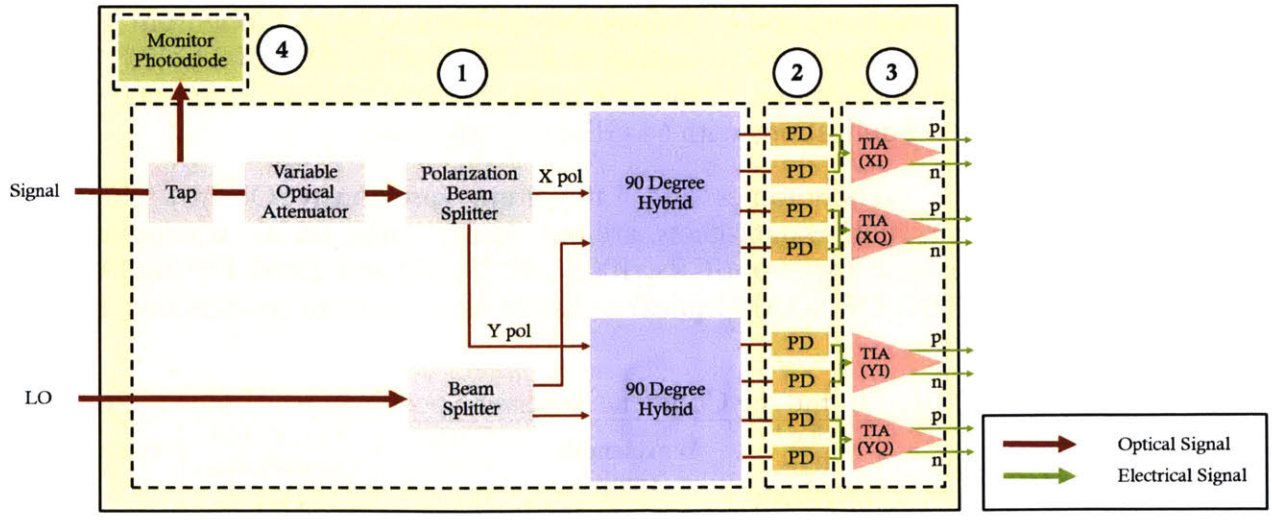

Figure 44. Functional block diagram of micro-intradyne coherent receiver [OIF, 2017]

PLCs are PICs made with doped silica glasses with controllable indices of refraction and are ideal for passive optical components due to the low coupling losses [Neophotonics, 2019]. The 90-degree hybrid functionality within the PLC is achieved using multimode interferometers (MMIs) [Dong et al., 2015]. Work by Tsunashima et al. [2012], Dong et al. [2015], and Yagi et al. [2015] describe examples of PLC chips co-packaged and coupled with TIAs and waveguide PD arrays for commercial μICRs. Tsunashima et al. [2012] can be referenced for images showing the side and top views of the optoelectronic coupling between a PLC chip, waveguide photodiode array, and TIA [Tsunashima et al., 2012]. Yagi et al. [2015] describes the details of design and fabrication of an InP chip with monolithic integration of 90 degree hybrid and pin photodiodes. Yagi et al. [2015] can be referenced for images showing a photomicrograph of an InP chip, a cross-section schematic diagram of the 90 degree hybrid and photodiodes, and a schematic diagram of the InP-based pin photodiode array integrated into the 90 degree hybrid.

4.1.2 Electrical Interface of Micro-Intradyne Coherent Receivers

The OIF IA for μICRs defines a standard pin-out for low speed electrical interface, shown in Figure 45 [OIF, (IA # OIF-DPC-MRX-02.0), 2017]. Evaluating the standardized pin-out for the μICR allows us to design the optical coherent modem with features for monitoring component telemetry and performance as well as for operating the μICR in a strategic manner for space application. For the optical hybrid PLC chip, pin 30 and pin 31 are used for providing voltage for adjusting the VOA. With exception to the VOA, the other sub-components in the PLC chip (tap, PBS, PS, 90-degree hybrids) are passive optical components. For the four-channel InP/InGaAs waveguide photodiode arrays, pins 6-9 and pins 26-29 provide voltages for biasing the photodiodes for each of the differential output phase channels XI, XQ, YI, YQ. There are two gain control modes for the TIAs, manual gain control (MGC) and automatic gain control (AGC) mode, which is controlled through pin 3. In MGC mode, a gain adjustment voltage is fixed, which determines the output amplitude voltage from the TIAs. Pin 11, pin, 16, pin 19, and pin 24 allow for control the gain adjustment voltage in MGC mode. In AGC mode, the output amplitude voltage is fixed by applying voltage to pin 12, pin 15, pin 20, and pin 23 and the gain adjustment voltage is dynamic. Pin 10, pin 17, pin, 18, and pin 25 can be used to detect the peak voltages for each of the phase channels at the output of the TIA. Pin 13 and pin 22 provide the supply voltage for the amplifiers in the TIAs. Pins 4 and 5 provide the bias voltage for the MPD. Section 4.3 provides details on modifications for the μICR in the optical coherent modem design. Features provided through the pin-out, such as reading bias voltage for the MPD to determine radiation degradation to MPD, are key for designing for space application.

Pin#	Symbol	Description	Pin#	Symbol	Description
1	RFU	Reserved for future use[4]	34	RFU	Reserved for future use[4]
2	RFU	Reserved for future use[4]	33	RFU	Reserved for future use[4]
3	MGC/AGC	MGC/AGC selection (optional)	32	SD	Shutdown (optional)
4	MPD-C	Monitor diode cathode (optional)[3]	31	VOA1	VOA1 Adjust voltage (optional)[2]
5	MPD-A	Monitor diode anode (optional)[3]	30	VOA2	VOA2 Adjust voltage (optional)[2]
6	PD-YI	Photodiode bias voltage YI[1]	29	PD-XQ	Photodiode bias voltage XQ[1]
7	PD-YI	Photodiode bias voltage YI[1]	28	PD-XQ	Photodiode bias voltage XQ[1]
8	PD-YQ	Photodiode bias voltage YQ[1]	27	PD-XI	Photodiode bias voltage XI[1]
9	PD-YQ	Photodiode bias voltage YQ[1]	26	PD-XI	Photodiode bias voltage XI[1]
10	PI-YI	Peak indicator YI	25	PI-XQ	Peak indicator XQ
11	GA-YI	Gain adjust YI	24	GA-XQ	Gain adjust XQ
12	OA-YI	Output amplitude adjust YI	23	OA-XQ	Output amplitude adjust XQ
13	VCC-Y	Supply voltage amplifier Y	22	VCC-X	Supply voltage amplifier X
14	GND	Ground Reference	21	GND	Ground Reference
15	OA-YQ	Output amplitude adjust YQ	20	OA-XI	Output amplitude adjust XI
16	GA-YQ	Gain adjust YQ	19	GA-XI	Gain adjust XI
17	PI-YQ	Peak Indicator YQ	18	PI-XI	Peak Indicator XI

Figure 45. Micro Intradyne Coherent Receiver low speed electrical interface defined by OIF, IA # OIF-DPC-MRX-02.0 [2017].

4.2 Radiation Susceptibility of Commercial Micro-Intradyne Coherent Receiver

The four main groups of sub-components of a commercial μICR (DPOH PLC chip, four-channel InP/InGaAs waveguide photodiode arrays, TIAs, and MPD) are susceptible to radiation based on the types of technologies and materials used for each sub-component. The specific technology processes and materials of the sub-components are proprietary to the μICR vendors. Thus, background research is used to infer the radiation susceptibility of each of the main sub-components.

The optical hybrid PLC chip integrates a VOA, a PBS, a BS, and two 90 degree hybrids on a single chip. The PLC chip is fabricated with silicon dioxide and doped silica glass used for waveguide circuits. The silicon photonic waveguides are susceptible to SEEs, particularly single event transients (SETs), and TID effects. A simulation by Goley et al. [2018] predicts that a heavy ion strike can ionize an integrated silicon photonic waveguide and generate high levels of free electrons and holes. While excess carriers recombine in the waveguide, transient optical power losses and phase shifts can occur. The simulation results indicate that the optical power losses are relatively small ($\leq 10\%$) for normally incident heavy ions for LETs up to 40 MeV·cm^2/mg [Goley et al., 2018]. Similar to silicon core optical fibers, integrated silicon photonic waveguides could experience darkening due to ionizing radiation, which creates centers of absorption where optical defects occur in silicon core optical fibers [Ott et al., 1997]. Displacement damage should not be an issue for the silicon photonic waveguides. We expect the integrated VOA in the PLC chip to be a diode, which can be biased with a voltage to change the index of refraction of the glass and attenuate the input optical signal. Diodes are typically susceptible to displacement damage effects and the glass is susceptible to TID effects.

We expect the waveguide photodiodes are InP/InGaAs PIN photodiode arrays and the MPD is based on InGaAs material [Tsunashima et al, 2012; Yagi et al, 2015]. InGaAs PIN photodiodes are susceptible to displacement damage effects, specifically increased dark

current and degraded responsivity due to the generation of defect traps and recombination centers in the active region [Troska et al., 1997; Barde et al., 2000; Aniceto et al, 2017].

Based on Dong et al. [2015], we expect the TIAs are made with a SiGe BiCMOS (Silicon Germanium heterojunction bipolar transistors (HBT) and CMOS) process. SiGe technology is susceptible to SEEs and TID effects. SEEs on SiGe BiCMOS technology include SEL and SEFIs due to the CMOS technology, SETs due to the SiGe HBTs technology, and SEUs due to both the SiGe HBT and CMOS technology. For TID effects, the CMOS content will be susceptible to parametric shifts, but the SiGe HBT technology is known to be "TID hard," tolerant to multi Mrad levels of TID [Cressler, 2013; Lourenco et al., 2013].

Table 42 outlines the technology process, materials, and radiation susceptibility for the four main sub-components of a commercial μICR.

Table 42. Radiation susceptibility of commercial micro-intradyne coherent receiver based on technology of sub-components

Sub-Components	Technology/Material	Radiation Susceptibility
1. DPOH PLC Chip	Doped Silica Glass	Single Event Transients Total Ionizing Dose
	VOA (Diode)	Displacement Damage Dose
	Integrated Optics	Total Ionizing Dose
2. Waveguide Photodiodes	InP-based PIN photodiode array	Displacement Damage Dose
3. Dual Transimpedance Amplifiers (TIAs)	SiGe BiCMOS	Single Event Latchup Total Ionizing Dose Displacement Damage Dose
4. Monitor Photodiode	InGaAs	Displacement Damage Dose

Proton radiation can serve as a source for DDD effects, equivalent TID effects, and SEEs. Displacement damage induced by proton testing could be used for testing effects on the VOA in the PLC chip, waveguide photodiode array, TIAs, and MPD. Equivalent TID from proton testing would induce effects on the doped silica class and integrated optics in the PLC chip and in the TIAs. Screening for SEL in the TIAs can be completed with proton testing.

4.3 Proposed Modifications for Commercial Micro-Intradyne Coherent Receiver

The OMA R-EDU, which is described in Chapter 3.6.1, was designed with modifications for the commercial μICR. A key modification was the development of a control loop to run the μICR TIAs in MGC mode rather than in AGC mode. If the TIAs are run in MGC mode with fixed gain adjustment voltage, changes in the output amplitude voltage of the TIA due to radiation effects could be observed and used to evaluate if there are radiation-induced impairments to sub-components, which are functionally in the block diagram chain prior to the TIAs. For example, we expected displacement damage to induce increased dark current on the waveguide photodiodes, then noise and reduced current levels into the TIA could yield

reduced output voltage amplitudes from the TIA for fixed gain voltages. Alternatively, we expected TID to induce darkening in the integrated optics of the PLC chip, which would reduce the optical signal detected by the waveguide photodiodes and reduce the input current to the TIAs. The final result would be reduced output voltage amplitudes from the TIAs. Designing the OMA R-EDU with the μICR TIAs operating in MGC mode instead of AGC mode provided higher radiation tolerance for the μICR. Operating the μICR in AGC mode would require more circuitry, specifically an additional op amp, and could be less robust to radiation due to higher number of susceptible parts.

The μICR TIA control loop modification includes operating the μICR TIAs in MGC mode and implementing AGC through an external circuit with the coherent DSP ASIC, Zynq SoC, and DAC. The control loop for operating the TIAs in MGC mode is shown in a functional block diagram in Figure 46. The μICR TIAs output XI, XQ, YI, and YQ channel voltage signals, which are input to the coherent DSP ASIC. Through an internal high-speed ADC, the coherent DSP ASIC outputs the peak voltage values detected into the Zynq SoC. A PID controller is implemented within the FPGA of the Zynq to set the gain voltage for the μICR TIAs.

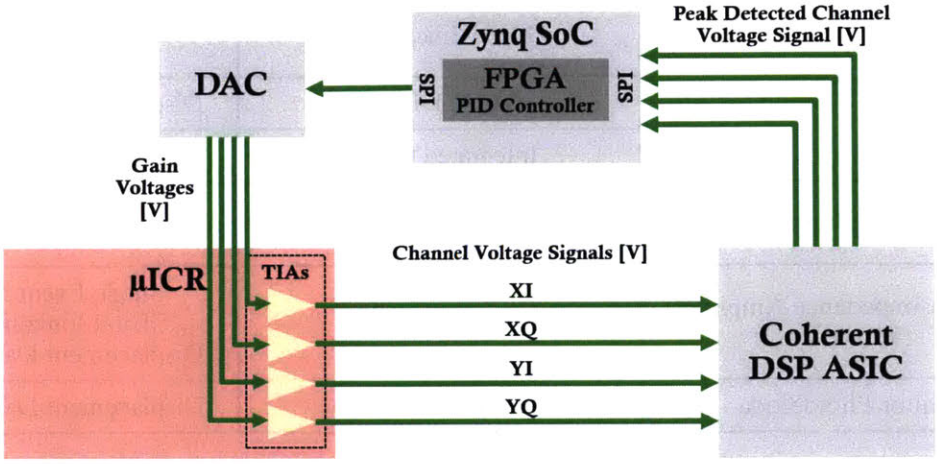

Figure 46. Functional diagram of μICR TIAs in manual gain control with external automatic gain control loop using coherent DSP ASIC, Zynq SoC, and DAC.

Due to the high level of integration of sub-components and the small size of the μICR packaging, it is difficult to isolate the proton beam to radiate only specific sub-components. There are limited parameters, which can be monitored for the μICR sub-components, making it difficult to identify which sub-component is impacted during proton radiation testing. Thus, there is limited visibility to understand if the main radiation induced impairments are on the PLC chip, waveguide photodiodes, or TIAs, since all sub-components are sensitive to proton radiation effects.

An optical signal with fixed power level is input to the μICR, therefore any changes to the output current readings of the MPD would be induced by displacement damage effects from proton radiation. The OMA R-EDU was designed to apply fixed voltage to the μICR VOA for minimum attenuation to allow maximum optical input power level into the μICR. There are no monitoring parameters to directly evaluate displacement damage effects on the VOA. The integrated optics and glass of the PLC chip are passive and there is no built-in

functionality in the μICR to monitor if there are radiation effects on these components and radiation impairments occurring prior to the waveguide photodiodes. The waveguide photodiodes are biased with a fixed voltage and the output current is directly input to the TIAs; there are no parameters that can be monitored to observe for displacement damage effects to the waveguide photodiodes. The OMA R-EDU was designed to collect telemetry on the current from the VCC supply voltage rail to monitor for SELs.

Overall component-level degradation to the μICR DUT on the OMA R-EDU would be observed through reduced optical power readings in the internal MPD, changes to the TIA output amplitude adjustment voltages, and changes to μICR output peak indicator voltages based on the TIA manual gain control loop. On an OMA system level, degradation to the μICR would be observed through reduced OMA ASIC line-side performance: post-FEC errors, increased pre-FEC BER, and loss of lock (LOL). The line-side performance parameters, current on all voltage rails, and temperatures were monitored on the coherent DSP ASIC.

For radiation testing of the μICRs, the OMA R-EDUs (described in Chapter 3.6.1) were designed with μICR reset capability, ASIC reset capability, ability to power cycle the ASIC, and ability to power cycle the OMA R-EDU.

4.4 Proton Radiation Assessments of Commercial Micro-Intradyne Coherent Receivers

Proton radiation test campaigns of commercial μICRs were completed to evaluate the radiation sensitivity of these integrated components to DDD, TID, and SEEs. A total of two identical commercial μICRs were tested in the proton test campaign at the TRIUMF particle accelerator center in Vancouver, Canada.

4.4.1 Proton Radiation Test Setup for Commercial Micro-Intradyne Coherent Receivers

Commercial μICRs integrated in OMA R-EDUs (described in Chapter 3.6.1) were used for proton radiation testing. For radiation testing of the commercial μICRs, the noise-loaded optical loopback configuration was adjusted by 2.0 dB to 2.5 dB above the ROSNR of the commercial optical coherent DSP ASICs. In an optical signal starved regime (less than 2.0 dB from ROSNR, as in the commercial optical coherent DSP ASIC radiation test campaigns), radiation degradation to the optical path in the μICR could easily shift the test configuration OSNR over the ASIC ROSNR and cause a LOL in the ASIC. The intention of operating at 2.0 dB or higher from the ASIC ROSNR was to provide sufficient optical signal power into the receive path of the ASIC and to observe gradual degradation to the DUT based on an increase in the pre-FEC BER of the ASIC in the optical receive path. The OSNR offset from the ASIC ROSNR was limited based on the commercial μICR optical signal versus LO power mask. The external tunable laser provided 12 dBm optical power to the μICR LO input, which required the μICR optical signal input to be less than or equal to -10 dBm.

The commercial μICRs were irradiated to 105 MeV proton fluence levels of 1.2×10^{12} p/cm^2 or equivalent TID of 110 krad(Si). The proton fluence level is two times higher than the expected DDD levels for 105 MeV protons on InP-based and InGaAs-based devices with 200 mils aluminum shielding in the Telesat radiation environment. Appendix Section A6 can be referenced for details on 105 MeV proton equivalent fluence for DDD on InP-based and

InGaAs-based devices in the Telesat mission environments. The equivalent TID level of 110 krad(Si) is greater than the 100 krad(Si) TID level requirement for the optical coherent modem (requirement L0-09 in Table 16). Testing at these higher levels provides margin to the DDD and TID requirements and extends the application of these commercial parts to more intense radiation environments.

For both μICR DUTs, the proton beam was configured for a 105 MeV proton energy level and proton flux of 1.00 (+/-0.02)$\times 10^8$ p/cm^2/sec (proton equivalent TID rate of ~ 9 rad(Si)/sec). The μICRs were irradiated from the top of the component. The OMA was mounted to the radiation test stand with the μICR DUT centered with the proton beam collimator using laser alignment. The dimensions of the μICR are 25 mm by 12 mm, and the proton beam collimator dimensions are 30 mm by 30 mm. The EDUs were designed with a "keep-out area" dimension of 20 mm by 20 mm from the outer edge of the μICR. The keep out area contains no peripheral supporting electronic components and provides clearance for peripheral components on the EDU away from direct proton beam irradiation during testing. Figure 47 shows the test setup for proton radiation testing of the μICRs. Figure 47(a) and Figure 47(b) show an OMA R-EDU mounted on the radiation test stand with the top of the μICR DUT aligned to the center of the proton beam collimator using laser alignment. A yellow arrow is included to highlight the μICR DUT on the OMA R-EDU. All supporting equipment, such as the GOMA, test computers, power supplies, and optical-noise loading equipment, were placed on a cart near the OMA R-EDU on the radiation test stand shown in Figure 47(c). The cart was positioned at an angle away from the direct proton beam path, and polyethylene degrader and cement blocks were used to shield the equipment from radiation scatter. Figure 47 (d) shows the full test radiation test setup in the radiation chamber room.

Figure 47. μICR proton radiation test setup. (a) and (b) OMA R-EDU mounted on radiation test stand with top of μICR DUT aligned to center of proton beam collimator using laser alignment. Yellow arrow indicates μICR DUT on OMA R-EDU. (c) supporting test equipment, such as the GOMA R-EDU, test computers, power supplies, and optical-noise loading equipment, on a cart near the radiation test stand. (d) Full proton radiation test setup in the radiation chamber room.

4.4.2 Proton Radiation Test of Micro-Intradyne Coherent Receiver #1

The μICR DUT #1 on OMA R-EDU #1 was irradiated for 3 hours, 22 minutes, and 4 seconds to a total fluence of 1.22×10^{12} p/cm^2 or equivalent TID of 110.4 krad(Si). In the test configuration, the receive path into the μICR DUT #1 on the OMA was optically noise-loaded at OSNR of 14.9 dB, which was 2.0 dB above the ROSNR for the R-EDU. The OMA ASIC pre-FEC BER was 7.4×10^{-3}. The optical input power to the μICR DUT #1 was -10.4 dBm. The receive path into the GOMA was optically noise-loaded at OSNR of 12.4 dB,

which was 2.5 dB above the ROSNR for the R-EDU. The GOMA ASIC pre-FEC BER was 6.1×10^{-3}.

During the test, there was no observable, gradual degradation of the µICR observed in the monitored parameters. Prior to radiation, the internal MPD optical power reading oscillated between values of 78.76 µWand 81.45 µW. At the end of the radiation test at ~ 110 krad(Si) TID level and 1.22×10^{12} p/cm^2 fluence level, the internal MPD optical power reading remained at 78.76 µW. The gain set voltages and peak indicator voltages for the HI, HQ, VI, VQ channels did not show any significant change in value through the radiation test. There was minimal drift in the gain set voltages and peak indicator voltages, comparable to nominal drift over time in the range of 2 mV to 14 mV.

Figure 48 shows the µICR DUT #1 telemetry collected during the proton radiation test. Figure 48 (a) shows the internal MPD optical power reading. Figure 48(b) shows the TIA gain setting values. Figure 48(c) shows the peak indicator voltages at output of µICR DUT #2. Figure 48(d) shows the I term for PID controller used for TIA manual gain control mode. During proton radiation of µICR DUT #1, radiation-scatter on test equipment had effects on the test setup and appeared on the µICR DUT #1 telemetry. Events associated with radiation effects to test equipment due to proton scatter are indicated with red boxes in Figure 48 and red numbered circles. There were two SEEs on µICR DUT #1 observed, but none of the events required a reset of the µICR. The two SEE occurrences indicated with the yellow circle labeled "R" and yellow boxes in Figure 48(a) and Figure 48(b).

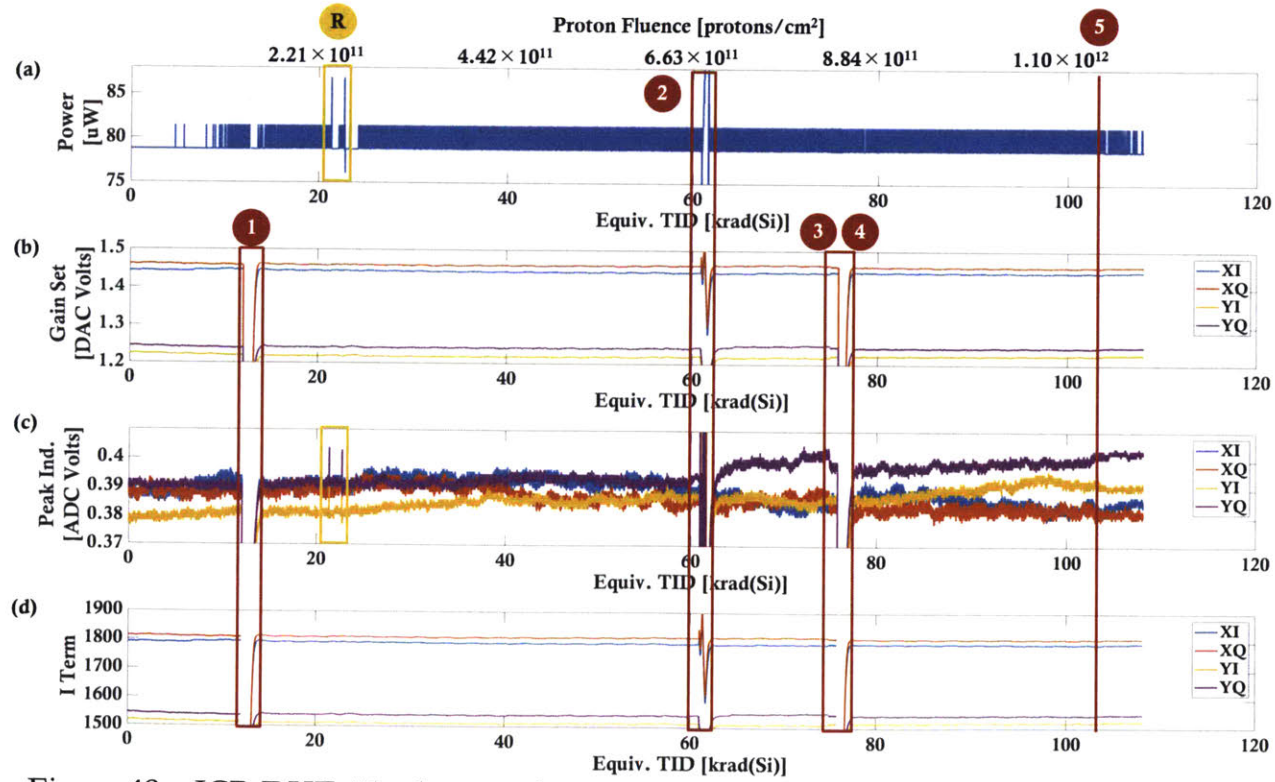

Figure 48. µICR DUT #1 telemetry from proton radiation test. (a) Internal MPD optical power reading, (b) TIA gain settings, (c) Peak indicator voltages at output of µICR, and (d) I term for PID controller used for µICR TIA manual gain control mode. Observed proton single event effects are indicated with yellow box and yellow circle labeled "R" on the MPD

optical power reading (a) and peak indicator voltages (c). Radiation scatter events are indicated with red box and red numbered circles.

During the first radiation scatter event (red circle labeled "1" in Figure 48 at ~ 13 krad(Si)) the telemetry plots for the OMA R-EDU stopped displaying and the command line showed that the OMA R-EDU automatically rebooted itself. A power cycle of the OMA R-EDU was required to establish the nominal state of the OMA and display the telemetry. In the second radiation scatter event shown with the red circle labeled "2" in Figure 48 at ~ 63 krad(Si), the GOMA computer restarted itself, causing the ASIC on the OMA R-EDU into a LOL state. In the third radiation scatter event shown with red circle labeled "3" in Figure 48 at ~77 krad(Si), the OMA computer froze. The OMA R-EDU was powered off and the proton beam was turned off. After successful restart of the OMA computer, the OMA R-EDU and the GOMA R-EDU were restarted then the proton beam was turned on. Shortly after the proton beam was turned on, the OMA R-EDU automatically rebooted itself for the fourth radiation scatter event shown with red circle labeled "4" in Figure 48 at ~ 78 krad(Si). A power cycle of the OMA R-EDU was completed while the proton beam was on. In the fifth radiation scatter event shown with red circle labeled "5" in Figure 48 at ~ 104 krad(Si), the remote desktop connection to the GOMA computer was lost and there was a freeze in the GOMA R-EDU telemetry displayed.

Figure 49 shows the μICR DUT #1 telemetry focused on the two proton SEEs observed, labeled with yellow circles "R1" and "R2". In both proton SEEs, there were observable peaks in both internal MPD optical power readings and peak indicator voltages.

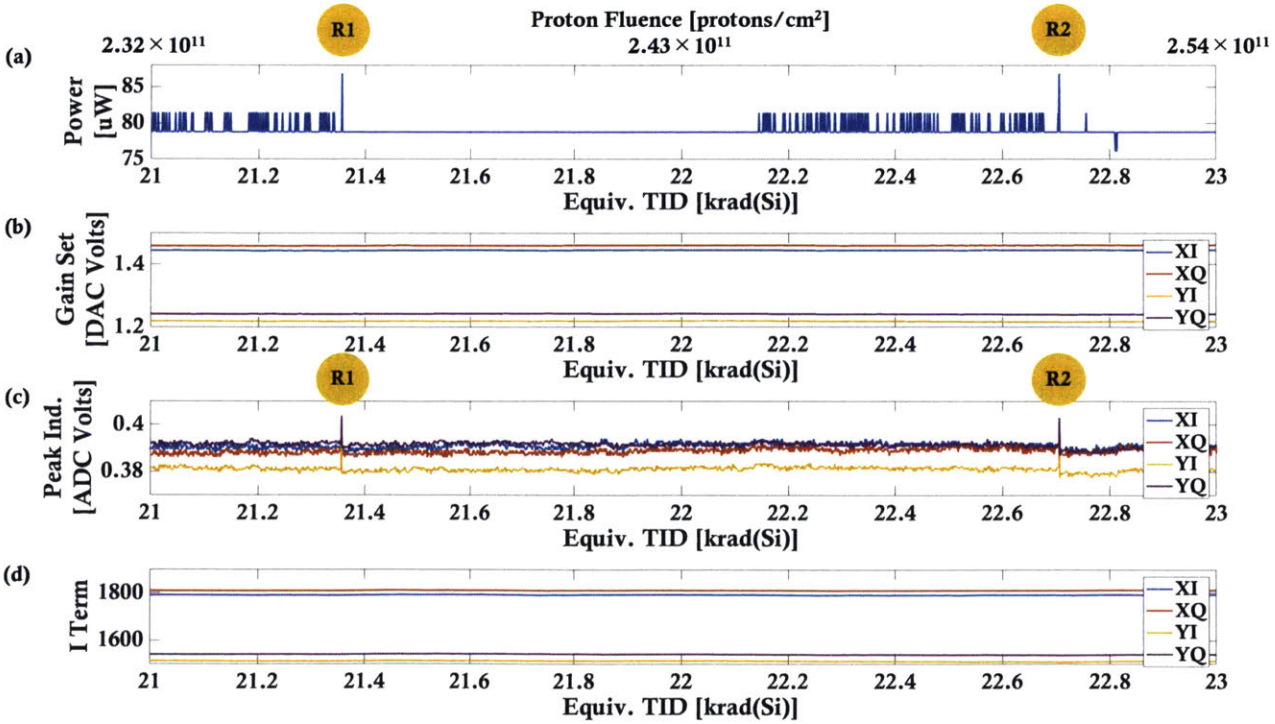

Figure 49. μICR DUT #1 telemetry from the proton radiation test focused on the two proton SEEs, which are labeled with yellow numbered circles on the MPD optical power reading (a) and peak indicator voltages (c). (a) Internal MPD optical power reading, (b) TIA

gain settings, (c) Peak indicator voltages at output of μICR, and (d) I term for PID controller used for μICR TIA manual gain control mode.

The first SEE occurred at equivalent TID level of 21.36 krad(Si) or fluence of 2.36 $\times 10^{11}$ p/cm^2. The internal MPD optical power reading peaked from 78.76 μW to 86.85 μW, then returned to nominal 78.76 μW. All peak indicator voltages displayed a peak, increasing between 10.4 mV and 12.9 mV then decreasing between 12.0 mV and 13.7 mV to nominal values. The event occurred over a duration of ~ 200 ms. Figure 50 shows a zoomed in portion of the MPD power plot and peak indicator voltages plot from Figure 49 where the first SEE occurred.

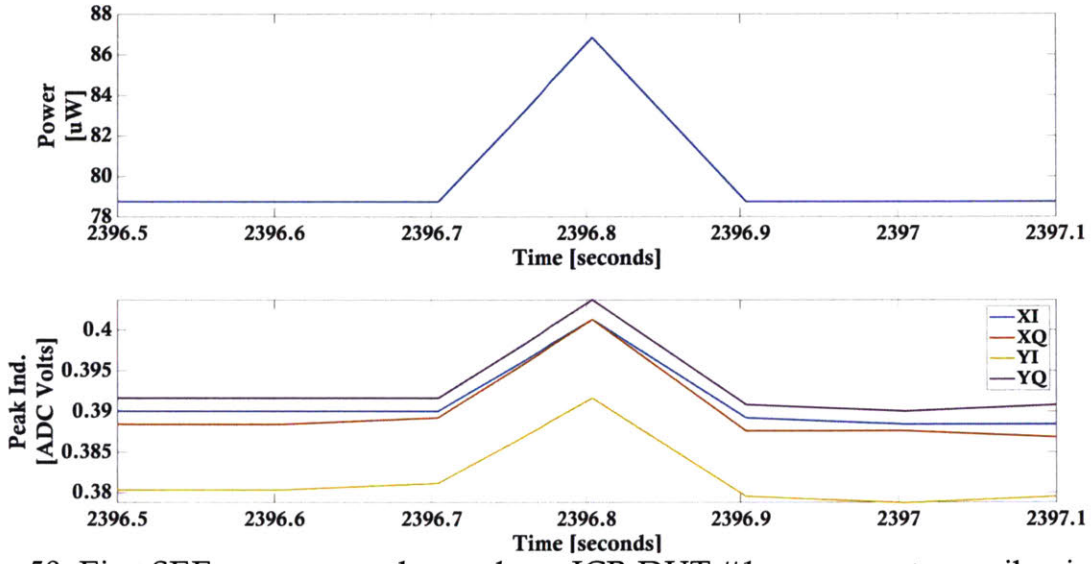

Figure 50. First SEE occurrence observed on μICR DUT #1 as momentary spikes in MPD power telemetry and peak indicator voltage telemetry over ~200 ms duration.

The second SEE occurred at equivalent TID level of 22.71 krad(Si) or fluence of 2.51 $\times 10^{11}$ p/cm^2. The internal MPD optical power reading peaked to the same values as the first SEE, from 78.76 μW to 86.85 μW, then returned to nominal 78.76 μW. All peak indicator voltages displayed a peak, increasing between 10.5 mV and 12.1 mV then decreasing between 13.7 mV and 16.2 mV to nominal values. Figure 51 shows a zoomed in portion of the MPD power plot and peak indicator voltages plot from Figure 49 where the second SEE occurred.

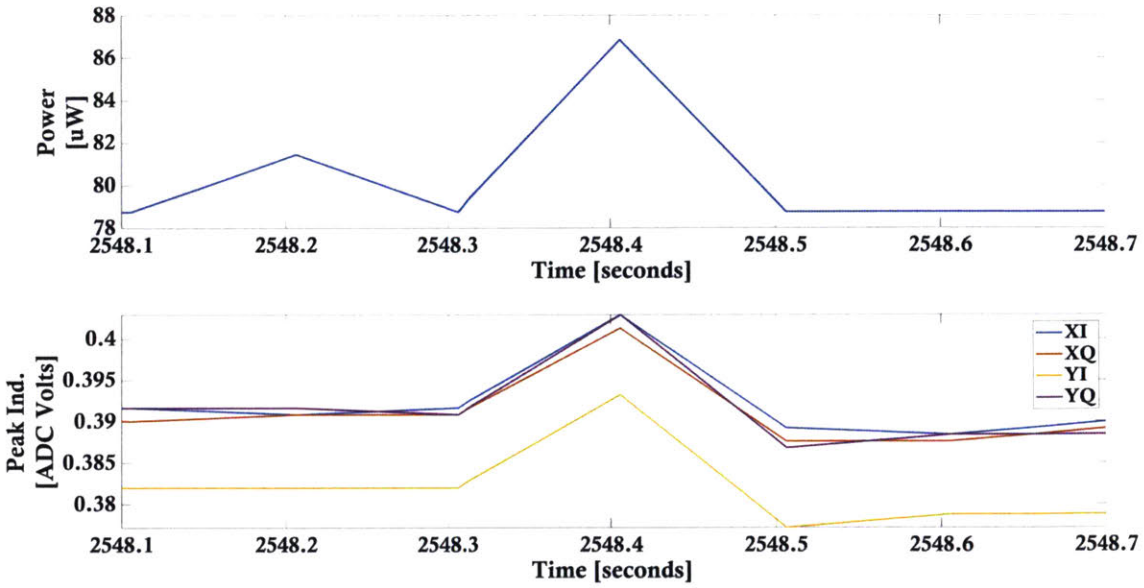

Figure 51. Second SEE occurrence observed on μICR DUT #1 as momentary spikes in MPD power telemetry and peak indicator voltage telemetry over ~200 ms duration.

Table 43 lists the changes to the internal MPD optical power readings and peak indicator voltages for the two SEEs. No reset or power cycle of the μICR DUT was performed after each observed event, since there were no impacts to OMA system performance and the peaked telemetry parameters returned to nominal levels immediately after the observed event. The two SEEs could be SETs, which are defined as a momentary voltage spike at a node in an integrated circuit caused by a single energetic particle strike [JESD, JESD89A 2006]. SETs are typically observed on linear devices, such as operational amplifiers (Op Amps) [George et al., 2005].

Table 43. μICR DUT #1 observed proton SEEs. Quantified changes to MPD optical power readings and peak indicator voltages.

SEE	Component		Initial Value	Peak	Post Peak	Initial-Peak Delta	Post-Peak Delta
1	MPD		78.76 μW	86.85 μW	78.76 μW	8.09 μW	- 8.09 μW
	Peak Indicator	HI	390.0 mV	401.3 mV	389.2 mV	11.3 mV	- 12.1 mV
		HQ	389.2 mV	401.3 mV	387.6 mV	12.1 mV	- 13.7 mV
		VI	381.2 mV	391.6 mV	379.6 mV	10.4 mV	- 12.0 mV
		VQ	391.6 mV	403.7 mV	390.8 mV	12.1 mV	- 12.9 mV
2	MPD		78.76 μW	86.85 μW	78.76 μW	8.09 μW	- 8.09 μW
	Peak Indicator	HI	391.6 mV	402.9 mV	389.2 mV	11.3 mV	- 13.7 mV
		HQ	390.8 mV	401.3 mV	387.6 mV	10.5 mV	- 13.7 mV
		VI	382.0 mV	393.3 mV	377.1 mV	11.3 mV	- 16.2 mV
		VQ	390.8 mV	402.9 mV	386.8 mV	12.1 mV	- 16.1 mV

There were no proton SELs observed. Figure 52 shows the μICR DUT #1 VCC voltage rail and current during the radiation test. Radiation scatter events, which affected VCC telemetry, are labeled with the red numbered circles in Figure 52.

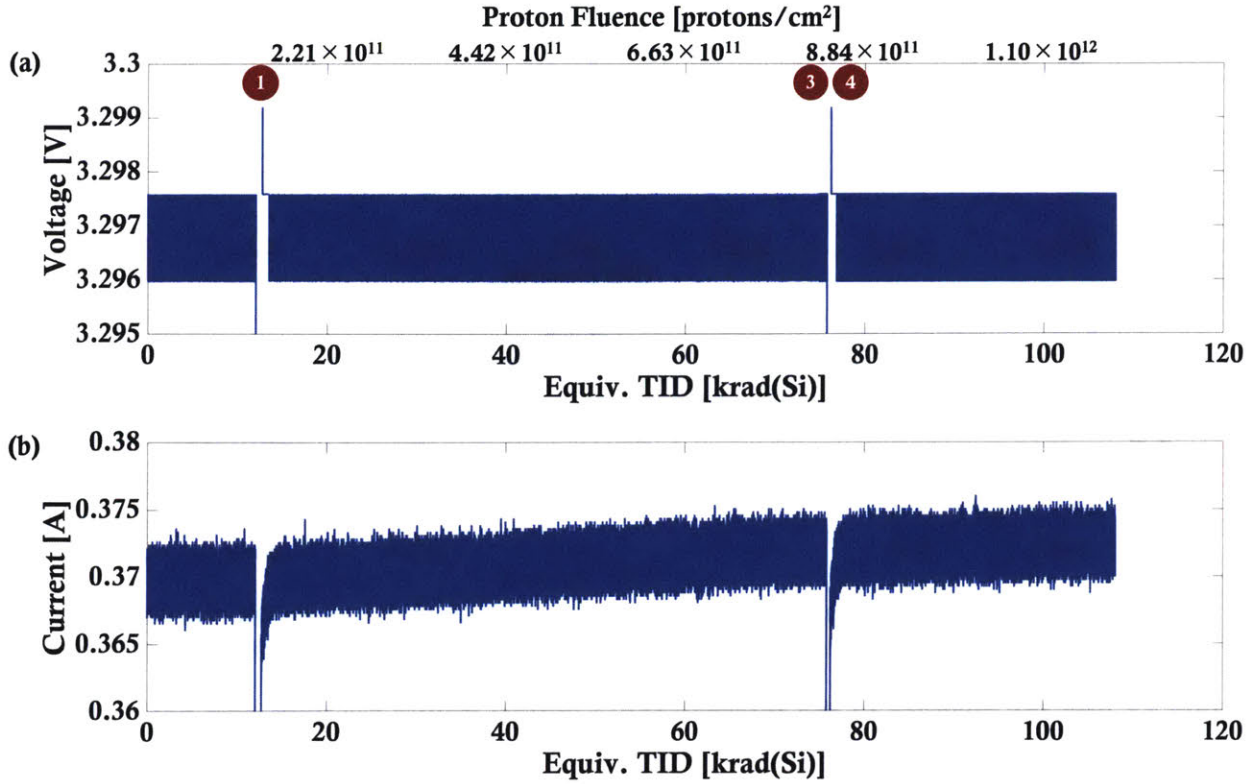

Figure 52. μICR DUT #1 proton radiation test VCC voltage rail and current. Radiation scatter events with effects on VCC voltage and current are labeled with red circles.

There was no degradation to the OMA system performance observed during the μICR DUT #1 proton radiation test. With exception to radiation scatter events on test equipment, no line post-FEC error bursts and no LOL were observed. The pre-FEC BER maintained a value of $\sim 7.5\times10^{-3}$, without observable degradation. From the radiation scatter event #5 at equivalent TID level of ~104 krad(Si), there was an observable drop in the ASIC pre-FEC BER from $\sim 7.5\times10^{-3}$ to $\sim 6.7\times10^{-3}$. The radiation scatter event did not have a significant effect to the overall OMA performance since the ASIC did not lose lock and did not have any post-FEC error bursts. Figure 53 shows the OMA line side parameters monitored during the μICR DUT #1 proton radiation test. Figure 53(a) shows the ASIC LOL monitor, with a "1" indicating LOL and "0" indicating no LOL. Figure 53(b) shows the ASIC line post-FEC error count, and Figure 53(c) shows the line pre-FEC BER. The radiation scatter events are labeled with numbered red circles in Figure 53.

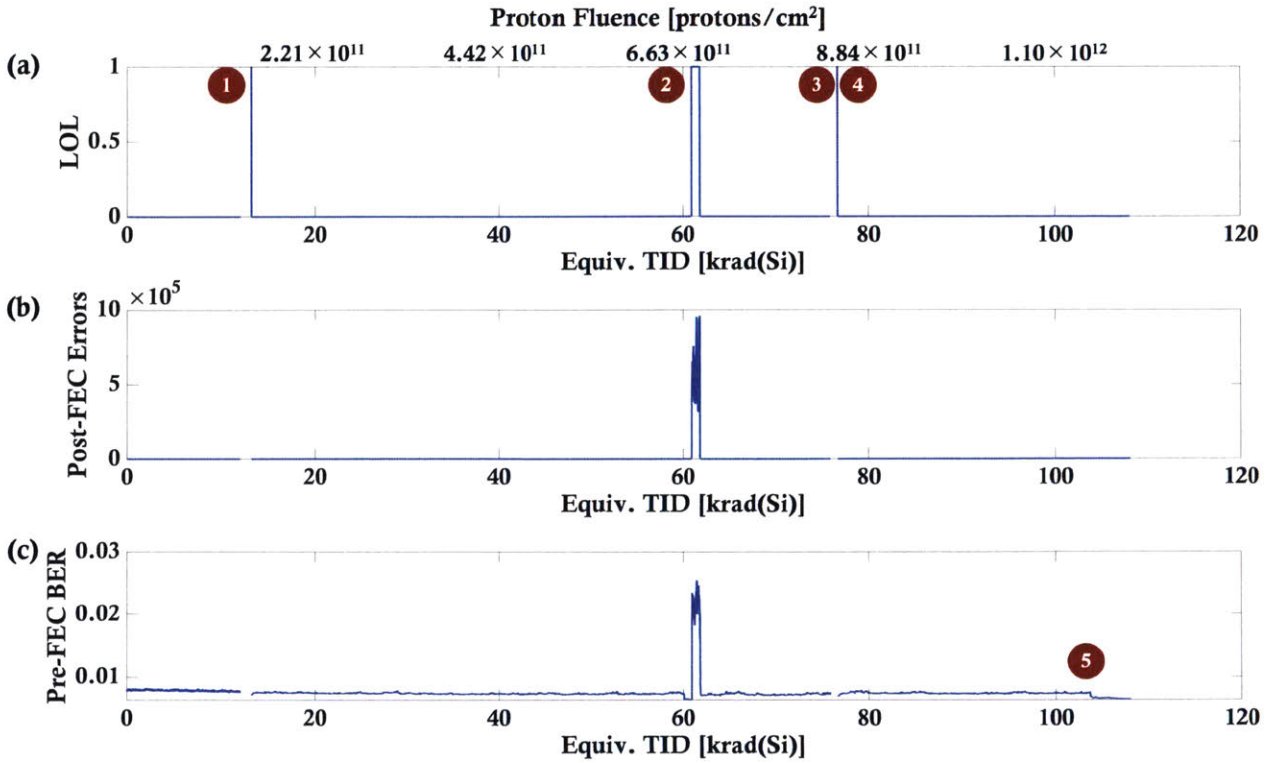

Figure 53. OMA R-EDU #1 ASIC line side performance telemetry during μICR DUT #1 proton radiation test. (a) ASIC Loss of Lock, indicated by "1", (b) ASIC line post-FEC error count, (c) ASIC line pre-FEC BER. Radiation scatter events with effects on ASIC line side performance are labeled with red circles.

4.4.3 Proton Radiation Test of Micro-Intradyne Coherent Receiver #2

μICR DUT #2 on OMA R-EDU #2 was irradiated for 3 hours, 26 minutes, and 23 seconds to a total fluence of 1.22×10^{12} p/cm^2 or equivalent TID of 110.4 krad(Si). In the test configuration, the receive path into the μICR DUT #1 on the OMA was optically noise-loaded at OSNR of 15.1 dB, which was 2.2 dB above the ROSNR for the R-EDU. The OMA ASIC pre-FEC BER was 6.0×10^{-3}. The optical input power to the μICR DUT #2 was -10.1 dBm. The receive path into the GOMA was optically noise-loaded at an OSNR of 12.5 dB, which was 2.6 dB above the ROSNR for the R-EDU. The GOMA ASIC pre-FEC BER was 6.7×10^{-3}.

The proton radiation test for μICR DUT #2 was completed with continuous irradiation (no proton beam stops). Figure 54 shows the μICR DUT #2 telemetry collected during the proton radiation test. Figure 54(a) shows the including the internal MPD optical power reading. Figure 54(b) shows the TIA gain setting values. Figure 54(c) shows the peak indicator voltages at output of μICR DUT #2. Figure 54(d) shows I term for PID controller used for TIA manual gain control mode. There were three SEEs observed on μICR DUT #2, but none of the events required a reset of the μICR. The three SEE occurrences are indicated with the yellow boxes and labeled with yellow circle "R" in Figure 54(a) and Figure 54(b). There was one radiation scatter event at equivalent TID level of ~108 krad(Si), which caused the GOMA test computer to freeze. The red line and red circle labeled "1" in Figure 54 indicate when the radiation

scatter event occurred. The radiation scatter event did not affect the μICR DUT #2 key parameters shown in Figure 54, but the event affected the OMA R-EDU ASIC pre-FEC BER.

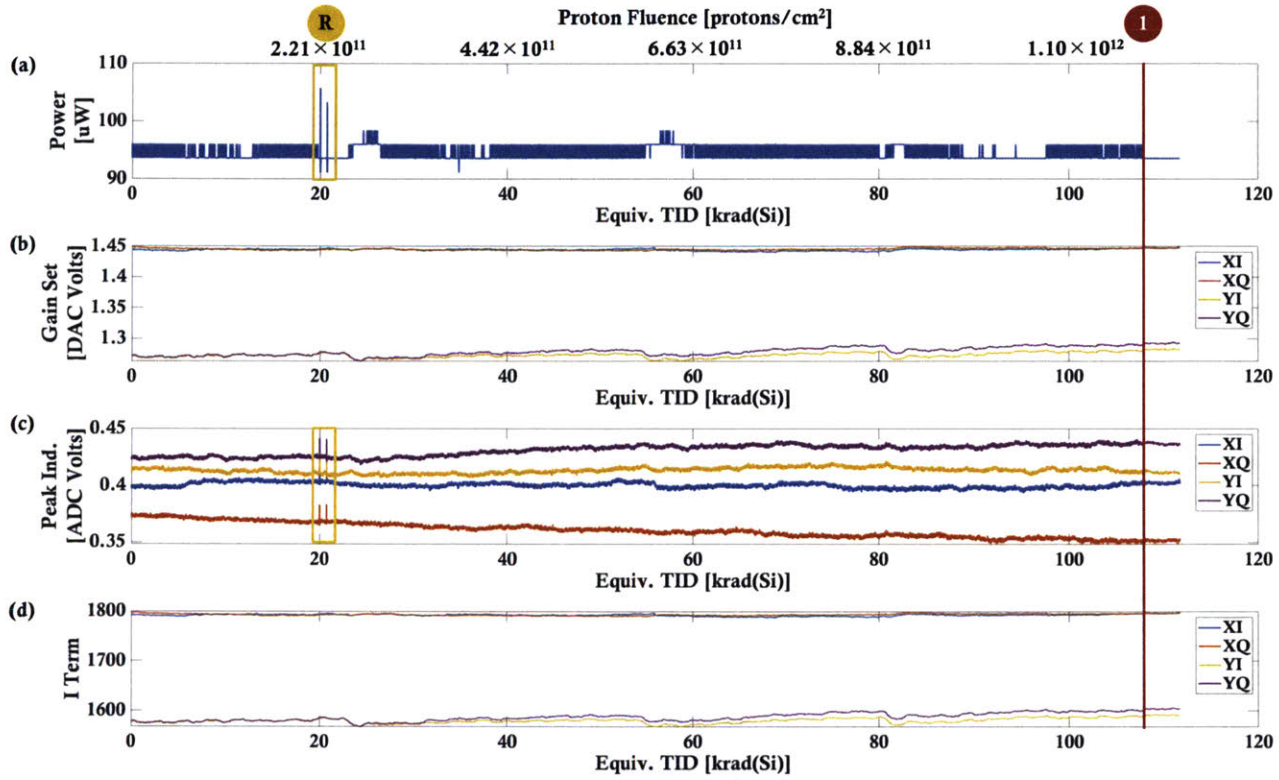

Figure 54. μICR DUT #2 telemetry from proton radiation test. (a) Internal MPD optical power reading, (b) TIA gain settings, (c) Peak indicator voltages at output of μICR, and (d) I term for PID controller used for μICR TIA manual gain control mode. Observed proton single event effects indicated with red box on MPD optical power reading (a) and peak indicator voltages (c). Observed proton single event effects indicated with yellow box and yellow circle labeled "R" on MPD optical power reading (a) and peak indicator voltages (c). Radiation scatter event indicated with red box and red numbered circle.

During the test, there was no observable gradual degradation of the μICR in the monitored parameters. Prior to radiation, the internal MPD optical power reading oscillated between values of 96.0 μWand 93.6 μW. At the end of the radiation test at ~ 110 krad(Si) TID level and 1.22×10^{12} p/cm^2 fluence level, the internal MPD optical power reading remained at 93.6 μW. The gain set voltages and peak indicator voltages for the HI, HQ, VI, VQ channels did not show any significant change in value through the radiation test. There was minimal drift in the gain set voltages and peak indicator voltages, comparable to nominal drift over time between 10 mV to 35 mV.

Figure 55 shows the μICR DUT #2 telemetry focused on the three proton SEEs observed, which are indicated with numbered yellow circles. Similar to the two SEEs observed from proton radiation testing of μICR DUT #1, three proton SEEs on DUT #2 had observable peaks in both internal MPD optical power readings and peak indicator voltages output and lasted a time period of ~ 200 ms.

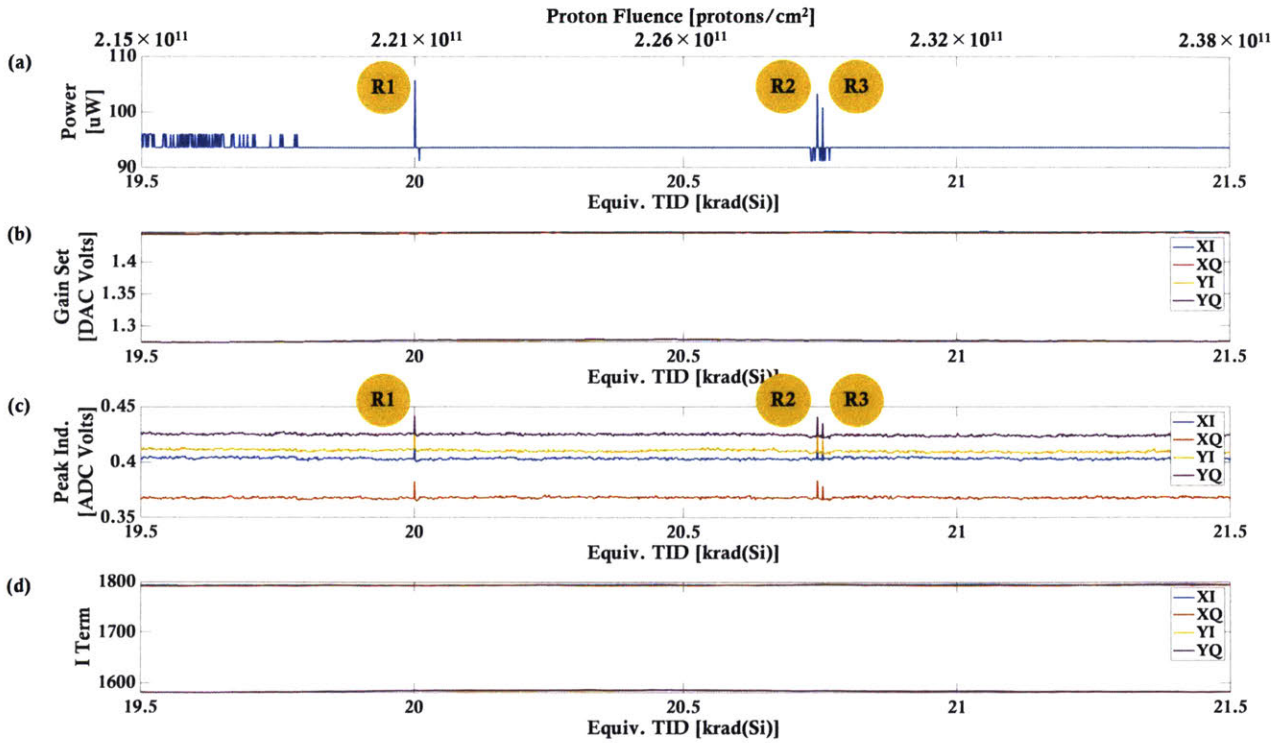

Figure 55. µICR DUT #2 telemetry from proton radiation test focused on the three proton SEEs, which are labeled with yellow numbered circles on MPD optical power reading (a) and peak indicator voltages (c). (a) Internal MPD optical power reading, (b) TIA gain settings, (c) Peak indicator voltages at output of µICR, and (d) I term for PID controller used for µICR TIA manual gain control mode.

The first SEE occurred at equivalent TID level of 20 krad or fluence of 2.21 $\times 10^{11}$ p/cm^2. The internal MPD optical power reading peaked from 93.58 µW to 105.8 µW, then returned to nominal 93.58 µW. All peak indicator voltages displayed a peak amplitude increasing between 15.3 mV and 17.7 mV then decreasing between 16.1 mV and 17.7 mV to nominal values. Figure 56 shows a zoomed in portion of the MPD power plot and peak indicator voltages plot from Figure 55 where the first SEE occurred.

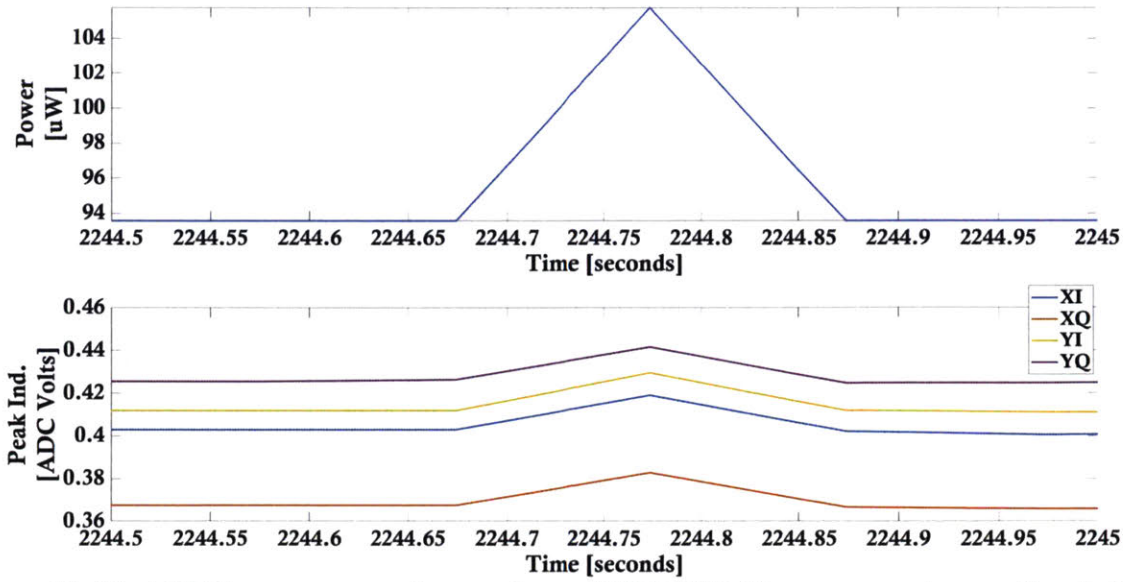

Figure 56. First SEE occurrence observed on μICR DUT #2 as momentary spikes in MPD power telemetry and peak indicator voltage telemetry over ~200 ms duration.

The second SEE occurred at equivalent TID level of 20.74 krad or fluence of 2.29 $\times 10^{11}$ p/cm^2. The internal MPD optical power reading peaked from 93.58 μW to 103.3 μW, then returned to nominal 93.58 μW. Similar to the first SEE, all peak indicator voltages in the second SEE displayed a peak amplitude increasing between 15.3 mV and 17.7 mV then decreasing between 16.1 mV and 18.5 mV to nominal values. The third SEE occurred at equivalent TID level of 20.75 krad or fluence of 2.29 $\times 10^{11}$ p/cm^2. The internal MPD optical power reading peaked from 91.14 μW to 100.9 μW, then returned to nominal 91.14 μW. For the third SEE, all peak indicator voltages displayed a peak amplitude increasing between 12.1 mV and 12.9 mV then decreasing between 12.9 mV and 13.7 mV to nominal values. Figure 57 shows a zoomed in portion of the MPD power plot and peak indicator voltages plot from Figure 55 where the first SEE occurred.

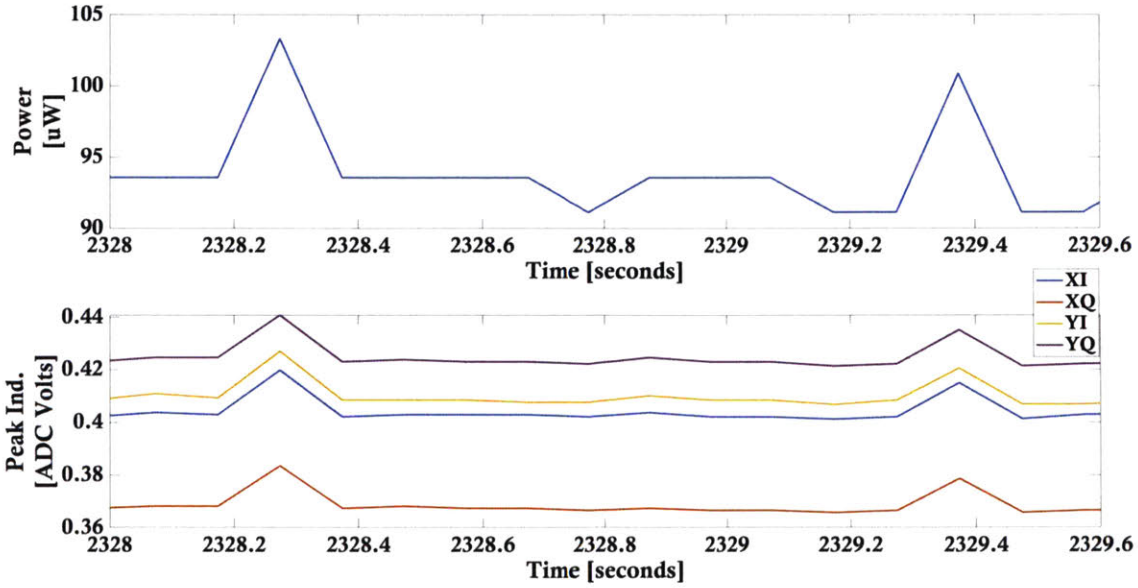

Figure 57. Second and third SEE occurrences observed on μICR DUT #2 as momentary spikes in MPD power telemetry and peak indicator voltage telemetry over ~200 ms duration.

Table 44 lists the changes to the internal MPD optical power readings and peak indicator voltages for the three SEU occurrences. No reset or power cycle of the μICR DUT was performed after each observed event, since there were no impacts to OMA system performance and the peaked telemetry parameters returned to nominal levels immediately after the observed event.

Table 44. μICR DUT #2 observed proton SEEs. Quantified changes to MPD optical power readings and peak indicator voltages.

SEE	Component		Initial Value	Peak	Post Peak	Initial-Peak Delta	Post-Peak Delta
1	MPD		93.6 μW	105.8 μW	93.6 μW	12.2 μW	- 12.2 μW
	Peak Indicator	HI	402.9 mV	419.0 mV	402.1 mV	16.1 mV	- 16.9 mV
		HQ	367.5 mV	382.8 mV	366.7 mV	15.3 mV	- 16.1 mV
		VI	411.8 mV	429.5 mV	411.8 mV	17.7 mV	- 17.7 mV
		VQ	426.3 mV	441.6 mV	424.7 mV	15.3 mV	- 16.9 mV
2	MPD		93.6 μW	103.3 μW	93.6 μW	9.7 μW	- 9.7 μW
	Peak Indicator	HI	402.9 mV	419.9 mV	402.1 mV	17 mV	- 17.8 mV
		HQ	368:3 mV	383.6 mV	367.5 mV	15.3 mV	- 16.1 mV
		VI	409.4 mV	427.1 mV	408.6 mV	17.7 mV	- 18.5 mV
		VQ	424.7 mV	440.8 mV	423.1 mV	16.1 mV	- 17.7 mV
3	MPD		91.1 μW	100.9 μW	91.1 μW	9.5 μW	- 9.8 μW
	Peak Indicator	HI	402.1 mV	415.0 mV	401.3 mV	12.9 mV	- 13.7 mV
		HQ	366.7 mV	378.8 mV	365.9 mV	12.1 mV	- 12.9 mV
		VI	408.6 mV	420.7 mV	407.0 mV	12.1 mV	- 13.7 mV
		VQ	422.3 mV	435.2 mV	421.5 mV	12.9 mV	- 13.7 mV

There were no proton SELs observed through steps in current on the VCC voltage rail. Figure 58 shows the μICR DUT #2 VCC voltage rail and current during the radiation test.

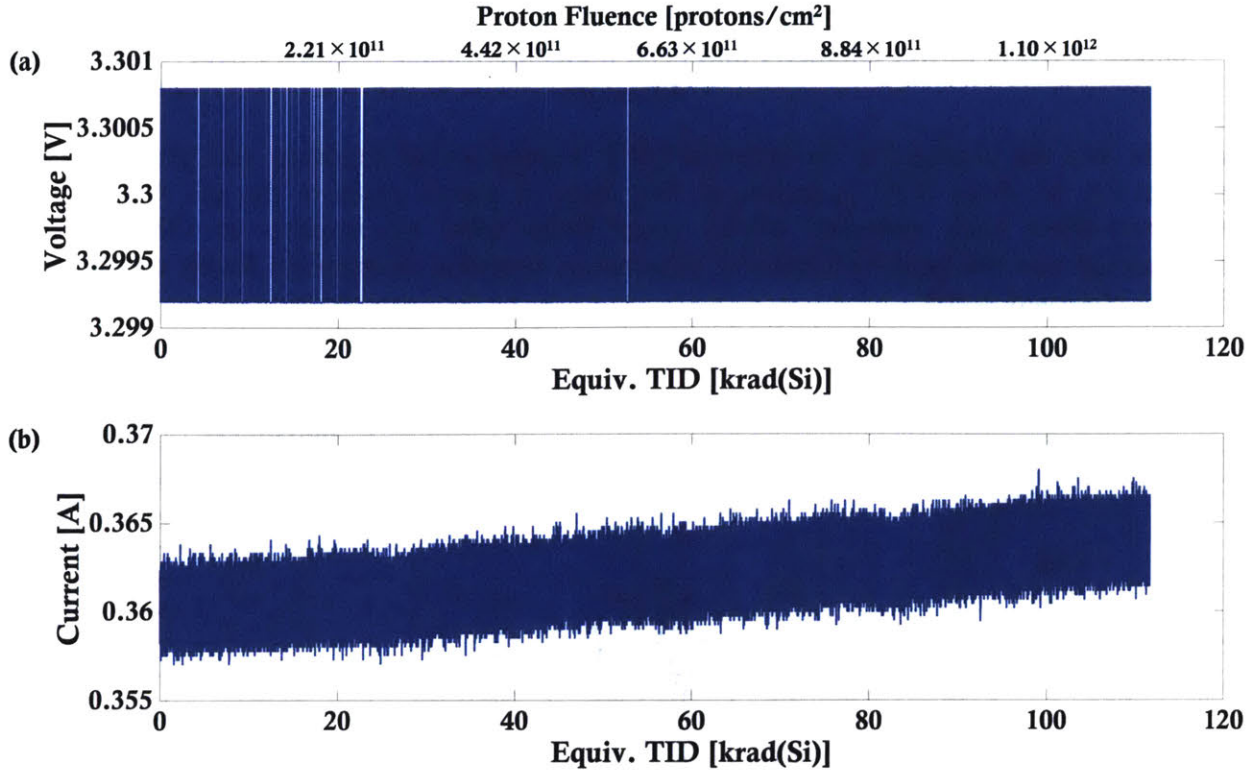

Figure 58. μICR DUT #2 proton radiation test VCC voltage rail and current.

There was no degradation to the OMA system performance observed during the μICR DUT #2 proton radiation test. No line post-FEC error bursts and no LOL were observed. The pre-FEC BER maintained a value of ~6.1×10^{-3}, without observable degradation. From the radiation scatter event at equivalent TID level of ~108 krad(Si), there was an observable drop in the ASIC pre-FEC BER from ~6.1×10^{-3} to ~4.8×10^{-3}. Note that a drop in pre-FEC BER represents better link performance, the drop in pre-FEC BER with a radiation scatter event is unexpected. The radiation scatter event did not have a significant effect to the overall OMA performance since the ASIC did not lose lock and did not have any post-FEC error bursts. Figure 59 shows the OMA line side parameters monitored during the μICR DUT #2 proton radiation test. Figure 59(a) shows the ASIC LOL monitor, with a "1" indicating LOL and "0" indicating no LOL. Figure 59(b) shows the ASIC line post-FEC error count, and Figure 59(c) shows the line pre-FEC BER. The radiation scatter event is labeled "1" with red circle in Figure 59(c).

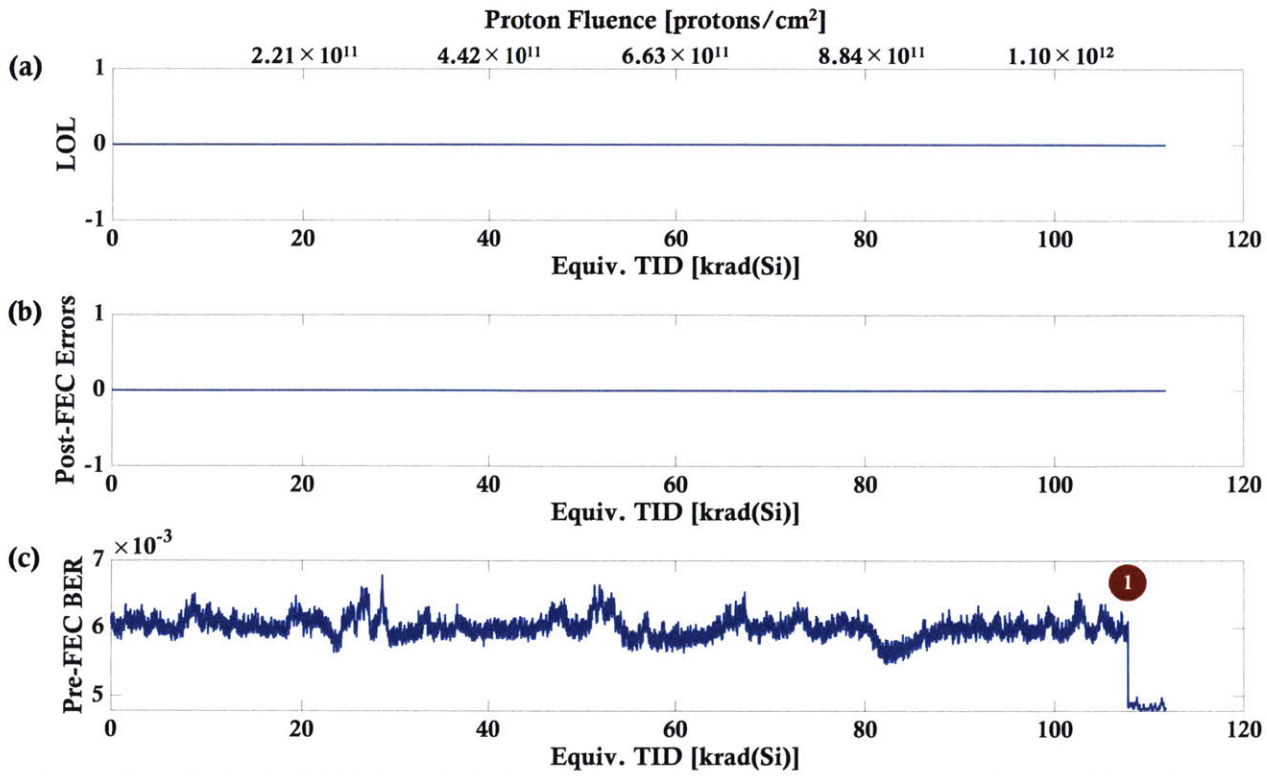

Figure 59. OMA R-EDU #2 ASIC line side performance telemetry during μICR DUT #2 proton radiation test. (a) ASIC Loss of Lock, indicated by "1", (b) ASIC line post-FEC error count, (c) ASIC line pre-FEC BER. Drop in pre-FEC BER from radiation scatter event labeled "1" with red circle in Figure 59(c).

4.4.4 Summary and Proton SEE Rate Calculations

Two commercial μICRs, integrated in OMA R-EDUs, were tested with 105 MeV protons to fluence level of 1.22×10^{12} p/cm^2 or equivalent TID of 110.4 krad(Si). Both μICRs survived radiation testing without degradation to the component performance or OMA system performance. No proton SELs were observed on the μICR TIA supply current. For both μICRs, proton SEEs were observed through spikes in the MPD and peak indicator voltage telemetry, which could indicate these events as SETs. No reset or power cycle of the μICR DUT was performed after each observed event, since there were no impacts to OMA system performance and the peaked telemetry parameters returned to nominal levels after ~ 200 ms. There were two proton SEEs observed during μICR DUT #1 testing, and there were three proton SEEs observed during μICR DUT #2 testing. Radiation scatter events on test equipment were observed, impacting the test setup and collected telemetry.

Table 45 summarizes the proton radiation test campaign data for the two μICRs tested and the resulting 105 MeV proton SEE cross section. The μICR joint SEE cross section was used to calculate the μICR proton SEE rate for the Telesat polar and Telesat inclined orbits.

Table 45. Proton SEE data from μICR 105 MeV proton test campaign

μICR	SEE Count	Total Fluence	Joint SEE Cross Section
DUT #1	2	1.22×10^{12} p/cm^2	2.05×10^{-12}
DUT #2	3	1.22×10^{12} p/cm^2	

CREME96 software was used to calculate the μICR proton SEE rate for the Telesat polar orbit (Table 46) and Telesat inclined orbit (Table 47). Appendix A4 describes the method and model details used for calculating the SEE rates with CREME96.

Table 46. Micro-intradyne coherent receiver proton SEE rate for Telesat polar orbit

μICR SEE Rate	Nominal	Flare		
		Worst Week	Worst Day	Peak 5 Minutes
[/Device/Second]	5.57×10^{-10}	2.16×10^{-9}	8.39×10^{-9}	3.05×10^{-8}
[/Device/Day]	4.81×10^{-5}	1.87×10^{-4}	7.25×10^{-4}	2.64×10^{-3}
[/Device/Year]	1.76×10^{-2}	6.82×10^{-2}	2.65×10^{-1}	9.63×10^{-1}

Table 47. Micro-intradyne coherent receiver proton SEE rate for Telesat inclined orbit

μICR SEE Rate	Nominal	Flare		
		Worst Week	Worst Day	Peak 5 Minutes
[/Device/Second]	2.58×10^{-9}	1.08×10^{-13}	1.24×10^{-13}	5.50×10^{-13}
[/Device/Day]	2.22×10^{-4}	9.36×10^{-9}	1.07×10^{-8}	4.75×10^{-8}
[/Device/Year]	0.08	3.42×10^{-6}	3.90×10^{-6}	1.73×10^{-5}

For the Telesat polar orbit and Telesat inclined orbit nominal and solar flare cases, the calculated μICR proton SEE rates are low – the expected proton SEE rates are less than 1 SEE per μICR per year. The observed μICR proton SEEs do not have impact to the optical coherent modem system performance and do not require any resets or power cycles. Thus, the proton SEE rates will not cause any potential OISL "down time" or have any impact to the OISL system availability.

Future work for the commercial μICR could include a heavy ion radiation assessment to observe for (1) heavy ion SETs to the DPOH PLC chip with doped silica glass and (2) heavy ion SEL to the dual TIAs with SiGe BiCMOS technology.

Chapter 5

Commercial Optical Coherent Transmitter

The coherent transmitter interfaces with the coherent DSP ASIC in an optical coherent modem as shown in Figure 60. A coherent transmitter has a single optical signal input via polarization maintained (PM) fiber and outputs a modulated optical signal. A RF driver uses the four differential RF signals from the optical coherent ASIC high speed DAC as the data source to modulate the optical signal. The coherent transmitter consists of a modulator and modulator driver.

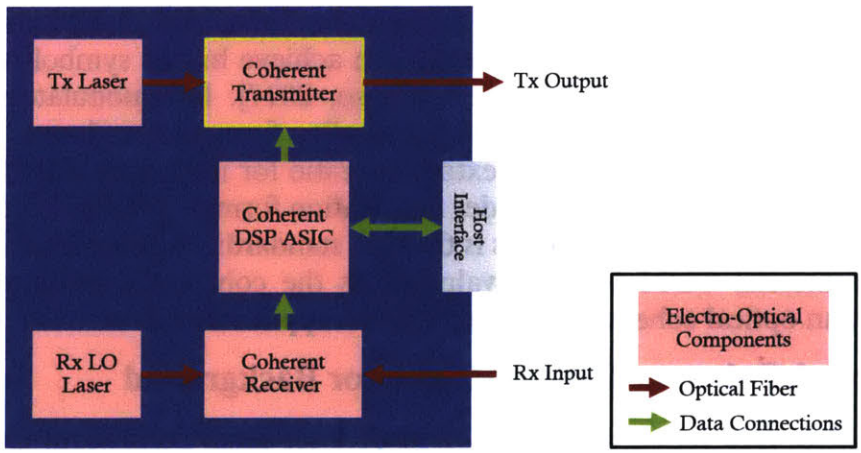

Figure 60. Optical coherent modem functional block diagram with coherent transmitter highlighted.

Commercial coherent IQ modulators have been developed with silica or polymer PLCs, co-packaged with lithium niobite ($LiNbO_3$), InP, and silicon photonics (SiPho) [Dong et al., 2014; Yamazaki et al., 2008; Way, 2016]. Each material uses different properties to modulate light in Mach-Zehnder interferometers (MZIs) – $LiNbO_3$ modulators use the electro-optic effect, InP modulators use the Stark effect (shifting and splitting of spectral lines of atoms and molecules due the presence of an external electric field), and silicon modulators use carrier depletion. The fundamental limit for all modulators is based on the product of the active electrode length (L) and the half-wave voltage (v_π), which is the voltage required for inducing a phase change of π or inducing maximum to minimum output of the modulator. Lower v_π

requires a large L and yields higher optical loss and extinction ratio, but the modulator has lower power consumption. $LiNbO_3$ modulators require a long length MZI, preventing these modulators from fitting into smaller optical coherent pluggable modules such as the CFP2-ACO. InP modulators can fit into smaller packages than $LiNbO_3$ modulators but have higher power consumption due to the thermo-electric cooler required to stabilize operations. SiPho modulators have a smaller chip sizes than the other two types of modulators, but have a high optical input to output coupling, low v_π, and low extinction ratio. SiPho modulators require using a booster EDFA as well as multiple variable optical attenuators (VOAs) or a DSP to compensate for the low extinction ratio [Way, 2016].

$LiNbO_3$ modulators have been the extensively used for 100G systems over the last few years. Space environment assessments of commercial $LiNbO_3$ modulators can be found in Ott et al. (2002), Thomes et al. (2007), and Kernec et al. (2010). iXblue currently offers space-grade $LiNbO_3$ modulators, qualified by gamma radiation, proton radiation, vibration, shock, thermal vacuum, damp heat operation, temperature cycling, ESD, hermeticity, outgassing, and destructive physical analysis tests. iXblue space-grade modulators have flight heritage, flown on GEO missions Sentinel 1a and Sentinel 2a as part of the Tesat OISL LCT as well as flown on the GRACE Follow-On mission (2017, LEO sun-synchronous orbit) for laser cavity stabilization application [iXblue, 2016].

InP modulators have been viewed as the promising solution for next generation and high capacity systems. Material properties of $LiNbO_3$, such as the dielectric constant, limit bandwidth extension and v_π reduction required for higher modulation formats. $LiNbO_3$ modulators are well developed for 32 and 64 Gbaud systems with 3 dB bandwidth of ~35 GHz and v_π of ~ 3.5 V, while InP modulators can achieve higher symbol rates with 3 dB bandwidth of ~40 GHz and v_π of < 2.0 V [Ogiso, 2017]. InP modulators have several advantages over $LiNbO_3$ modulators, such as smaller form factor, lower drive voltages yielding lower power dissipation, higher extinction ratio for improved OSNR performance, and higher bandwidth to enable higher order modulation formats [Wang, 2015]. The state of the art for InP-based coherent transmitters is the OIF standardized coherent driver modulator (CDM). A commercial CDM will be evaluated as the coherent transmitter solution for development of an optical coherent modem for OISL applications.

5.1 Commercial Coherent Driver Modulator Background

In November 2018, OIF released IA OIF-CDM-01.0 for High Bandwidth Coherent Driver Modulator, which is the most recent standardized coherent transmitter. The key innovation of CDMs is the integration of the modulator driver with the modulator in a smaller package than previous PM-Q modulators. The CDM currently has the smallest form factor of commercial modulators with maximum dimensions of 30 mm by 12 mm by 5.5 mm, allowing integration of CDMs in CFP2-ACO modules. The modulators can support 100 Gbps with 32 Gbaud symbol rate and 400 to 600 Gbps with 64 Gbaud symbol rate. Figure 61 shows the mechanical configuration for the CDM [OIF, OIF-CDM-01.0, 2018].

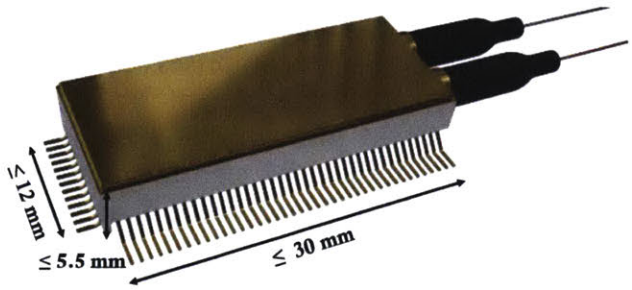

Figure 61. Mechanical configuration for the coherent driver modulator [OIF, OIF-CDM-01.0, 2018].

In 2017, Neophotonics was the first to commercially release a 64-GBaud, polarization multiplexed, quadrature CDM, which combined a quad-channel differential 64-Gbaud driver with an InP based MZ quadrature modulator chip in a 3.9 mm by 27 mm by 13 mm package [Neophotonics, 2017]. The quad driver amplifies and biases the four RF differential signal pairs (XI, XQ, YI, YQ), which are input to the quadrature modulators from a coherent DSP ASIC high speed DAC. Table 48 displays key parameters of the Neophotonics and Lumentum CDMs, based on limited publicly available data [Neophotonics, 2019; Lumentum, 2019].

Table 48. Commercial coherent driver modulators and key parameters

Vendor – Part	3dB EO Bandwidth	Power Consumption
Neophotonics 64 GBaud HB-CDM	> 40 GHz	4.5 W
Lumentum 64 GBaud HB-CDM	35 GHz	-

5.1.1 Functionality and Sub-Components of Commercial Coherent Driver Modulators

The sub-components of the commercial CDM are divided into five main groups: (1) RF driver integrated circuit (IC), (2) InP modulator chip, (3) TEC, (4) MPD, and (5) coupling optics. Figure 62 displays a functional diagram of a CDM based on IA OIF-CDM-01.0 and labels the five major components within a CDM.

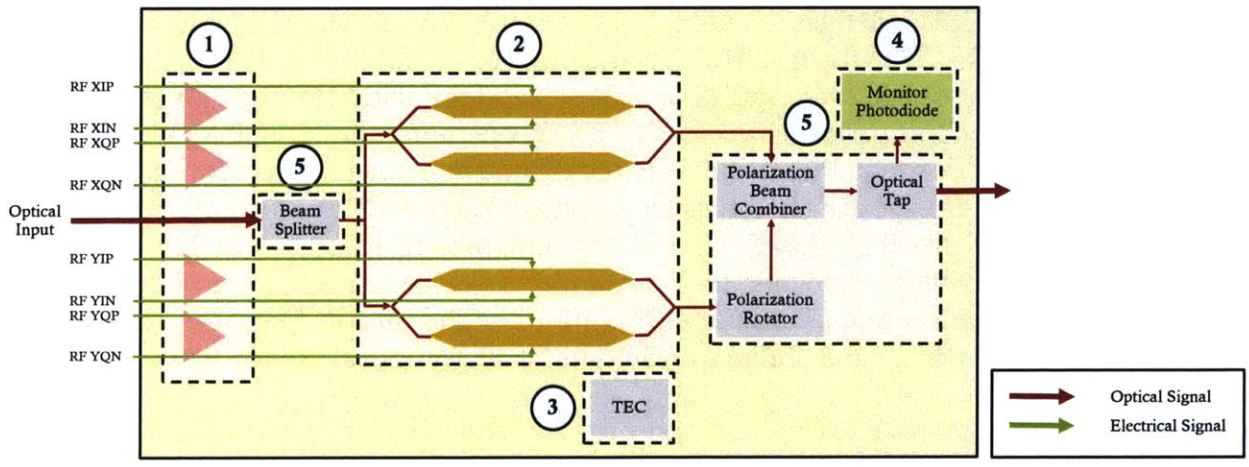

Figure 62. Functional block diagram of coherent driver modulator [OIF-CDM-01.0].

An optical signal via polarization maintained (PM) fiber and four differential RF modulation signals (differential voltages) from the optical coherent ASIC high speed DAC are inputs to

the CDM. The input optical signal is divided into two signals with the optical beam splitter. Each of the optical signals enters a quadrature modulator, one for X polarization and one for Y polarization. Each quadrature modulator comprises two Mach-Zehnder modulators (MZMs), a child MZM with two arms and a parent MZM. The four differential RF modulation signals are input to the CDM through the CDM RF driver integrated circuit, where the signals are amplified. The amplified RF signals are input to the child MZM arms to encode the in-phase (I) and quadrature (Q) data for the X and Y polarizations.

Substrate bias voltages are applied to the MZMs and are used to control V_{π}. Phase adjusters, such as on-chip heating resistors, adjust the modulator phase setting points for the child and parent arms of the MZMs. An external circuit to the CDM is used for automatic bias control (ABC) of MZMs. Substrate bias voltages shift due to DC-drift and drifting bias conditions can significantly degrade transmission performance [Li et al., 2017]. The external control is used to adjust the substrate bias voltages and control phase adjusters. For QPSK signals (100G applications), monitoring the bias conditions is more complex compared to other classical modulation formats since the averaged optical power is not affected by bias voltage shift or optical phase shift. Approaches for monitoring and controlling QPSK modulator bias conditions include using backward light, RF power spectrum, information of peak to average power ratio, differential phasor monitor, and asymmetric bias dithering [Kawakami et al., 2012]. CDM vendors have developed proprietary ABC algorithms and circuits. The external circuit is commercially sold with CDMs. The CDM includes a thermo-electric cooler (TEC) to control the internal temperature, which can affect the phase control.

The output optical signal from one of the quadrature modulators is input to a polarization rotator to shift the phase by 90 degrees. This optical signal is combined with the optical signal output of the other quadrature modulator into a polarization beam combiner. A portion of the combined optical signal is tapped and input to an MPD, which can be used as feedback for modulation bias control. A 100G QPSK modulated optical signal is the final output of the CDM [OIF (IA # OIF-CDM-01.0), 2018].

5.1.2 Electrical Interface of Commercial Coherent Driver Modulators

The OIF IA for HB-CDMs defines a standard pin-out for low speed electrical interface (Figure 63) [OIF, (IA # OIF-CDM-01.0), 2018]. Evaluating the standardized pin-out for the HB-CDM allows us to design the optical coherent modem with features for monitoring component telemetry and performance as well as for operating the HB-CDM in a strategic manner for space application. Pins 4 and 5 are the ground and power supply for the RF driver IC and pin 11 provides the RF driver far end voltage bias. A SPI bus interface is used to control the CDM RF driver IC. For the InP MZM chip, pins 12-15 can be used to control the MZM substrate bias voltages and pins 16-27 can be used for MZM phase control. Pins 30 and 31 supply the TEC power and pins 28 and 29 control the thermistor. Pins 33-37 provide the bias voltage for the MPD(s) and ability to read out the detect optical power on the MPD(s).

Pin DC#	Signal Name	Description	Pin DC#	Signal Name	Description
1	VSA1	VSA / pre-SOA 3, 4 Anode (current)	21	PHASE3N	MZ Phase control or VSA
2	VSA2	VSA / pre-SOA 1, 2 Anode (current)	22	PHASE4P	MZ Phase control
3	VSA3	VSA / Pilot (voltage)	23	PHASE4N	MZ Phase control or VSA
4	GND	Ground	24	PHASE5P	MZ Phase control
5	VCC	3.3V supply	25	PHASE5N	MZ Phase control or VSA
6	SPI-RST	SPI Reset	26	PHASE6P	MZ Phase control
7	SPI-MISO	SPI MasterInSerialOut	27	PHASE6N	MZ Phase control or VSA
8	SPI-MOSI	SPI MasterOutSerialIn	28	THERMP	Thermistor +
9	SPI-CLK	SPI Clock	29	THERMN	Thermistor -
10	SPI-CS	SPI ChipSelect	30	TECN	TEC power -
11	VDR-BIAS	Driver far end bias	31	TECP	TEC power +
12	VSUB1	MZ substrate bias (voltage)	32	GND	Ground
13	VSA4	VSA / MZ substrate bias2	33	MPD-A3	Monitor PD Anode 3 or VSA
14	VSA5	VSA / MZ substrate bias3	34	MPD-C3	Monitor PD Cathode 3 or VSA
15	VSA6	VSA / MZ substrate bias4 (or GND)	35	MPD-A1	Monitor PD Anode 1 or VSA
16	PHASE1P	MZ Phase control	36	MPD-A2	Monitor PD Anode 2 or VSA
17	PHASE1N	MZ Phase control or VSA	37	MPD-C12	Monitor PD Cathode 1 and 2 or VSA
18	PHASE2P	MZ Phase control	38	VSA7	VSA / post SOA 1, 2 Anode (current)
19	PHASE2N	MZ Phase control or VSA	39	VSA8	VSA / post SOA 3 ,4 Anode (current)
20	PHASE3P	MZ Phase control	40	VSA9	VSA / post SOA Cathode (current)

Figure 63. High Bandwidth Coherent Driver Modulator low speed electrical interface defined by OIF, IA # OIF-CDM-01.0) [2018].

Section 5.3 provides details on modifications for the HB-CDM in the optical coherent modem design. Features provided through the pin-out, such as reading substrate bias voltages to determine radiation-induced degradation to the HB-CDM modulator chip, are key for designing for space application.

5.2 Radiation Susceptibility of Commercial Coherent Driver Modulator

The five main groups of sub-components of a commercial CDM are susceptible to radiation based on the types of technologies and materials used for each sub-component. The specific technology processes and materials of the sub-components are proprietary to the CDM vendors. Background research is used to infer the radiation susceptibility of each of the main sub-components.

We expect the RF driver IC to be based on SiGe BiCMOS technology. Lopez et al. [2015] proposed a hybrid optical transmitter architecture with integrated IHP 130 nm SiGe BiCMOS linear driver and InP segmented MZM for optical coherent systems with high order modulation formats. Milivojevic et al. [2016] demonstrated an optical transmitter packaged with linear BiCMOS MZM-driver and InP MZM in an optical coherent polarization multiplexed 100G system. As described in Section 4.2, commercial ICRs have SiGe BiCMOS TIAs, and SiGe BiCMOS technology is susceptible to SEEs and TID effects [Cressler, 2013; Lourenco et al., 2013].

The MZM modulator chip for CDMs is InP-based technology [Neophotonics, 2017]. InP-based MZMs are the leading candidates for miniaturized modulators due to the small chip size, low driving voltage, and ability for monolithic integration with semiconductor devices

[Kohtoku, 2015]. We expect the chip to contain integrated diodes used for applying substrate bias voltages and resistors used for phase adjustment. InP materials and diodes are susceptible to displacement damage effects. Seki et al. [2015] can be referenced for images showing the top view and cross sectional diagram of an InP-based modulator section.

Indium phosphide is a III-V material, and III-V semiconductor devices are primarily susceptible to displacement damage effects and single event upsets [Weaver et al., 2003]. There have been limited published radiation assessment studies of InP based PICs. However, there have been numerous studies on radiation effects on other InP devices, such as solar cells, high electron mobility transistor (HEMTs), heterojunction bipolar transistor (HBTs) [Brandhorst, 1989; Walters, 1994; Messenger, 1996] . InP solar cells were observed to be more radiation resistant to 1 MeV electron irradiation in comparison to GaAs and Si solar cells [Weinberg et al., 1987]. InP solar cells have been observed to have a hardness of one order of magnitude higher than GaAs solar cells for electron and total dose radiation, and InP heterostructure devices, such as HEMTs and HBTs, are expected to be an order of magnitude harder than GaAs structures for total dose [Vu and Yaung, 1989]. A radiation hard space power system was developed by the US Navy using InP solar cells grown on Si substrates [Walters et al., 1998]. Overall, radiation studies of InP based devices conclude greater radiation tolerance of InP in comparison to other III-V based devices. Based on evaluating radiation tests of PIC building block components in silicon and InP, a study by the NASA Electronic parts and Packaging (NEPP) program concluded performance of integrated optics devices will not be affected by harsh radiation environments expected in space missions, if appropriate measures are taken to control for temperature fluctuations. [Alt, 2016].

Similar to commercial μICRs, we expect the internal MPD to be InGaAs-based and the passive coupling optics to be commercial glass materials. The MPD will be susceptible to DDD and the coupling optics will be susceptible to TID effects, such as glass darkening. The CDMs samples, which were provided for proton testing, did not have fully functional MPDs.

TECs within optical modules typically comprise two kinds of materials, such as ceramics or metals. An input DC current to the TEC is used to transfer heat from one side of the device to the other to control temperature of the CDM. The input current is provided through a TEC control circuit with an external microcontroller. The TEC control loop uses information from a thermistor internal to the CDM to set the TEC current level based on set temperature requirements [Maxim Integrated Products, Inc., 2015]. The external microcontroller for TEC control will be susceptible to SEEs. External ABC circuits for CDMs will contain a commercial microcontroller and other commercial electronic components, which are susceptible to SEEs. Table 49 outlines the technology process and materials and radiation susceptibility for the four main sub-components of a commercial μICR.

Table 49. Radiation susceptibility of commercial high bandwidth coherent driver modulator based on technology of sub-components

Sub-Components	Technology/Material	Radiation Susceptibility
1. RF Driver IC	SiGe BiCMOS	Single Event Effects Total Ionizing Dose
2. Modulator Chip	InP-based Chip	Single Event Effects Displacement Damage Dose

3.Thermoelectric-Cooler (TEC)	Ceramic / metal alloy exchange surface plates	-
4.Monitor Photodiode	InGaAs	Displacement Damage Dose
5. Coupling Optics	Commercial Glasses	Total Ionizing Dose

The radiation hardness assurance performance of InP based MZMs were investigated by Gajanana et al. [2013]. The devices under test (DUTs) were Oclaro MZMs in bar form, based on active-P MQW on N-doped InP substrate technology. The DUTs were irradiated with 24 GeV proton radiation in the IRRAD-1 facility at CERN and biased to operating conditions during irradiation. The study had limited experiment results due to problems with transporting the sample and only one sample could be measured after irradiation. The modulation response is almost absent for the 10^{15} protons/cm^2 irradiated sample. Outside of work by Gajanana et al. [2013], there are no other published studies on radiation testing of commercial InP based MZMs.

5.3 Proposed Modifications to Commercial High Bandwidth Coherent Driver Modulator

Commercial electronic components, such as op-amps, Analog to Digital Converters (ADCs), Digital to Analog Converters (DACs), and microcontrollers, which are used for CDM automatic bias control (ABC) control and TEC control, may be radiation-sensitive. Either radiation-hardened (space-grade) versions of these components would be used to design the TEC control and ABC circuits, or radiation-tolerant commercial components would need to be identified through radiation test campaigns. References to commercial op-amps, ADCs, DACs, and microcontrollers, which could have potential for space applications, are discussed in the next few paragraphs. Completing radiation assessments and test campaigns for commercial electronic components is outside the scope of this work.

Renesas offers a product line of radiation-hardened op-amps (ISL70XXXSEH, ISL71XXXSEH) and radiation tolerant op-amps (ISL71218M, ISL71444M). The Renesas radiation-hardened op-amps are qualified for NASA low outgassing specifications, operating temperature range between -55°C to +125°C, LET threshold of 86 MeV·cm^2/mg, SEL immunity, TID levels up to 300 krad(Si), ELDRS TID levels up to 100 krad(Si), and less than 5 microsecond recovery from SEEs [Renesas, 2019]. The Renesas radiation tolerant op-amps are qualified for NASA low outgassing specifications, operating temperature range between -55°C to +125°C, and LET threshold of 43 MeV·cm^2/mg [Renesas, 2019]. JPL has published compendiums of SEL and TID test results of commercial ADCs and DACs with 8-bit to 24-bit resolution [Irom and Agarwal, 2012; Irom and Agarwal 2015]. Commercial ADCs and DACs listed in these compendiums could be implemented in the CDM TEC control and ABC circuits.

The OMA R-EDU was designed with a commercial system on chip (SoC), Xilinx Zynq. The Zynq serves as a more radiation tolerant solution compared to the commercial microcontroller, which is typically used for CDM TEC control and ABC control. The FPGA in the Xilinx Zynq SoC was used to implement a PID controller for CDM ABC and TEC control. Optimized control loop and software development are not within the scope of this

work. This work focuses on the system level implementation of ABC and TEC control of the CDM.

The CDM ABC circuit was based on a modulation-format-free dither-correlation detection method by Li et al. [2017]. This method uses a low bandwidth photodetector to detect a small portion of the optical signal from the output of the modulator. A low speed (25 kHz) ADC samples the output signal of the photodetector. Two sine waves with frequencies of 3.9 kHz and 4.9 kHz, respectively, are generated and applied to dither the bias signal of the two child MZMs. ADCs sample the two dither signals for signal processing. The ADCs provide input to the microprocessor, which monitors both the average optical signal power and the correlation integration of the transmitter dither signals and detected dither signals for ABC. The dither correlation detection is used to adjust the bias voltages of the modulator [Li et al., 2017]. Further details of the method can be found in Li et al. [2017].

Figure 64 shows a functional block diagram of the CDM ABC circuit implemented for the OMA EDU. Similar to the Li et al. [2017] method, the output optical signal from the CDM is input to a tap photodiode. The commercial CDM contains an internal tap photodiode, but initial samples received for this work do not have fully functional internal tap photodiodes. The OMA R-EDUs were designed with external tap photodiodes for CDM ABC. The tap photodiode converts a portion of the detected optical signal into current levels, which is input to a TIA. The TIA converts the current into voltage, which is input to an ADC. The ADC output is input to the Xilinx Zynq SoC through SPI. In an alternate approach from the Li et al. [2017] method, we use the Xilinx Zynq SoC to generate the two dither signals (sine waves) and to minimize the values of the parent and child cross correlation values with a PID controller in the FPGA. The detailed development of the PID controller and software are not in the scope of this work. The PID controller outputs DAC counts, which are converted into the bias voltages and input to phase adjusters of the CDM.

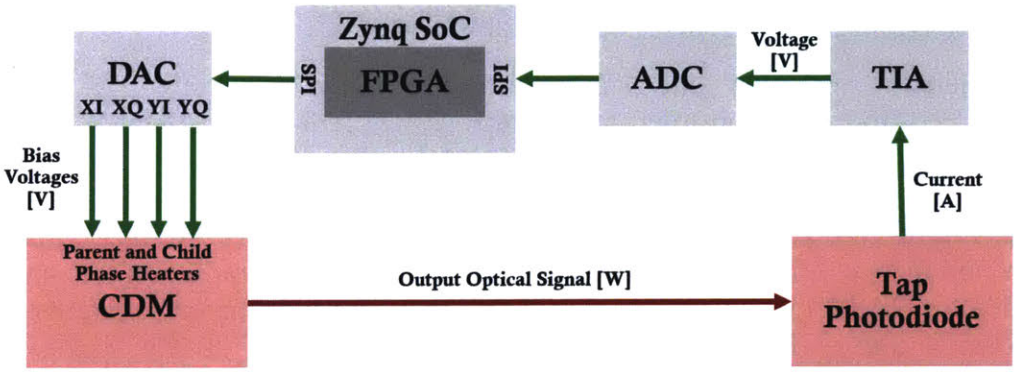

Figure 64. Functional Block Diagram of CDM Automatic Bias Control Loop

Figure 65 shows a functional block diagram of the CDM TEC control loop. A PID controller is implemented within a TEC control analog circuit. The Zynq SoC provides the CDM internal temperature setpoint 50°C, which is output as a voltage from a DAC and input the TEC control analog circuit. The TEC control analog circuit uses the internal temperature setpoint input from the Zynq and the internal temperature sensor reading from the CDM as feedback for a PID controller. The TEC control analog circuit PID controller outputs current to control the CDM TEC.

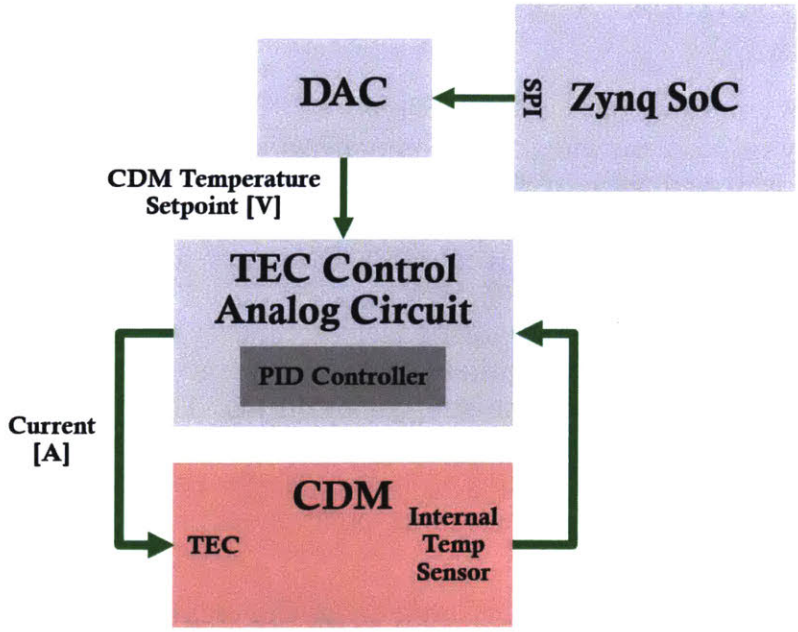

Figure 65. Functional Block Diagram of CDM TEC Control Loop

The OMA R-EDU was designed with a software feature implemented through the Zynq SoC to check static read registers and read–write registers against a register data file in Zynq memory, throw an error message if an anomalous register value was detected, and correct any anomalous read-write register values. The sampling rate for the register check software was 100 Hz.

The OMA R-EDU was designed to monitor CDM telemetry for observing radiation degradation on a component level and OMA system level. On a component level, degradation to the CDM modulator chip would be observed through changes in the substrate bias voltages, equalizer X and Y polarization anode voltages, child phase adjuster voltages, and parent phase adjuster voltages. Changes to these voltage values will show an attempt of the ABC circuit to compensate for drift in bias and shift in phase control with radiation-induced degradation to the InP-based modulator chip. Degradation to the CDM optical output would be observed through reduced optical power detected by the external tap photodiode at the output of the CDM. The VCC supply current and the VDR driver far end bias current were monitored for proton SEL. The CDM temperature was monitored through TEC power and internal thermistor telemetry. On an OMA system level, degradation to the CDM performance would be observed through reduced GOMA ASIC line-side performance: post-FEC errors, increased pre-FEC BER, and LOL. The line-side performance parameters, current on all voltage rails, and temperature were monitored on the GOMA ASIC.

For radiation testing of the CDMs, the OMA R-EDUs (described in Chapter 3.6.1) were designed with CDM SPI reset capability, CDM power cycle, ASIC reset capability, ASIC power cycle, and OMA R-EDU power cycle.

5.4 Proton Radiation Assessments of Commercial Coherent Driver Modulators

Proton radiation test campaigns of commercial CDMs were completed to evaluate the radiation sensitivity of these integrated components to DDD, TID, and SEEs. Proton radiation testing was completed at the TRIUMF particle accelerator center in Vancouver, Canada. Two identical commercial CDMs were each irradiated to proton fluence levels of 1.2×10^{12} p/cm^2 or equivalent TID of 110 krad(Si). The proton fluence level is two times higher than the expected DDD levels for 105 MeV protons on InP-based devices with 200 mils aluminum shielding in the Telesat radiation environment. Appendix Section A6 can be referenced for details on 105 MeV proton equivalent fluence for DDD on InP-based and InGaAs-based devices in the Telesat mission environments. The equivalent TID level of 110 krad(Si) is greater than the 100 krad(Si) TID level requirement for the optical coherent modem (requirement L0-09 in Table 16). Testing at these higher levels provides margin to the DDD and TID requirements and extends the application of these commercial parts to more intense radiation environments.

5.4.1 Proton Radiation Test Setup for Commercial Coherent Driver Modulators

The CDMs on OMA R-EDUs were tested in the noise-loaded optical loopback test configuration described in Chapter 3.6.1. Similar to proton radiation testing of the commercial μICRs, the commercial CDM test configuration was adjusted 2.0 dB to 2.5 dB from the ROSNR of the commercial optical coherent DSP ASICs.

The CDMs were irradiated from backside of the component and through the OMA R-EDU PCB. The OMA was mounted to the radiation test stand with the CDM DUT centered with the proton beam collimator using laser alignment. The dimensions of the CDM are 25 mm by 12 mm, and the proton beam collimator dimensions are 30 mm by 30 mm. The EDUs were designed with a "keep-out area" dimension of 20 mm by 20 mm from the outer edge of the CDM. The keep out area contains no peripheral, supporting electronic components and provides clearance for peripheral components on the EDU away from direct proton beam irradiation during testing. Figure 66 shows the test setup for proton radiation testing of the CDMs. Figure 66(a) and Figure 66(b) show an OMA R-EDU mounted on the radiation test stand for back-side irradiation of the CDM through the PCB. The CDM DUT was aligned to the center of the proton beam collimator using laser alignment. The yellow box in Figure 66(a) indicates the μICR DUT on the OMA R-EDU and the yellow arrow in Figure 66 (b) indicates the proton beam path to the back-side CDM area on the PCB. All supporting equipment, such as the GOMA, test computers, power supplies, and optical-noise loading equipment, were placed on a cart near the OMA R-EDU on the radiation test stand shown in Figure 66(c). The cart was positioned at an angle away from the direct proton beam path, and polyethylene degrader and cement blocks were used to shield the equipment from radiation scatter. Figure 66(d) shows the full test radiation test setup in the radiation chamber room.

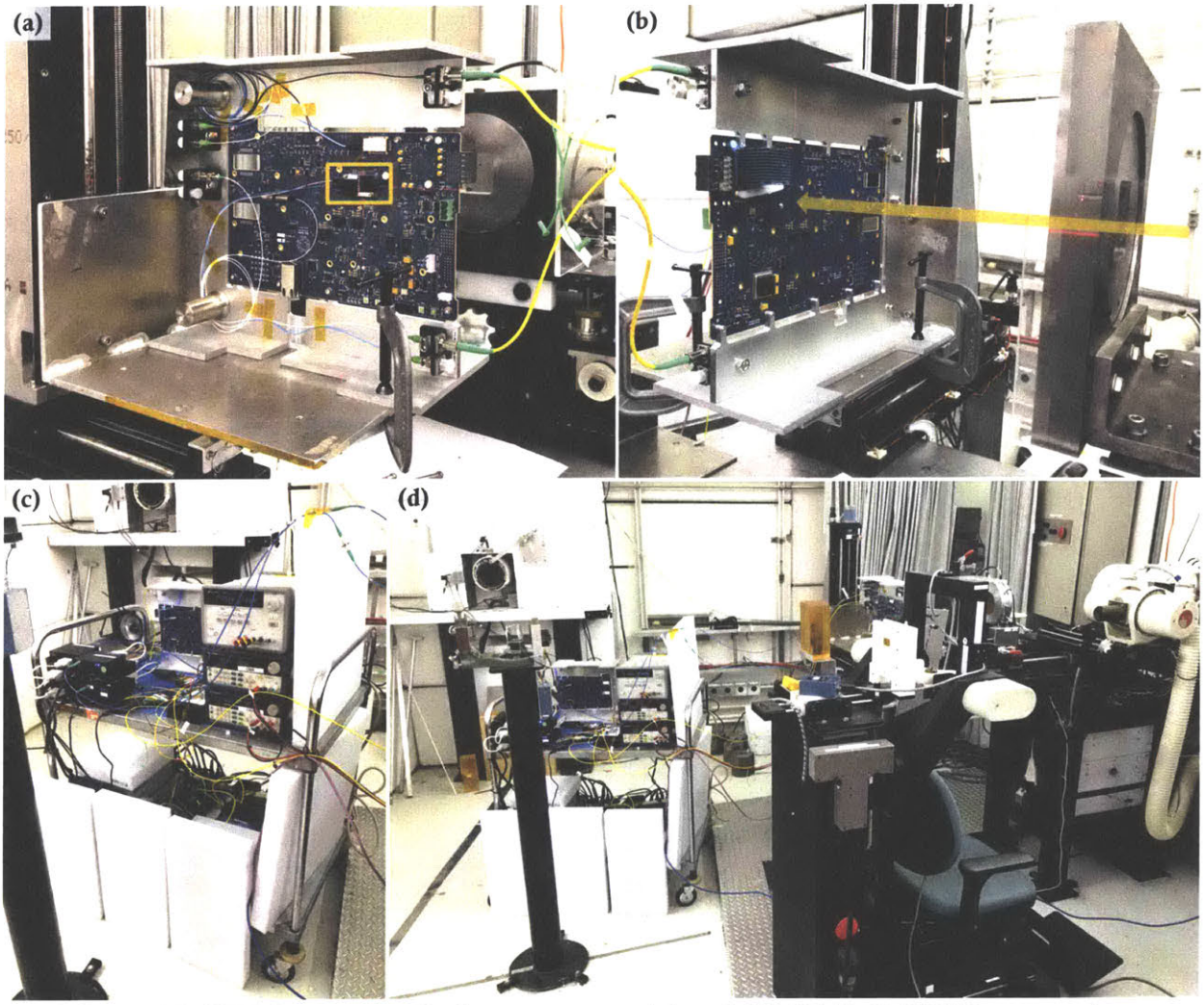

Figure 66. CDM proton radiation test setup. (a) and (b) OMA R-EDU mounted on radiation test stand for irradiation through PCB and CDM DUT aligned to center of proton beam collimator using laser alignment. Yellow box in (a) indicates CDM DUT on OMA R-EDU. Yellow arrow in (b) indicates CDM DUT area on back-side of PCB. (c) supporting test equipment, such as the GOMA R-EDU, test computers, power supplies, and optical-noise loading equipment, on a cart near the radiation test stand. (d) Full proton radiation test setup in the radiation chamber room.

5.4.2 Proton Radiation Test of Coherent Driver Modulator #1

For CDM DUT #1 testing, the proton beam was configured for a 105 MeV proton energy level and a proton flux of 1.00 (+/-0.02)$\times 10^8$ p/cm^2/sec (proton equivalent TID rate of ~9 rad(Si)/sec). CDM DUT #1 on OMA R-EDU #1 was irradiated for 3 hours, 24 minutes, and 14 seconds to a total fluence of 1.22×10^{12} p/cm^2 or equivalent TID of 110.4 krad(Si). CDM DUT #1 on R-EDU #1 was tested in the noise-loaded optical loopback test configuration with the GOMA R-EDU. In the test configuration, the receive path into the µICR on OMA R-EDU #1 was optically noise-loaded to an OSNR of 15.2 dB, which was 2.3 dB above the ROSNR for R-EDU #1 ASIC. The OMA ASIC pre-FEC BER was 5.8×10^{-3}. The optical input power to the µICR on OMA R-EDU #1 was -10.3 dBm. The CDM transmit path

(receive path into the GOMA R-EDU) was optically noise-loaded to an OSNR of 14.7 dB, which was 2.3 dB above the ROSNR for the GOMA R-EDU ASIC. The GOMA ASIC pre-FEC BER was 6.0×10^{-3}. The optical input power to the µICR on GOMA R-EDU #1 was -10.1 dBm. The optical input to the CDM on OMA R-EDU #1 was 9.0 dBm.

A total of ten proton SEEs were observed, consisting of ten SEUs and four SEFIs. There were three radiation scatter events observed to the GOMA and OMA test computers. Six SEUs were bit flips to "0", consisting of single bit flips or multiple bit flips or upsets (MBUs). The CDM register check software successfully corrected the flipped bits from the six SEU occurrences and no reset or action was required. The flipped bits did not appear to have affected the CDM performance prior to the software correcting the errors. Four of the six SEUs were bit flips to "0" in the gain and peak control mode register, which shifts the control mode from default digital mode to analog mode. Two of the SEU occurrences were bit flips to "0" for the XI and YI peaking setting. The peaking setting is used to "sharpen" the channel voltage signal edges to appear more like a square value than a sine wave. Sharpening the channel voltage signals is needed to more accurately determine the peak voltage levels of signals input to the CDM. Table 50 lists the details of the CDM DUT #1 SEU occurrences of bit flips.

Table 50. CDM DUT #1 SEU bit flips to "0"

SEU Bit Flip Occurrence	Proton Fluence [p/cm²]	Equivalent TID [krad(Si)]	Bit Flip to 0 / 1	Number of Bit Flips	Register
SEU-BF-1	1.72×10^{11}	15.6	0	9	Read – Write: Gain/Peak Control Mode
SEU-BF-2	2.96×10^{11}	26.8	0	2	Read – Write: Gain/Peak Control Mode
SEU-BF-3	3.06×10^{11}	27.7	0	2	Read – Write: Gain/Peak Control Mode
SEU-BF-4	7.61×10^{11}	68.9	0	1	Read – Write: XI Peaking Setting
SEU-BF-5	8.74×10^{11}	79.1	0	1	Read – Write: YI Peaking Setting
SEU-BF-6	9.60×10^{11}	86.9	0	2	Read – Write: Gain/Peak Control Mode
Total Number of SEU Bit Flips				**21**	-

Four SEFI occurrences were bit flips in static read registers. To correct the static-read register values, a CDM SPI reset was used to reload the correct values from a copy of volatile RAM in the CDM. Repetitive error messages appeared for the register with bit flips until the SPI reset was performed. The flipped bits did not appear to have affected the CDM performance prior to the CDM SPI reset correcting the errors. One SEFI occurred on the static read register for the serial ID of the die X-Y location on the wafer and three SEFIs occurred on the static read register for the serial ID of the wafer and lot number. Three SEFIs were bit flips to "1" and one SEFI was a bit flip to "0." Table 51 lists the details of the CDM DUT #1 SEFI

occurrences of bit flips. Figure 67 shows the CDM DUT #1 proton test telemetry for bit flips. Figure 67(a) shows the bit flips to "0," including six SEUs labeled with yellow numbered circles and one SEFI labeled with red numbered circle. Figure 67(b) shows the bit flips to "1," including three SEFIs labeled with red numbered circles.

Table 51. CDM DUT #1 SEFI bit flips

SEFI Bit Flip Occurrence	Proton Fluence [p/cm^2]	Equivalent TID [krad(Si)]	Bit Flip to 0 / 1	Number of Bit Flips	Register
SEFI-BF-1	1.18×10^{11}	10.7	1	1	Static Read: Serial ID of Wafer and Lot Number
SEFI-BF-2	2.91×10^{11}	26.3	1	1	Static Read: Serial ID of Die X-Y Location on Wafer
SEFI-BF-3	3.03×10^{11}	27.4	1	1	Static Read: Serial ID of Wafer and Lot Number
SEFI-BF-4	9.53×10^{11}	86.3	0	1	Static Read: Serial ID of Wafer and Lot Number
Total Number of SEFI Bit Flips				**4**	-

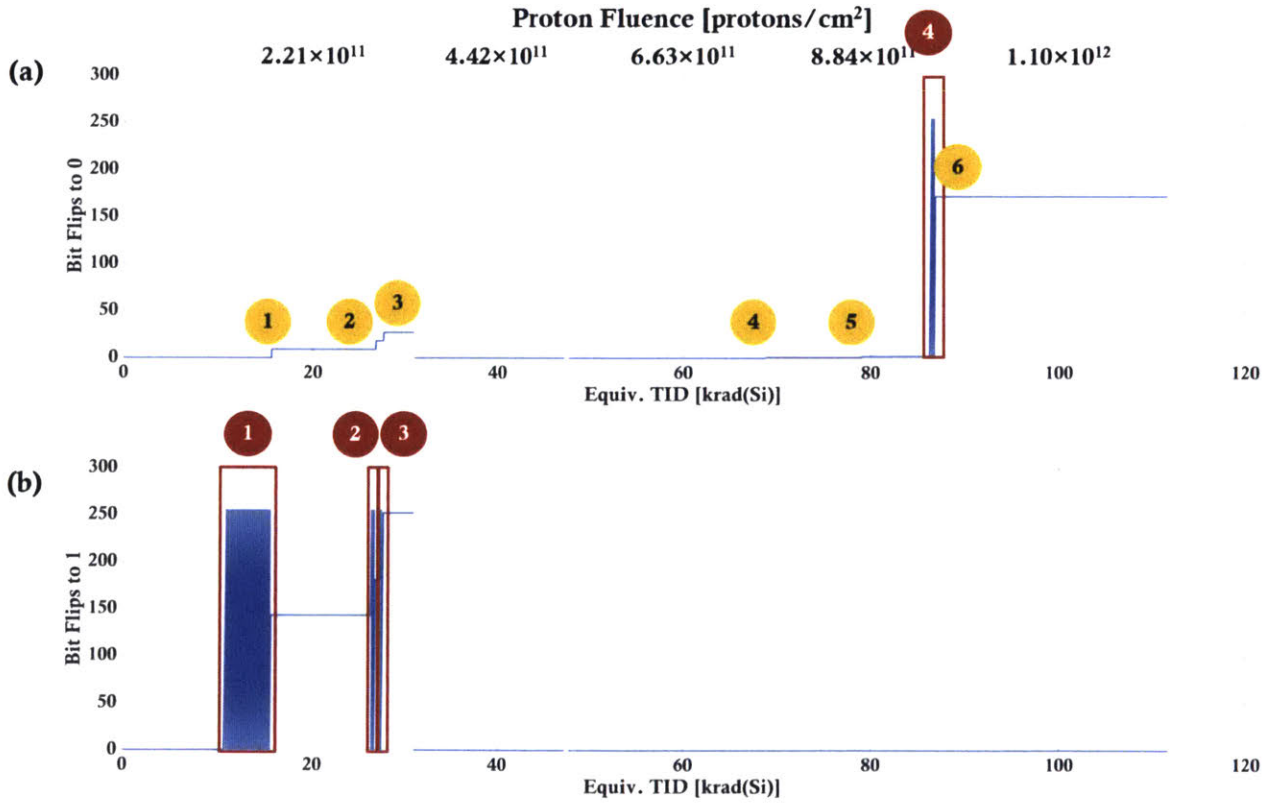

Figure 67. CDM DUT #1 proton test bit flip telemetry. (a) Bit flips to "0," (b) Bit flips to "1".

Figure 68 shows a set of CDM DUT #1 telemetry for SEFI #1 of stuck bit flip to "1" (SEFI-BF-1). In Figure 68(f) SEFI #1 is labeled with red circle "1" and red rectangle. SEU #1 of the nine bit flips to "0" is also indicated in Figure 68(e) with the yellow circle "1." Beyond the increasing bit flips to "1," there were no significant effects observed to other CDM DUT #1 parameters shown in the other subplots of Figure 68. There was no observed impact to telemetry collected on the modulator chip, the gain read and peak detect values of the RF driver IC, the CDM ABC, TEC, external tap photodiode, and GOMA ASIC optical performance. A CDM SPI reset was performed to resolve the stuck flip "1" bits for SEFI #1. The green rectangle across Figure 68, labeled with green "R" circle for reset, shows the SPI reset. Shortly after the reset, there was a radiation scatter event to the GOMA computer, which caused the computer to freeze and required a GOMA restart. The radiation scatter event to the GOMA computer is indicated with an orange rectangle across the ASIC sub-graphs in Figure 68(n), Figure 68(o), and Figure 68(p) and labeled with orange "S" circle for scatter.

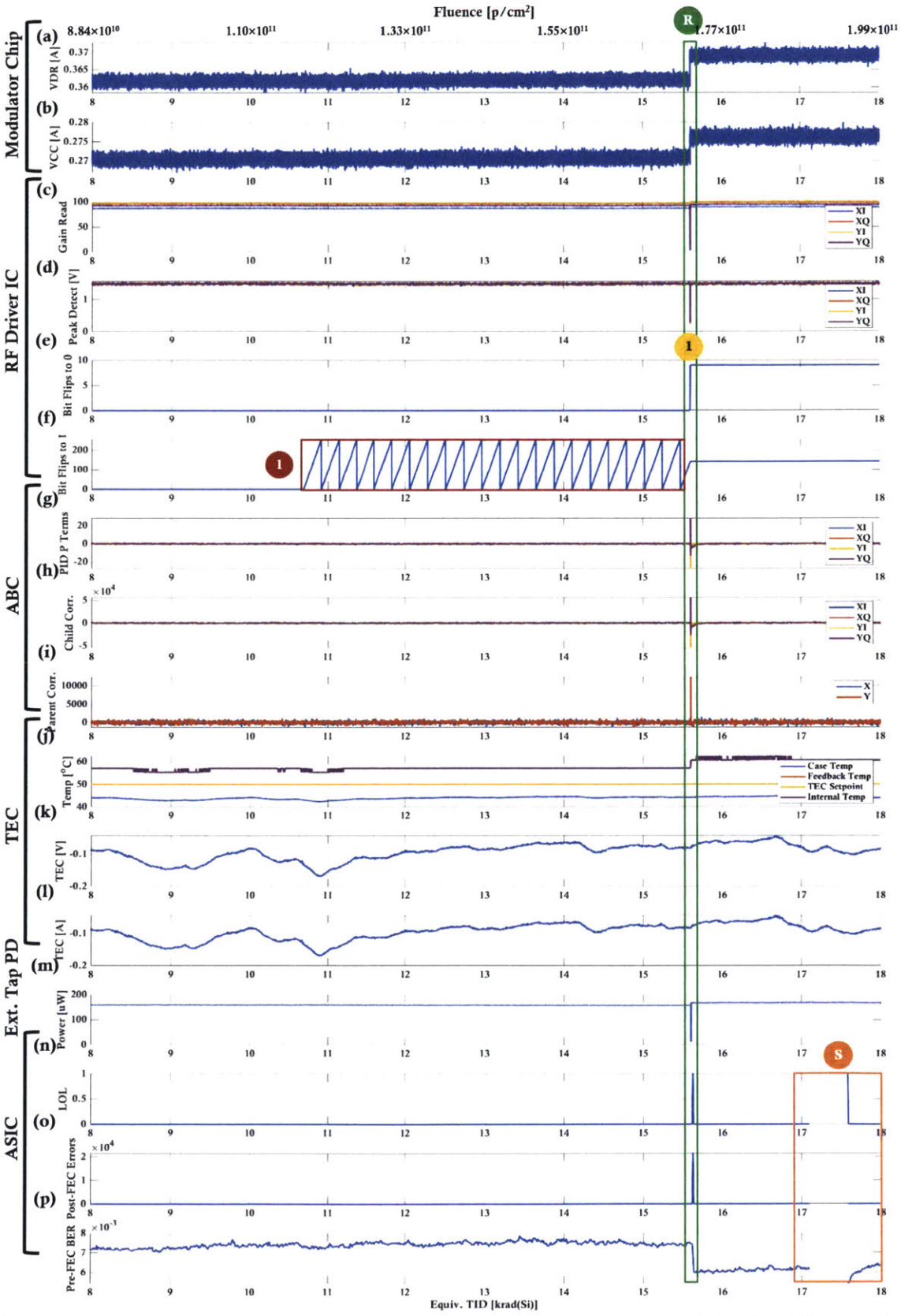

Figure 68. CDM DUT #1 proton test telemetry for SEFI #1 repetitive bit flips to "1."

Four SEUs to the CDM RF driver IC were observed. Table 52 summarizes the four RF Driver IC SEUs observed during proton radiation testing of CDM DUT #1. The coherent DSP ASIC provides XI, XQ, YI, YQ voltage signals as input to the RF driver IC in the CDM. Amplifiers in the RF driver IC apply gain to the input signals and the peak values of the amplified signals are detected. A PID controller implemented with the Zynq SoC uses the peak detect values as an input for controlling the gain of the RF driver IC amplifiers to ensure sufficient signal input to CDM modulator chip. VDR and VCC current rails are applied to bias signals in the modulator chip section of the CDM. CDM ABC, which is controlled with a PID controller implemented with the Zynq SoC, biases the child and parent MZM arms in the modulator chip section. A TEC controls the temperature of the modulator chip. An external tap photodiode detects the optical output power of the CDM. At the end of the optical receive path, the coherent DSP ASIC line-side performance parameters, such as loss of lock, post-FEC uncorrected errors, and pre-FEC BER, are used to evaluate how radiation effects to the CDM affect OMA system performance.

Table 52. CDM DUT #1 RF Driver IC SEUs

RF Driver IC SEU	**Proton Fluence [p/cm^2]**	**Equivalent TID [krad(Si)]**	**RF Driver IC Impact**	**OMA System Performance / ASIC Line Side Impact**
SEU-RF-1	1.22×10^{10}	1.1	XI, XQ, YI, YQ Channel Amplifiers	Post-FEC Uncorrected Error Burst
SEU-RF-2	2.44×10^{11}	22.1	ADC Voltage Reference	None
SEU-RF-3	8.78×10^{11}	79.5	XQ Channel Amplifier	None
SEU-RF-4	8.78×10^{11}	97.9	YI Channel Amplifier	None

The first RF driver IC SEU (SEU-RF-1) occurred at proton fluence level of 1.22×10^{10} p/cm^2 or equivalent TID level of 1.1 krad(Si). The CDM DUT #1 telemetry for the first RF driver IC SEU is shown in Figure 69. The SEU appears to have impacted the amplifiers in the RF driver IC based on an observable spike in the peak detector voltages for XI, XQ, YI, and YQ, shown in Figure 69(d). Channel XI had the greatest spike in peak detector voltage with an increase of 86 mV. The peak detector voltages for channels XQ and YQ increased by 58 mV and the peak detector voltage for channel YI increased by 29 mV. In response to the peak detector voltage spikes, the PID controller reduced the gain applied to the amplifiers, as seen with the decrease in gain read values indicated with the red rectangle in Figure 69(c).

There was an observable stepped decrease in both VDR and VCC current rail, indicated with the red rectangles in Figure 69(a) and Figure 69(b), respectively. VDR dropped by ~10 mA, and VCC dropped by ~7.5 mA. The spike in peak detector voltages affected the CDM ABC parameters. All channels had a spike in the ABC PID P terms, shown in Figure 69(g), and in the child correlation values, shown in Figure 69(h). There were no observable effects to the X and Y parent correlation values. There was an observable step decrease of ~3.5 °C in the CDM internal temperature from 60.6 °C to 57.1 °C, shown in Figure 69(j).

The decrease in internal temperature, resulted in reduced TEC current and voltage, shown in Figure 69(k) and Figure 69(l), respectively. The external tap photodiode detected reduced CDM optical output power of 13 µW from 173.5 µW to 160.5 µW, shown in Figure 69(m).

The first RF driver IC SEU had minimal impact to system performance of the GOMA R-EDU, based on observed effects to the GOMA coherent DSP ASIC line side post-FEC uncorrected error count and pre-FEC BER. There was a burst of 24 post-FEC uncorrected errors shown in Figure 69(o), and an increase in the pre-FEC BER from 5.9×10^{-3} to 7.1×10^{-3} shown in Figure 69(p). There was no loss of lock for the GOMA coherent DSP ASIC shown in Figure 69(n). No reset or power cycle of the CDM DUT #1 was performed. Nominal functionality was observed after the spike in CDM peak detector voltages.

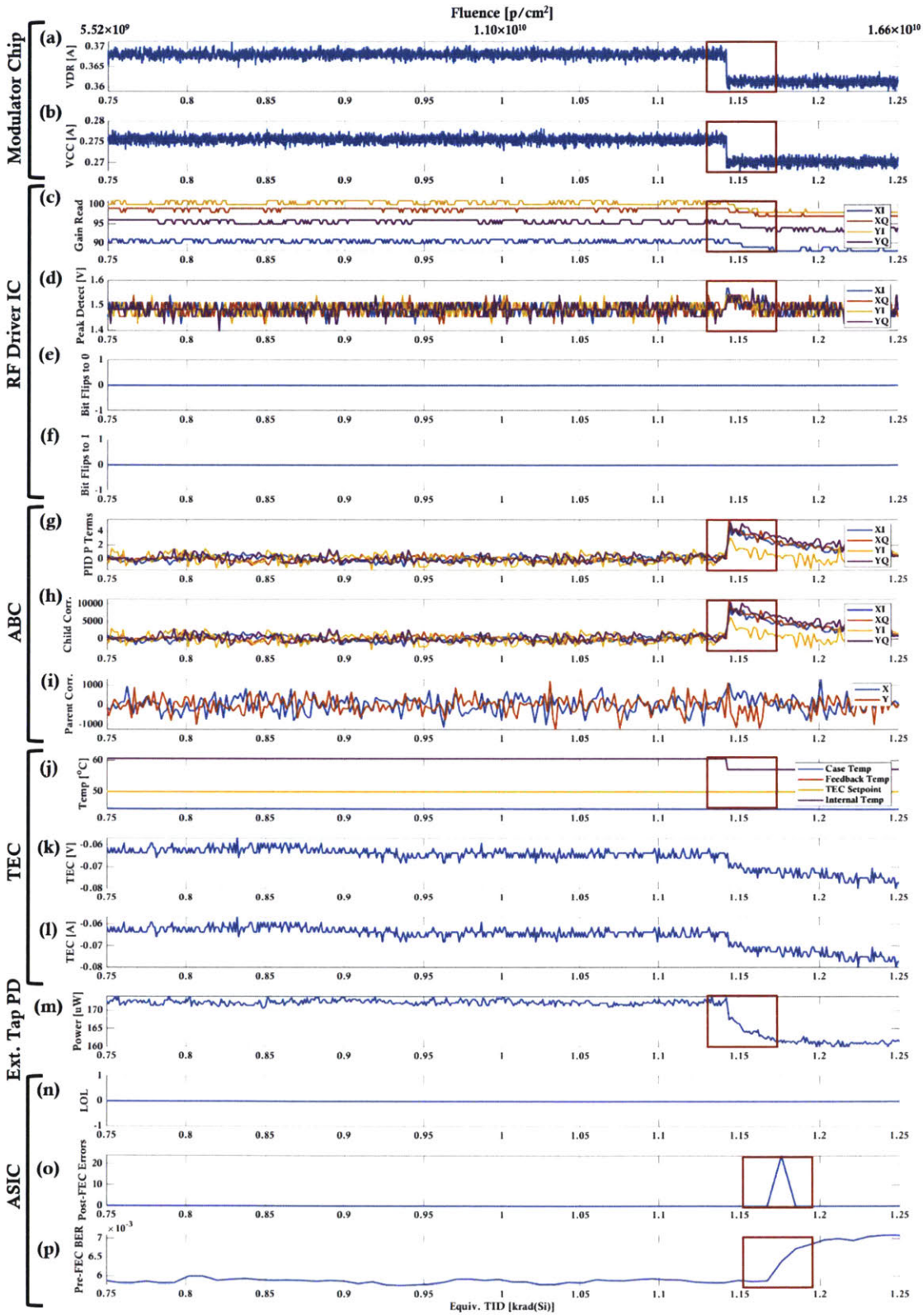

Figure 69. CDM DUT #1 proton test telemetry for RF Driver SEU #1 on XI, XQ, YI, YQ channel amplifiers on RF driver IC. Red rectangles showing impact of SEU to other parts of the CDM, the external tap photodiode, and GOMA coherent DSP ASIC performance.

The second CDM DUT #1 RF driver IC SEU (SEU-RF-2) occurred at a proton fluence level of 2.44×10^{11} p/cm^2 or equivalent TID level of 22.1 krad(Si). The CDM DUT #1 telemetry for the second RF driver IC SEU is shown in Figure 70. The SEU to the RF driver IC appears to cause a shift in the ADC voltage reference, resulting in a DC offset of 4 bits. We observe dips in both the peak detector voltages and gain read values for XI, XQ, YI, and YQ channels. In the other SEUs, an increase in the gain read values would be observed with a dip in peak detector values. The amplifier gain values in the RF driver IC are adjusted by a PID controller in response to the peak detector values. The peak detector voltages dip in values ranging from 115 mV (XI, XQ, YQ) to 144 mV (YI), indicated with the red rectangle in Figure 70(d). The raw telemetry values of the peak detectors show the dip ranging in values from 3 (YQ) to 4 (XI, XQ, YI). The gain read for all the channels dip in values ranging from 3 (YI and YQ) to 4 (XI and XQ), indicated with the red rectangle in Figure 70(c). There was a step increase of ~7 °C in the CDM internal temperature from 62.4 °C to 69.4 °C, indicated with the red rectangle in Figure 70(j). The raw telemetry values of the internal temperature shifted by a value of 4.

During the second RF driver SEU, there were no bit flip occurrences, shown in Figure 70(e) and Figure 70(f). There were no observable effects on VDR and VCC current rails, shown in Figure 70(a) and Figure 70(b), respectively. The SEU impact to the RF driver IC gain read values and peak detector voltages had effects on the CDM ABC parameters. There were large deviations in the ABC PID P term values and child correlations for the YI and YQ channels, shown in Figure 70(g) and Figure 70(h), respectively. There were no observable effects to the X and Y parent correlations (Figure 70(i)).

The optical output power from the CDM increased by 16 μW from 167.2 μW to 183.2 μW, shown in Figure 70(m). With higher optical power into the receive path of the GOMA R-EDU, the GOMA coherent DSP ASIC pre-FEC BER reduced from 6.3×10^{-3} to 4.8×10^{-3} (Figure 70(p)). The second CDM DUT #1 RF driver SEU did not impact the GOMA R-EDU system performance. No reset or power cycle of the CDM DUT #1 was performed. Nominal functionality was observed after the SEU occurred.

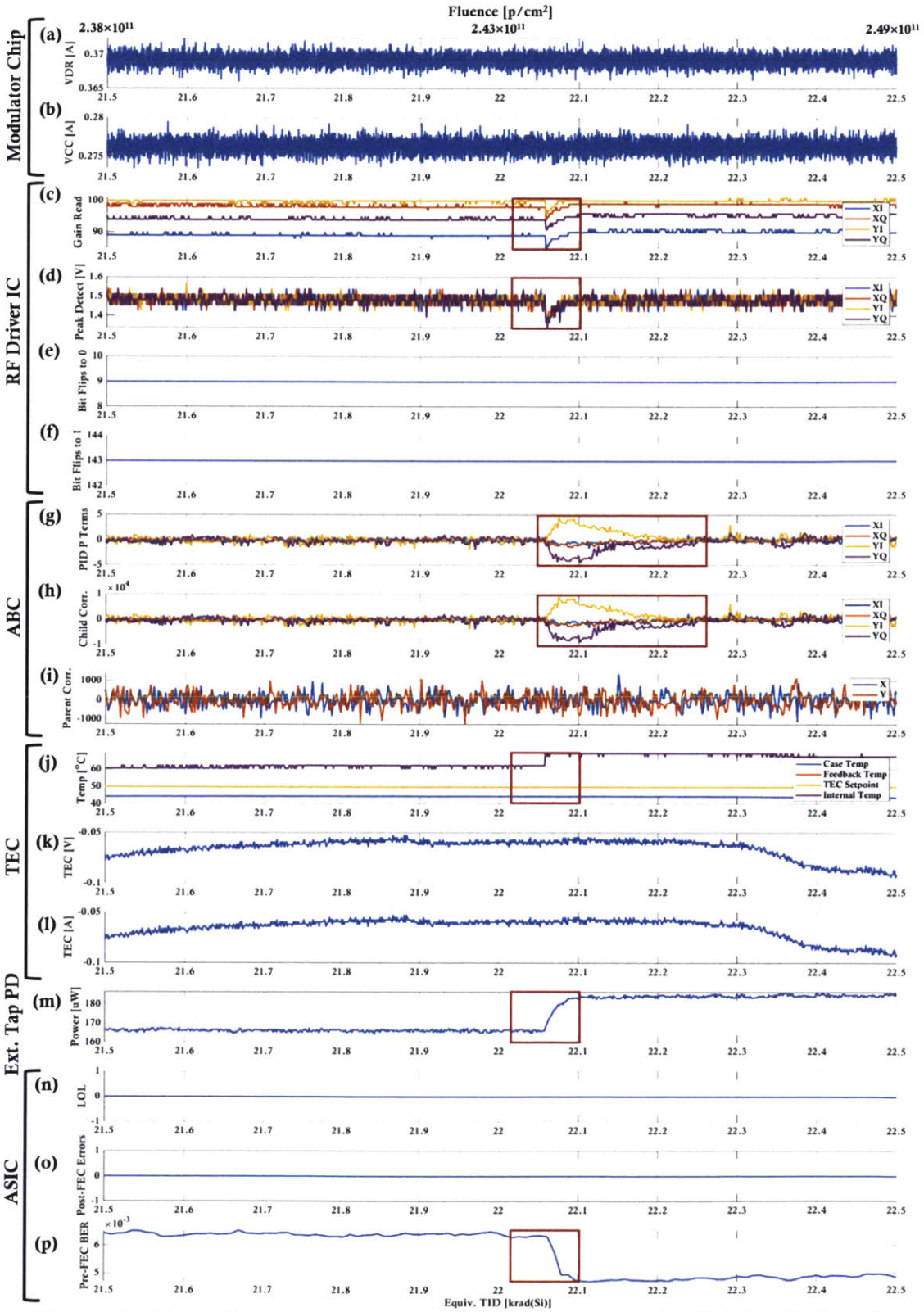

Figure 70. CDM DUT #1 proton test telemetry for RF Driver SEU #2, which shifted the ADC voltage reference. Red rectangles show impact to RF driver IC, ABC, internal temperature, external tap photodiode, and ASIC pre-FEC BER telemetry.

The third CDM DUT #1 RF driver SEU (SEU-RF-3) occurred at proton fluence level of 8.78×10^{11} p/cm^2 or equivalent TID level of 79.5 krad(Si). The CDM DUT #1 telemetry for the third RF driver IC SEU is shown in Figure 71. The SEU appears to have impacted the XQ channel amplifier in the RF driver IC, based on observable dip in the XQ channel peak detector voltage of 317 mV, indicated with the red rectangle in Figure 71(d). To compensate for the XQ channel peak detector voltage dip, the PID controller increased the XQ channel gain read value from 98 to 115, indicated with the red rectangle in Figure 71(c). During the third RF driver SEU, there were no bit flip occurrences, shown in Figure 71(e) and Figure 71(f). Prior to the third RF driver SEU, there was a bit flip to "0" SEU (SEU-BF-4). SEU-BF-4 did not have correlated effects to SEU-RF-3.

There were no observable effects on VDR and VCC current rails, shown in Figure 71(a) and Figure 71(b), respectively. The SEU impact to the RF driver IC gain read values and peak detector voltages had effects on the XQ channel CDM ABC parameters. There were large deviations in the ABC PID P term values and child correlations for the XQ channel, shown in Figure 71(g) and Figure 71(h), respectively. There were no observable effects to the X and Y parent correlations (Figure 71(i)).

There were no observable changes to the temperature readings, TEC current, or TEC voltage, shown in Figure 71(j), Figure 71(k), and Figure 71(l). As expected from the increase in gain of the XQ channel, the optical output power from the CDM increased. The external tap photodiode detected an increase of 15 μW from 166.5 μW to 181.5 μW, shown in Figure 71(m). The third CDM DUT #1 RF driver SEU did not impact the GOMA R-EDU system performance. There were no observable effects to the GOMA coherent DSP ASIC line side performance: no loss of lock shown in Figure 71(n), no post-FEC uncorrected error bursts shown in Figure 71(o), and no change to the pre-FEC BER shown in Figure 71(p). No reset or power cycle of the CDM DUT #1 was performed. Nominal functionality was observed after the SEU occurred.

The fourth CDM DUT #1 RF driver SEU (SEU-RF-4) occurred at proton fluence level of 8.78×10^{11} p/cm^2 or equivalent TID level of 97.9 krad(Si). The CDM DUT #1 telemetry for the fourth RF driver IC SEU shows the same behavior as SEU-RF-3, with exception that the SEU appears to have impacted the YI channel amplifier, instead of the XQ channel amplifier as in SEU-RF-3.

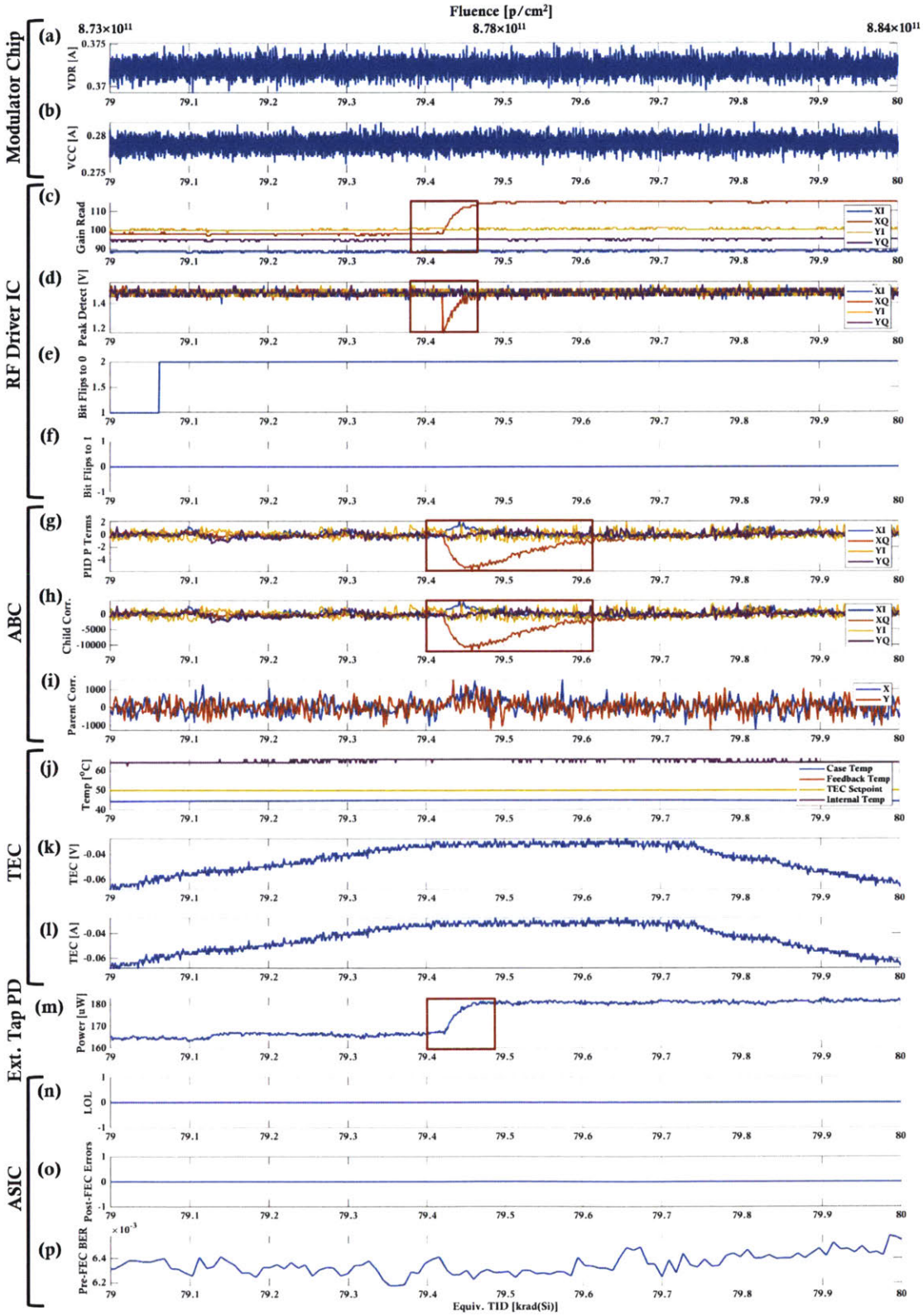

Figure 71. CDM DUT #1 proton test telemetry for RF Driver SEU #3 to the XQ channel amplifier in the RF driver IC. Red rectangles show impact to XQ channel detected peak voltage, ABC PID P term and child correlation, and external tap photodiode.

5.4.3 Proton Radiation Test of Coherent Driver Modulator #2

For CDM DUT #2 testing, the proton beam was configured for a 105 MeV proton energy level and proton flux of $1.20(+/-0.02)\times10^{8}$ p/cm^2/sec (proton equivalent TID rate of ~ 10.7 rad(Si)/sec). CDM DUT #2 was tested at a slightly higher flux than CDM DUT #1 (1.00×10^{8} p/cm^2/sec) due to time constraints for the radiation test. CDM DUT #2 on OMA R-EDU #2 was irradiated for 2 hours, 52 minutes, and 39 seconds to a total fluence of 1.22×10^{12} p/cm^2 or equivalent TID of 110.4 krad(Si). CDM DUT #2 on R-EDU #2 was tested in a self-noise-loaded optical loopback test configuration, without a GOMA R-EDU. The OMA R-EDU #2 transmit path (CDM and tap photodiode) was noise-loaded and input to the OMA R-EDU #2 receive path (μICR).

Radiation testing of CDM DUT #2 was completed after radiation testing of the coherent DSP ASIC. At the end of the coherent DSP ASIC proton test, radiation scatter caused permanent damage to the OMA R-EDU test computer. The GOMA R-EDU computer was used for CDM DUT #2 testing with OMA R-EDU #2 in a self-noise-loaded loopback test configuration. The optical path was noise-loaded to an OSNR of 14.9 dB, which was 2.0 dB above the ROSNR for the R-EDU #1 ASIC. The OMA ASIC pre-FEC BER was 7.2×10^{-3}. The optical input power to the μICR on OMA R-EDU #1 was -10.5 dBm. The optical input to the CDM was 9.0 dBm.

A total of twelve proton SEEs were observed, consisting of eight SEUs and four SEFIs. Seven SEUs were bit flips to "0", consisting of single bit flips or multiple bit flips or upsets (MBUs). The OMA SPI register check software feature successfully corrected the flipped bits from the seven SEU occurrences and no reset or action was required. Six SEU bit flip occurrences were bit flips to "0" in the gain and peak control mode register. One SEU bit flip occurrence was a bit flip to "0" for the XQ peaking setting. The flipped bits did not appear to have affected the CDM performance prior to the software correcting the errors. Table 53 lists the details of the SEU occurrences of bit flips to "0."

Table 53. CDM DUT #2 SEU bit flips to "0"

SEU Occurrence	Proton Fluence Level [p/cm^2]	Equivalent TID Level [krad(Si)]	Bit Flips to "0"	Register
SEU-BF-1	5.51×10^{10}	5.0	1	Gain/Peak Control Mode
SEU-BF-2	6.68×10^{10}	6.0	9	Gain/Peak Control Mode
SEU-BF-3	8.48×10^{10}	7.7	1	Gain/Peak Control Mode
SEU-BF-4	2.25×10^{11}	20.4	9	Gain/Peak Control Mode
SEU-BF-5	7.01×10^{11}	63.5	1	Gain/Peak Control Mode
SEU-BF-6	8.33×10^{11}	75.4	9	Gain/Peak Control Mode
SEU-BF-7	1.07×10^{12}	97.0	1	XQ Peaking Setting
Total Bit Flips to "0"			31	-

Three SEFIs were bit flips to "1" in static read registers and required a CDM SPI reset to clear repetitive error messages. The flipped bits did not appear to have affected the CDM performance prior to the CDM SPI reset correcting the errors. Two SEFIs occurred on the static read register for the serial ID of the die X-Y location on the wafer and one SEFI occurred on the static read register for the serial ID of the wafer and lot number. Table 54 lists the details of the SEFI occurrences of bit flips to "1." Figure 72 shows the CDM DUT #2 proton test telemetry for bit flips. Figure 72(a) shows the seven SEU occurrences of bit flips to "0"

labeled with yellow numbered circles, and Figure 72(b) shows the three SEFI occurrences of bit flips to "1" labeled with red numbered circles.

Table 54. CDM DUT #2 SEFI bit flips to "1"

SEFI Occurrence	Proton Fluence Level [p/cm^2]	Equivalent TID Level [krad(Si)]	Bit Flips to "1"	Register
SEFI-BF-1	2.01×10^{11}	18.2	2	Serial ID of Die X-Y Location on Wafer
SEFI-BF-2	8.00×10^{11}	72.4	1	Serial ID of Wafer and Lot Number
SEFI-BF-3	9.07×10^{11}	82.1	1	Serial ID of Die X-Y Location on Wafer
Total Bit Flips to "0"			4	-

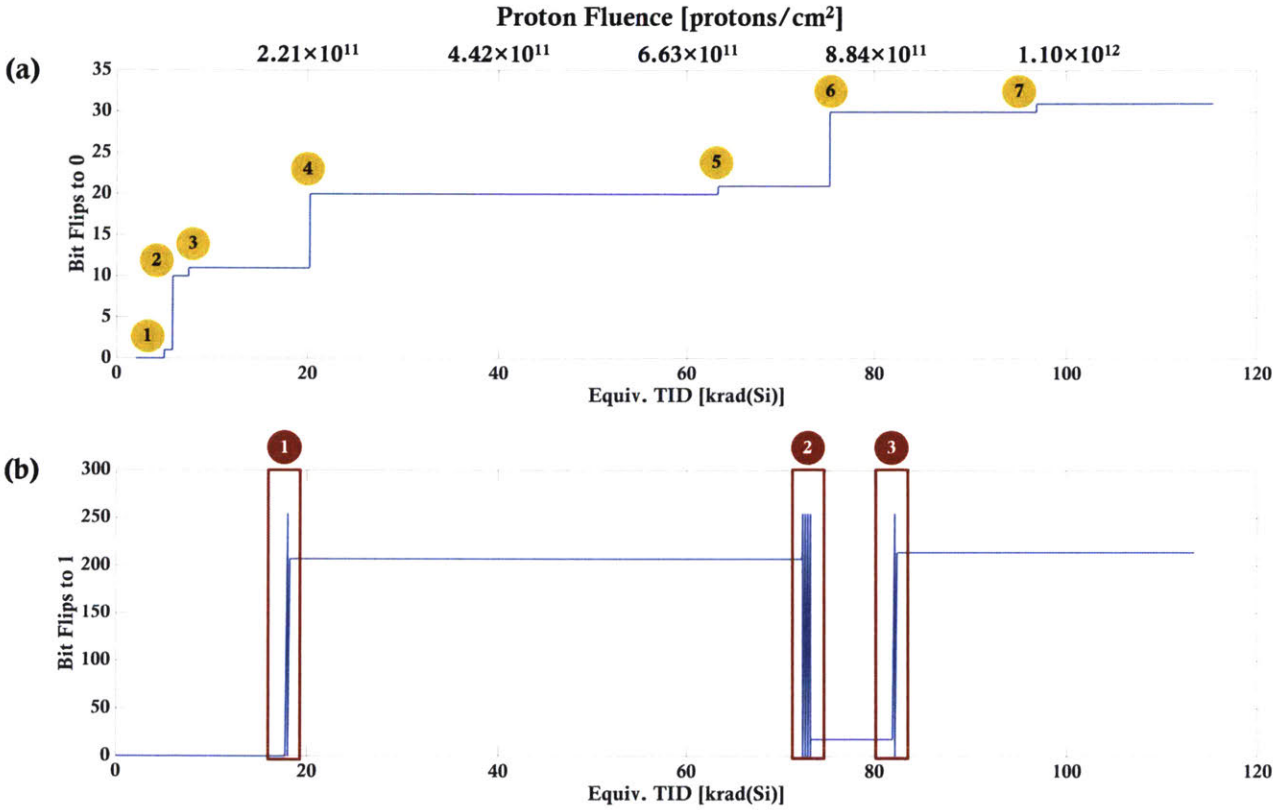

Figure 72. CDM DUT #2 proton test bit flip telemetry. (a) Seven SEU occurrences of bit flips to "0". (b) Three SEFI occurrences of stuck bit flips to "1".

One SEU occurrence and one SEFI occurrence were related to the CDM DUT #2 RF driver IC. The RF driver IC SEFI occurred at proton fluence level of 5.03×10^{11} p/cm^2 or equivalent TID level of 45.5 krad(Si) and appears to be caused by a proton SEE to the amplifier in the RF driver IC. The CDM DUT #2 telemetry for the RF driver IC SEFI is shown in Figure 73. Figure 73(a) and Figure 73(b) show the current rails for VDR and VCC, respectively, applied to the modulator chip section of the CDM DUT. There was no observable impact to the current rails in the first RF driver IC SEFI. Figure 73(c), Figure 73(d), Figure 73(e), and Figure 73(f) show the RF driver IC telemetry such as, the gain values applied by the amplifiers in the RF driver IC, the peak voltages of the amplified signals, the bit flips to "0", and the bit

flips to "1", respectively. In the first RF driver IC SEFI, the peak detect values for all four signals (XI, XQ, YI, XQ) dropped in from ~1.5 V to ~0.1 V as indicated with the red box in Figure 73(d). From the drop in peak detect voltages, an increase to the gain is observed as indicated with the red box in Figure 73(c). During this SEFI, no bit flips occurred. The drop in peak detect voltages impacted the CDM ABC parameters, including the PID P terms, child correlation values, and parent correlation values shown in Figures 74(g) to Figure 74(i). Red boxes in these subplots indicate the ABC instability and shift in XI, XQ, YI, YQ PID p terms, child correlation values, and parent correlation values. There were no impacts observed in the temperature readings shown in Figure 73(j). The TEC voltage and current, shown in Figure 74(k) and Figure 74(l) were not significantly impacted from the SEFI, except that the data appears noisier after the SEFI occurrence. The external tap photodiode detected an optical output power drop to 0 μW, indicated with the red box in Figure 73(m). Since the OMA R-EDU was in self noise-loaded optical loopback during proton testing of the CDM DUT #2, the RF driver IC SEFI impacted the receive path of the OMA and the ASIC line-side performance, shown in Figure 74(n) to Figure 74(p). The impact includes ASIC LOL, post-FEC uncorrected errors of 10^5 order magnitude, and pre-FEC BER increase from 9.2×10^{-3} to 1.7×10^{-2}. A power cycle of the CDM successfully restored nominal functionality.

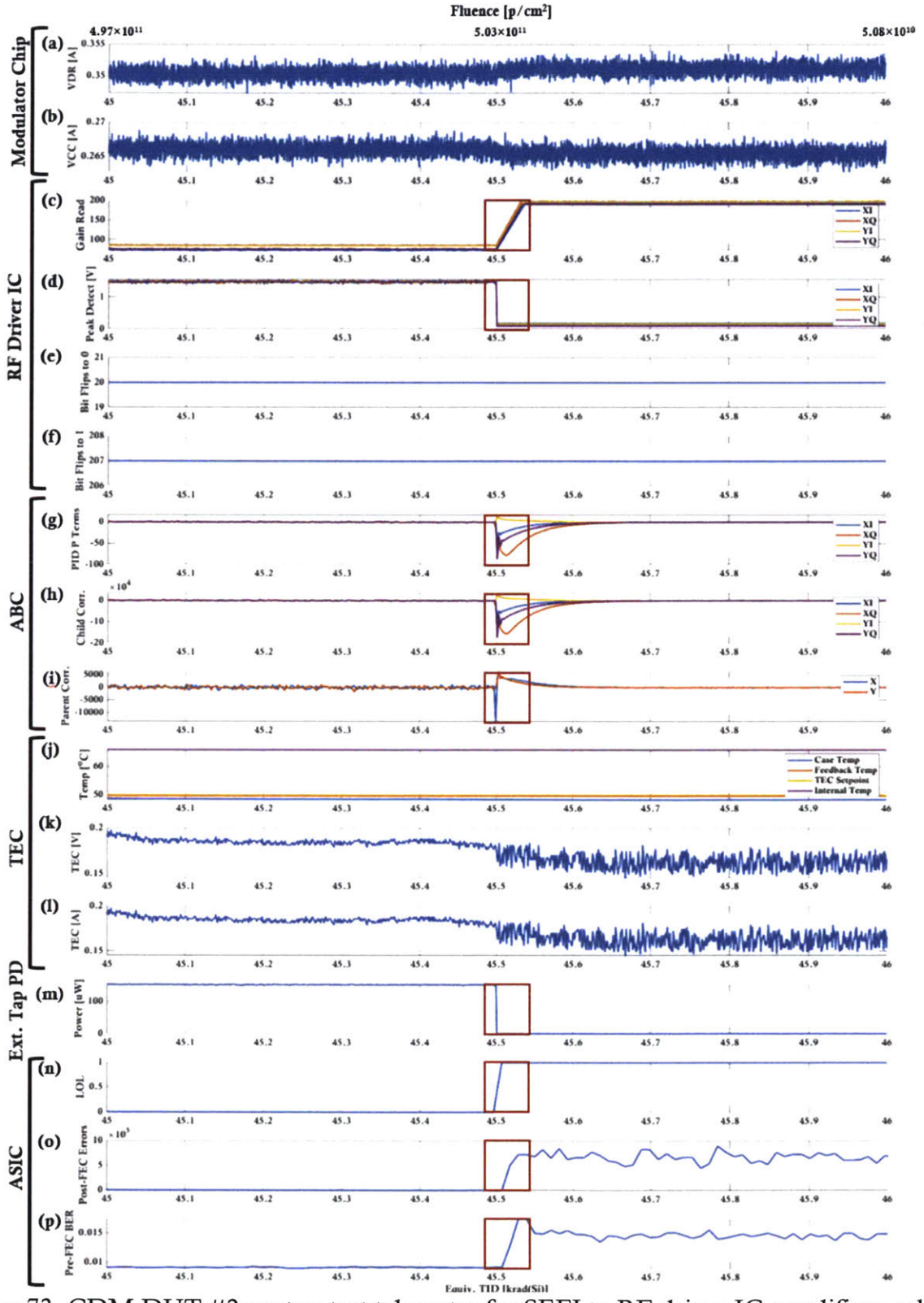

Figure 73. CDM DUT #2 proton test telemetry for SEFI to RF driver IC amplifiers, which resulted in an increase of gain read telemetry and drop in peak detected voltage telemetry. Red rectangles show impact to ABC telemetry and GOMA ASIC performance telemetry.

The RF driver IC SEU occurred at proton fluence level of 1.06×10^{12} p/cm^2 or equivalent TID level of 90.7 krad(Si) and appears to be caused by a proton SEE to the amplifier in the RF driver IC. The CDM DUT #2 telemetry for the RF driver IC SEU is shown in Figure 74. Figure 74(a) and Figure 74(b) show the current rails for VDR and VCC, respectively, applied to the modulator chip section of the CDM DUT. There was an observable step of ~2 mA in the VDR current rail from 361 mA to 363 mA, but this change in current is not significant. VDR is used to apply a bias voltage in the modulator chip to the amplified XI, XQ, YI, and YQ signals. Figure 74(c), Figure 74(d), Figure 74(e), and Figure 74(f) show the RF driver IC telemetry such as the gain values applied by the amplifiers in the RF driver IC, the peak voltages of the amplified signals, the bit flips to "0", and the bit flips to "1", respectively. There were no observable changes to the RF driver IC telemetry parameters. There were observable peaks for the XQ channel CDM ABC PID P term, shown in Figure 74(g), and for the child correlation values, shown in Figure 74(h). There was an observable dip in the X signal parent correlation values shown in Figure 74(i). Red boxes in these subplots indicate the shifts in the XQ channel PID P term, XQ channel child correlation values, and X channel parent correlation values. There were no impacts observed in the temperature readings shown in Figure 74(j). The observed impact to the VDR current rail and the ABC parameters implies a SEU to the RF driver IC that may not have been observed through the collected RF driver IC telemetry.

The TEC voltage and TEC current, shown in Figure 75(k) and Figure 74(l) respectively, were not significantly impacted from the SEFI, except that the data appears to be slightly increasing. There was no significant change in optical output power detected by external tap photodiode shown in Figure 74(m). The ASIC maintained lock, shown in Figure 74(n), and there was no significant change to the pre-FEC BER shown in Figure 74(p). There was a burst of 24 post-FEC errors observed, indicated with the red box in Figure 74(o). No CDM reset or power cycle was performed, since the post-FEC error count returned to zero and ABC parameters appeared to return to nominal values.

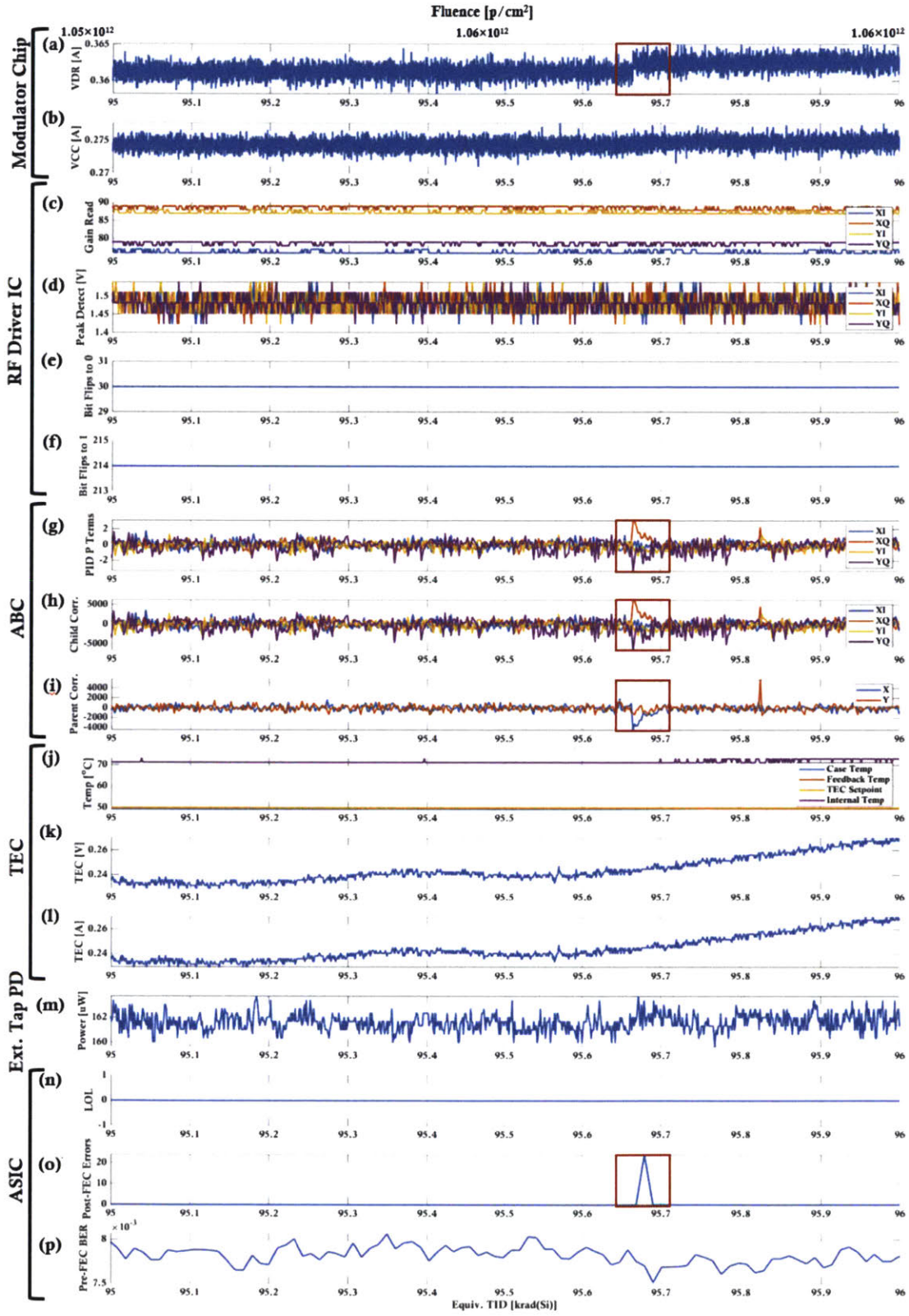

Figure 74. CDM DUT #2 proton test telemetry for SEU to amplifier in the RF driver IC. Red rectangles show impact to VDR current, X channel ABC parameters, and GOMA ASIC post-FEC error count.

5.4.4 Summary and Proton SEE Rate Calculations

Two commercial CDMs, integrated in OMA R-EDUs, were tested with 105 MeV protons to a fluence level of 1.22×10^{12} p/cm^2 or equivalent TID of 110.4 krad(Si). Both CDMs survived radiation testing without permanent degradation to the component performance or OMA system performance. No proton SELs were observed on the VDR and VCC current rails. From the CDM DUT #1 proton test, there were 14 proton SEEs observed, consisting of ten SEUs and four SEFIs. Six SEUs were bit flips in read-write registers, which were corrected with software, and four SEUs occurred in the RF driver IC. The four SEFIs were all bit flips in static-read registers, which required a reset of the CDM SPI to restore the bit flips. From the CDM DUT #2 proton test, there were 12 proton SEEs observed, consisting of eight SEUs and four SEFIs. Seven SEUs were bit flips in read-write registers, which were corrected with software, and one SEU occurred in the RF driver IC. Three SEFIs were bit flips in static-read registers, which required a reset of the CDM SPI to restore the bit flips. One SEFI occurred with the RF driver IC and impacted system performance (loss of lock for GOMA R-EDU coherent DSP ASIC). A power cycle of the CDM was used to restore nominal functionality. Table 55 summarizes the observed proton SEEs for both CDM DUTs.

Table 55. Proton SEE data from CDM 105 MeV proton test campaign

CDM	SEU			SEFI			Total SEEs
	Bit Flips	RF Driver IC	Total	Bit Flips	RF Driver IC	Total	
DUT #1	6	4	**10**	4	0	**4**	**14**
DUT #2	7	1	**8**	3	1	**4**	**12**

Proton SEE cross section values were calculated based on the CDM DUT SEE test results. Table 56 summarizes the 105 MeV proton cross section data from CDM testing at TRIUMF and shows SEU cross section values and SEFI cross section values based on type of reset performed.

Table 56. 105 MeV proton SEE cross section data from CDM proton test campaign

	SEU Cross Section	SEFI Cross Section – CDM SPI Reset	SEFI Cross Section – CDM Power Cycle
CDM DUT #1	8.20×10^{-12}	3.28×10^{-12}	-
CDM DUT #2	6.56×10^{-12}	2.46×10^{-12}	8.20×10^{-13}
Average	7.38×10^{-12}	2.87×10^{-12}	8.20×10^{-13}

CREME96 software was used to calculate the CDM proton SEE rate for the Telesat polar orbit (Table 57) and Telesat inclined orbit (Table 58). Appendix A4 describes the method and model details used for calculating the SEE rates with CREME96.

Table 57. Coherent driver modulator proton SEU rate for Telesat polar orbit

	SEE Rate Units	Nominal	Flare		
			Worst Week	Worst Day	Peak 5 Minutes
CDM SEU Rate	**[/Device/Second]**	2.00×10^{-9}	7.79×10^{-9}	3.02×10^{-8}	1.10×10^{-7}
	[/Device/Day]	1.73×10^{-4}	6.73×10^{-4}	2.61×10^{-3}	9.50×10^{-3}
	[/Device/Year]	6.32×10^{-2}	2.46×10^{-1}	9.52×10^{-1}	3.47
	[/Device/Second]	7.79×10^{-10}	3.03×10^{-9}	1.17×10^{-8}	4.28×10^{-8}

CDM SEFI SPI Reset Rate	**[/Device/Day]**	6.73×10^{-5}	2.62×10^{-4}	1.01×10^{-3}	3.69×10^{-3}
	[/Device/Year]	2.46×10^{-2}	9.55×10^{-2}	3.70×10^{-1}	1.35
CDM SEFI Power Cycle Rate	**[/Device/Second]**	2.23×10^{-10}	8.66×10^{-10}	3.35×10^{-9}	1.22×10^{-8}
	[/Device/Day]	1.92×10^{-5}	7.48×10^{-5}	1.90×10^{-4}	1.06×10^{-3}
	[/Device/Year]	7.02×10^{-3}	2.73×10^{-2}	6.93×10^{-2}	3.85×10^{-1}

Table 58. Coherent driver modulator proton SEU rate for Telesat inclined orbit

	SEE Rate Units	**Nominal**	**Flare**		
			Worst Week	**Worst Day**	**Peak 5 Minutes**
CDM SEU Rate	**[/Device/Second]**	9.27×10^{-9}	3.90×10^{-13}	4.45×10^{-13}	1.98×10^{-12}
	[/Device/Day]	8.01×10^{-4}	3.37×10^{-8}	3.84×10^{-8}	1.71×10^{-7}
	[/Device/Year]	0.29	1.23×10^{-5}	1.40×10^{-5}	6.24×10^{-5}
CDM SEFI SPI Reset Rate	**[/Device/Second]**	3.61×10^{-9}	1.52×10^{-13}	1.73×10^{-13}	7.69×10^{-13}
	[/Device/Day]	3.11×10^{-4}	1.31×10^{-8}	1.49×10^{-8}	6.65×10^{-8}
	[/Device/Year]	0.11	4.78×10^{-6}	5.46×10^{-6}	2.43×10^{-5}
CDM SEFI Power Cycle Rate	**[/Device/Second]**	1.03×10^{-9}	4.33×10^{-14}	4.94×10^{-14}	2.20×10^{-13}
	[/Device/Day]	8.90×10^{-5}	3.74×10^{-9}	4.27×10^{-9}	1.90×10^{-8}
	[/Device/Year]	0.03	1.37×10^{-6}	1.56×10^{-6}	6.93×10^{-6}

For the Telesat polar orbit and Telesat inclined orbit nominal and solar flare cases, the calculated CDM proton SEE rates are low – the expected proton SEE rates are less than 1 SEE per CDM per year. The observed CDM SEUs do not require any resets or power cycles and do not affect the optical modem performance. Thus, CDM SEUs will not cause any potential OISL "down time" or have any impact to the OISL system availability. CDM SEFIs, which require a SPI reset, have slight impact to optical modem performance. The SPI reset disrupts the optical coherent modem performance for a two second period, during which the coherent DSP ASIC has LOL and a burst of post-FEC uncorrected errors. After two seconds, coherent DSP ASIC re-locks and the post-FEC uncorrected error count returns to zero. CDM SEFIs, which require a CDM power cycle, impact the optical modem performance. After performing a CDM power cycle, it takes ~40 seconds for CDM ABC to converge and for the coherent DSP ASIC line-side to lock. Both CDM SEFIs will cause potential OISL "down time" or impact to the OISL system availability.

Future work for the commercial CDM could include a heavy ion radiation assessment to observe for heavy ion SEEs to the RF Driver IC, which is based on SiGe BiCMOS technology.

Chapter 6

Commercial Laser

An optical coherent communication modem requires two lasers to serve as local oscillator input to the coherent receiver and as an input to the modulator. The lasers must be tunable to set the required transmitter optical frequency and to adjust the receiver local oscillator based on Doppler shift effects in FSOC space applications. The fine frequency tuning range of the selected laser must encompass the expected Doppler shift. Otherwise, for an OISL application, the transmit laser on satellite A and the receive LO laser on satellite B must be tuned as a function of time and Doppler. To reduce degradation to FSOC system performance, particularly OSNR, the laser linewidth must be in the range of a few hundred kilohertz [Ip, 2008]. A narrow linewidth represents stable phase of the signal. Errors in the extracted phase information of the signal induce penalties to OSNR.

6.1 Space Qualification and Radiation Assessments of Commercial Lasers

There are numerous studies on space qualification and radiation assessments of commercial lasers, including the NASA NEPP program assurance research on opto-electronics, radiation assessments of semiconductor optical sources, and summaries of radiation-induced effects in lasers [Barnes et al., 2005; Adamiec et al., 2016; Hemmati, 2009]. This literature review is focused on commercial lasers for 1550 nm applications and based on InP material. Laser diodes for 1550 nm applications have InGaAsP active region on InP substrate [Johnston, 2001]. Displacement damage induced by proton radiation is the primary concern for semiconductor lasers [Todd and Farrell, 2006].

A commercial, Telcordia GR-468 qualified, planar waveguide (PW) external cavity diode laser (ECL), "PLANEX" by Redfern Integrated Optics (RIO) was space-qualified for the development of a fiber space laser solution for the GRACE Follow-On mission [Numata and Camp, 2012]. The RIO PLANEX has an optical output power from 10 mW to 20 mW, center wavelength along ITU grid from 1530 nm to 1565 nm, minimum thermal wavelength tuning range of 30 pm, and narrow linewidth of less than or equal to 15 kHz. Figure 75 shows the packaging of the RIO PLANEX laser [RIO, 2014].

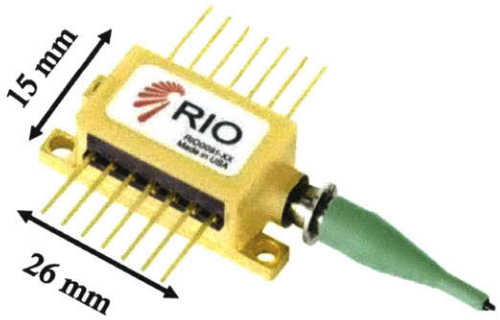

Figure 75. RIO PLANEX PW ECL Laser – Commercial laser space-qualified for NASA GRACE Follow-On Mission [RIO, 2014].

The RIO PLANEX PW-ECL laser cavity is formed by a high-reflective coated facet on an InP multiple quantum well gain chip and an anti-reflection coated waveguide grating formed in a silica-on-silicon PLC. The components are integrated into a 14-pin butterfly package (36 mm by 26 mm footprint) on top of thermoelectric cooler [RIO, 2014]. Space qualification tests included active thermal vacuum cycling between -10°C to 40°C over 1000 cycles, thermal cycling between 25°C to 80°C, hermeticity, gamma radiation to total dose level of 200 krad(Si), and proton radiation to total dose of a few krad with 20 and 50 MeV energy. Differences in the optical output power levels from a nominal level of 10 mW were observed in the range of 0.5 to 1.8 mW at temperature extremes during active thermal vacuum cycling. The differences were due to the temperature difference between the gain chip and the PLC at the temperature extremes. Similar steady performance was observed for temperature cycling tests. The module passed the hermeticity tested based on fine leak, gross leak and residual gas analysis. Small changes in center wavelength of +10 pm and in optical output power of – 0.30 dB were observed from the gamma radiation test. A maximum change in optical output power of -0.15 dB as well as a maximum change in the center wavelength of +50 pm with annealing recovery to +25 pm was observed from proton radiation tests. No mode hop or significant change to the phase noise performance was observed from the radiation tests. Numata and Camp [2012] can be referenced for further details of the results of the space qualification tests of the RIO PLANEX and for plots showing stable optical output power during thermal vacuum tests and change in optical output power from proton radiation tests.

In 2001, Johnston et al. studied proton damage in advanced commercial laser diodes with applications ranging from 650 nm to 1550 nm. The Mitsubishi ML976H11 InP/InGaAs DFB for 1550 nm application was tested with 50 MeV proton radiation, resulting in a shift in the threshold current from 10 mA to ~15 mA with fluence level of 3×10^{13} p/cm^2. Displacement damage induced by proton radiation did not induce any significant change (less than 0.2 nm) in wavelength for all the lasers in the study [Johnston et al., 2001]. Johnston and Tetsuo [2004] evaluated commercial 1550 nm InGaAsP laser diodes (C1550) by Lasermate for displacement damage effects. The study found a linear dependence of shift in threshold voltage with increasing proton fluence for the 1550 nm lasers but did not observe this effect for 1300 nm lasers [Johnston and ß, 2004]. The NASA NEPP program assurance research on opto-electronics studied gamma and proton radiation effects on commercial VCSELs and found these devices to be robust to radiation [Barnes et al., 2005].

Todd and Farrell [2006] completed a radiation hardness assessment of commercially widely tunable and DFB lasers, including Avanex DFB and JDSU DBR lasers in 14-pin butterfly packages for 1550 nm applications. The lasers were tested with 10 MeV protons to fluence of 4×10^{9} p/cm^2 and equivalent dose level of 2.2 krad and with 50 MeV protons to fluence of 6.4×10^{12} p/cm^2 and equivalent dose level of 101.5 krad. The butterfly packaging provided shielding for the lasers at low dose levels from 10 MeV protons and no significant radiation effects were observed on the lasers. For the 10 MeV proton test, the lasing threshold (lowest excitation level at which laser output is dominated by stimulated emission rather than by spontaneous emission) of the Avanex DFB laser did not change by more than 2% and the wavelength measurements had a variation of less than 2 pm. The JDSU DBR had a variation less than 0.5% in lasing threshold and did not have any observable change in the mode position. For the 50 MeV tests, the Avanex DFB lasing threshold increased linearly with fluence by up to 15% and the wavelength stability degraded with a shift up to 10 pm, based on potential degradation in temperature stability. The JDSU DBR had a 4% deviation in lasing threshold over the course of the 50 MeV proton test and there was a shift in the mode position. The mode pattern of the DBR laser did not change, implying that displacement damage effects impacted the laser efficiency but not the tunability of the laser. Todd and Farrell [2006] can be referenced for further details and plots of the 50 MeV proton test results of the Avanex DFB and JDSU DBR lasers.

Gooch and Housego are developing a space-qualified DFB laser in 14-pin butterfly package for 1550 nm applications as a part of the ESA "Space validation of High-power DFB laser at 1550 nm" program [MacDougall et al., 2017]. Specifications of the pre-qualification lot include optical power of 80 mW, linewidth of less than 650 kHz, isolation of greater than 32 dB, and power consumption at 65°C of less than 4.1 W. According to the Gooch and Housego evaluation test plan, qualification of the lasers will include tests, such as hermeticity, ionizing radiation, non-ionizing radiation, vibration, shock, thermal cycling, and thermal vacuum. No data has been released of the qualification testing of these DFB lasers.

6.2 RIO PLANEX for Optical coherent Modem Assembly Design

The RIO PLANEX is a strong candidate for the optical modem lasers, which are required as an optical input to the CDM and the local oscillator source to the μICR. The RIO PLANEX has flight heritage and meets optical modem laser performance requirements for linewidth, mode hop free tunability over ITU grid, and optical output power. The RIO PLANEX lasers are pre-set to a specific wavelength. For this work, two RIO PLANEX lasers were ordered with 1563.86 nm center wavelength (191.7 THz). One RIO laser was designated as the transmit laser, which provided the optical input to the CDM in the optical modem R-EDU (Chapter 3.6.1). The second laser was designated as the receive laser, which provided the μICR LO input in the optical modem R-EDU.

6.2.1 RIO Laser Characterization

The RIO lasers were characterized through laboratory measurements of the center wavelengths, peak optical power levels and linewidths. Benchtop laboratory testing was used to evaluate the coherent DSP ASIC carrier frequency offset (CFO) tolerance between the μICR signal and μICR LO.

6.2.1.1 Laser Center Wavelength Measurement

The optical spectrum of the transmit and receive lasers were measured with a JDSU Multiple Application Platform (MAP-200) high resolution optical spectrum analyzer (OSA). Figure 76(a) shows the spectrum of the transmit laser, and Figure 76(b) shows the spectrum of the receive laser. Both lasers have a center wavelength of 1563.86 nm. At the center wavelengths, the peak optical power of the transmit laser is 13.25 dBm and the peak optical power of the receive laser is 12.33 dBm. Both lasers are operating at 85% maximum power rating.

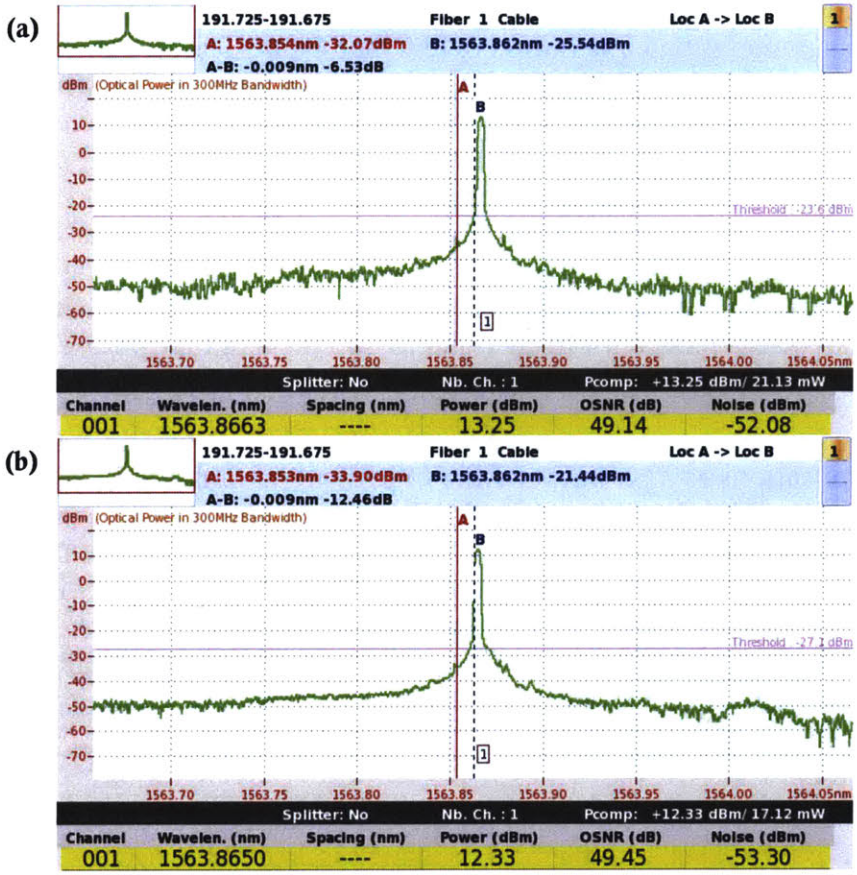

Figure 76. Optical spectrum of transmit and receive RIO PLANEX lasers, showing the center wavelength and peak optical power. (a) Transmit laser, (b) Receive laser.

6.2.1.2 Laser Linewidth Measurements

The laser output contains phase noise due to spontaneous emission noise amplified inside a resonant cavity. Laser phase noise will cause the signal constellation to rotate in a time-varying manner based on the instantaneous phase. Phase noise is characterized by linewidth, which is a two-sided 3 dB bandwidth of the laser spectrum. Lasers, which serve as a μICR LO, should have a linewidth of less than 100 kHz. ECLs, such as the RIO PLANEX, have linewidths on the order of tens of kilohertz, which is much faster than polarization changes [Ip, 2018].

The OEWaves OE400 phase noise measurement system was used to measure frequency versus frequency noise of the RIO lasers, shown in Figure 77. The linewidth is characterized

at the point where the frequency noise power spectral density (y-axis in Figure 77) is constant (white noise) and multiplied by factor of π [Ip, 2018]. In Figure 77, the transmit laser and receive laser frequency noise power spectral density becomes constant at ~ 200 Hz. With the factor of π, the transmit laser and receiver laser linewidths are ~600 Hz, which is below the RIO PLANEX linewidth specification of less than 15 kHz.

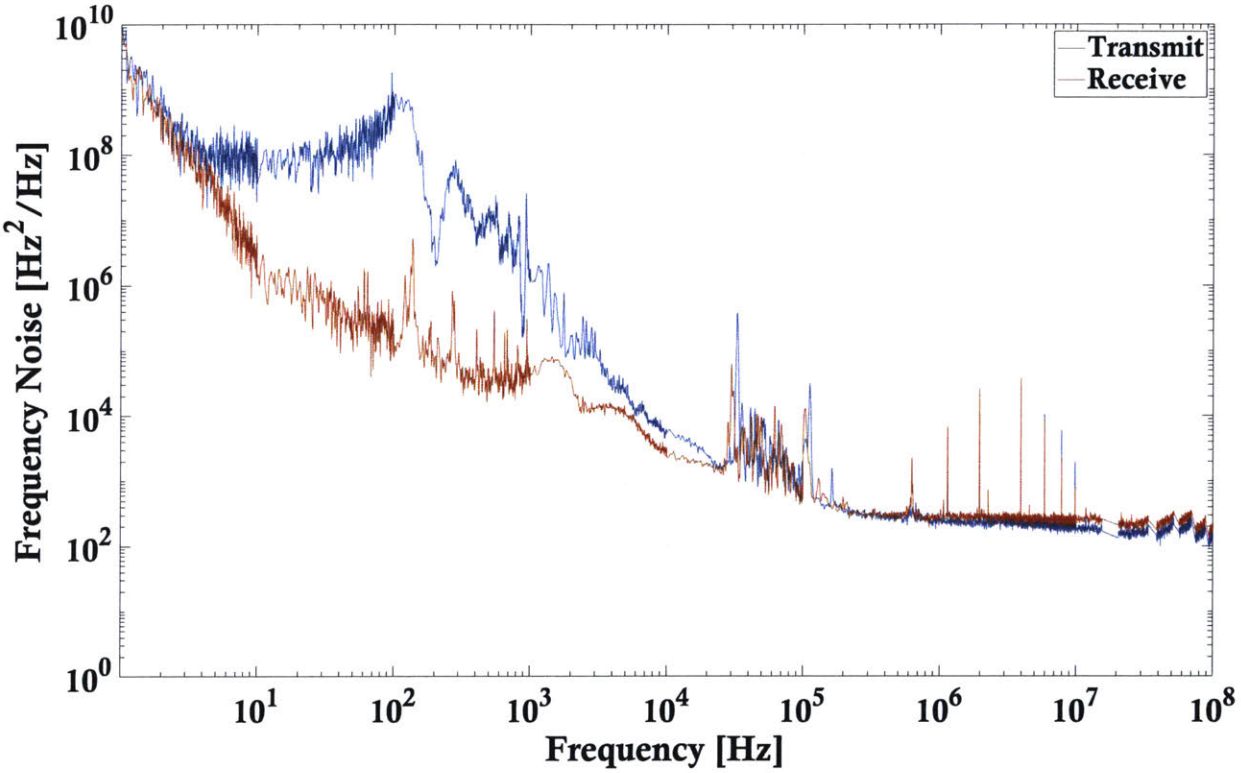

Figure 77. RIO PLANEX transmit and receive lasers frequency versus frequency noise power spectral density.

6.2.1.3 Carrier Frequency Offset Tests

The commercial optical coherent DSP ASIC with 16 nm FinFET plus CMOS technology (Chapter 3) includes a carrier frequency offset (CFO) measurement feature, which measures the frequency offset between the received optical signal and LO optical signal input to the μICR. Laboratory testing was completed to test shifting the laser center frequency by changing the laser TEC temperature setpoint and evaluate the CFO tolerance for the ASIC. The test was completed with the optical modem (OMA R-EDU) in a self-optical loopback configuration with the transmit path of the optical modem directly input to the receive path.

The nominal TEC temperature setpoint for the transmit RIO laser is 21.5 °C. Figure 78 shows the telemetry from the laser frequency offset test, based on sweeping the TEC temperature setpoint. A shift in the laser TEC temperature setpoint results in a shift in the laser center frequency. The transmit laser TEC temperature setpoint was swept from 26.5 °C to 16.5 °C (Figure 78(a.i)), while the receive laser (μICR LO) was fixed at its nominal TEC temperature setpoint of 22.5 °C. Based on the results of the transmit laser frequency offset test, the coherent DSP ASIC can tolerate a CFO of -7.71 GHz to +0.14 GHz without line-side performance degradation, such as loss of lock, post-FEC uncorrected errors bursts, and pre-FEC BER

below the required threshold of 2×10^{-2}. Figure 81(a.ix) shows the ASIC CFO measurement changing with transmit laser TEC temperature sweep in setpoint from 26.5 °C to 16.5 °C shown in Figure 81(a.i). ASIC performance telemetry is shown in Figure 81(a.x) through Figure 81(a.xii). The yellow box in Figure 78(a) indicates the CFO tolerance range without ASIC line-side performance degradation for all the telemetry. The coherent DSP ASIC had no LOL for CFO between -7.90 GHz and +2.72 GHz, although there were post-FEC uncorrected errors.

In Figure 78(b.i), the transmit laser TEC temperature setpoint was swept in the reverse direction from 16.5 °C up to 26.5 °C while the receiver laser (μICR LO) TEC temperature setpoint was fixed at its nominal value. For CFO between +5.67 GHz to +0.33 GHz, there was no performance degradation to the coherent DSP ASIC, specifically no LOL, no post-FEC uncorrected errors, and pre-FEC BER remained below threshold. The yellow box in Figure 78(b) indicates the CFO tolerance range without ASIC line-side performance degradation for all the telemetry.

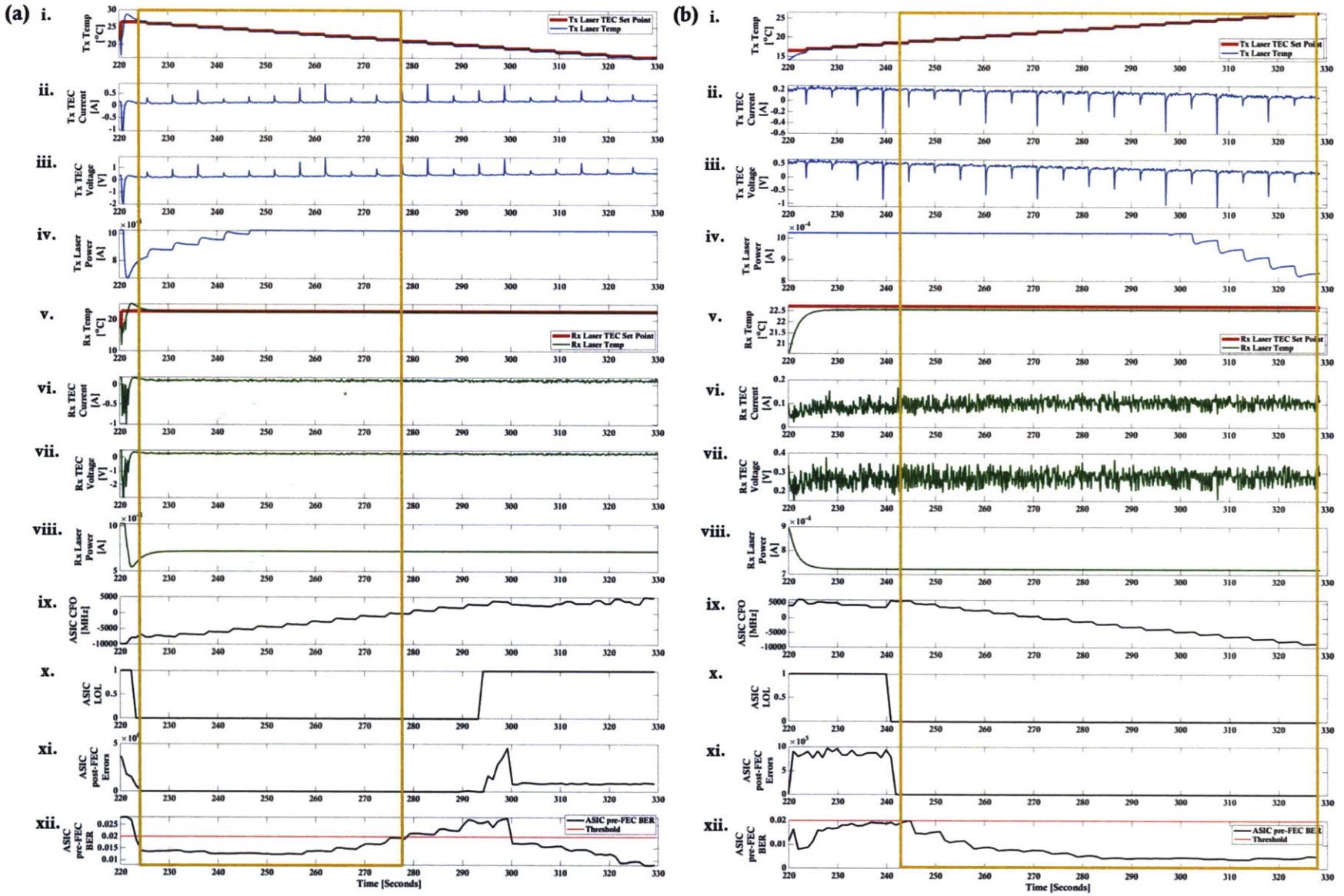

Figure 78. Transmit laser frequency offset test, based on sweeping the TEC temperature setpoint between 26.5 °C and 16.5 °C.

A Doppler shift analysis was completed for the Telesat OISL constellation in Chapter 2.2. For the Telesat inclined orbit, the highest Doppler shift values are +/- 5.44 GHz. For the Telesat polar orbit, the highest Doppler shift values between satellites in adjacent planes are +/-2.053 GHz, and the highest Doppler shift values between satellites in planes at the seam of the constellation are +/-7.86 GHz. Based on the Doppler shift analyses, we defined requirement L1-04 "The optical coherent DSP ASIC shall compensate for carrier frequency offset (CFO) of ≤ - 5.5 GHz and ≥ + 5.5 GHz with less than 1.0 dB impact to OSNR" [Table 16].

Initial laboratory tests with RIO lasers as CDM optical input (direct loopback into μICR optical input) and μICR LO indicate the commercial optical coherent DSP ASIC with 16 nm FinFET plus CMOS technology can tolerate a CFO between -7.71 GHz and +5.67 GHz. The CFO tolerance range of the ASIC encompasses the expected Doppler shift values for OISLs in the Telesat inclined orbit and non-seam Telesat polar orbit. The coherent DSP ASIC with 16 nm FinFET plus CMOS technology meets requirement L1-04. Coherent DSP ASICs can compensate for CFO and frequency noise with penalty to performance, such as the ROSNR [Bennett et al., 2014]. We expect the CFO will have a penalty to the coherent DSP ASIC ROSNR of less than 1 dB. This impact will have to be considered for the optical link budget requirements.

The system requirement L0-08 states "The optical coherent modem shall tolerate Doppler shift between -8.0 and +8.0 GHz." To meet requirement L0-08, additional modifications to the RIO lasers in the coherent modem system must be implemented to compensate for the expected Doppler shift beyond the coherent DSP ASIC CFO tolerance.

6.3 Proposed Modifications for RIO Laser

To use the RIO lasers in the optical coherent modem for OISL application, a laser control circuit with temperature monitor, TEC driver, and current controller must be developed for setting and maintaining the required laser optical output signal frequency through temperature control.

A control loop can be developed to compensate for expected Doppler shift on the receive optical input signal, by adjusting the frequency of the Rx LO laser. This control loop can be used to minimize the CFO compensation of the coherent DSP ASIC and reduce OSNR penalty to the link budget and expand the optical coherent modem Doppler shift tolerance since the coherent DSP ASIC has a limited range of CFO compensation. Figure 79 shows a functional block diagram of an example Rx LO Doppler shift control loop and external laser control circuitry. Both the Rx LO signal with set center frequency (Figure 79 label 1B) and the received optical signal with shifted frequency due to Doppler shift (Figure 79 label 1A) are input to the μICR. The differential voltage signals (phase information of the QPSK signal) output from the μICR (Figure 79 label 2) are input to the commercial optical coherent DSP ASIC. The commercial optical coherent DSP ASIC can detect the carrier frequency offset (CFO) between the Rx LO and Rx signal input and provide this output (Figure 79 label 3) to the Zynq SoC. The Zynq SoC can use the CFO information to adjust the temperature cavity of the Rx Lo through the external laser control circuitry (Figure 79 label 4). The OMA EDU described in Chapter 8 will incorporate the Rx LO Doppler shift control loop and external control circuitry.

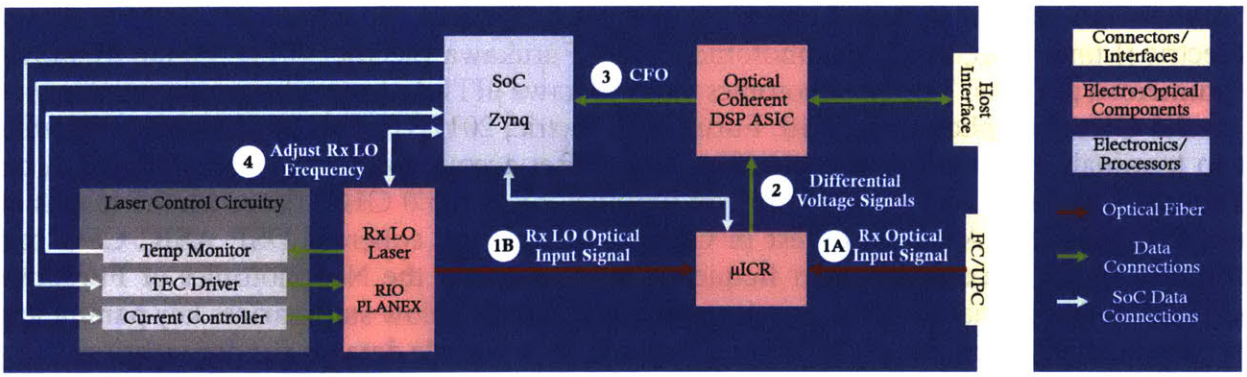

Figure 79. Functional block diagram of the Rx LO Doppler shift control loop and external laser control circuitry.

6.4 Commercial Lasers for Future Consideration

The first "Tunable Laser Implementation Agreement" was released by OIF in 2002 (OIF-TL-01.1) and served as the building block for subsequent IAs based on the development of tunable continuous wave (CW) lasers for coherent systems. The "Integrable" Tunable Laser Assembly (ITLA) MSA (OIF-ITLA-MSA 1.1, OIF-ITLA-MSA 1.2) was released in 2005 and updated in 2008. This IA standardized a CW laser subassembly for integration into both the 3.5" by 4.5" transponder and small form factor transponder. The most recent OIF IA released is the "Micro" ITLA (2015), which defines an alternate smaller form-factor than previous ITLA modules with 60% reduction in area and 30% reduction in height as well as lower power consumption by 25% while maintaining the performance of an ITLA [Lightwave, 2011]. The total length of the module, including the fiber boot area, is 65 mm, the width of the module is 20 mm, and the height of the module is 7.5 mm. The maximum temperature rating ranges from -5°C to + 75°C , and the absolute maximum rating for total power dissipation is 5W [OIF-MicroITLA-01.1, 2015].

Commercial μITLAs can include an additional microcontroller or CPU, which interfaces to a semiconductor optical amplifier (SOA) for optical output power control as well as a temperature monitor, thermal electric cooling (TEC) driver, laser current source, and frequency locker, for frequency tuning, stabilization, and control. Figure 80 shows a block diagram of a general μITLA module.

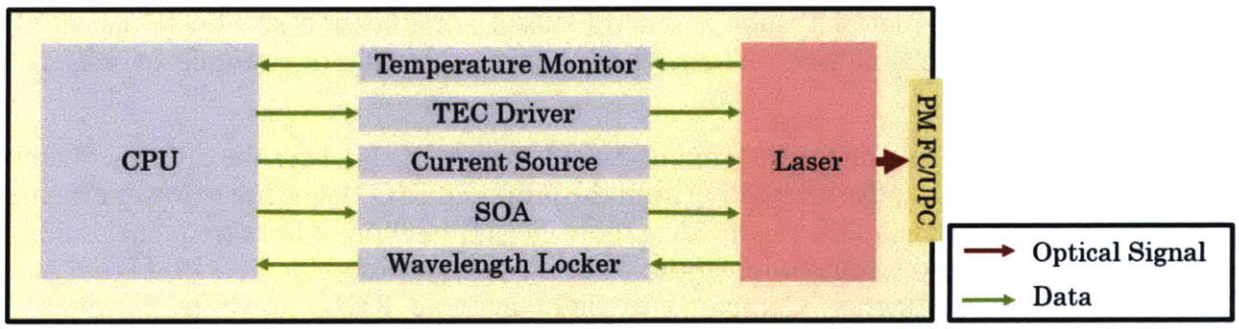

Figure 80. Functional block diagram of μITLA

Some μITLA vendors include Lumentum (previously Oclaro), Neophotonics, and Furukawa Electric [Lumentum, 2018; Neophotonics, 2018; Furukawa Electric, 2017]. Figure 81 shows commercial μITLAs. The Neophotonics and Furikawa μITLAs have a frequency accuracy of +/- 2.5 GHz [Neophotonics, 2018; Furukawa Electric, 2017]. For an OISL application with two terminals, the maximum center frequency offset accounting for the transmit μITLA on terminal 1 and the receive LO μITLA on terminal 2 is +/- 5.0 GHz. Based on the results of the coherent DSP ASIC CFO test in Chapter 6.2.1.3, the coherent DSP ASIC CFO can compensate for maximum center frequency inaccuracy for the Neophotonics or Furikawa μITLAs with minimal performance degradation. Table 59 below summarizes key parameters of commercially available μITLAs based on publicly available data on vendor websites.

Figure 81. Commercial micro-integrable tunable laser assemblies from (a) Neophotonics, (b) Lumentum, and (c) Furukawa. [Lumentum, 2018; Neophotonics, 2018; Furukawa Electric, 2017]

Table 59. Commercially available micro-integrable tunable laser assemblies.

Vendor – Part	Linewidth	Maximum Optical Output Power	Frequency Accuracy	Maximum Power Consumption
Neophotonics	-	+17.0 dBm	[-2.5, +2.5] GHz	4.6 W
Lumentum TL5400	< 100 kHz	+17.0 dBm	-	-
Furikawa	100 kHz	+19.0 dBm	[-2.5, +2.5] GHz	5 W

The Lumentum TL5400 μITLA is a DS-DBR laser based on fully monolithic InP chip [Lumentum, 2019]. Recent laser technology has been developed using integration of InP on silicon PICs [Dong et al., 2015]. Single mode distributed feedback (DFB) and distributed Bragg reflector (DBR) lasers have been developed by etching Bragg gratings on silicon waveguides with III-V material, such as an InP-based amplification section [Duan et al., 2014]. Duan et al. [2014] can be referenced for images showing an example hybrid III-V silicon laser.

Using commercial μITLAs as the transmit laser and receive LO laser for the optical coherent modem would be an attractive alternative from the proposed RIO lasers due to lower cost and lower SWaP. Commercial μITLAs provide a more elegant method of laser frequency tuning, in comparison to the proposed modifications of using a control loop for RIO PLANEX laser center frequency adjustments. Compared to flight heritage RIOs, however, commercial μITLAs have risks which have not yet been mitigated with space qualification testing, such as radiation testing.

The commercial supporting electronics and microcontroller included with μITLAs are susceptible to radiation effects. These components would need to be radiation tested to evaluate the radiation sensitivity, particularly to SEEs. Commercial μITLAs are individually calibrated, and the calibration data is stored in non-volatile memory in the microcontroller. Commercial flash memories are sensitive to total ionizing dose (TID) effects and SEEs [Gerardin et al., 2013; Bagatin, 2018]. As InP-based technologies, μITLAs would be susceptible to radiation effects from DDD. A proton radiation assessment of commercial μITLAs would be completed to evaluate SEEs, TID effects, and DDD effects. Commercial μITLAs are currently not sold as "gold boxes" without supporting electronics. If vendors sell μITLAs as "gold boxes" in the future, the supporting electronics and microcontroller could be replaced with radiation tolerant commercial components or radiation hardened space grade components.

Chapter 7

Summary

7.1 Contributions

In this work we developed the electro-optical design of an optical coherent modem for LEO-to-LEO in-plane and cross-plane optical inter-satellite links (OISLs) with improvement in data rate performance by 10 times from state of the art [DLR, 2008]. The optical coherent communications modem was designed for data rate of 100 Gbps using COTS components from telecommunications industry, including an optical coherent DSP ASIC, a coherent transmitter, a coherent receiver, and two lasers. The key innovation of this work is the design of a LEO OISL optical coherent modem, based on discrete optical coherent COTS, as a reliable and fault tolerant system to space radiation effects. The novelty of this work is the design of a radiation mitigation approach with hardware, software, and firmware techniques for minimal system impact and recovery time. This work makes the following contributions:

1. Developed a process to select commercial optical coherent technologies, which can meet the performance requirements
2. Assessed the selected commercial optical coherent technologies for the LEO space environment
3. Identified and developed cost-effective modifications, which ensure the optical coherent modem meets performance requirements and operates successfully in space.

Figure 82 shows a high-level, functional block diagram of the 100 Gbps optical coherent modem with the selected commercial optical coherent technologies and the cost-effective modifications for LEO-to-LEO OISL space use. The optical modem assembly (OMA) engineering development unit (EDU) was developed for laboratory characterization and radiation testing of the commercial optical coherent components.

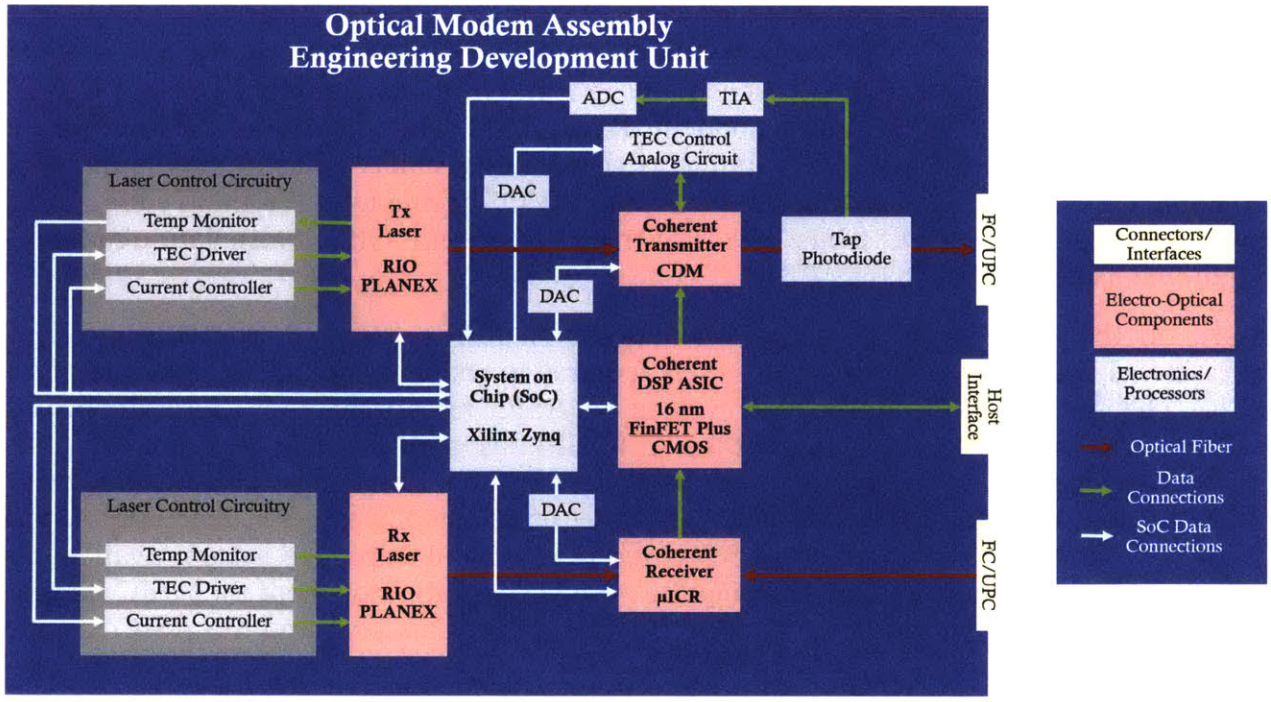

Figure 82. Functional block diagram of 100 Gbps coherent optical modem assembly engineering development unit

7.1.1 LEO OISL Requirements

The Telesat constellation was used as the OISL application case study for this work. Chapter 2 includes the details of defining performance requirements for the optical coherent modem based on the Telesat OISL application. The Telesat constellation radiation environment was modeled and used to generate radiation requirements for the optical coherent modem. The Telesat constellation polar orbit and inclined orbit were modeled and used to determine the expected Doppler shift values and OISL ranges. A LEO-to-LEO OISL link budget analysis for a 100 Gbps system was used to evaluate the open trade space for the OISL system design. The radiation environment, orbit modeling, and link budget analyses were used to define requirements for the optical coherent modem and to select commercial optical coherent components for the modem. Table 16 in Chapter 2.4 lists the requirements used for the design of the 100 Gbps optical coherent modem for LEO-to-LEO OISL application.

7.1.2 Optical Coherent DSP ASIC

The commercial optical coherent DSP ASIC with 16 nm FinFET plus CMOS technology was the selected coherent DSP ASIC for the OISL coherent modem. The ASIC has lower power consumption and lower ROSNR in comparison to previous generation coherent DSP ASICs. The selected ASIC meets all L1 requirements for the coherent DSP ASIC.

Benchtop laboratory testing in Chapter 6 showed the carrier frequency offset (CFO) tolerance range of the ASIC encompasses the expected Doppler shift values for OISLs in the Telesat inclined orbit and non-seam Telesat polar orbit and meets requirement L1-04.

Two heavy ion assessments and a proton radiation assessment of this coherent DSP ASIC were completed. The ASIC was exposed to heavy ion radiation up to LET of 65

MeV·cm^2/mg, and up to proton fluence level of 1.01×10^{12} p/cm^2 or equivalent TID of 91.6 krad(Si). There were no destructive heavy ion or proton SELs observed in the assessments, reducing the risk of increased SEL sensitivity in FinFET in comparison to planar CMOS technologies for this commercial component [Karp, 2018]. The calculated SEE rates for the nominal heavy ion and proton environments show the feasibility of using the commercial coherent DSP ASIC with 16 nm FinFET plus CMOS technology for the Telesat OISL constellation or similar LEO orbits. The ASIC meets the Telesat OISL constellation radiation requirements defined in Chapter 2.1.

Based on the seven types of heavy ion and proton SEFIs observed from the radiation assessments, we propose four types of resets required to restore nominal functionality of the ASIC. The four resets include a power cycle of the ASIC, reset of the ASIC, reset of only the ASIC internal microprocessor, reset of the ASIC SPI bus, and reset of the external circuitry for ASIC temperature sensors. SEFIs to the ASIC will cause downtime for optical links and impact system availability based on the ASIC reset time period. Chapter 7.2 includes further details of expected downtime due to ASIC reset period and impact to system availability. Future work would include collaborating the ASIC vendor to implement the ASIC internal microprocessor reset without disruption to the transceiver data path and the ASIC SPI bus reset.

As seen in Figure 82, we designed the OMA EDU using the Xilinx Zynq Ultrascale+ SoC to initialize and sequence the power supply for bring-up of the coherent DSP ASIC. The Zynq SoC is a hardware modification to replace the commercial FPGA typically used in coherent DSP ASIC evaluation boards. Numerous radiation assessments of the Zynq Ultrascale+ SoC have shown the potential of using this SoC in LEO radiation environments. Designing a coherent modem for space application will require designing a thermal control solution for the coherent DSP ASIC such as heat sinking the ASIC to the chassis of the coherent modem.

7.1.3 Coherent Receiver

A commercial micro-intradyne coherent receiver (μICR) was selected as the coherent receiver for the OISL coherent modem. The selected μICR meets all L1 requirements for the coherent receiver. Commercial μICRs are based on Indium Phosphide (InP) photonic integrated circuits (PICs), which have allowed for miniaturization, cost reduction, high volume manufacturability, and high symbol rate capabilities in comparison to previous ICRs [Takechi et al., 2013].

As seen in Figure 82, we developed the OMA EDU with the Xilinx Zynq Ultrascale+ SoC to implement a PID control loop for external AGC of the μICR TIAs. The μICR TIA control loop modification includes operating the μICR TIAs in MGC mode and implementing AGC through an external circuit with the coherent DSP ASIC, Zynq SoC, and DAC. Operating the TIAs in MGC mode requires less peripheral circuitry than AGC mode, and thus serves as lower radiation risk. The OMA R-EDU was designed with the ability to perform a reset of the μICR.

A proton radiation assessment of two identical μICRs was completed. We observed SEEs, which appear to be SETs. These SEEs did not require any reset or power cycle and did not have any impact to the system performance. There was no component or system performance degradation observed from the proton radiation assessments to fluence level of 1.22×10^{12}

p/cm^2 or equivalent TID of 110.4 krad(Si). The expected proton SEE rates are less than one SEE per μICR per year and will not cause any potential OISL "down time" or have any impact to the OISL system availability. Based on the results of our test campaign, the commercial μICR appears robust to the Telesat OISL LEO radiation environment.

7.1.4 Coherent Transmitter

A commercial coherent driver modulator (CDM) was selected as the coherent transmitter for the OISL coherent modem because of (1) the integration of the modulator driver with the modulator in a smaller package than previous PM-Q modulators and (2) the capability to support 100 Gbps with 32 Gbaud symbol rate and up to 400 to 600 Gbps with 64 Gbaud symbol rate. The selected CDM meets all L1 requirements for the coherent transmitter.

As seen in Figure 82, the OMA EDU used the Zynq Ultrascale+ SoC as the replacement to the commercial microcontroller, which is typically used for CDM TEC control and ABC control. The FPGA in the Xilinx Zynq SoC was used to implement a PID controller for CDM ABC and TEC control. We developed a software feature, which is implemented through the Zynq SoC, to check static read registers and read–write registers against a register data file in Zynq memory, throw an error message if an anomalous register value was detected, and correct any anomalous read-write register values. The software feature was successful in correcting flipped bits in the read-write registers of the CDM SPI bus during proton radiation testing. The OMA R-EDUs were designed with CDM SPI reset and CDM power cycle capabilities.

A proton radiation assessment of two identical CDMs was completed. Two types of SEUs and two types of SEFIs were observed. The proton SEEs were bit flips in the CDM SPI register and effects on the RF driver IC. The "stuck bit" SEFIs required a CDM SPI reset. The SEFI to the RF driver IC impacted system performance (loss of lock for GOMA R-EDU coherent DSP ASIC) and required a CDM power cycle. Both CDM SEFIs will cause potential OISL "down time" or impact to the OISL system availability. For the Telesat OISL constellation and similar LEO environments, the commercial CDM is a viable solution for the coherent transmitter since the expected proton SEE rates are less than 1 SEE per CDM per year. Since no component or system performance degradation was observed up to fluence level of 1.22×10^{12} p/cm^2 or equivalent TID of 110.4 krad(Si), the commercial CDM meets the Telesat OISL radiation requirements.

7.1.5 Lasers

The RIO PLANEX was selected for the transmit laser source and coherent receiver LO because it meets the coherent modem requirements for center wavelength range, output optical power, and laser linewidth. The RIO PLANEX has space flight heritage and has been space qualified with active thermal cycling, gamma radiation testing up to TID level of 200 krad(Si), and proton radiation testing with 20 MeV and 50 MeV protons [Numata and Camp, 2012].

We performed benchtop laboratory testing of two RIO PLANEX lasers, which served as a transmit laser source into the CDM and as the μICR LO input on the OMA R-EDU. We characterized the center wavelengths, optical output power, and laser linewidth of the lasers. We tested shifting the laser center frequency by changing the laser TEC temperature setpoint

and analyzed the changes to the CFO telemetry and line-side performance of the coherent DSP ASIC.

As seen in Figure 82, a laser control circuit with temperature monitor, TEC driver, and current controller was designed to set and maintaining the required laser optical output signal frequency through temperature control. A control loop must be developed to compensate for expected Doppler shift on the receive optical input signal, by adjusting the frequency of the Rx LO laser. This control loop can be used to (1) minimize the CFO compensation of the coherent DSP ASIC and reduce OSNR penalty to the link budget and (2) expand the optical coherent modem Doppler shift tolerance since the coherent DSP ASIC has a limited range of CFO compensation.

7.1.6 Summary of Cost-Effective Modifications and Impact

The modifications for the key electro-optical components are summarized in Table 60. Table 60 includes the impact of the modifications to the optical coherent modem for OISL application and indicates if the modification was implemented in the OMA EDU or will be evaluated in future work.

Table 60. Summary of modifications for key electro-optical components and impact to optical coherent modem for OISL application.

Modification		Impact	Status
Coherent DSP ASIC – 16 nm FinFET plus CMOS Technology			
A1	**ASIC Reset Capability – Only Internal Embedded Microprocessor**	Restores nominal line side pre-FEC BER values and resolves persistent line and host post-FEC errors after proton or heavy ion SEFI	Future Work
A2	**ASIC Reset Capability – Only SPI Interface**	Restores loss in coherent DSP ASIC telemetry induced by proton or heavy ion SEFI	Future Work
A3	**Full ASIC Reset Capability**	Restores nominal line side pre-FEC BER values and resolves persistent line and host post-FEC errors after proton or heavy ion SEFI	Implemented on OMA EDU
A4	**ASIC Power Cycle Capability**	Restores nominal temperature sensor values after proton or heavy ion SEFI	Implemented on OMA EDU
A5	**Reset ASIC External Temperature Sensor Circuitry Capability**	Restores nominal temperature sensor values after proton or heavy ion SEFI	Implemented on OMA EDU
A6	**Xilinx Zynq Ultrascale+ SoC to bring up, initialize, reset, and power cycle coherent DSP ASIC**	Reduces radiation sensitivity: Xilinx Zynq SoC is more radiation tolerant than the typical commercial FPGA used to bring up, initialize, reset, and power cycle coherent DSP ASIC	Implemented on OMA EDU
Coherent Receiver – Micro-Intradyne Coherent Receiver (μICR)			
R1	**μICR TIA Manual Gain Control (MGC) Mode with PID Control Loop**	Reduces radiation sensitivity: less supporting EE-component circuitry compared to AGC mode. PID control loop ensures TIA gain voltages set to sufficient levels required for coherent DSP ASIC.	Implemented on OMA EDU
R2	**μICR Reset Capability**	Restores potential anomalous behavior observed in TIAs induced by proton or heavy ion SEFI *Did not need to use during radiation testing	Implemented on OMA EDU
Coherent Transmitter – Coherent Driver Modulator (CDM)			

T1	**Automatic Bias Control (ABC) circuit using external tap photodiode and Xilinx Zynq Ultrascale+ SoC for PID controller**	Reduces radiation sensitivity: Xilinx Zynq SoC is more radiation tolerant than the typical commercial microcontroller used for CDM ABC	Implemented on OMA EDU
T2	**TEC control circuit using Zynq SoC for PID controller**	Reduces radiation sensitivity: Xilinx Zynq SoC is more radiation tolerant than the typical commercial microcontroller used for CDM TEC control	Implemented on OMA EDU
T3	**CDM SPI register software checker and corrector**	Restores CDM SPI bus flipped bits in read-write registers from proton SEEs	Implemented on OMA EDU
T4	**CDM SPI Reset Capability**	Restores stuck flipped bits in CDM SPI bus static read registers from proton SEEs	Implemented on OMA EDU
T5	**CDM Power Cycle Capability**	Restores nominal CDM functionality after proton SEFI occurs	Implemented on OMA EDU
		Lasers – RIO PLANEX	
L1	**Receive local oscillator laser control loop with coherent DSP ASIC CFO measurement & Xilinx Zynq Ultrascale+ SoC**	Compensates for expected Doppler shift to receive optical input signal	Future Work
L2	**Transmit and receive laser control circuits with temperature monitor, TEC driver, and current controller**	Sets and maintains required laser optical output center wavelength using temperature control	Implemented on OMA EDU

7.2 Optical Coherent Modem System Proton SEE Rate and Availability

The optical coherent modem system proton SEE rate is calculated from the sum of the coherent component proton SEE rates, which impact the optical coherent modem system performance (coherent DSP ASIC line-side loss of lock, post-FEC uncorrected errors, and increased pre-FEC BER above threshold) or cause "down time" during reset or power cycle. The contributing proton SEE rates include coherent DSP ASIC SEFIs, which require an ASIC reset and ASIC power cycle, and CDM SEFIs, which require a CDM SPI bus reset and CDM power cycle. CDM SEUs and μICR SEEs did not impact system performance and did not require any resets or power cycles of the device. Table 61 and Table 62 show the calculated optical coherent modem system SEE rates for the Telesat polar orbit and Telesat inclined orbit, respectively.

Table 61. Optical coherent modem system proton SEE rate for Telesat polar orbit

Component / SEE Type	SEE Rate	Nominal	Solar Flare		
			Worst Week	Worst Day	Peak 5 Minutes
ASIC SEFI Reset	[/Device/Second]	1.39×10^{-8}	5.42×10^{-8}	2.10×10^{-7}	7.65×10^{-7}
	[/Device/Day]	1.21×10^{-3}	4.69×10^{-3}	1.82×10^{-2}	6.61×10^{-2}
	[/Device/Year]	0.44	1.71	6.63	24.14
ASIC SEFI Power Cycle	[/Device/Second]	5.38×10^{-10}	2.09×10^{-9}	8.10×10^{-9}	2.95×10^{-8}
	[/Device/Day]	4.65×10^{-5}	1.81×10^{-4}	7.00×10^{-4}	2.55×10^{-3}

	[/Device/Year]	0.02	0.07	0.26	0.93
CDM SEFI SPI Reset	[/Device/Second]	7.79×10^{-10}	3.03×10^{-9}	1.17×10^{-8}	4.28×10^{-8}
	[/Device/Day]	6.73×10^{-5}	2.62×10^{-4}	1.01×10^{-3}	3.69×10^{-3}
	[/Device/Year]	0.02	0.10	0.37	1.35
CDM SEFI Power Cycle	[/Device/Second]	2.23×10^{-10}	8.66×10^{-10}	3.35×10^{-9}	1.22×10^{-8}
	[/Device/Day]	1.92×10^{-5}	7.48×10^{-5}	1.90×10^{-4}	1.06×10^{-3}
	[/Device/Year]	7.02×10^{-3}	0.03	0.07	0.39
Coherent Modem System SEE	**[/Device/Second]**	1.55×10^{-8}	6.02×10^{-8}	2.33×10^{-7}	8.50×10^{-7}
	[/Device/Day]	1.34×10^{-3}	5.20×10^{-3}	2.01×10^{-2}	7.34×10^{-2}
	[/Device/Year]	0.49	1.90	7.32	26.80

Table 62. Optical coherent modem system proton SEE rate for Telesat inclined orbit

Component / SEE Type	**SEE Rate**	**Nominal**	**Solar Flare**		
			Worst Week	**Worst Day**	**Peak 5 Minutes**
ASIC SEFI Reset	[/Device/Second]	6.47×10^{-8}	2.72×10^{-12}	3.10×10^{-12}	1.38×10^{-11}
	[/Device/Day]	5.59×10^{-3}	2.35×10^{-7}	2.68×10^{-7}	1.19×10^{-6}
	[/Device/Year]	2.04	8.58×10^{-5}	9.79×10^{-5}	4.35×10^{-4}
ASIC SEFI Power Cycle	[/Device/Second]	2.49×10^{-9}	1.05×10^{-13}	1.19×10^{-13}	5.31×10^{-13}
	[/Device/Day]	2.15×10^{-4}	9.04×10^{-9}	1.03×10^{-8}	4.59×10^{-8}
	[/Device/Year]	0.08	3.30×10^{-6}	3.76×10^{-6}	1.67×10^{-5}
CDM SEFI SPI Reset	[/Device/Second]	3.61×10^{-9}	1.52×10^{-13}	1.73×10^{-13}	7.69×10^{-13}
	[/Device/Day]	3.11×10^{-4}	1.31×10^{-8}	1.49×10^{-8}	6.65×10^{-8}
	[/Device/Year]	0.11	4.78×10^{-6}	5.46×10^{-6}	2.43×10^{-5}
CDM SEFI Power Cycle	[/Device/Second]	1.03×10^{-9}	4.33×10^{-14}	4.94×10^{-14}	2.20×10^{-13}
	[/Device/Day]	8.90×10^{-5}	3.74×10^{-9}	4.27×10^{-9}	1.90×10^{-8}
	[/Device/Year]	0.03	1.37×10^{-6}	1.56×10^{-6}	6.93×10^{-6}
Coherent Modem System SEE	**[/Device/Second]**	7.18×10^{-8}	3.02×10^{-12}	3.45×10^{-12}	1.53×10^{-11}
	[/Device/Day]	6.20×10^{-3}	2.61×10^{-7}	2.98×10^{-7}	1.32×10^{-6}
	[/Device/Year]	2.26	9.53×10^{-5}	1.09×10^{-4}	4.83×10^{-4}

For optical coherent modems in the Telesat polar orbit, the expected system SEE rate is 0.49 SEEs per modem per year for the nominal trapped proton environment and 26.80 SEEs per modem per year for worst case proton solar flare environment based on peak 5 minute solar flare model. For optical coherent modems in the Telesat inclined orbit, the expected system SEE rate is 2.26 SEEs per modem per year for the nominal trapped proton environment and significantly less than 1 (10^{-5} to 10^{-4}) SEEs per modem per year for worst case proton solar flare environment.

The optical coherent modem system availability is calculated based on the proton SEE rates and expected "down time" from performing the reset or power cycle (Table 63). For the OMA prototype and OMA R-EDU, performing an ASIC reset or ASIC power cycle takes ~60 seconds for the ASIC line-side to establish lock and nominal functionality. We assume an

ASIC reset period or power cycle period of 90 seconds (additional 50% margin from 60 seconds) for system outage time. For the OMA R-EDU, performing a CDM SPI reset takes 2 seconds for the ASIC line-side to establish lock. The CDM SPI reset causes a 2 second gap in CDM telemetry, but CDM ABC is not impacted. For the availability calculations, we assume an outage period of four seconds for CDM SPI reset. After performing a CDM power cycle on the OMA R-EDU, it takes a period of ~40 seconds for CDM ABC to converge and for the coherent DSP ASIC on the OMA R-EDU to lock on the line-side. For the availability calculations, we assume an outage period of 60 seconds (additional 50% margin from 40 seconds) for CDM power cycle.

Table 63. Optical coherent modem system availability calculations for Telesat constellation

Orbit	Nominal	Solar Flare		
		Worst Week	Worst Day	Peak 5 Minutes
Telesat Polar	99.99988%	99.99954%	99.99820%	99.99347%
Telesat Inclined	99.99945%	≥ 99.99999%	≥ 99.99999%	≥ 99.99999%

For the nominal trapped proton environment cases, the Telesat polar orbit and Telesat inclined orbit OISL system availability is greater than 99.999% ("five nines"), which is the typical required availability for satellite operators and commercial industry [Young, 2010]. The Telesat polar orbit OISL system availability is greater than 99.99% ("four nines") for the worst case proton solar flare environments based on the worst day and peak 5 minute solar flare modes. The Telesat inclined orbit OISL system availability is greater than 99.99999% ("seven nines") for all worst case proton solar flare environment modeled.

The OISL system downtime can be further reduced if redundant optical coherent modems are used on a single satellite. The OISL system would need to include a switch with capability to switch between modems during a reset.

7.3 Future Work

For the selected optical coherent components, future work should include additional radiation assessments. Heavy ion radiation test campaigns could be used to test more coherent DSP ASICs and to test the ASICs at different angles. Heavy ion radiation assessments of the commercial μICR and CDM could be completed to evaluate heavy ion SEEs on the devices. Additional proton radiation test campaigns could be completed to test more coherent DSP ASIC devices and to test coherent DSP ASIC, μICRs, and CDMs at different proton energy levels.

Future collaboration with the coherent DSP ASIC vendor could be used to develop proposed ASIC reset techniques. Performing resets to the coherent DSP ASIC SPI bus or to the internal microprocessor without disrupting transceiver data path could be used to mitigate SEFIs while reducing system outage time. Performing a full ASIC reset or power cycle typically will result in ~ 60 seconds of OISL system "downtime."

Using commercial μITLAs as the transmit laser and receive LO laser for the optical coherent modem would be an attractive alternative from the proposed RIO lasers due to lower cost and lower SWaP. Commercial μITLAs provide a more elegant method of laser frequency tuning,

in comparison to the proposed modifications of using a control loop for RIO PLANEX laser center frequency adjustments. Compared to flight heritage RIOs, however, commercial μITLAs have risks which have not yet been mitigated with space qualification testing, such as radiation testing. The commercial supporting electronics and microcontroller included with μITLAs are susceptible to radiation effects. These components would need to be radiation tested to evaluate the radiation sensitivity, particularly to SEEs. Commercial μITLAs are currently not sold as "gold boxes" without supporting electronics. If vendors sell μITLAs as "gold boxes" in the future, the supporting electronics and microcontroller could be replaced with radiation tolerant commercial components or radiation hardened space grade components.

The terrestrial fiber optic communications industry is rapidly developing next generation optical coherent technologies, such as coherent DSP ASICs with 7 nm FinFET plus CMOS technology [Melle, 2018; Stiller, 2018]. The coherent DSP ASICs with 7 nm FinFET technology are developed for 16-QAM 400 Gbps applications and samples of these ASICs will be released in late 2019 to early 2020 [OFC, 2019]. An optical coherent modem with the new coherent DSP ASICs could be used for optical communication links with data rates up to 400 Gbps (16-QAM, 64 GBaud), but have modes for 100 Gbps (QPSK, 32 GBaud) or 200 Gbps (QPSK, 64 GBaud). For 200 Gbps to 400 Gbps modes which require symbol rates of 64 GBaud, commercial high bandwidth μICRs and CDMs with 64 GBaud capabilities would need to be used.

Reduced technology nodes of future commercial coherent DSP ASICs can provide higher reductions in SWaP and cost for space OISL applications in comparison to previous generation ASICs. As coherent DSP ASICs move toward FinFET plus CMOS technologies with thinner active regions, we expect increased TID tolerance and reduced probability of a heavy ion or proton SEE strike to the active region. Heavy ion and proton radiation assessments of commercial coherent DSP ASICs with 7 nm FinFET plus CMOS technology would need to be completed to screen for destructive SELs and to collect SEE cross section data for SEE rate calculation.

Based on the movement of the fiber optics communication industry toward integrated optical coherent component packages for applications beyond 100 Gbps, we believe developing an optical coherent modem using discrete commercial optical coherent components is the solution for OISL applications. The OIF has current work focused releasing implementation agreements the integrated coherent transmitter-receiver optical sub-assembly (IC-TROSA). The IC-TROSA combines a CDM and μICR in a single package with option to include a laser internal or external to the package. The optical output of the integrated laser would be split to serve as both the CDM input and μICR LO input. New integrated optical coherent packages, such as the IC-TROSA, with a single laser could not be used for an OISL application, which uses transmit and receive wavelength diversity. Transmit and receive polarization diversity could not be used for an optical coherent system. Previous CFP2-ACO modules with separate transmit and receive lasers are currently becoming obsolete. At the end of 2018, Finisar released an end of life notification for 100 Gbps and 200 Gbps coherent CFP2-ACO generation #1 transceivers as a shift toward generation #2 transceivers with shared transmitter and receiver wavelengths [Finisar EOL18.048, 2018].

Using commercial optical coherent technologies for an OISL application provides advantages of low cost, low lead time, ensured compatibility, and high performance components, but presents the challenge of the space industry keeping in pace with the rapid timeline of the terrestrial fiber optics communication industry. Over the last decade, next generation optical coherent DSP ASICs have been released every two to three years. For the space industry, a two to three year period could be shorter than the required timeline to finish space qualification for a commercial component and design of a coherent system with the qualified component. There are currently optical coherent systems for space applications in development using commercial integrated coherent transceivers with second generation coherent DSP ASICs with 28 nm bulk CMOS technology, such as NASA's TBIRD system [Robinson et al., 2018]. This system is two generations behind the latest coherent DSP ASIC technology in fiber optics communications industry and uses a first generation transceiver (independent transmit and receiver lasers), which could shortly become obsolete. Although thousands of sets of commercial optical coherent components or integrated transceivers would be required for an OISL constellation, these quantities are still "low volume" for the terrestrial fiber optics communications industry and are not significant enough to influence the industry to continue producing previous generation components required for OISLs. An OISL system manufacturer would need to consider buying optical coherent technologies in bulk with quantity margins required for constellation replenishment.

Appendix

A1. LEO OISL Link Budget Calculations for 100 Gbps Optical Coherent Modem

The MATLAB code used for LEO OISL link budget calculations for FSOC system with 100 Gbps coherent optical modem is shown below.

```
%% 10 dB Link Margin - Loop over Power, Aperture, Range
clc; clear all; close all;

lambda = 1550E-09; % [m]

loss_fiber_coupling_Tx = 0; % [dB]
loss_throughput_Tx = 10*log10(.70); % [dB] Assume 80%
loss_WFE_Tx_RMS = 0.10; % [waves RMS]
loss_WFE_Tx = 10*log10(1/(exp((2*loss_WFE_Tx_RMS*pi)^2))); % [dB]
loss_pointing_Tx_urad = 5; % [urad] 99.9%

loss_fiber_coupling_Rx = 10*log10(.80); % [dB]
loss_throughput_Rx = 10*log10(.70); % [dB] Assume 80%
loss_WFE_Rx_RMS = 0.10; % [waves RMS]
loss_WFE_Rx = 10*log10(1/(exp((2*loss_WFE_Rx_RMS*pi)^2))); % [dB]
loss_pointing_Rx_urad = 5; % [urad] 99.9%

NF_OAA = 4.0; % [dB]
receiver_ideal = 58.0; % [dB]
OSNR_req = 11.0; % [dB] ASIC

range = [1000E3:100E3:8500E3]; % [m]
power_OAA = [30:0.5:37]; % [dB]
aperture = [.07:.005:.135]; % [m]

power_receive = zeros(length(power_OAA), length(range), length(aperture));
OSNR = zeros(length(power_OAA), length(range), length(aperture));
LM = zeros(length(power_OAA), length(range), length(aperture));
%param_3dB = zeros(2*length(range), 3);
a = zeros(1,3);

figure;
plot3(1,1,1);
hold on;
for i = 1:length(aperture)
   aperture_gain_Tx(i) = 20.*log10(pi*aperture(i)./lambda); % [dB]
   loss_pointing_Tx(i) = 10.*log10(1./exp(((loss_pointing_Tx_urad./ ...
      (2*(lambda)./pi./(aperture(i))./(0.8922).*1000000))).^2)); % [dB]
   loss_total_Tx(i) = loss_fiber_coupling_Tx + loss_throughput_Tx + ...
```

```
    loss_WFE_Tx + loss_pointing_Tx(i);

  aperture_gain_Rx(i) = 20.*log10(pi*aperture(i)./lambda); % [dB]
  loss_pointing_Rx(i) = 10.*log10(1./exp(((loss_pointing_Rx_urad./ ...
    (2*(lambda)./pi./(aperture(i))./(0.8922).*1000000))).^2));
  loss_total_Rx(i) = loss_fiber_coupling_Rx + loss_throughput_Rx + ...
    loss_WFE_Rx + loss_pointing_Rx(i);

  for j = 1:length(range)
    FSPL(j) = 20.*log10(lambda./(4*pi.*range(j))); % [dB]

    for k = 1:length(power_OAA)
      power_receive = (power_OAA(k) + aperture_gain_Tx(i) + loss_total_Tx(i) ...
        + FSPL(j) + (aperture_gain_Rx(i) + loss_total_Rx(i))); % [dB]

      OSNR = receiver_ideal + power_receive - NF_OAA; % [dB]

      LM = OSNR - OSNR_req% [dB]
      if LM >= 10
        if LM <= 13
          plot3(range(j)/1E3, power_OAA(k) , aperture(i)*1E2, '.', 'Color', [0.92 0.7 0.12], 'MarkerSize', 20);
        elseif LM <= 16
          plot3(range(j)/1E3, power_OAA(k) , aperture(i)*1E2, '.', 'Color', [0.5 0.18 0.55], 'MarkerSize', 20);
        elseif LM <= 19
          plot3(range(j)/1E3, power_OAA(k) , aperture(i)*1E2, '.', 'Color', [0 0.6 0.3], 'MarkerSize', 20);
        end

      end
%       if LM >= 10
%
%
%       end
    end
  end
end

grid on;
xlim([0 8500]);
ylim([30 37]);
zlim([5 15]);
xlabel('Range [km]', 'Rotation', 10);
ylabel('Transmit Output Power [dBm]', 'Rotation', -1);
zlabel('Aperture [cm]');
set(gca,'FontSize', 30, 'FontWeight', 'bold', 'FontName', 'Calisto MT');
```

A2. Coherent DSP ASIC Heavy Ion Assessment 1 Linear Energy Transfer Calculations

The commercial optical coherent DSP ASIC with 16 nm FinFET plus CMOS technology was irradiated through the back-side of the PCB for the first heavy ion test campaign. In the original test setup plan an aluminum heat sink was mounted on top of the ASIC and we planned to irradiate from the back-side of the PCB, which would be the path of least attenuation for the heavy ions in comparison to the front side path through the heat sink. In the final test setup, the aluminum heat sink was removed to stabilize the ASIC temperature at the maximum rated junction temperature, but the OMA had been mounted and aligned with the proton beam for back-side irradiation.

There are multiple paths of attenuation for heavy ions traveling through back-side of the OMA into the active region of the ASIC. The PCB has 32 layers of alternating dielectric material, signal layers, and internal planes of copper. The signal layers and internal places are not uniform and contain copper vias distributed throughout the layer. For heavy ions penetrating through the PCB in the back-side irradiation scenario, there are four main attenuation paths. Above the PCB is a layer of solder balls and underfill, followed a layer of the flip chip substrate, then a layer of smaller solder balls and underfill, and finally the ASIC layer. The path of highest attenuation for heavy ions after the PCB ("Path A") is penetrating through the large solder balls, the flip chip substrate, the small solder balls, and finally into the ASIC active region. The path of second highest attenuation for heavy ions after the PCB ("Path B") is penetrating through the large solder balls, the flip chip substrate, underfill (layer 2), and finally into the ASIC active region. The path of third highest attenuation for heavy ions after the PCB ("Path C") is penetrating through the underfill (layer 1), the flip chip substrate, small solder balls, and finally into the ASIC active region. The path least attenuation for heavy ions after the PCB ("Path D") is penetrating through the underfill (layer 1), the flip chip substrate, underfill (layer 2), and finally into the ASIC active region. Figure 83 shows a diagram of heavy ion penetration paths into the ASIC active region for back-side irradiation of the OMA prototype, and labels the four main attenuation paths for heavy ions after PCB penetration. Note that the diagram does not accurately represent the scale of differences in layer thicknesses for the materials (i.e. polyethylene degrader vs. PCB vs. solder balls). Table 64 summarizes the differences between the four main attenuation paths for heavy ions after PCB penetration.

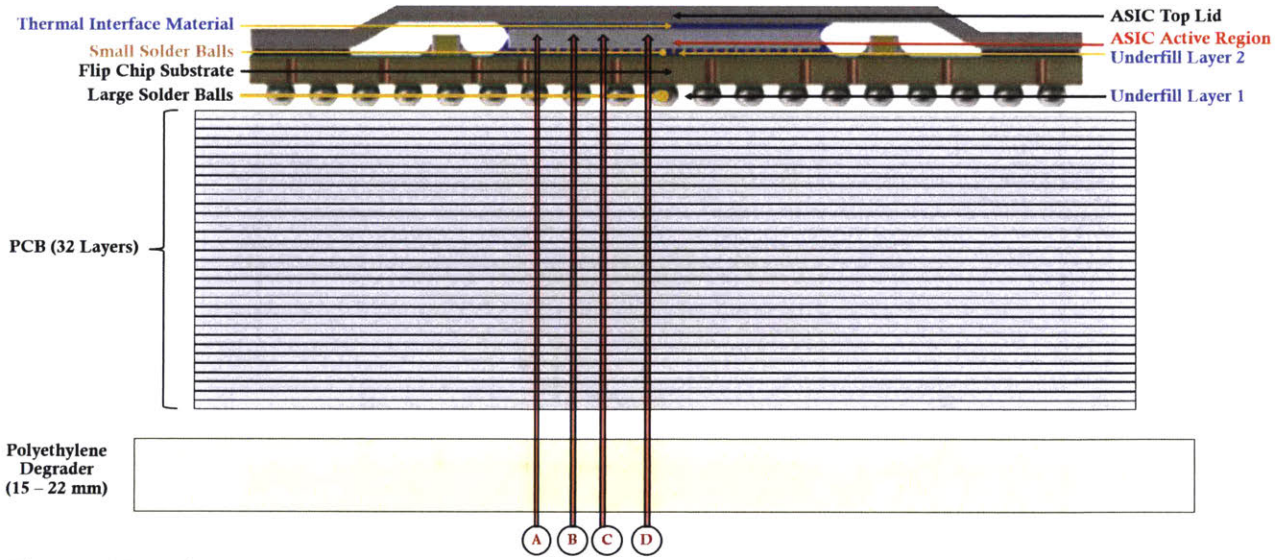

Figure 83. Diagram showing heavy ion penetration path through back-side irradiation of the OMA prototype. The four main attenuation paths after the PCB are labeled A, B, C, and D. Note that the diagram does not accurately represent the scale of differences in layer thicknesses for the materials (i.e. polyethylene degrader vs. PCB vs. solder balls).

Table 64. The four main heavy ion attenuation paths after PCB penetration for back-side irradiation of the ASIC.

Attenuation Path Model	**Post PCB Attenuation Layers**			
	Post PCB Layer 1	**Post PCB Layer 2**	**Post PCB Layer 3**	**Post PCB Layer 4**
A	Large Solder Balls	Flip Chip Substrate	Small Solder Balls	ASIC Active Region
B	Large Solder Balls		Underfill Layer 2	
C	Underfill Layer 1		Small Solder Balls	
D	Underfill Layer 1		Underfill Layer 2	

To analyze the different attenuation paths for heavy ions through back-side irradiation of the ASIC, X-ray images were taken of the OMA prototype board. The top lid of the ASIC was removed to avoid contribution of this layer to the X-ray image. Different attenuation paths can be observed through differing shades of gray in the X-ray image. Figure 84 shows a diagram of the OMA prototype board labeled with respect to an X-ray image of the section of the OMA prototype board with the ASIC top lid removed.

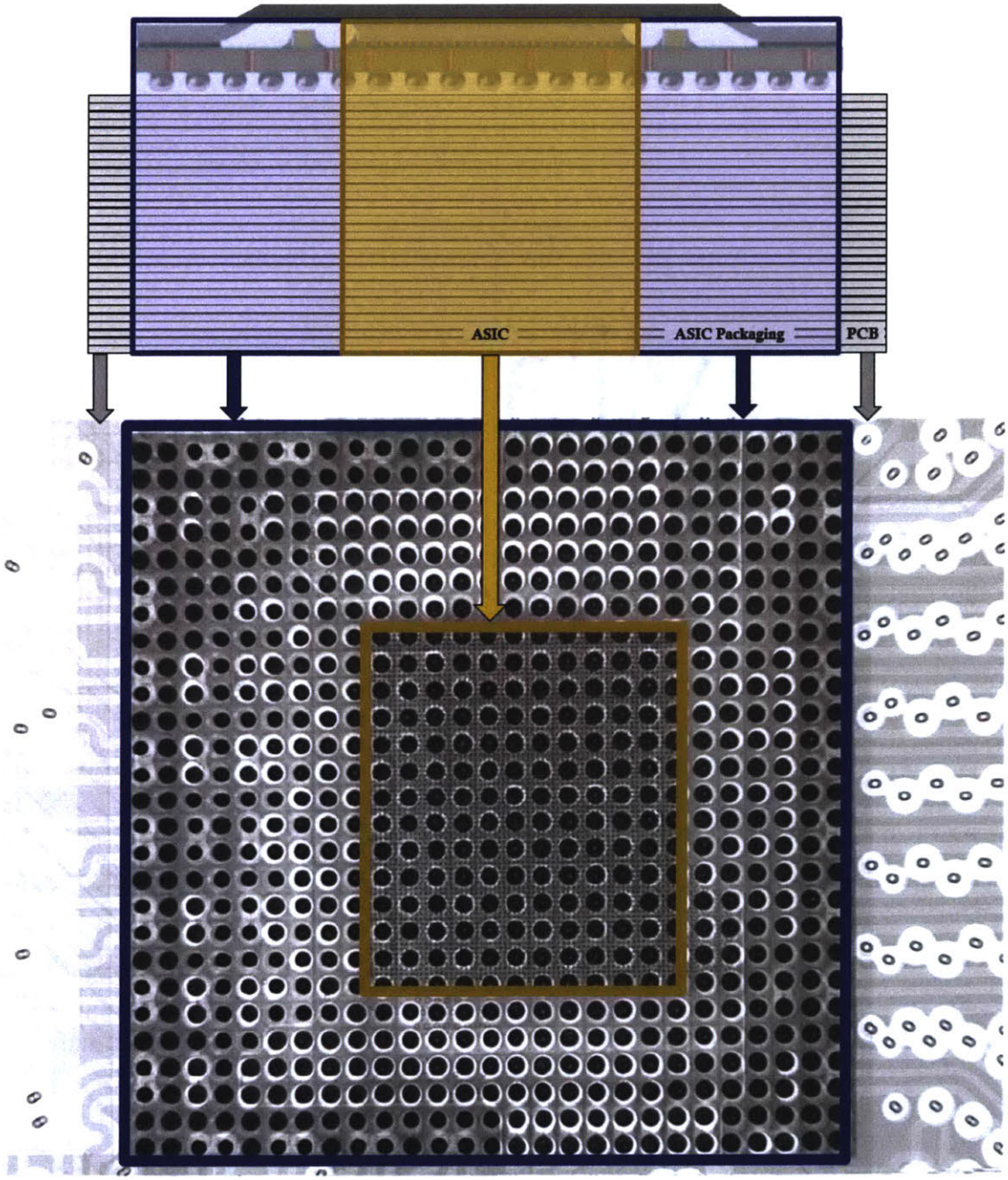

Figure 84. Diagram of the OMA prototype board labeled with respect to an X-ray image of the section of the OMA prototype board with the ASIC top lid removed

Figure 85 shows a labeled X-ray image of a section of the ASIC area with indicated regions of solder balls and underfill. Figure 85 can be analyzed to observe the four main attenuation path models as well as the varying attenuation paths due to copper vias in the PCB layers. Darker areas represent areas of higher attenuation. The darkest areas encompass regions of large solder balls, which are the densest material in comparison to the other attenuation layers in the OMA prototype board.

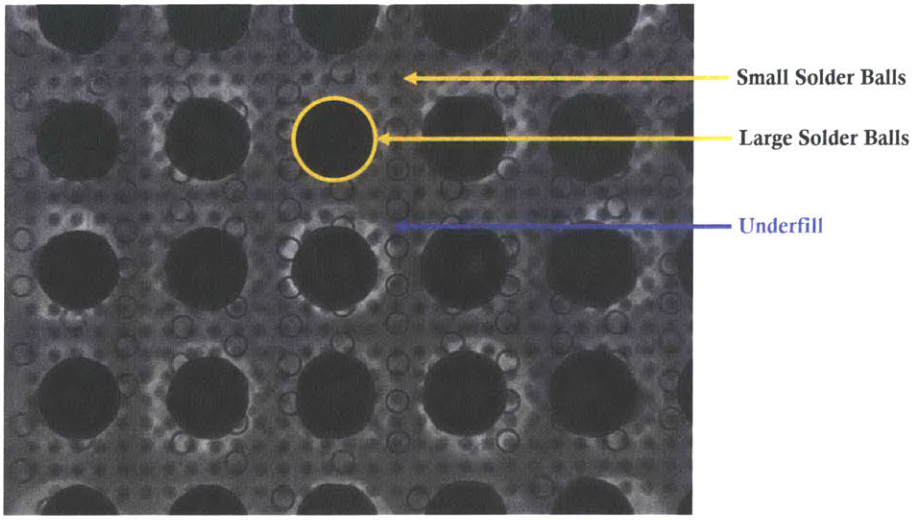

Figure 85. X-ray image of section of ASIC area with labels indicating solder balls and underfill.

A MATLAB script was used to create a histogram for the grayscale of the X-ray image of a section of the OMA prototype board with the ASIC (top lid removed) and PCB layers. Figure 86(a) is the X-ray image of only the section of the OMA prototype board with ASIC (top lid removed) and PCB layers, and Figure 86(b) shows the image grayscale histogram. The histogram shows varying attenuation paths based on the range of different values with peaks along with grayscale. The X-ray image of only the section of OMA prototype board with ASIC and PCB layers has grayscale values ranging from 30 to 256. The X-ray image histogram has two distinct peaks: the highest peak has grayscale value of 69 with 47724 pixels and the second highest peak has a grayscale value of 154 with 30675 pixels.

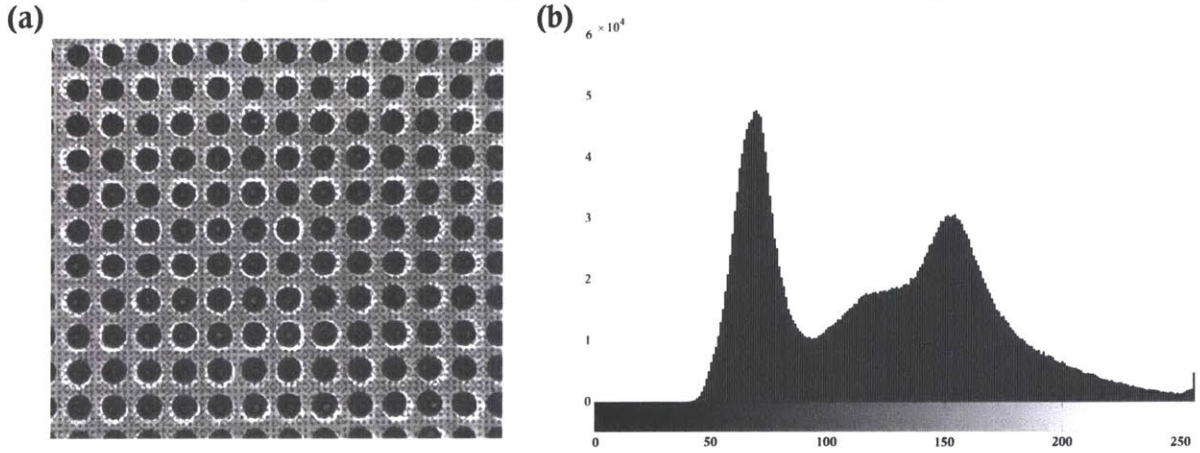

Figure 86. (a) X-ray image of only the section of the OMA prototype board with ASIC (top lid removed) and PCB layers. (b) X-ray image grayscale histogram

Due to the high number of different attenuation paths (as seen in Figure 86(b)) and the uncertainty of ASIC packaging and PCB material details, we could not directly use software modeling and simulation to determine the LET of heavy ions penetrating the ASIC active region through back-side irradiation. Typically, software program Stopping Range In Matter (SRIM) is used to model heavy ions penetrating through defined layers of material with given

thickness, density, and chemical composition and to determine the exit energy, LET, or other properties. We created an approximated attenuation model based on comparing X-ray images of copper coupons of seven different thicknesses ranging from 0.0762 mm (0.003") to 1.5875 mm (0.0625") to the X-ray image section of the OMA prototype board with ASIC (top lid removed) and PCB layers. The copper coupons were imaged with the same X-ray settings as the OMA prototype board. Figure 87 shows the X-ray images of the OMA prototype board without ASIC top lid and the copper coupons of different thicknesses.

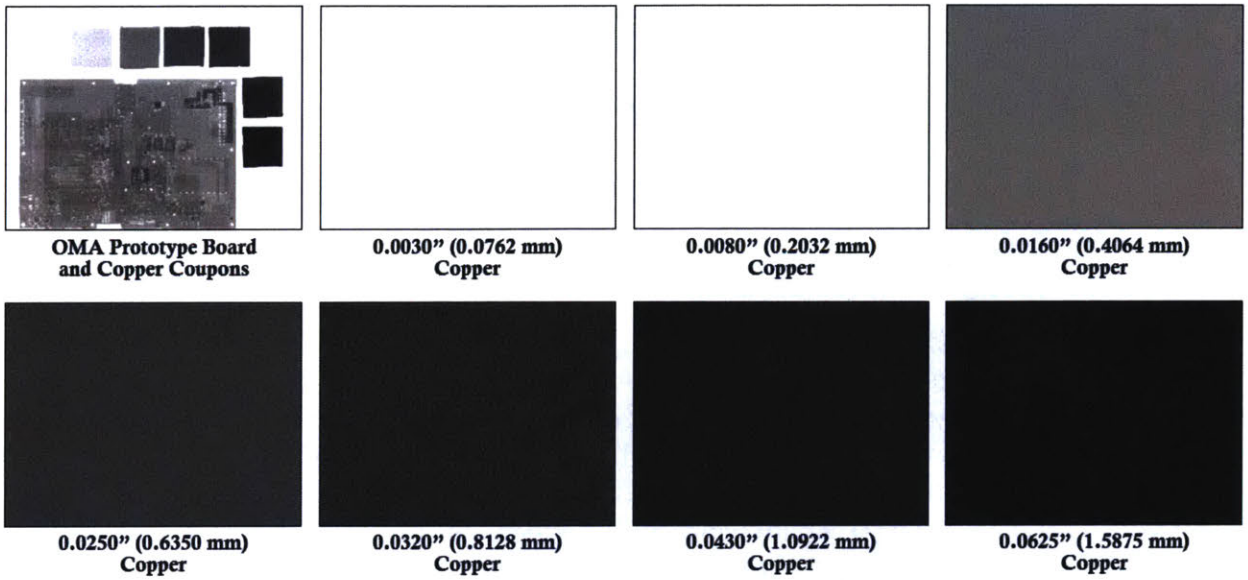

Figure 87. X-ray image of OMA prototype board without ASIC top lid and copper coupons next to board for comparison, and X-ray images of individual copper coupons.

A script in MATLAB was used to create a grayscale histogram of the X-ray images. Table 65 lists the copper coupon X-ray image histogram grayscale values. Figure 88 shows the grayscale histograms of the X-ray images of the copper coupons overlaid on the grayscale histogram of the X-ray image of the OMA prototype board without ASIC top lid and copper coupons. Key grayscale values from the histogram of section of the OMA prototype board with ASIC top lid removed and PCB layers are labeled in the figure.

Table 65. Copper coupon X-ray image histogram grayscale values

Copper Coupon Thickness	Grayscale Range	Grayscale Peak
1.5875 mm	16 – 33	25
1.0922 mm	46 – 63	54
0.8128 mm	65 – 83	73
0.6350 mm	90 – 109	99
0.4064 mm	142 – 170	156
0.2032 mm	242 – 255	255
0.0762 mm	255	255

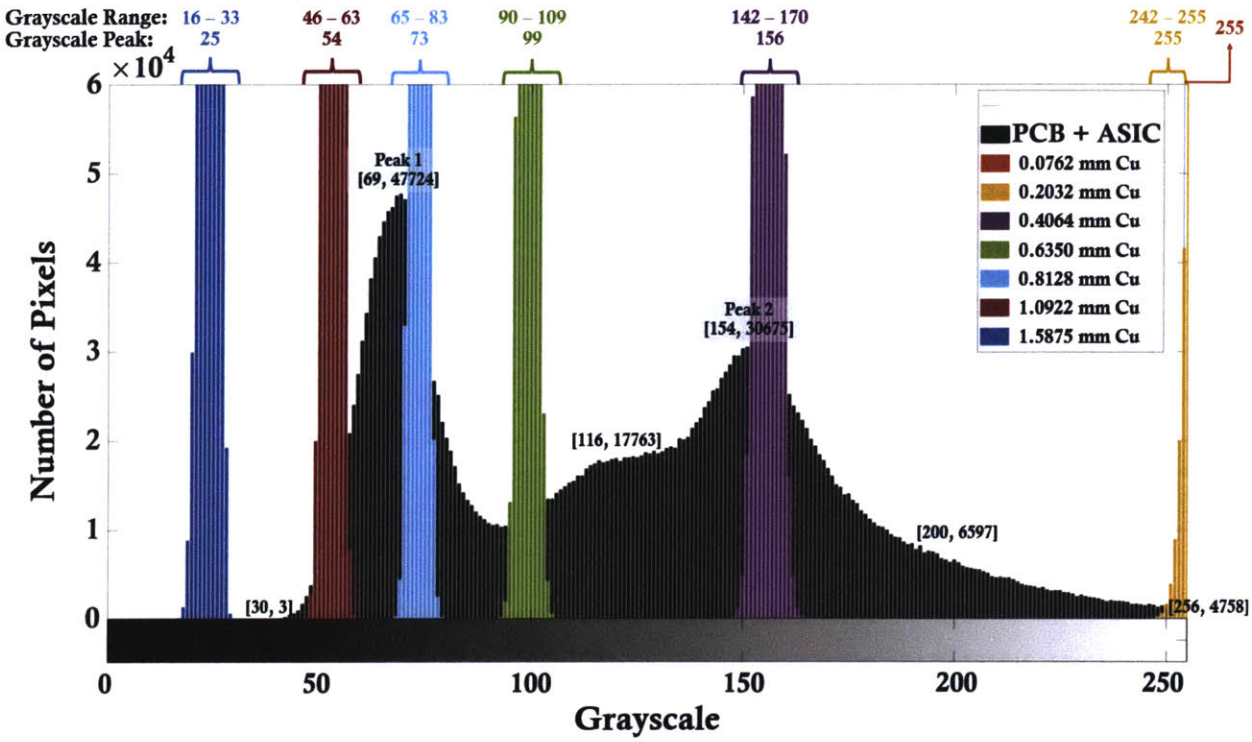

Figure 88. Grayscale histograms of copper coupon X-ray images overlaid on grayscale histogram of section of the OMA prototype board with ASIC (top lid removed) and PCB layers X-ray image.

The thinnest copper coupon and thickest copper coupon bound the minimum and maximum grayscale values for the X-ray image of the OMA prototype board with ASIC (top lid removed) and PCB layers. An exponential fit was determined from the grayscale values for each copper coupon X-ray image (Equation 5) and used to approximate copper thickness for X-ray image grayscale values. An exponential fit was used due to the exponential decay relationship for X-ray mass attenuation coefficients, which determines the intensity of a narrow beam of monoenergetic photons penetrating through a layer of material [NIST, 2019]. Table 66 lists the key grayscale values from the X-ray image histogram of the OMA prototype board with ASIC and PCB layers with the approximated copper thickness values. Figure 89 shows a graph of copper thickness versus grayscale value for the copper coupon X-ray image data and the exponential fit based on the copper coupon X-ray image data. Figure 89 identifies the approximated copper thickness values for key grayscale values from the histogram of section of the OMA prototype board with ASIC top lid removed and PCB layers.

$$y = 311.7\, e^{(-1.662\, x)}$$

Equation 5. Exponential fit to grayscale values for each copper coupon X-ray image.

Table 66. Key grayscale values from the X-ray image histogram of the OMA prototype board with ASIC and PCB layers with the approximated copper thickness values

Key Grayscale Value Description	Key Grayscale Value	Approximated Copper Thickness
Minimum Grayscale Value (Highest Attenuation Path)	30	1.408 mm
Peak 1	69	0.907 mm

(Highest Number of Pixels)		
Leveled Area Between Peak 1 and Peak 2	116	0.595 mm
Peak 2 (2nd Highest Number of Pixels)	154	0.424 mm
Decline Post Peak 2	200	0.267 mm
Highest Grayscale Value (Lowest Attenuation Path)	256	0.118 mm

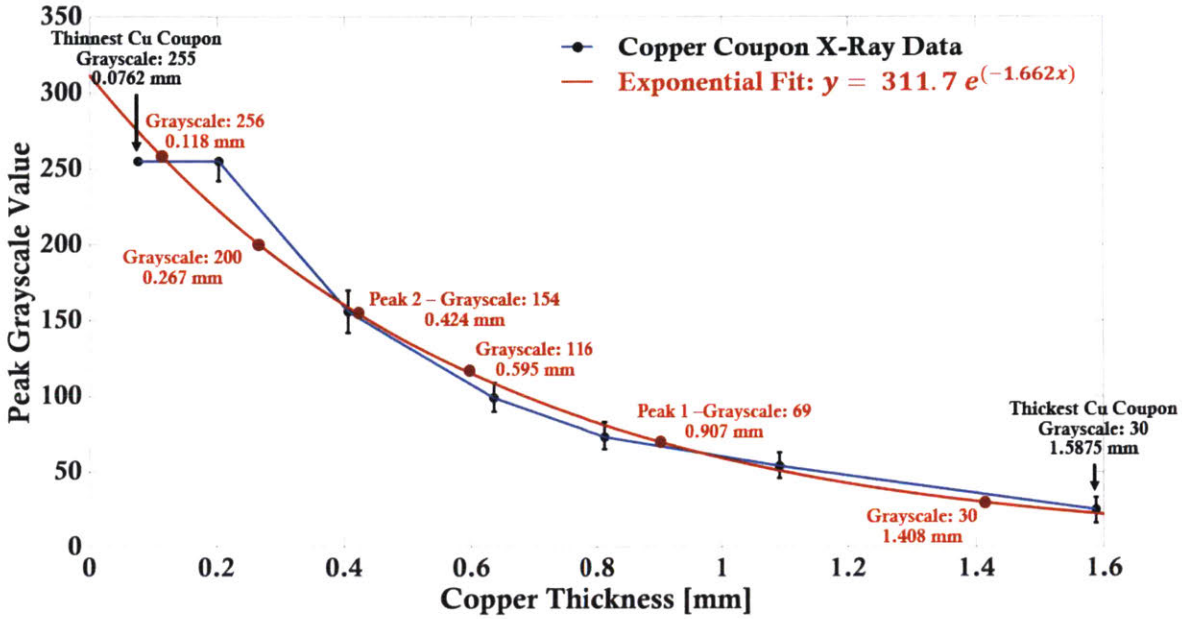

Figure 89. Graph of copper thickness versus grayscale value for the copper coupon X-ray image data and the exponential fit based on the copper coupon X-ray image data.

We used an approximated copper attenuation path model to represent ASIC back-side irradiation for SRIM simulations. Figure 90 shows a diagram of the approximated copper attenuation path model. The goal was to approximate the maximum LET achieved into the ASIC silicon active region.

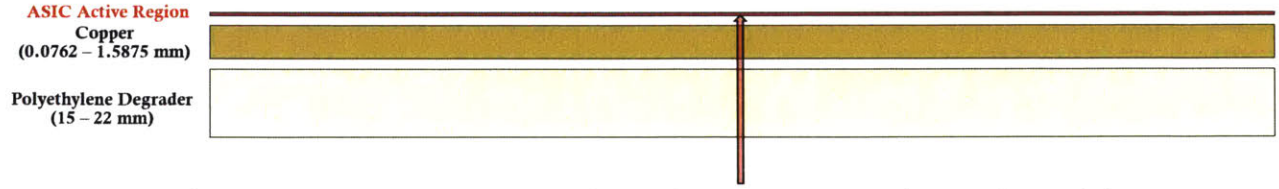

Figure 90. Diagram of approximated copper attenuation path model.

SRIM was used to model the radiation rounds 3 through 10 with 46.2 GeV Xenon ions penetrating polyethylene degrader ranging from 15.0 mm to 22. 0 mm and to determine the exit energy of Xenon ions penetrating through the degrader. Table 67 lists the exit energy of Xenon ions penetrating through the polyethylene degrader.

Table 67. Xenon ion exit energy from SRIM simulation of 46.2 GeV Xenon ions penetrating polyethylene degrader

Radiation Round	Polyethylene Degrader Thickness	Xenon Exit Energy
3	15.0 mm	31.0 GeV
4	16.0 mm	29.8 GeV
5	17.0 mm	28.6 GeV
6	18.0 mm	27.2 GeV
7	19.0 mm	26.1 GeV
8	20.0 mm	24.7 GeV
9	21.0 mm	23.5 GeV
10	22.0 mm	22.1 GeV

Another set of SRIM simulations were conducted using Xenon ions with the calculated exit energy from the polyethylene degrader. The SRIM model input the Xenon ions through copper. We evaluated the ionization energy loss of the ions based on copper thicknesses which corresponded to the key grayscale values from the X-ray image histogram of the OMA prototype board with ASIC and PCB layers. Figure 91 shows the copper thickness vs ionization loss for SRIM model of radiation round 10 with 22.1 GeV Xenon ions (exit energy from 22.0 mm polyethylene degrader) penetrating 1.8 mm copper. For radiation round 10 (22.0 mm polyethylene degrader case), the highest LET of Xenon ions in silicon would be achieved by ions moving through an equivalent attenuation path of 1.5800 mm copper, which corresponds to the Bragg peak ionization loss. The maximum range that a heavy ion penetrates through a target material is characterized by the Bragg peak, which is the point of maximum ionizing energy loss. For the thickest copper coupon of 1.5875 mm, the ionization loss of Xenon ions surpasses the Bragg peak. As seen in Figure 91, the ionization loss for equivalent copper thickness of 1.5875 mm lies on the curve to the right of the Bragg peak. Thus, for radiation round 10 with 22.0 mm polyethylene degrader, the ions through the highest attenuation path (PCB → large solder balls → flip chip substrate → small solder balls) are fully attenuated and not penetrating the silicon active region of the ASIC. The reduced number of possible attenuation paths of ions into the ASIC active region is correlated to the reduced number of heavy ion induced SEUs for radiation round 10 with 22.0 mm polyethylene degrader (quantity one) in comparison to radiation round 9.2 with 21.0 mm polyethylene degrader (quantity nine). Radiation rounds 10 and 9.2 were irradiated the ASIC to fluence levels of 1.6×10^4 ions/cm^2 at similar spill flux levels of ~ 300 ions/spill.

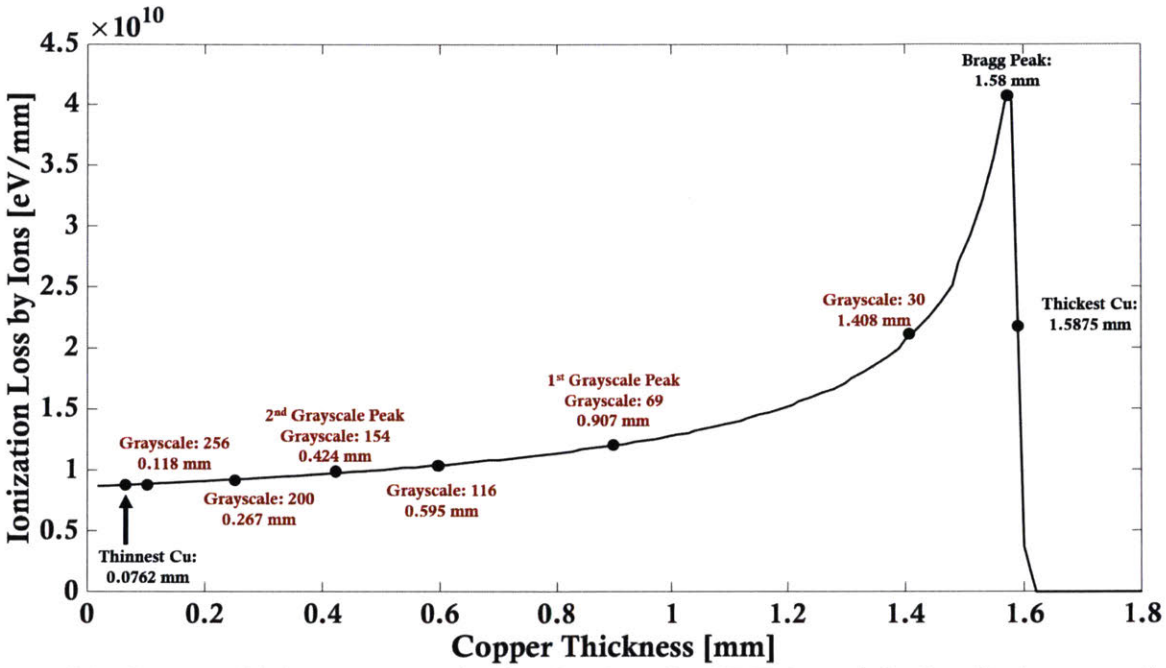

Figure 91. Copper thickness versus ionization loss for SRIM model of radiation round 10 with 22.1 GeV Xenon ions (exit energy from 22.0 mm polyethylene degrader) penetrating 1.8 mm copper.

Figure 92 shows comparisons of copper thickness versus ionization loss for SRIM models of radiation rounds 7, 8, 9, and 10 with 26.1 GeV, 24.7 GeV, 23.5 GeV, and 22.1 GeV Xenon ions (exit energy from 19.0, 20.0, 21.0, and 22.0 mm polyethylene degrader), respectively, penetrating copper material. For radiation rounds 7, 8, and 9, the Xenon ion ionization losses for equivalent copper thickness points did not surpass the Bragg peak. Thus, in radiation rounds 7, 8, and 9, the Xenon ions penetrated through all attenuation paths represented by equivalent copper thicknesses and into the ASIC active region.

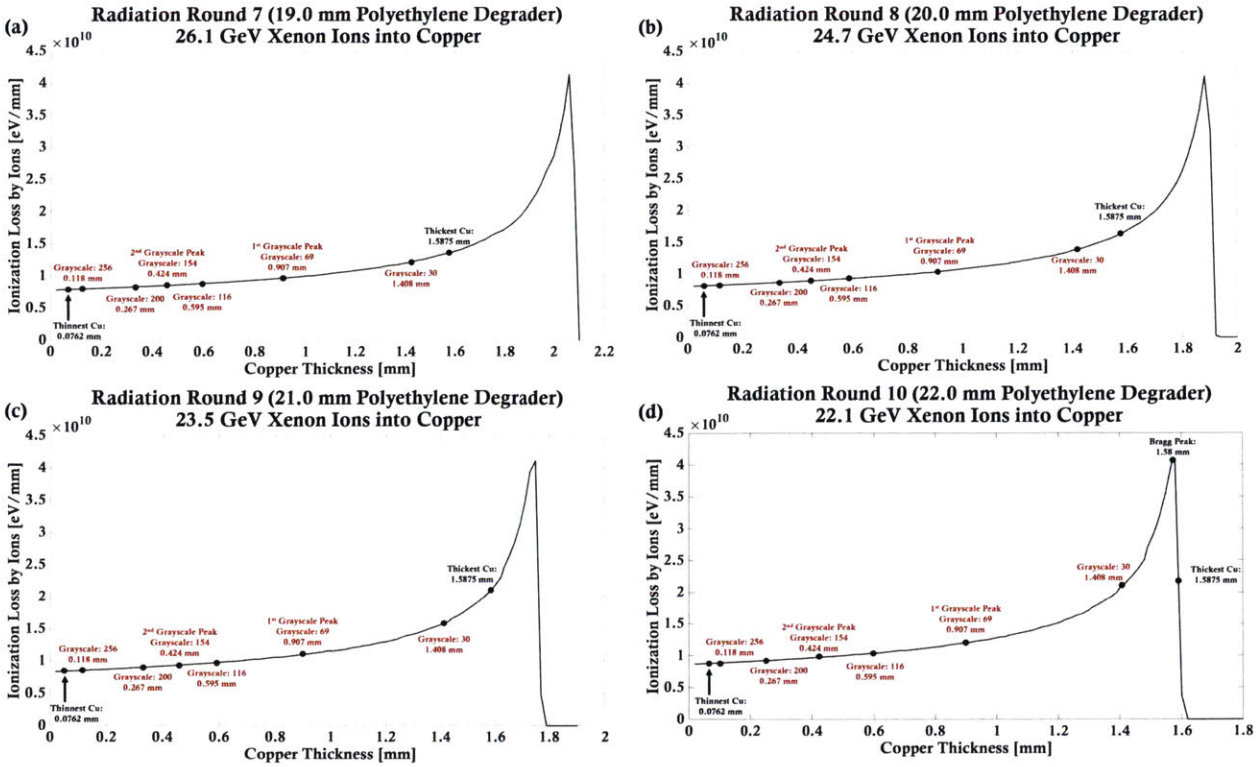

Figure 92. Comparison of copper thickness versus ionization loss for SRIM models of (a) radiation round 7 case with 19.0 mm polyethylene degrader, (b) radiation round 8 case with 20.0 mm polyethylene degrader, (c) radiation round 9 case with 21.0 mm polyethylene degrader, and (d) radiation round 10 case with 22.0 mm polyethylene degrader.

For the final set of SRIM simulations, Xenon ions with the calculated exit energy from the copper SRIM model were input into a target material of silicon, representing the ASIC active region. Due to the different attenuation paths, as represented by various copper thicknesses, heavy ions in each radiation round had a range of LET values. Figure 93 shows the radiation round 10 SRIM output for silicon thickness versus Xenon ion LET values for various copper thicknesses representing the different attenuation paths. From Figure 93, the achieved LET in the ASIC active region would be the first data point or initial LET value. For radiation round 10, the achieved LET of Xenon ions into the ASIC active region ranged from ~12 MeV·cm^2/mg to ~65 MeV·cm^2/mg, based ions penetrating through an attenuation path in which the ions reach Bragg peak entering the ASIC active region.

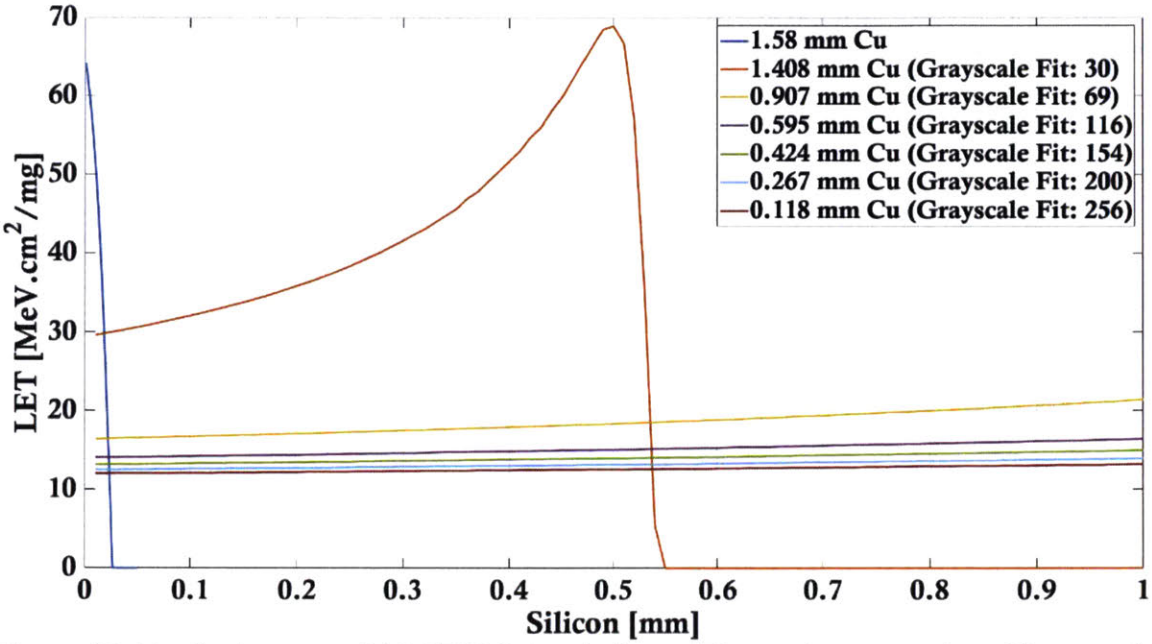

Figure 93. Radiation round 10 SRIM simulation of Xenon ions entering silicon active region of the ASIC. Different Xenon ion energies enter the silicon active region based on attenuation path of the ions through the PCB and layers before the active region as represented by various copper coupon thicknesses.

The final set of SRIM simulations for ions entering the silicon ASIC active region was completed for all radiation round cases. Figure 94 shows the summary of the SRIM simulations in which only the thinnest attenuation path (represented by 0.0762 mm Cu) and the thickest attenuation path (represented by 1.5875 mm Cu) scenarios are plotted for all radiation rounds to determine the range minimum and maximum achieved LET in the ASIC active region. Table 68 summarizes the minimum and maximum LET values achieved for each radiation round.

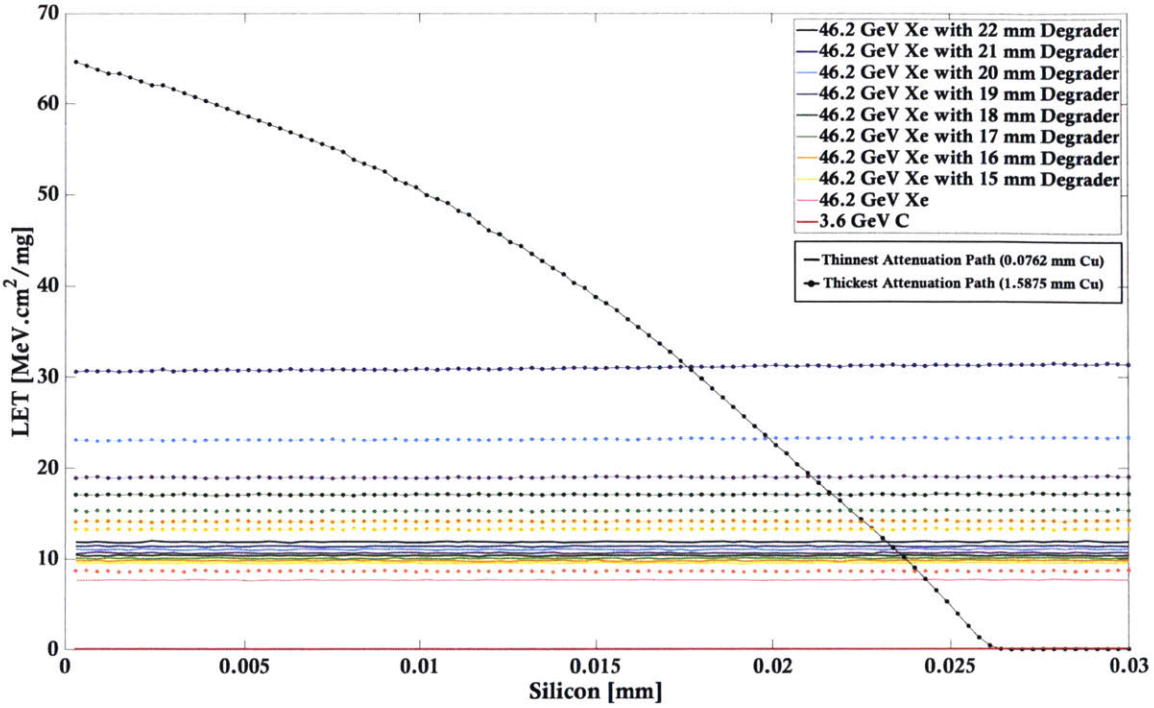

Figure 94. SRIM simulations of ions entering the silicon ASIC active region for all radiation rounds. Only the thinnest and thickest attenuation paths for ions are modeled to evaluate the minimum and maximum achieved LET values into the ASIC active region.

Table 68. Summary of minimum and maximum achieved LET in silicon ASIC active region for each radiation round.

Radiation Round	Ion	Initial Energy [GeV]	Polyethylene Degrader Thickness [mm]	Minimum LET in Si (0.0762 mm Cu) [MeV·cm²/mg]	Maximum LET in Si (1.5875 mm Cu) [MeV·cm²/mg]
1	C	3.6	-	0.1	0.1
2	Xe	46.2	-	7.7	30.6
3	Xe	46.2	15.0	9.6	13.3
4	Xe	46.2	16.0	9.9	14.1
5	Xe	46.2	17.0	10.1	15.3
6	Xe	46.2	18.0	10.5	17.1
7	Xe	46.2	19.0	10.6	18.9
8	Xe	46.2	20.0	11.1	23.1
9	Xe	46.2	21.0	11.4	30.6
10	Xe	46.2	22.0	11.9	64.6*

To calculate the achieved LET values of heavy ions into the active region of the commercial coherent DSP ASIC, we created an approximated attenuation model based on comparing X-ray images of copper coupons to the X-ray image section of the OMA prototype board with ASIC (top lid removed) and PCB layers. SRIM was used to model copper material of different thicknesses to represent the various attenuation paths. The analysis results suggest that we irradiated the commercial coherent DSP ASIC to a LET value of ~65 MeV·cm²/mg in the first heavy ion radiation test campaign. In the first heavy ion radiation test campaign, no destructive heavy-ion SEEs were observed up to an LET of ~65 MeV·cm²/mg.

A3. Coherent DSP ASIC Heavy Ion Assessment 2 – Linear Energy Transfer Calculations

SRIM software was used to model the front-side irradiation of the commercial optical coherent DSP ASIC with heavy ions penetrating first through the top lid of the packaging and followed by thermal interface material prior to entering the silicon die. Material and dimensional information of the ASIC packaging is proprietary, thus the details of the vendor-provided information used for SRIM modeling cannot be discussed. The top lid of the packaging was modeled as Aluminum. The thermal interface material was modeled as a silicone compound with density of 3.0 g/cm^3, which is estimated based on commercial thermal interface materials from Shin-Etsu Chemical Co. [Shin-Etsu, 2019]. For radiation round 2 and radiation round 3, the polyethylene degrader was modeled as the initial layer of heavy ion penetration prior to the top lid. Figure 95(a) shows a diagram of the modeled layers input to SRIM software. Figure 95(b) shows an example of the SRIM software interface for modeling the front side heavy ion irradiation of the commercial optical coherent DSP ASIC for radiation round 1.

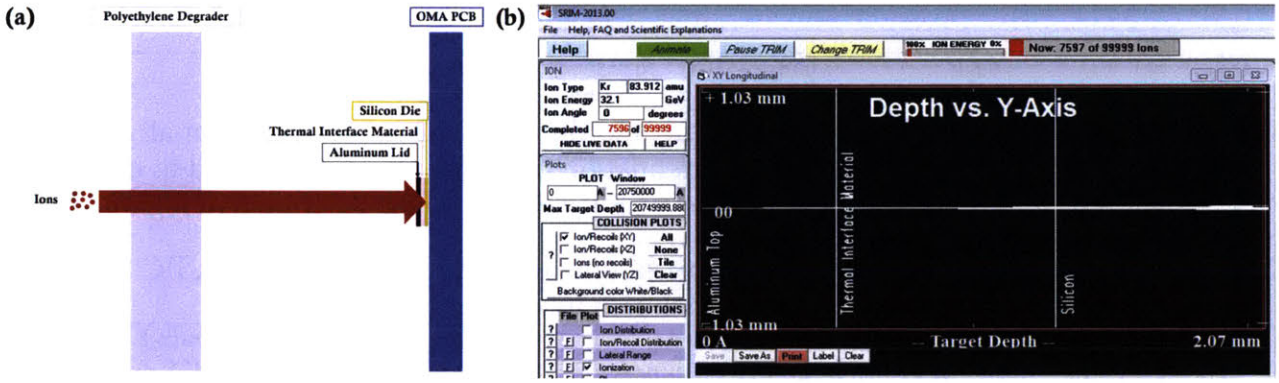

Figure 95. (a) Diagram of modeled layers for commercial optical coherent DSP ASIC front-side irradiation input to SRIM simulation software. (b) SRIM software interface for modeling front-side heavy ion irradiation of the commercial optical coherent DSP ASIC for radiation round 1 with 32.172 GeV Krypton ions (no polyethylene degrader) through aluminum top lid of ASIC, thermal interface material, and silicon die.

For the modeled layers, the SRIM ionization distribution provided the ionizing energy loss from ions and recoils in units of eV per Angstrom for the target depth of ion penetration. The ionizing energy loss was converted to LET units of MeV·cm^2 per mg and the depth was converted to mm. Figure 96 shows the LET of ions versus depth of ions penetrating through the modeled layers in SRIM for each radiation round. Table 69 summarizes the LET levels of the ions, which penetrated through to silicon die layer of the commercial optical coherent DSP ASIC for each radiation round. Based on SRIM modeling of radiation round 4, a LET of 36.58 MeV·cm^2/mg entered the ASIC silicon die. From OMERE radiation environment modeling of the Telesat OISL mission in Chapter 2.1, the highest minimum onset LET value is 26.20 MeV·cm^2/mg for the Telesat polar orbit with 100 mils aluminum shielding. The second heavy ion test serves as another destructive SEE screening assessment by testing to a LET greater than 26.20 MeV·cm^2/mg and observing no destructive SEEs.

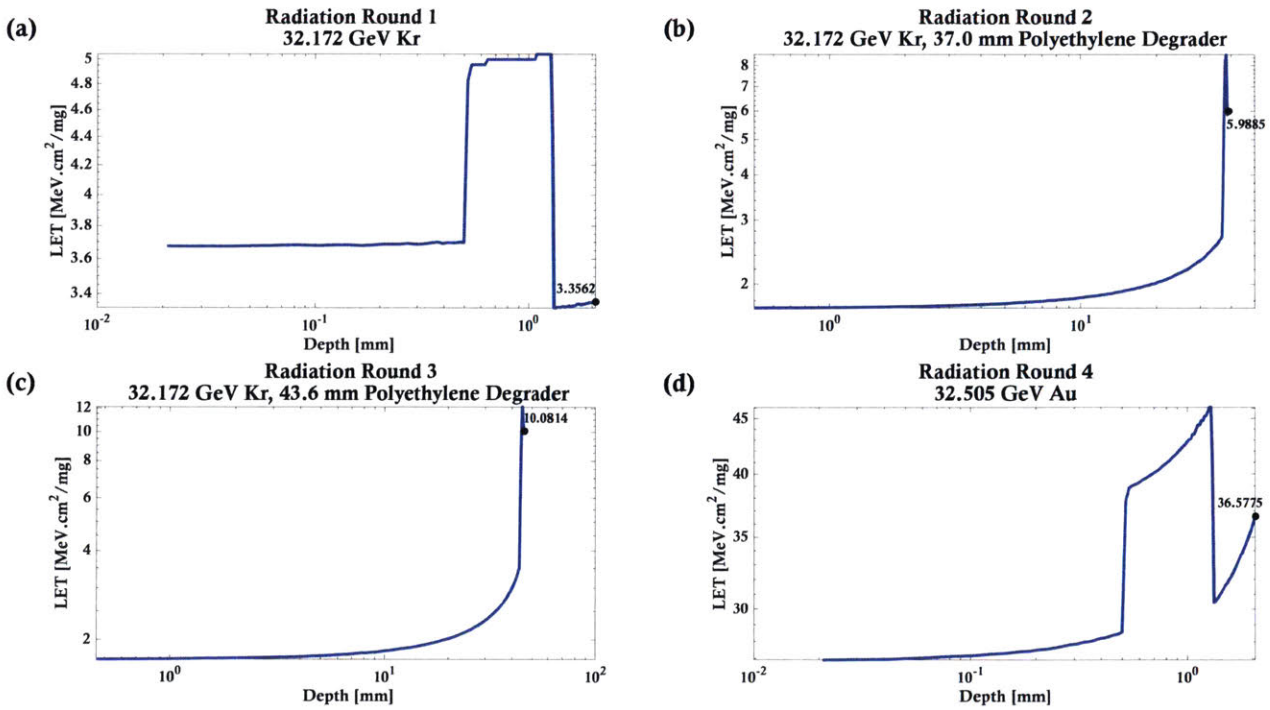

Figure 96. Heavy ion LET versus target depth of ion penetration from SRIM modeled layers of front-side irradiation of the commercial optical coherent DSP ASIC.

Table 69. LET values for each heavy ion radiation round

Round	Ion	Polyethylene Degrader	LET [MeV·cm²/mg]
1	32.172 GeV Krypton	0 mm	3.36
2	32.172 GeV Krypton	37 mm	5.99
3	32.172 GeV Krypton	43.6 mm	10.08
4	32.505 GeV Gold	0 mm	36.58

A4. Coherent DSP ASIC Heavy Ion Assessment 2 – Heavy Ion SEE Rate Calculations

The LET and heavy ion SEE cross section data were input to the OMERE SEE Rate Estimate tool, which uses the ECSS standard Integral Rectangular Parallelepipeds (IRPPs) model to calculate SEE rates and to generate Weibull distribution fits based on LET and cross section data. In the IRPP model, the device is modeled to contain a collection of RPPs with identical geometries, but different threshold LETs, and each RPP makes an additive contribution to the cross section when the incident particle LET is above the threshold LET for that RPP. If RPP dimensions are selected to agree with directional dependence, the resulting model will correctly predict the cross section as function of both LET and incidence angle [Edmonds, 2005]. Figure 97 shows the Weibull distribution based on the input LET and SEE cross section data to the IRPP model.

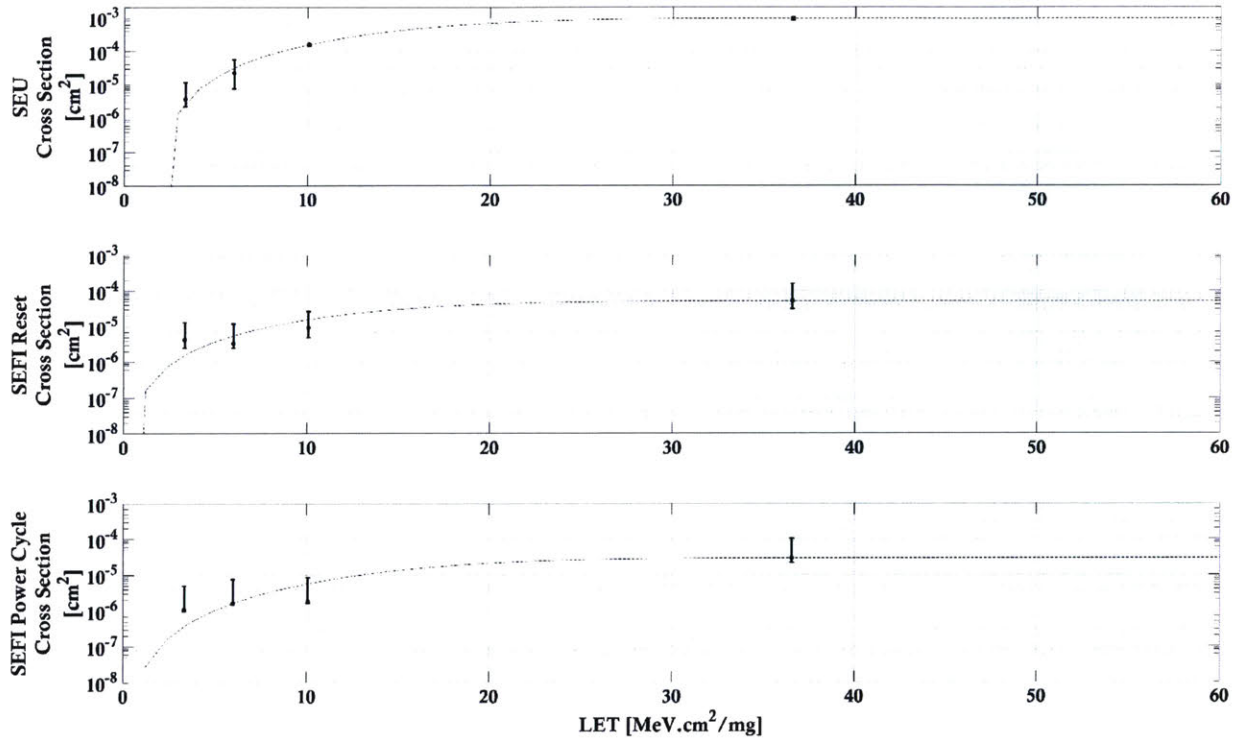

Figure 97. Weibull distribution based on input LET and heavy ion SEE cross section data from second heavy ion radiation test. OMERE uses the IRPP model to generate Weibull distribution used for SEE rate calculations.

SEE rate estimates are calculated based on two different assumptions regarding the directional dependence of device susceptibility. The "best estimate" is closest to reality but not guaranteed. A "best estimate" SEE rate is calculated by assuming the two lateral RPP dimensions are equal and the RPP thickness is on the order of one-fifth the lateral dimensions. A "worst case" SEE rate is typically recommended for conservative design purposes and is calculated by assuming the two lateral RPP dimensions are equal and the RPP thickness is on the order of one-hundredth the lateral dimensions. The spread between two rate estimates

is a measure of the uncertainty in the predicted rate associated with directional effects [Edmonds, 2005]. Table 70 lists the IRPP model dimensions generated from the SEE rate estimate and the RPP thickness values used for "best estimate" and "worst case" SEE rate calculations.

Table 70. IRPP model dimensions for best estimate and worst case heavy ion SEE rate calculations.

Parameter	**SEU Cross Section**		**SEFI Cross Section**	
Weibull – W Parameter	16.394		16.633	
Weibull – S Parameter	2.463		2.305	
Limit Cross Section [cm²/device]	9.239×10^{-4}		8.068×10^{-5}	
LET Threshold [MeV·cm²/mg]	1.769		0.001	
RPP lateral dimensions [μm]	303.961		89.8224	
Assumption	**Best Estimate**	**Worst Case**	**Best Estimate**	**Worst Case**
RPP Thickness [μm]	60.792	3.040	17.964	0.898
Critical Charge [pC]	1.109	0.055	1.852×10^{-4}	9.259×10^{-6}

GCR ions from the Telesat polar and inclined orbit radiation environment modeling are used as the environment input for heavy ion SEE rate calculation. Table 71 summarizes the heavy ion best estimate and worst case SEE rates for the Telesat polar and inclined orbits.

Table 71. Heavy ion SEE rate calculations for Telesat polar and inclined orbits.

	Telesat Polar Orbit [Events/Year]			**Telesat Inclined Orbit [Events/Year]**		
SEE Rate Assumption	**100 mils Al Shielding**	**200 mils Al Shielding**	**300 mils Al Shielding**	**100 mils Al Shielding**	**200 mils Al Shielding**	**300 mils Al Shielding**
SEU Rate Best Estimate	4.60×10^{-2}	4.38×10^{-2}	4.16×10^{-2}	8.10×10^{-3}	7.99×10^{-3}	7.85×10^{-3}
SEU Rate Worst Case	1.14×10^{-1}	1.10×10^{-1}	1.05×10^{-1}	3.48×10^{-2}	3.39×10^{-2}	3.31×10^{-2}
SEFI Rate Best Estimate	1.25×10^{-2}	1.20×10^{-2}	1.15×10^{-2}	3.69×10^{-2}	3.60×10^{-2}	3.51×10^{-2}
SEFI Rate Worst Case	2.08×10^{-2}	2.00×10^{-2}	1.92×10^{-2}	6.94×10^{-3}	6.75×10^{-3}	6.57×10^{-3}

A5. CREME96 Proton SEE Rate Calculations

The CREME96 TRP module calculated omnidirectional orbit-averaged and peak trapped proton spectra using the NASA AP8MIN trapped proton flux model. The CREME96 GTRN module evaluates the Earth's geomagnetic shielding effect for galactic cosmic ray particles. For input orbit parameters, the module outputs the orbit-averaged ionizing particle fluxes inside Earth's magnetosphere. The nominal GCR environment is based on the "quiet" magnetic weather condition, while solar flares are based on the "stormy" magnetic weather condition. The trapped proton spectra from the TRP module and the ionizing particle fluxes from the GTRN module are input to the CREME96 FLUX module. This module provides a numerical model of the space ionizing radiation environment at the surface of the spacecraft. Ion species with atomic numbers ranging from 1 to 92 are included in the FLUX calculation. The CREME96 GCR model with solar minimum conditions is used for the "nominal" case with input GTRN "quiet" magnetic weather condition flux and TRP orbit-averaged trapped proton spectra. The CREME96 GCR model with solar flare conditions and GTRN "stormy" magnetic weather condition flux file to calculate the averaged fluxes for solar flare worst week, worst day, and peak 5-minute. CREME96 uses the October 1989 solar energetic particle flux models. The CREME96 TRANS module transports the input particle fluxes from the FLUX module through shielding. Aluminum shielding thickness of 200 mils was input to the TRANS module.

The proton SEE rates due to proton-induced nuclear recoils are calculated with the CREME96 PUP module. The transported particle flux files from the TRANS module are input to the PUP module to generate nominal case, solar flare worst week, solar flare worst day, and solar flare peak 5 minute SEE rates. A Weibull distribution is fit from a single proton energy and cross section value by setting the onset LET to 15 MeV·cm^2/mg (maximum LET achieved by 100 MeV proton radiation), the width parameter (W) to 0.1 MeV·cm^2/mg and the power parameter (S) to 1 (dimensionless) [Hiemstra, 2003]. This method for single proton energy Weibull distribution fit is the typical protocol used by the JPL radiation effects group.

A6. 105 MeV Proton Fluence for Telesat Mission Displacement Damage Dose

The radiation susceptibility assessments of the commercial μICR and CDM in Section 4.2 and Section 5.2 determined sub-component displacement damage dose (DDD) sensitivity. The μICR contains InP-based waveguide photodiodes and an InGaAs-based monitor photodiode. The HB-CDM contains an InP-based modulator chip. For 105 MeV proton radiation testing of the μICR and CDM, OMERE radiation modeling software was used to determine the expected proton equivalent fluence levels for InP and InGaAs based devices in the Telesat mission. For 100 MeV protons, the expected equivalent fluence level for InP-based devices with 200 mils of aluminum shielding is 3.78×10^{11} p/cm^2 for the Telesat polar orbit mission and 8.59×10^{10} p/cm^2 for the Telesat inclined orbit mission. For 100 MeV protons, the expected equivalent fluence level for InGaAs-based devices with 200 mils of aluminum shielding is 3.81×10^{11} p/cm^2 for the Telesat polar orbit mission and 8.66×10^{10} p/cm^2 for the Telesat inclined orbit mission.

Figure 98 shows a plot of equivalent fluence level for 100 MeV protons versus aluminum shielding for the Telesat polar orbit mission. Figure 99 shows a plot of equivalent fluence level of 100 MeV protons versus aluminum shielding for the Telesat inclined orbit mission.

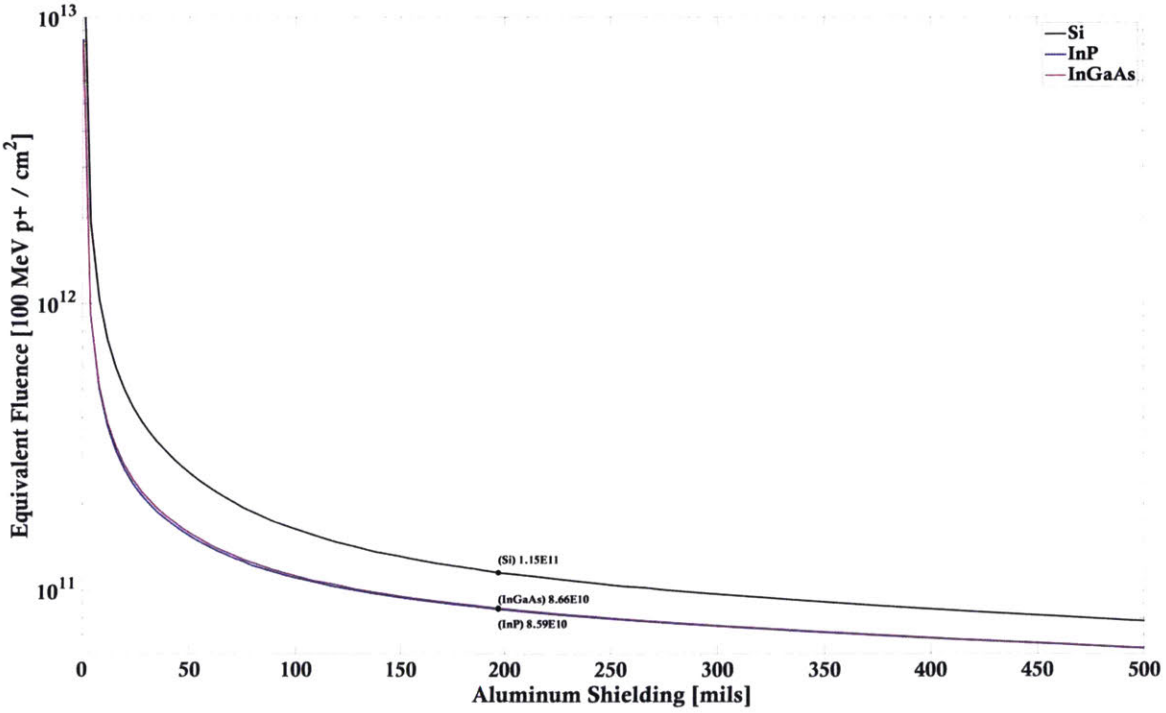

Figure 98. 105 MeV proton equivalent fluence versus aluminum shielding for Telesat polar mission expected displacement damage dose on Si, InP, and InGaAs based devices.

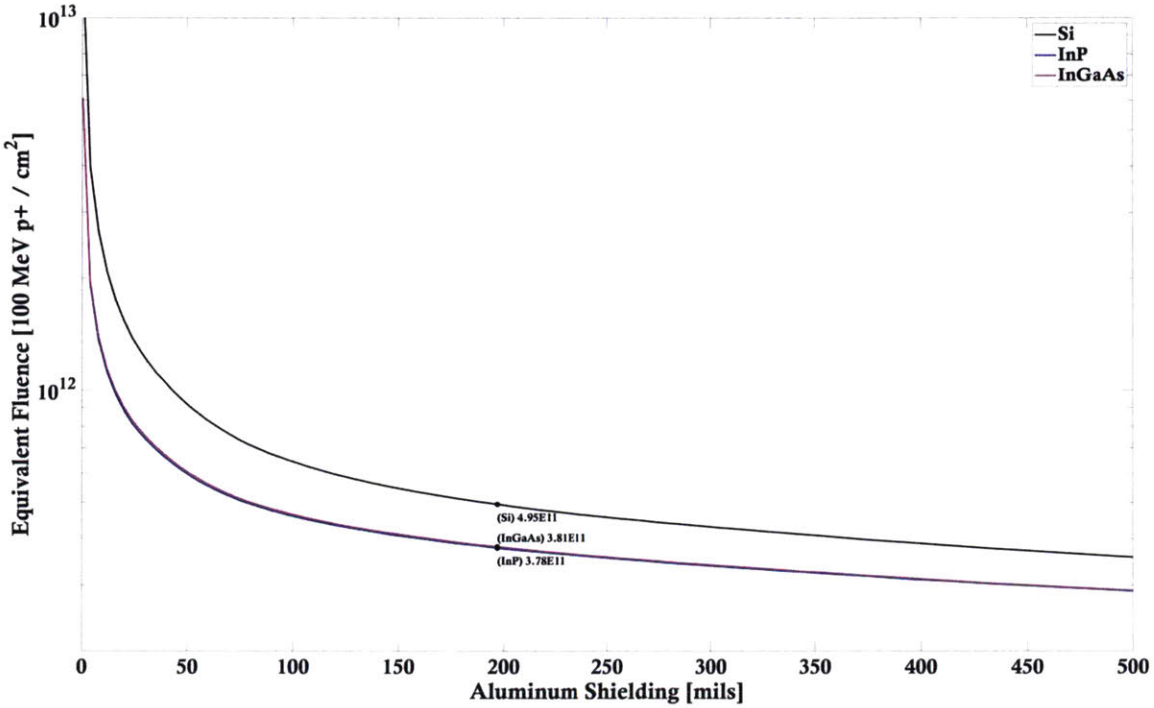

Figure 99. 105 MeV proton equivalent fluence versus aluminum shielding for Telesat inclined mission expected displacement damage dose on Si, InP, and InGaAs based devices.

For the proton radiation assessments at the TRIUMF National Laboratory, the commercial μICRs and CDMs were tested with a 105 MeV proton beam to fluence levels of 1.2×10^{12} p/cm^2. This fluence level encompasses and includes more than 2× margin of equivalent proton fluence levels for displacement damage dose of InP-based and InGaAs based devices in the Telesat mission.

References

Adamiec, P., et al. "Radiation tests on semiconductor optical sources for space applications." International Conference on Space Optics—ICSO 2016. Vol. 10562. International Society for Optics and Photonics, 2017.

Agrawal, Govind P. Fiber-optic communication systems. Vol. 222. John Wiley & Sons, 2012.

Agrell, Erik, et al. "Roadmap of optical communications." Journal of Optics 18.6 (2016): 063002.

Alig, R. C., and S. Bloom. "Electron-hole-pair creation energies in semiconductors." Physical Review Letters 35.22 (1975): 1522.

Alliss, Randall J., and Billy Felton. "The mitigation of cloud impacts on free-space optical communications." Atmospheric Propagation IX. Vol. 8380. International Society for Optics and Photonics, 2012.

Alonso, Reyes, and Sodnik, "Performance of satellite-to-ground communications link between ARTEMIS and the Optical Ground Station," Proc. SPIE 5572, Optics in Atmospheric Propagation and Adaptive Systems VII, (11 November 2004); doi: 10.1117/12.565516

Alt, Shannon. "Photonic integrated circuit (PIC) device structures: Background, fabrication ecosystem, relevance to space systems applications, and discussion of related radiation effects." (2016).

Aniceto, Raichelle Joy. Evaluation of the performance of optical coherent communications commercial DSP ASICs in low earth orbit radiation environments. Diss. Massachusetts Institute of Technology, 2017.

Aniceto, Raichelle J., et al. "Single Event Effect and Total Ionizing Dose Assessment of Commercial Optical Coherent DSP ASIC." Nuclear and Space Radiations Effects Conference (NSREC) (2017), Data Workshop.

Aniceto, Raichelle J., et al. "Proton Radiation Effects on Hamamatsu InGaAs PIN Photodiodes." RADiation Effects Conferences on (RADECS) (2017), Data Workshop.

Aniceto, Raichelle J., et al. "Assessment of Gamma and Proton Radiation Effects on 100 Gbps Commercial Optical coherent Transceiver." International Conference on Space Optics (ICSO) (2018), Data Workshop.

Araki, K et al. "Experimental operations of laser communication equipment onboard ETS-VI satellite." Photonics West'97. International Society for Optics and Photonics, 1997.

Badhwar, Gautam D. "The radiation environment in low-Earth orbit." Radiation research 148.5s (1997): S3-S10.

Bagatin, M. "Non-Volatile Memories for Space: The Threat of Ionizing Radiation." RADECS 2018 Topical Day. 2018.

Barde, S., et al. "Displacement damage effects in InGaAs detectors: experimental results and semi-empirical model prediction." IEEE Transactions on Nuclear Science 47.6 (2000): 2466-2472.

Barnes, C., et al. "NASA Electronic Parts and Packaging (NEPP) Program: assurance research on optoelectronics." Photonics for Space Environments X. Vol. 5897. International Society for Optics and Photonics, 2005.

Bennett, Geoff, et al. "A review of high-speed coherent transmission technologies for long-haul DWDM transmission at 100G and beyond." IEEE Communications Magazine 52.10 (2014): 102-110.

Berthold, Joe, et al. "100G Ultra Long Haul DWDM Framework Document." Opt. Internetw. Forum. 2009.

Bogorad, A.L., Likar, J.J., Lombardi, R.E., Herschitz, R., and Kircher G. (2010): On-Orbit Total Dose Measurements from 1998 to 2007 Using pFET Dosimeters, IEEE Transactions on Nuclear Science, 57(6), 3154-3162, doi:10.1109/TNS.2010.2076832.

Boroson, Don M., and Bryan S. Robinson. "The Lunar Laser Communication Demonstration: NASA's First Step Toward Very High Data Rate Support of Science and Exploration Missions." Space Sci Rev 185, no. 1–4 (December 2014): 115–128.

Brandhorst, Henry W. "Indium Phosphide-Into The Future." 1st Intl Conf on Indium Phosphide and Related Materials for Advanced Electronic and Optical Devices. Vol. 1144. International Society for Optics and Photonics, 1989.

Buchner, Stephen, et al. "Proton Test Guideline Development – Lessons Learned." NASA/Goddard Space Flight Center. 2002.

Cahoy, K. et al. "The CubeSat Laser Infrared CrosslinK Mission (CLICK)." International Conference on Space Optics – ICSO 2018. Vol. 11180. International Society for Optics and Photonics, 2019.

CFP, 2010. "CFP MSA Hardware Specification." Revision 1.4.

CFP, 2013. "CFP2 MSA Hardware Specification." Revision 1.0.

CFP, 2015. "CFP4 MSA Hardware Specification." Revision 1.1.

CFP, 2017. "CFP8 MSA Hardware Specification." Revision 1.0.

Chan, "Inter-Satellite Optical Heterodyne Communication Systems," Proc. SPIE 1131, Optical Space Communication, (6 October 1989); doi:10.117/12.961548

Chien, James, et. Al. "Flex Coherent DWDM Transmission Framework Document." OIF-FD-FLEXCOH-DWDM-01.0. 2017.

Ciminelli, Caterina, Francesco Dell'Olio, and Mario Nicola Armenise. PHOTONICS IN SPACE: Advanced Photonic Devices and Systems. World Scientific, 2016.

Clements, Emily, et al. "Nanosatellite optical downlink experiment: design, simulation, and prototyping." Optical Engineering 55.11 (2016): 111610.

Cornwell, Donald. "Space-based laser communications break threshold." Optics and Photonics News 27.5 (2016): 24-31.

Cressler, John D. "Radiation effects in SiGe technology." IEEE transactions on Nuclear Science 60.3 (2013): 1992-2014.

Dailey, J. M., et al. "High output power laser transmitter for high-efficiency deep-space optical communications." Free-Space Laser Communications XXXI. Vol. 10910. International Society for Optics and Photonics, 2019.

Donald Cornwell. National Aeronautics and Space Administration, Commercial Laser Communications Interoperability and Regulatory Workshop, 2017. https://www.nasa.gov/directorates/heo/scan/engineering/technology/lasercomminteroperability_regulatory_workshop.

Del Portillo Barrios, Iñigo. Optimal locations for the ground segment of optical space communications networks. Diss. Massachusetts Institute of Technology, 2016.

Dodd, P. E., et al. "Current and future challenges in radiation effects on CMOS electronics." IEEE Transactions on Nuclear Science 57.4 (2010): 1747-1763.

Doerr, Christopher R. "Integrated photonic platforms for telecommunications: InP and Si." IEICE Transactions on Electronics 96.7 (2013): 950-957.

Dong, Po, et al. "Monolithic silicon photonic integrated circuits for compact 100-Gb/s optical coherent receivers and transmitters." IEEE Journal of Selected Topics in Quantum Electronics 20.4 (2014): 1-8.

Duan, Guang-Hua, et al. "Hybrid III--V on Silicon Lasers for Photonic Integrated Circuits on Silicon." IEEE Journal of selected topics in quantum electronics 20.4 (2014): 158-170.

Edmonds, Larry D. "Recommendations regarding the use of CREME96 for heavy-ion SEU rate calculations." JPL Technical Report (Unpublished) (2005).

Engin, Doruk, et al. "51W, 1.5 um, 7 WDM (25nm) channels PPM downlink Tx and 500W, 1um, uplink PPM Tx for deep space lasercom." Free-Space Laser Communications XXXI. Vol. 10910. International Society for Optics and Photonics, 2019.

ESA. "Space Environment Standard ECSS-E-ST-10-04C" (PDF). ESA Requirements and Standards Division. November 15, 2008. Retrieved 2013-09-27.

Everett, D. "Chapter 14: Overview of Spacecraft Design." Space Mission Engineering: The New SMAD. 2011.

Farwell, Selina, et al. "InP coherent receiver chip with high performance and manufacturability for CFP2 modules." Optical Fiber Communications Conference and Exhibition (OFC), 2014. IEEE, 2014.

Fletcher, G. D., et al. "The SILEX optical interorbit link experiment." Electronics and communication engineering journal 3.6 (1991): 273-279.

Fuchs C. and Schmidt C., "Update on DLR's OSIRIS program." ICSO 2018.

Fujitsu. "100G/400G Integrated Coherent Receiver." Website. http://www.fujitsu.com /jp/group/foc/en/products/optical-devices/100grm/. 2019

Fujiwara, Yuuichi, et al. "Optical inter-orbit communications engineering test satellite (OICETS)." Acta Astronautica 61.1 (2007): 163-175.

Furukawa Electric, "Sampling of Narrow Linewidth and High Output Power Micro ITLA for beyond-100Gbps optical digital coherent transmission." News Release. 2017.

Gajanana, Deepak, et al. "Irradiation tests on InP based Mach Zehnder modulator." Journal of Instrumentation 8.02 (2013): C02025.

George, J., et al. "Single event transients in operational amplifiers." IEEE Radiation Effects Data Workshop, 2005. IEEE, 2005.

Gerardin, Simone, et al. "Radiation effects in flash memories." IEEE Transactions on Nuclear Science 60.3 (2013): 1953-1969.

Glorieux, Maximilien, et al. "Single-Event Characterization of Xilinx UltraScale+® MPSOC under Standard and Ultra-High Energy Heavy-Ion Irradiation." 2018 IEEE Radiation Effects Data Workshop (REDW). IEEE, 2018.

Grigoryev, V., V. Kovalev, and V. Shargorodskiy. "High-bit-rate laser space communication technology and results of onboard experiment." Proceedings of International Conference on Space Optical Systems and Applications (ICSOS), Kobe. 2014.

Goley, Patrick S., Zachary E. Fleetwood, and John D. Cressler. "Potential Limitations on Integrated Silicon Photonic Waveguides Operating in a Heavy Ion Environment." IEEE Transactions on Nuclear Science 65.1 (2018): 141-148.

Gonthier, F., et al. "1550 nm combined transmission booster amplifier and receiver preamplifier for satellite to satellite laser communication." ICSO, 2018.

Hamamatsu Photonics K.K., Solid State Division. "InGaAs PIN photodiode G6849 series." PDF Datasheet (2013).

Hastings, Daniel, and Henry Garrett. Spacecraft-environment interactions. Cambridge university press, 2004.

Hauschildt H, Le Gallou N, Mezzasoma S, Ludwig Moeller H, Armegol J, Witting M, Herrmann J, Carmona C. "Global Quasi-Real-Time-Service back to Europe: EDRS Global." ICSO 2018.

Hemmati, Hamid, ed. Near-earth laser communications. Chapter 10 Reliability and Flight Qualification. CRC press, 2009.

Heynderickx, D. "Review on modelling of the radiation belts." International Journal of modern physics A 17.12n13 (2002): 1675-1684.

Heine, Frank, et al. "The European Data Relay System, high speed laser based data links." Advanced satellite multimedia systems conference and the 13th signal processing for space communications workshop (ASMS/SPSC), 2014 7th. IEEE, 2014.

Hiemstra, David M., and Ewart W. Blackmore. "LET spectra of proton energy levels from 50 to 500 MeV and their effectiveness for single event effects characterization of microelectronics." IEEE Transactions on Nuclear Science 50.6 (2003): 2245-2250.

Hiemstra, David M., Valeri Kirischian, and Jakub Brelski. "Single event upset characterization of the Zynq UltraScale+ MPSoC using proton irradiation." 2017 IEEE Radiation Effects Data Workshop (REDW). IEEE, 2017.

Ip, Ezra, et al. "Coherent detection in optical fiber systems." Optics express 16.2 (2008): 753-791.

Inphi, CL20010A1 Coherent Transceiver/Framer EVK data sheet [PDF], April 18, 2014.

Ip, Ezra. "Optical Coherent Detection and Digital Signal Processing of Channel Impairments." Handbook of Optical Fibers (2018): 1-70.

Irom, Farokh, and Shri G. Agarwal. "Compendium of single-event latchup and total ionizing dose test results of commercial analog to digital converters." 2012 IEEE Radiation Effects Data Workshop. IEEE, 2012.

Irom, Farokh, and Shri G. Agarwal. "Compendium of single-event latchup and total ionizing dose test results of commercial digital to analog converters." 2015 IEEE Radiation Effects Data Workshop (REDW). IEEE, 2015.

Ishida, Osamu, Kazuhito Takei, and Etsushi Yamazaki. "Power efficient DSP implementation for 100G-and-beyond multi-haul coherent fiber-optic communications." Optical Fiber Communications Conference and Exhibition (OFC), 2016. IEEE, 2016.

iXblue, "iXblue Photonics Space Activities." 2016. https://photonics.ixblue.com/files/files/pdf/iXBlue_Space_modulators_06-2016-2.pdf

Janson, S. et al. "The NASA Optical Communications and Sensor Demonstration Program: Initial Flight Results." (2016).

JEDEC. "Measurement and Reporting of Alpha Particle and Terrestrial Cosmic Ray Induced Soft Errors in Semiconductor Devices." JESD89A. 2006.

Johnston, A. H., T. F. Miyahira, and B. G. Rax. "Proton damage in advanced laser diodes." IEEE Transactions on Nuclear Science 48.6 (2001): 1764-1772.

Johnston, A. H., and Tetsuo F. Miyahira. "Radiation degradation mechanisms in laser diodes." (2004).

Karp, James, et al. "Single-Event Latch-Up: Increased Sensitivity from Planar to FinFET." IEEE Transactions on Nuclear Science 65.1 (2018): 217-222.

Kaushal, Hemani, and Georges Kaddoum. "Optical communication in space: Challenges and mitigation techniques." IEEE communications surveys & tutorials 19.1 (2017): 57-96.

Kawakami, Hiroto, Eiji Yoshida, and Yutaka Miyamoto. "Auto bias control technique based on asymmetric bias dithering for optical QPSK modulation." Journal of Lightwave Technology 30.7 (2012): 962-968.

Kikuchi, Kazuro. "Optical coherent communications: Historical perspectives and future directions." High Spectral Density Optical Communication Technologies. By Nakazawa et al. Springer Berlin Heidelberg, 2010. 11-49.

Kisaka, Y., Masahito, T., and Miyamoto, Y. "Digital Signal Processor (DSP) for Beyond 100G Optical Transport". NTT Technical Review. 2016.

Kohtoku, Masaki. "Compact InP-based optical modulator for 100-Gb/s coherent pluggable transceivers." 2015 Optical Fiber Communications Conference and Exhibition (OFC). IEEE, 2015.

LaBel, Kenneth A., et al. "On the suitability of fiber optic data links in the space radiation environment: a historical and scaling technology perspective." Aerospace Conference, 1998 IEEE. Vol. 4. IEEE, 1998.

Lacoe, Ronald C., et al. "Application of hardness-by-design methodology to radiation-tolerant ASIC technologies." IEEE Transactions on Nuclear Science 47.6 (2000): 2334-2341.

Laser Light Communications. "HALO Global Optical Network." Website www.laserlightcomms.co/halo_network.php. 2017.

Leeb, W. and Winzer, P. "Photodetectors and Receivers." Chapter 7. Near-Earth Laser Communications. 2009.

Le Kernec, Arnaud, et al. "Space evaluation of optical modulators for microwave photonic on-board applications." International Conference on Space Optics—ICSO 2010. Vol. 10565. International Society for Optics and Photonics, 2017.

Li, S. "p-n Junction Diodes." Li S.S. (eds) Semiconductor Physical Electronics. Spring, New York, NY. 2006.

Li, Xiaolei, et al. "Modulation-format-free and automatic bias control for optical IQ modulators based on dither-correlation detection." Optics express 25.8 (2017): 9333-9345.

Lightwave, "OIF approves Micro Integrable Tunable Laser Assembly Implementation Agreement." 2011.

Lilja, K., et al. "Single-event performance and layout optimization of flip-flops in a 28-nm bulk technology." IEEE Transactions on Nuclear Science 60.4 (2013): 2782-2788.

Lipscomb, F, 2015. "CFP2-DCO and CFP2-ACO Transceivers – Basic Definitions." Neophotonics.

Lohmeyer, Whitney Q. "Space Radiation Environment Impacts on High Power Amplifiers and Solar Cells On-Board Geostationary Communications Satellites." Thesis. Massachusetts Institute of Technology, 2015.

López, Iria García, et al. "High speed BiCMOS linear driver core for segmented InP Mach-Zehnder modulators." Analog Integrated Circuits and Signal Processing 87.2 (2016): 105-115.

Lourenco, Nelson E., et al. "An investigation of single-event effects and potential SEU mitigation strategies in fourth-generation, 90 nm SiGe BiCMOS." IEEE Transactions on Nuclear Science 60.6 (2013): 4175-4183.

Lumentum, "Modulator, 100G/200G DP-QPMZ." https://www.lumentum.com/en/products/modulator-100g-200g-dp-qpmz. 2019.

Lumentum, "High Bandwidth Coherent Driver Modulator." https://www.lumentum.com/en/products/high-bandwidth-coherent-driver-modulator. 2019.

Lumentum, "Narrow Linewidth Micro-Integrable Tunable Laser Assembly – 6205-u-ITLA." Datasheet. 2018.

Lumentum, "Micro-Integrable Tunable Laser Assembly (ITLA), 100 kHz Linewidth, LambdaFLEX." https://www.lumentum.com/en/products/micro-itla-tunable-laser-100-khz . 2019.

Lumentum, "Micro-Integrated Coherent Receiver up to 64 Gbaud Symbol Rates." https://www.lumentum.com/en/products/micro-integrated-coherent-receiver-64-gbaud. Website. 2019.

MacDougall, J., et al. "Transmission and pump laser modules for space applications." Free-Space Laser Communication and Atmospheric Propagation XXIX. Vol. 10096. International Society for Optics and Photonics, 2017.

Maillard, Pierre, et al. "Neutron, 64 MeV Proton & Alpha Single-event Characterization of Xilinx 16nm FinFET Zynq® UltraScale+™ MPSoC." 2017 IEEE Radiation Effects Data Workshop (REDW). IEEE, 2017.

Maxim Integrated, Inc. "Thermoelectric Cooler Control Using the DS4830A Optical Microcontroller." Application Note 5425. 2015.

McMorrow, Dale, Joseph S. Melinger, and Alvin R. Knudson. "Single-event effects in III-V semiconductor electronics." International journal of high speed electronics and systems 14.02 (2004): 311-325.

Mecozzi, Antonio, and Mark Shtaif. "Information capacity of direct detection optical transmission systems." Journal of Lightwave Technology 36.3 (2018): 689-694.

Melle, S. "Will Coherent DSP Control Reshape the Optical Vendor Landscape?" LightReading. 2018.

Messenger, S. R. "Electron-and gamma-induced displacement damage effects in indium phosphide semiconductor devices." (1996): 2701-2701.

Milivojevic, Biljana, et al. "Demonstration of optical transmission at bit rates of up to 321.4 Gb/s using compact silicon based modulator and linear BiCMOS MZM driver." Journal of Lightwave Technology 35.4 (2017): 768-774.

Miroshnichenko, Leonty I. "Radiation Conditions in Space." Radiation Hazard in Space. Springer Netherlands, 2003. 23-46

Morsy-Osman, Mohamed, et al. "DSP-free 'coherent-lite'transceiver for next generation single wavelength optical intra-datacenter interconnects." Optics express 26.7 (2018): 8890-8903.

Mutuel, L.H. "Single Event Effect Mitigation Techniques Report." Federal Aviation Administration. DOT/FAA/TC-15/62 (2016).

Mynaric, "Inter-Satellite Link Terminal: MLT-80." Website. https://mynaric.com/products/space/. 2018.

Nelson, Lynn E., et al. "A robust real-time 100G transceiver with soft-decision forward error correction [Invited]." Journal of Optical Communications and Networking 4.11 (2012): B131-B141.

Neophotonics, "NeoPhotonics to Showcase 64 Gbaud Coherent Product Suite at ECOC 2017." Investor News Release. 2017.

Neophotonics, "Photonic IC Enabled Optical coherent Systems." 2018.

Neophotonics, "Micro-ITLA." https://www.neophotonics.com/product/uitla/. Website. 2018.

Neophotonics, "Micro-Intradyne Coherent Receiver." https://www.neophotonics.com/product/uicr/. Website. 2019.

Neophotonics, "Silicon Technology." https://www.neophotonics.com/technology/silicon. Website. 2019.

Neophotonics, "High Bandwidth Coherent Driver Modulator. "https://www.neophotonics.com/product/high-bandwidth-coherent-driver-modulator-hb-cdm/. 2019.

NIST. "X-Ray Mass Attenuation Co-efficients." https://physics.nist.gov/PhysRefData/XrayMassCoef/chap2.html?fbclid=IwAR10IS3l8NFc7ObQ_pUY0_0R8-J_45-XxJXXsmTrFsH0ofD2uEXYPlHnt5E. Website. 2019.

Normand, Eugene. "Single event effects in avionics and on the ground." International journal of high speed electronics and systems 14.02 (2004): 285-298.

Numata, Kenji, and Jordan Camp. "Precision laser development for interferometric space missions NGO, SGO, and GRACE Follow-On." Journal of Physics: Conference Series. Vol. 363. No. 1. IOP Publishing, 2012.

Oaida, Bogdan V., et al. "Optical link design and validation testing of the Optical Payload for Lasercomm Science (OPALS) system." SPIE LASE. International Society for Optics and Photonics, 2014.

Oclaro, "CDM." https://www.oclaro.com/product/CDM/. Website. 2018

Oclaro, "Micro-iTLA TL5400 Series." https://www.oclaro.com/product/micro-itla-tl5400-series-rel3/. Website. 2018.

OFC "OFC Post-show Report." https://www.ofcconference.org/library/images/ofc/PDF/2019/2019-OFC-Post-Show-Report.pdf, 2019.

Ogiso, Yoshihiro, et al. "Ultra-high bandwidth InP IQ modulators for next generation coherent transmitter." Compound Semiconductor Integrated Circuit Symposium (CSICS), 2017 IEEE. IEEE, 2017.

OIF, 2015. "Implementation Agreement for Integrated Dual Polarization Micro-Intradyne Coherent Receivers." IA # OIF-DPC-MRX-01.0.

OIF, 2015. "Implementation Agreement for Integrated Polarization Multiplexed Quadrature Modulated Transmitters for Metro Applications." IA # OIF_PMQ_MTX-01.0.

OIF, 2015. "Micro Integrable Tunable Laser Assembly Implementation Agreement." OIF-MicroITLA-01.1.

OIF, 2018. "Implementation Agreement for High Bandwidth Coherent Driver Modulator (HB-CDM)." OIF-HB-CDM-01.0.

O'Sullivan M. and Cartledge, J. "Digital Optical coherent System Performance Basics: Transceiver Technology and Performance." OFC Short Course, SC460. 2018.

Ott, Melanie, et al. "Fiber optic cable assemblies for space flight applications-Issues and remedies." 1997 World Aviation Congress. 1997.

Ott, Melanie, et al. "Reliability of optical fiber modulators for space flight environments." NASA Parts and Packaging Program Report, IPPAQ Task Report, NASA GSFC greenbelt, Maryland (2002): 1-17.

Petersen, E. "Approaches to proton singe-event rate calculations." IEEE Transactions on Nuclear Science 43.2 (1996): 496-504.

Pfau, Timo, et al. "Optical coherent communication: Towards realtime systems at 40 Gbit/s and beyond." Optics Express 16.2 (2008): 866-872.

Piazzolla, Sabino and Hemmati, Hamid. "Near-earth laser communications." Chapter 8 Atmospheric Channel. CRC press, 2009.

Poivey, Christian, and John H. Day. "Radiation hardness assurance for space systems." (2002).

Poizat, Marc. Space Radiation and its Effects on EEE Components - Total Ionizing Dose Mechanisms and Effects. N.p.: ESA/ESTEC, June 2009.

Porte, Henri, et al. "Optimization and evaluation in space conditions of multi-ghz optical modulators." International Conference on Space Optics—ICSO 2014. Vol. 10563. International Society for Optics and Photonics, 2017.

Pribil, Klaus and Hemmati, Hamid. "Near-Earth Laser Communications." Chapter 4. Laser Transmitters: Coherent and Direct Detection. Taylor & Francis Group, LLC, 2008.

Quinn, Heather, et al. "Single-event effects in low-cost, low-power microprocessors." Radiation Effects Data Workshop (REDW), 2014 IEEE. IEEE, 2014.

Rasmussen, Christian, et al. "Real-time DSP for 100+ Gb/s." Optical Fiber Communication Conference. Optical Society of America, 2013.

Renesas. "Rad Tolerant Op Amps." https://www.renesas.com/us/en/products/space-harsh-environment/rad-tolerant-analog/rt-op-amps.html. 2019.

Renesas. "Rad Hard Op Amps." https://www.renesas.com/us/en/products/space-harsh-environment/rad-hard-analog/rh-op-amps.html. 2019.

Rito, P., et al. "A monolithically integrated segmented driver and modulator in 0.25 μm SiGe: C BiCMOS with 13 dB extinction ratio at 28 Gb/s." 2016 IEEE MTT-S International Microwave Symposium (IMS). IEEE, 2016.

Roberts, Kim, et al. "Performance of dual-polarization QPSK for optical transport systems." Journal of lightwave technology 27.16 (2009): 3546-3559.

Robinson, B. et al. "Overview of the lunar laser communications demonstration." Free-Space Laser Communication Technologies XXIII. Vol. 7923. International Society for Optics and Photonics, 2011.

Robinson, Boroson, Schieler, Khatri, Guldner, Constantine, Shih, Burnside, Bilyeu, Hakimi, Garg, Allen, Clements, Cornwell, "TeraByte InfraRed Delivery (TBIRD): a demonstration of large-volume direct-to-Earth data transfer from low-Earth orbit ," Proc. SPIE 10524, Free-Space Laser Communication and Atmospheric Propagation XXX, 105240V (15 February 2018); doi: 10.1117/12.2295023

Roche, Philippe, et al. "Technology downscaling worsening radiation effects in bulk: SOI to the rescue." 2013 IEEE International Electron Devices Meeting. IEEE, 2013.

Rose, Todd, et al. "Optical Communications Downlink from a 1.5 U CubeSat: OCSD Program." (2018).

Samaras, Anne. "Single Event Effects and Rate Calculation." TRAD Short Course, 2014.

Savory, Seb J. Electronic signal processing in optical communications. Proc. SPIE 7136, Optical Transmission, Switching, and Subsystems VI, 71362C (2008, November 11); doi:10.1117/12.806530

A. Seas, B. Robinson, T. Shih, F. Khatri, and M. Brumfield. "Optical Communications Systems for NASA's Human Space Flight Missions." ICSO, 2018.

Seki, Morihiro, et al. "Compact 224-Gbit/s Modulator Modules for Digital Optical coherent Communication Systems." SEI TECHNICAL REVIEW 80 (2015): 61.

Seltzer, S.M. "SHIELDOSE, A Computer Code for Space-Shielding Radiation Dose Calculations." National Bureau of Standards, NBS-IR 74457. 1980.

Seltzer, S.M. "Updated calculations for routine space-shielding radiation dose estimates: SHIELDOSE-2." NIST Publication, NISTIR 5477. 1994.

Serra, P. et al. "Optical Communications Crosslink Payload Prototype Development for the Cubesat Laser Infrared CrosslinK (CLICK) Mission." 33rd Annual AIAA/USU Conference on Small Satellites. 2019.

Shin-Etsu Chemical Compound Co. "Thermal Interface Material." https://www.shinetsusilicone-global.com/products/function/heat/index.shtml. 2019.

Sinclair, Doug, and Kathleen Riesing. "The Rainbow Connection-Why Now is the Time for Smallsat Optical Downlinks." (2017).

Stanley, 2017. "100G Growth Fuels Race to 5400G and Beyond." LightReading, Networking the Communications Industry. https://www.lightreading.com/components/optical-components/100g-growth-fuels-race-to-400g-and-beyond/a/d-id/734838

Stark, John P.W. "Chapter 2 The Spacecraft Environment and Its Effect on Design." Space Systems Engineering. Ed. Peter W. Stark, 2011.

Stiller, Marc. "Coherent DSP Evolution and Trade-Offs." Neophotonics Blog. https://www.neophotonics.com/digital-signal-processing-dsp/. 2018.

Sukhaseum, Nicolas. "Radiation Engineering." TRAD Short Course (2017).

Suparta, Wayan. "The variability of space radiation hazards towards LEO spacecraft." Journal of Physics: Conference Series. Vol. 539. No. 1. IOP Publishing, 2014.

Takechi, Masaru, Yoshihiro Tateiwa, and Shoichi Ogita. "Compact 100G coherent receiver using InP-based 90° hybrid integrated with photodiodes." Optical Communication (ECOC 2013), 39th European Conference and Exhibition on. IET, 2013.

Takechi, Masaru, et al. "Compact Optical Receivers for Optical coherent Communication." SEI TECHNICAL REVIEW 85 (2017): 25.

Tambara, Lucas Antunes, et al. "On the Characterization of Embedded Memories of Zynq-7000 All Programmable SoC under Single Event Upsets Induced by Heavy Ions and Protons." Radiation and Its Effects on Components and Systems (RADECS), 2015 15th European Conference on. IEEE, 2015.

Tambara, Lucas Antunes, et al. "Analyzing the impact of radiation-induced failures in programmable SoCs." IEEE Transactions on Nuclear Science 63.4 (2016): 2217-2224.

Telcordia, "Generic Reliability Assurance Requirements for Passive Optical Components." GR-1221. 2010.

Telcordia, "Generic Reliability Assurance Requirements for Optoelectronic Devices Used in Telecommunications Equipment." GR-468. 2004.

Thomes, William J., et al. "Investigation of hermetically sealed commercial LiNbO3 optical modulator for use in laser/LIDAR space-flight applications." Nanophotonics and

Macrophotonics for Space Environments. Vol. 6713. International Society for Optics and Photonics, 2007.

Todd, Michael, and Tom Farrell. "Radiation hardness assessment of widely tunable and DFB lasers." International Conference on Space Optics—ICSO 2006. Vol. 10567. International Society for Optics and Photonics, 2017.

Toni Tolker-Nielsen, Gotthard Oppenhauser, "In-orbit test result of an operational optical inter-satellite link between ARTEMIS and SPOT4, SILEX," Proc. SPIE 4635, Free-Space Laser Communication Technologies XIV, (26 April 2002); doi: 10.1117/12.464105

Toyoshima, Morio, et al. "Ground-to-satellite optical link tests between Japanese laser communications terminal and European geostationary satellite ARTEMIS." Lasers and Applications in Science and Engineering. International Society for Optics and Photonics, 2004.

Troska, Jan, et al. "Neutron, proton and gamma radiation effects in candidate InGaAs pin photodiodes for the CMS tracker optical links." No. CERN-CMS-NOTE-1997-102. 1997.

Tsunashima, Satoshi, et al. "Silica-based, compact and variable-optical-attenuator integrated coherent receiver with stable optoelectronic coupling system." Optics express 20.24 (2012): 27174-27179.

Tuite, Don. "Understanding In-Flight and In-Space Radiation Effects On CMOS Devices." Electronic Design. N.p., 21 Oct. 2013. Web. <http://electronicdesign.com/circuit-protection/understanding-flight-and-space-radiation-effects-cmos-devices>.

Varotsou, Athina. "Space Radiation Environment." TRAD Short Course, 2017.

Venghaus, Herbert, and Norbert Grote, eds. Fibre optic communication: key devices. Vol. 161. Springer, 2017.

Vora, Pavan and Lad, Ronak. "A Review paper on CMOS, SOI and FinFET Technology." 2017.

Vu, K. N., and J. Y. Yaung. "Radiation Effects on InP-Based Electrical & Optical Devices." 1st Intl Conf on Indium Phosphide and Related Materials for Advanced Electronic and Optical Devices. Vol. 1144. International Society for Optics and Photonics, 1989.

Walker, R. G., et al. "Electro-optic modulators for space using gallium arsenide." International Conference on Space Optics—ICSO 2016. Vol. 10562. International Society for Optics and Photonics, 2017.

Walters, R. J. "A review of radiation effects in InP solar cells." Indium Phosphide and Related Materials, 1994. Conference Proceedings., Sixth International Conference on. IEEE, 1994.

Walters, R. J., et al. "Radiation response of InP/Si and InGaP/GaAs space solar cells." solar energy materials and solar cells 50.1-4 (1998): 305-313.

Wang, Gary, "Optical IQ modulators for coherent 100G and beyond." Lightwave. Mar/Apr 2015.

Way, Winston, "Coherent IQ Modulator Performance." 2016. Neophotonics.

Weaver, B. D., D. A. L. E. McMORROW, and L. M. Cohn. "Radiation effects in III-V semiconductor electronics." International journal of high speed electronics and systems 13.01 (2003): 293-326.

Weinberg, I., et al. "Radiation and temperature effects in gallium arsenide, indium phosphide and silicon solar cells." (1987).

Xapsos, et al. "Near-Earth space radition models." IEEE Transactions on Nuclear Science 60.3 (2012): 1691-1705.

Xiang, L., Chandrasekhar, S., and Winzer, P. "Digital Signal Processing Techniques Enabling Multi-Tb/s Superchannel Transmission: An overview of recent advances in DSP-enabled superchannels." IEEE Signal Processing Magazine 31.2 (2014): 16-24.

Xilinx. "Zynq UltraScale+ MPSoc Data Sheet: Overview." https://www.xilinx.com/support/documentation/data_sheets/ds891-zynq-ultrascale-plus-overview.pdf. 2018.

Yagi, Hideki, et al. "High receiver responsivity and low dark current of InP-based pin-photodiode array monolithically integrated with 90° hybrid and spot-size converter using selective embedding regrowth." IEICE Electronics Express 12.2 (2015): 20141018-20141018.

Yamazaki, Hiroshi, et al. "Integrated 100-Gb/s PDM-QPSK modulator using a hybrid assembly technique with silica-based PLCs and LiNbO 3 phase modulators." 2008 34th European Conference on Optical Communication. IEEE, 2008.

Young, J. "Is 99.999% Operational Availability Practical for Department of Defense Systems?" Defense AT&L. January – February 2010.

Zhang Q., Wang G. (2017) Influence of HY-2 Satellite Platform Vibration on Laser Communication Equipment: Analysis and On-Orbit Experiment. In: Urbach H., Zhang G. (eds) 3rd International Symposium of Space Optical Instruments and Applications. Springer Proceedings in Physics, vol 192. Springer, Cham

Zech, H., et al. "LCT for EDRS: LEO to GEO optical communications at 1, 8 Gbps between Alphasat and Sentinel 1a." Unmanned/Unattended Sensors and Sensor Networks XI; and Advanced Free-Space Optical Communication Techniques and Applications. Vol. 9647. International Society for Optics and Photonics, 2015.

Zech, H., et al. "LCTS on Alphasat and Sentinel 1A: in orbit status of the LEO to GEO data relay system." International Conference on Space Optics—ICSO 2014. Vol. 10563. International Society for Optics and Photonics, 2017.

Zech, Herwig, et al. "Optical inter-satellite links for navigation constellations." International Conference on Space Optics—ICSO 2018. Vol. 11180. International Society for Optics and Photonics, 2019.